Frataxin deficiency coordinates iron-sulfur-dependent metabolic and genomic stress to promote endothelial senescence in pulmonary hypertension

by

Miranda Kay Culley

Bachelor of Arts, Case Western Reserve University, 2014

Submitted to the Graduate Faculty of the

School of Medicine in partial fulfillment

of the requirements for the degree of

Doctor of Philosophy

University of Pittsburgh

2020

UNIVERSITY OF PITTSBURGH

SCHOOL OF MEDICINE

This dissertation was presented

by

Miranda Kay Culley

It was defended on

August 3, 2020

and approved by

Mark Gladwin, M.D., Jack D. Myers Professor and Chair of the Department of Medicine

Wendy Mars, Ph.D., Associate Professor, Department of Pathology

Alison Morris, M.D., M.S., Professor, Department of Medicine

Timothy Oury, M.D., Ph.D., Professor, Department of Pathology

Bennett Van Houten, Ph.D., Richard M. Cyert Professor of Molecular Oncology, Department of Pharmacology and Chemical Biology

Dissertation Director: Stephen Y. Chan, M.D., Ph.D., Professor, Department of Medicine

Frataxin deficiency coordinates iron-sulfur-dependent metabolic and genomic stress to promote endothelial senescence in pulmonary hypertension

Miranda Kay Culley, Ph.D.

University of Pittsburgh, 2020

Pulmonary hypertension (PH) is a heterogeneous, fatal disease of the lung vasculature with incompletely defined molecular underpinnings. Specifically, the pathological contributions of endothelial cells to this panvasculopathy remain controversial and unresolved. Endothelial mitochondrial dysfunction and DNA damage have been separately linked to PH, but any shared mechanistic regulation, joint contribution to shifting endothelial phenotypes, and relevance across PH subtypes are unknown. Mutations in the iron-sulfur (Fe-S) biogenesis gene frataxin (*FXN*) disrupt metabolism and genomic integrity, causing Friedreich's ataxia (FRDA). This multisystem disease is defined by neurodegeneration and hypertrophic cardiomyopathy (HCM) with the latter driving patient mortality. HCM is often complicated by PH but few studies have interrogated pulmonary vascular phenotypes in FRDA. Separately, deficiencies of other Fe-S cluster assembly genes induced endothelial mitochondrial dysfunction and PH development *in vivo*. Therefore, we hypothesized that endothelial FXN deficiency and its metabolic and genomic consequences may predispose to PH. Here, we demonstrated acute FXN knockdown abrogated Fe-S biogenesis to attenuate mitochondrial respiration and induce replication stress and growth arrest. Sustained FXN deficiency led to inhibition of Fe-S-containing nuclear proteins, persistent DNA damage response, and apoptosis resistance, culminating in increased vasomotor tone and senescence. Consequently, endothelial FXN deficiency in hypoxic mice increased senescence and worsened PH, which could be prevented with senolytic treatment. Supporting this mechanism, reduced FXN expression alongside elevated senescence markers were observed in animal and patient lung tissues

representing multiple PH etiologies. Specifically, we defined HIF-α-dependent epigenetic reduction of FXN, illustrating the relevance of acquired FXN deficiency in the pulmonary endothelium. Notably, FXN-dependent endothelial senescence was also demonstrated in inducible pluripotent stem cells-derived endothelial cells from patients with FRDA, offering a plausible explanation for a predisposition to PH, independent of or additive to left ventricular dysfunction. Altogether, these data demonstrate that epigenetic or genetic FXN deficiency orchestrates Fe-S-dependent metabolic and replication stress which converge on irreversible senescence, signifying a novel endothelial-specific mechanism across PH subtypes, including PH due to left heart disease. In doing so, this work offers foundational evidence for the identification of a cohort of FRDA patients at risk for PH and endorse several Fe-S-related treatment options including senotherapies.

Table of Contents

List of Tables

List of Figures

Preface

This dissertation is a compilation of reviews (1), manuscripts (in preparation), and ongoing projects I pursued as a graduate student in the Cellular and Molecular Pathology program at the University of Pittsburgh School of Medicine. While this thesis and these works were my responsibility over the last four years, I acknowledge the tremendous scientific, professional, and personal support of many in the rigor, innovation, and potential impact of this product.

To my thesis mentor, Dr. Stephen Chan – Preceding your arrival to the university, three separate people lauded your science and recommended you as a potential thesis mentor. Exceeding even these high expectations, I am now confident that I would not have been able to complete this training with any other mentor. I have had the great privilege of learning from your example about what it means to be collaborative, innovative, and relentless in one's pursuit of a research question. Moreover, true to your words on your commitment to being my advisor 4 years ago, you have demonstrated what it means to be an affable, available, and adaptable mentor. Thank you for your belief in and dedication to our work; this unwavering support allowed for numerous local, national, and even international presentations, awards, and (future) manuscripts. Thank you also for your belief in my potential as a physician scientist; this commitment to my training included professional opportunities to write reviews and editorials, submit grant proposals, and mentor my own undergraduate students. Equal to your professional impact, I have appreciated working with someone with your optimism and integrity. I am extremely grateful for your guidance and friendship. I hope to make you proud, and I hope to pay it forward.

To my committee members – Despite your incredibly busy schedules, you all have gone above and beyond the typical biannual advisement. You have made yourselves available, sending

emails, attending my presentations, and meeting one-on-one. Both your scientific and professional feedback have enriched my work and my pursuit of this career path. I consider it a great honor to have received your council.

To Dr. Mars – You have been a constant advocate since before I even matriculated as an MSTP student. I sincerely appreciate your understanding and efforts in helping me finding my thesis lab.

To Dr. Steinman – Thank you for seeing my potential and giving me the opportunity and privilege to pursue this career path. I have always appreciated your equal concern for my scientific training and personal well-being. To me, that is the mark of a great leader and mentor.

And though less involved during my graduate training, no less crucial to my arrival at this milestone are my previous mentors and teachers. Thank you to *Dr. Robert Koeth, Jennifer Buffa, and Dr. Stanley Hazen* for their continued guidance and support. The opportunity to work as an member of the Hazen laboratory team was the foundational experience that instilled a passion and appreciation for the importance of bringing science to medicine. Thank you to *Mrs. Toni Purcell* who taught me how to conduct a primary literature search and encouraged me to be both a critical and creative thinker from a very young age. Lastly thank you to *Mr. Brett Becker* (also a University of Pittsburgh graduate), who taught me that I was capable of any intellectual challenge if I put in the work and who was by far the best teacher I have ever had.

To members of the Chan laboratory – Thank you for your continued contributions to these projects, your patience, and your friendships. This truly took a village, and I have appreciated being a part of the same team and learning from all of you.

To my friends and family (near and far) – Your companionship as well as calls, texts, visits and check-ins have brought perspective, comfort, levity, and joy to the sometimes frustrating and monotonous day-to-day realities of this process.

To my parents – Your contributions to my success are innumerable, and I have struggled to convey even a few here…As musicians, you both have modeled for me the importance of humility, a strong work ethic, and finding a way to share your passion and your talents with others. As teachers, you have set an example of patience, generosity and service to others. To mom, you have taught me resiliency in the pursuit of long-term goals and the importance of self-reflection and self-improvement. To dad, you have taught me the importance of listening and curiosity and have inspired a love of learning. Thank you both for your sacrifices, encouragement, and love. I am so grateful and proud to be your daughter.

1.0 Introduction

1.1 Pulmonary hypertension

Pulmonary hypertension (PH) is a progressive, enigmatic disease marked by pathological narrowing and occlusion of the distal arterioles and small vessels of the lung. In turn, this panvascular remodeling causes elevated pulmonary vascular resistance (PVR $\geq$3 Wood units) and mean pulmonary arterial pressure (mPAP >20mmHg), resulting in right ventricular failure and thus significant morbidity and mortality in this patient population (2, 3).

1.1.1 Cellular pathology

Addressing the primary pathology, histologic imaging of lungs from patients with the particularly severe PH subtype, pulmonary arterial hypertension (PAH), illustrates medial layer hypertrophy and hyperplasia, proliferation and fibrosis of the intimal and adventitial layers, perivascular inflammation, *in situ* thrombosis, and the distinctive, end-stage plexiform lesions (4). The pathological vessel architecture provides some insight into the fundamental cell-specific dysfunction present. For example, the hypertrophy and hyperplasia of the medial and adventitial layers reflects an apoptosis-resistant, pro-proliferative phenotype in pulmonary artery smooth muscle cells (PASMCs) (a synthetic phenotype as compared to a contractile phenotype) (5) and adventitial fibroblasts (PAAFs) (6). Accumulation of these cells results in enhanced vasoconstriction (7), vessel stiffening due to fibrotic matrix deposition (8, 9), and perivascular inflammation (10, 11), altogether contributing to the structural remodeling that precipitates disease.

1.1.1.1 Controversial endothelial phenotypes

Pulmonary endothelial dysfunction is another defining feature of panvascular remodeling in PAH but remains incompletely understood. Histologic evaluation provides evidence of significant microvascular loss (vessel rarefaction) (12, 13) as well as neointimal proliferation and "angio-obliterative" lesions in lungs from patients with end-stage PAH (4). Therefore, unlike the unilateral hyperproliferation observed in other vascular types, both apoptosis and proliferation have been ascribed to pulmonary endothelial dysfunction. Controversy exists over the timing and relative pathogenicity of these cell fates in pulmonary vessel remodeling and disease development (14-16). Specifically, induction of endothelial apoptosis in different animal models resulted in pulmonary vessel rarefaction prior to disease development and endothelial proliferation (17, 18); these time-dependent studies highlight endothelial apoptosis as a trigger of PAH and suggest proliferation could be an epiphenomenon later in disease.

Separately, other *in vivo* models have established a causative role for endothelial proliferation in neointimal formation and PAH development (19, 20). Altogether, the major hypothesis in the field postulates that the endothelium is the site of inciting injury and apoptosis followed by hyperproliferation (21-24); however, dynamic control and the causative importance of these divergent cell fates remains unclear. Furthermore, how these changes in endothelial cell survival impact the other aspects of endothelial cell function important in PH, such as permeability, vasomotor tone, inflammatory and thrombolytic signaling, as well as cell-to-cell communication with circulating immune cells and smooth muscle cells (25), is not well-defined.

This observed shift in endothelial cell phenotype may also support the notion of heterogenous endothelial populations in the pulmonary vascular tree with the added possibility of other cell fates (*e.g.*, endothelial-to-mesenchymal transition (EndoMT) (26-28)) beyond the

accepted apoptosis *versus* proliferation binary. Senescence, defined by irreversible growth arrest and a pro-inflammatory senescence-associated secretory phenotype (SASP) (29, 30), represents one alternative endothelial outcome important in the pathology of extrapulmonary vascular beds (31, 32) that has been linked but not yet described in depth in PAH (33, 34). In aging and age-associated diseases, multiple aberrant processes converge to drive senescence, including attenuated mitochondrial (35-37) and genomic integrity (29, 30). However, the complex regulatory events that control putative endothelial senescence and how such events fit into the evolution of pulmonary endothelial cell function are not known.

1.1.2 Molecular pathology

1.1.2.1 Mitochondrial dysfunction

Extensive basic, translational, and clinical analyses spanning over two decades support a causative link between metabolic reprogramming and PAH (5). Parallel to Warburg's observations that proliferating tumor cells display mitochondrial respiratory repression followed by increased glucose uptake and glycolysis (38, 39), foundational studies demonstrated a mechanism for diminished glucose oxidation and increased glycolysis in PASMCs. Specifically, in PH, hypoxia-inducible factor alpha (HIF-α)-dependent upregulation of pyruvate dehydrogenase kinases 1 and 2 (PDK1/2) inhibits pyruvate dehydrogenase (PDH)-mediated conversion of pyruvate to acetyl-CoA (40, 41). Notably, the master transcription factors HIF-1 and HIF-2α are critical effectors in this metabolic shift and are stabilized by hypoxic, inflammatory, and metabolic stress – known pathologic triggers of PH (42-44). Coupled with metabolically-driven hyperpolarization of the mitochondria membrane (40, 41, 45, 46), "aerobic glycolysis" results in less efficient energy production but more biomass for cell division, giving rise to the anti-apoptotic and pro-

proliferative PASMC phenotype observed in disease. While prior studies initially focused on tissues with high bioenergetic requirement and high mitochondrial content, like PASMCs, this metabolic shift has since been observed in other pulmonary vascular cell types (10, 11, 47-50), the right ventricle (51), and even cells outside the RV-PA circuit (52-55) in animal models and patients with PH.

In addition, while the Warburg effect has served as a conceptual anchor, additional data has expanded the focus to include other forms of metabolic rewiring (*e.g.*, glutaminolysis (56, 57), fatty acid oxidation (58, 59), pentose phosphate pathway (60-62)) as well as changes in mitochondrial structure and function including altered ROS signaling (63) and iron handling (64), increased fission (65-67), and decreased mitochondrial mass due to an imbalance in mitochondrial biogenesis (53, 68) and clearance (mitophagy) across multiple cell types (1). For endothelial cells specifically, an understanding of metabolic reprogramming and mitochondrial dysfunction is still developing. Studies have characterized attenuated oxidative phosphorylation with elevated compensatory glycolysis (49, 50, 69-72), altered fatty acid handling (73), and increased glutaminolysis (74, 75); in turn this metabolic rewiring has been linked to decreased mitochondrial biogenesis (76, 77) and increased mitophagy (78). Interestingly, these data attribute mitochondrial dysfunction as drivers of both apoptosis and proliferation. Despite the fact that PH pathogenesis seems to converge at the mitochondria, fundamental questions still remain, including the causal mechanism(s) of mitochondrial dysfunction and how the dysregulated metabolic programs promote cell specific-dysfunction, particularly in the endothelium, during different disease stages. Further interrogation of endothelial mitochondrial function could be instrumental in characterizing the maladaptive shift between early-stage apoptosis and late-stage hyperproliferation (21, 23) or

in explaining alternative cell fates already associated with mitochondrial dysfunction in PH (79) or in other vascular diseases (80).

In sum, more work is required to define spatio-temporal phenotypes and their functional consequences in the pulmonary endothelium of patients with PAH as well as other, lesser characterized forms of PH. Ultimately, an understanding of the dynamic phenotypic landscape could have significant translational implications, potentially facilitating diagnostic determination of disease stage and therapy options.

1.1.2.2 DNA damage

DNA damage represents a less defined molecular driver recently been linked to PH pathogenesis (81-83). Broadly, DNA lesions represent a diverse number of chemical modifications to the genome, including but not limited to single- and double-stranded DNA breaks, that can inhibit normal replication and transcription, result in mutations (*i.e.*, genomic instability), alter cell viability, and ultimately influence human disease. There are several endogenous drivers of DNA damage, including products of metabolism, like oxidative stress, and replication stress (84). Addressing the latter, replication stress disrupts genomic integrity by compromising efficient, error-free replication fork progression and resulting in pathological DNA breaks (84). In turn, replication stress (or another endogenous drivers) results in the DNA damage response (DDR), a multi-step process that detects damage and signals for DNA repair (85); measurement of enhanced signaling within this network of proteins of is often used as a surrogate for the underlying DNA damage. If repair is fundamentally impaired or overwhelmed by an increase in the causative agents of endogenous DNA damage, cell-fate outcomes vary between apoptosis and senescence depending upon length and severity of stressor and cell type (86, 87).

Both pulmonary smooth muscle cells (88) and endothelial cells exhibit markers of DNA damage. Speaking to the latter, initial studies highlighted the presence of microsatellite and chromosomal instability in the clonal endothelial population of neointimal lesions in PAH (82, 89-91). Additional data demonstrated elevated baseline as well as oxidative stress-induced DNA damage in cultured pulmonary artery endothelial cells (PAECs) from these patients (82) with both studies attributing endothelial survival and proliferation to the underlying genomic instability. Conversely, other studies have shown that decreased expression of DDR markers associated with an increased sensitivity to apoptosis in PAH (92, 93). Therefore, to date there is no consensus or definitive mechanism by which DNA damage promotes proliferation versus apoptosis (versus senescence) in endothelial cells. Moreover, there is little data describing the driver(s) of this genomic damage. Whether DNA damage promotes disease outside of PAH is not yet defined; however, given that DNA damage accumulates as we age, DNA damage-associated outcomes could be particularly important in PH subtypes due to age-associated comorbidities.

In summary, the underlying endothelial dysfunction in PAH is controversial and incompletely defined. Endothelial mitochondrial dysfunction and DNA damage have been separately linked to PAH, but any shared mechanistic regulation of dynamic endothelial phenotypes and relevance across PH subtypes other than PAH are unknown.

1.1.3 Epidemiology and classification

PH is a heterogenous disease driven by multiple disparate triggers. The term PH encompasses several groups of patients categorized based upon clinical criteria and etiology. These distinctions reflect patient prognosis and therapeutic options as our understanding of disease pathophysiology (1.1 and 1.2) as well as existing treatments are largely exclusive to Group 1 PAH

which is the result of idiopathic or heritable causes or associated with conditions such as connective tissue disease, infection, toxin exposure, and congenital heart disease. Separately, PH in groups 2-5 occurs secondary to a myriad of comorbidities: left heart disease (Group 2), hypoxic lung diseases (Group 3), chronic thromboembolic disease (CTEPH, Group 4), as well as other multifactorial, ill-defined conditions such as hematologic and metabolic disorders (Group 5) (3).

According to the Registry to Evaluate Early and Long-term PAH Disease Management (REVEAL registry) (94), there is an estimated incidence and prevalence are 2.3 and 12.4 cases of PAH per million adults, respectively (95). Within this population, there is female: male predominance (~4:1) and paradoxically a female survival benefit (96) that remains incompletely defined. Although characterized as a disease of previously healthy, young-to-middle-aged adults in the past, recent data suggests the PAH population has an increased proportion of older adults with the average age of enrollment in the REVEAL registry being 53$\pm$15 years (97). Moreover, these older patients are more likely to present with more advanced disease, decreased exercise capacity, and multiple co-morbidities, making management more complicated (97-99).

As the population ages, the number of patients with chronic illnesses rises with cardiovascular disease (30.3%) and chronic respiratory illnesses (9.5%) among the leading contributors in patients $\geq$60 years old (100). Therefore, Group 2 PH due to left heart disease (101, 102) and Group 3 PH due to hypoxic lung disease (103, 104) represent an emerging majority of PH patients. The prevalence of the most common Group 2 PH is dependent upon the specific type of left ventricular dysfunction. For example, specific studies have shown that PH was present in 51% of patients with obstructive hypertrophic cardiomyopathy (HCM) and advanced heart failure (105) and 83% of patients with heart failure with preserved ejection fraction (HFpEF) (106). Similarly, Group 3 PH resulting from chronic lung diseases is also relatively common, especially

in with more severe disease (103); for patients with advanced or severe disease, up to 90% of those with chronic obstructive pulmonary disease (COPD) (107, 108), up to 50% with emphysema (109), and between 30-60% with idiopathic pulmonary fibrosis (IPF) exhibited PH (110, 111). In sum, PH represents a significant disease burden in patients with left heart disease or chronic lung disease; however, there are no treatment strategies available.

The clinical distinction between Group 2 PH and the other PH groups is made using right heart catheterization, which directly measures mPAP, cardiac output (CO), and pulmonary artery wedge pressure (PAWP) with the latter achieved by occluding a smaller branch of the pulmonary artery with the balloon catheter tip ('wedging') and allowing for evaluation of the pressure beyond the balloon tip – a reflection of pulmonary venous and left heart hemodynamics. From these values, pulmonary vascular resistance can be calculated using the principles of Ohm's law and the following equation: PVR=(mPAP–PAWP)/CO. A mPAP >20mmHg coupled with varying PAWP and PVR measurements delineates between pre-capillary PH, post-capillary, or combined pre- and post-capillary PH. Pre-capillary hemodynamic values (PAWP $\leq$15mmHg, PVR $\geq$3WU) reflect intrinsic pulmonary vasculopathy often observed in Groups 1, 3, 4, and 5 PH while post-capillary values (PAWP >15mmHg, PVR <3WU) reflect backward transmission of elevated left-sided filling pressures into the pulmonary circulation in Group 2 PH (3). Importantly, many patients meet the criteria for multiple PH categories, especially as the PH population ages, often reflected as combined pre- and post-capillary PH pressures (PAWP >15mmHg, $\geq$3WU). Specifically, there is emerging evidence that "Group 1-like" primary vascular pathophenotypes contribute to Group 2 PH (112), and are not solely due to vascular reactions to increased left heart afterload (105, 113). Consequently, Group 1 versus Group 2 PH can be difficult to diagnose and treat and often portends increased morbidity and mortality (114).

As our understanding of this enigmatic disease develops, this classification schema and its defining clinical features are modified by the by the World Symposium on Pulmonary Hypertension (WSPH) Task Force every five years. Specifically, the hemodynamic features of disease were recently updated to reflect a mean pulmonary artery pressure (mPAP) above 20 mmHg instead of the previously arbitrary 25 mmHg threshold (3). It should be noted that some data included in this dissertation will be based upon prior hemodynamic guidelines. While these WSPH groups provide necessary guidelines for diagnosis and treatment, the distinctions between these clinical phenotypes are not always clear, especially with co-morbidities in patients of advanced age. Furthermore, these classifications do not yet adequately incorporate emerging molecular drivers of this disease. Thus whether there is overlap in the mechanisms that underlie PAH and other PH groups, in particular Group 2 and 3 PH, remains incompletely defined. The molecular classification of PH will require a better understanding of the shared pulmonary vascular pathophysiology but has the potential for improved management and prognosis in lesser characterized subtypes as well as those patients with a mixed clinical picture.

1.1.4 Prognosis and therapies

According to the REVEAL registry, 1-, 3-, 5-, and 7-year survival rates in PAH patients from the time of diagnosis were 85%, 68%, 57%, and 49%, respectively (95). More specifically, five-year survival of newly diagnosed patients as stratified modified New York Hear Association (NYHA)/World Health Organization (WHO) functional class (I, II, III, IV) remains poor at 72.2%, 71.7%, 60.0%, and 43.8% (115). Routine evaluation of the patient's exercise and functional capacity (as measured by the 6-minute walk distance (6MWD) and NYHA/WHO functional class), hemodynamic instability (*e.g.,* right atrial pressure, cardiac index), and limited biomarkers (*e.g.,*

the N-terminal fragment of brain natriuretic peptide (NT-proBNP)) allows for the assessment of response to treatment and well as risk of mortality (116).

PH-specific treatments are only effective for patients with Group 1 PAH and target three primary mechanisms involved in vasomotor tone regulation: endothelin-1 (ET-1), nitric oxide (NO), and prostacyclin signaling pathways (117). To start, endothelin-1 (ET-1) acts at G-protein coupled receptors ET_A and ET_B: ET_A exists predominately on pulmonary smooth muscles cells and controls vasoconstriction as well as cellular proliferation, hypertrophy, and fibrosis while ET_B is expressed on both endothelial and smooth muscle cells, inducing vasodilatory and anti-proliferative signaling and vasoconstrictive signaling in these respective cell types (118). There is simultaneous elevation of ET-1 in the plasma (119) and lungs (120) and receptor expression in smooth muscle cells of patients with PH (118). Consequently, endothelin receptor antagonists that target ET_A (ambrisentan) or both ET_A and ET_B (bosentan, macitentan) each improved functional outcomes (121, 122) or prevented morbidity and mortality (123).

Separately, nitric oxide (NO) is produced by endothelial nitric oxide synthase (eNOS) and promotes vasodilation by binding soluble guanylyl cyclase (sGC), which in turn, converts guanosine triphosphate (GTP) to the secondary messenger cGMP to activate cGMP-dependent protein kinase (PKG) and relax smooth muscle cell contractile filaments. In multiple forms of PH, NO bioavailability is diminished due to reduced expression of eNOS (124) or inadequate levels of enzymatic cofactors required for NO biosynthesis (uncoupling) (125, 126). While NO reduction contributes to the vasoconstrictive pathophenotype of this disease, data also suggest the NO-sGC-cGMP pathway alters platelet aggregation, leukocyte recruitment, inflammation, fibrosis, smooth muscle proliferation, and pulmonary vascular remodeling. Currently two drug classes work to improve NO signaling: sGC stimulators and PDE5 inhibitors. First, the sGC stimulator riociguat

binds the prosthetic heme group of sGC to enhance cGMP production either independent of or in tandem with available NO (127) and represents the first in its drug class approved for treatment of different subtypes of Group 1 PAH (128-130) and refractory Group 4 CTEPH (131) with significant improvements in 6MWD and WHO functional class. Notably, emerging data in pre-clinical models suggests the use of riociguat may be beneficial for other PH groups (132). Downstream of sGC, the secondary messenger cGMP is degraded by the enzyme phosphodiesterase 5 (PDE5), which is highly expressed in vascular smooth muscle cells (133). PDE5 inhibitors, like sildenafil and tadalafil, interfere with the catalytic domain to prevent hydrolysis and thus enhance cGMP activity in PAH (134-136).

Lastly, prostacyclin is an endothelial prostanoid and also acts as a vasodilator by binding its prostaglandin I2 (PGI_2) receptor on smooth muscle cells. From there, activation of adenylyl cyclase (AC) leads to the conversion of adenine triphosphate (ATP) to cAMP and subsequent activation of protein kinase A (PKA), exerting anti-platelet, anti-thrombotic, and anti-proliferative effects in addition to vasodilation of the vasculature (137). Patients with Group 1 PAH exhibit decreased prostacyclin levels (138) as well as reduced synthase (139) and receptor expression (140). Continuous infusion of the prostanoid analogue, epoprostenol, improves exercise capacity, hemodynamic instability, and overall survival, and remains a foundational therapy in patients with severe PAH. Newer formulations that are longer-lasting and do not require continuous administration, like treprostinil, are approved for treatment-naïve patients (141) or in combination with other vasodilatory therapies (142). In addition to these analogues, selexipag (hydrolyzed by the liver to the active metabolite ACT-333679) acts as a selective agonist for the prostacyclin IP receptor and reduces worsening of PH (e.g. diminished 6MWD or worsened WHO functional class) or complications related to PH (*e.g.*, hospitalizations, listing for transplantation) (143).

While these therapies, particularly in combination (144), may improve clinical measures of disease, there is still no cure for PAH and patients remain functionally impaired despite these drugs with extreme interventions such as the creation of a right to left shunt (a bridge to transplant) or bilateral lung transplant required for refractory patients (145). Moreover, these vasodilatory therapies have been clinically tested in patients with Group 2 and 3 PH with mixed outcomes that do not comprehensively support their use in these patient populations (103, 146), leaving a majority of PH patients without available treatments. Therefore, the search for diagnostic and therapeutic tools that target the causative mechanisms of disease continues. In response, there are several emerging therapies aimed at targeting inflammation and immune modulation (e.g., rituximab NCT01086540, tocilizumab IL6 receptor antagonist NCT02676947), metabolic dysfunction (*e.g.*, metformin NCT03349775, ranolazine NCT02829034, dichloroacetate NCT01083524 (147)), iron deficiency (148), DNA damage (*e.g.*, olapirib, NCT03782818), and epigenetic modulation (*e.g.*, apabetalone, NCT03655704 (149)) with a particular emphasis on drug repurposing to ensure an expedited drug to treatment pipeline (150, 151). However, whether these drugs will be effective in not only PAH but across diverse etiologies is unknown, providing the impetus to better understand any shared cellular and molecular mechanisms across multiple PH classifications to treat these increasingly prevalent subtypes.

1.2 Iron-sulfur clusters

Separately, iron-sulfur (Fe-S) clusters are evolutionarily conserved bioinorganic cofactors essential for a diverse number of processes (152), including those involved in mitochondrial respiration (153) as well as DNA replication and repair (154, 155). First, these clusters have potent

reduction-oxidation (redox) potential with the iron able to reversibly switch between oxidative states (Fe^{2+} or Fe^{3+}) and serve as a competent electron donor and acceptor (152). This function is particularly important for electron transfer between mitochondrial complexes (I-IV) during oxidative phosphorylation and the TCA cycle (succinate dehydrogenase in complex II) (153). Others studies have expanded the roles of Fe-S centers to include enzymatic catalysis (*e.g.,* lipoate synthase (156)), environmental sensing and transcription activation (*e.g.,* IRP1 (157), and even structural integrity (*e.g.,* XPD, FANJ (158)).

Notably, Fe-S centers have more recently been identified in nuclear proteins. In particular, helicase (*e.g.,* DNA2), primase, and B-family DNA polymerase proteins operate at the level of the replication fork; these as well as glycosylases (*e.g.,* MUTYH involved in base excision repair (BER)) and specialized helicases, like XPD in nucleotide excision repair (NER) or RTEL1 in homologous recombination and telomere maintenance, participate in multiple DNA repair pathways to maintain overall genomic stability (154, 155). Human disease, particularly cancers and progeroid syndromes, associated with loss-of-function mutations in these Fe-S-containing nuclear proteins confirm their importance in DNA synthesis and repair (159-162). Although some data supports contributions to stability of tertiary and quaternary protein structure (158, 163), the study of these proteins is difficult and the exact function(s) of these cofactors within their respective nuclear apoproteins are still incompletely defined.

1.2.1 Iron-sulfur biogenesis

The synthesis, trafficking, and integration of Fe-S cofactors into their respective apoproteins depends upon a group of mitochondrial and cytosolic Fe-S assembly (CIA) proteins with the former ensuring the integrity of the latter (155, 164). Conserved across bacteria (*E. coli*)

and eukaryotic cells, *de novo* cluster formation beings via a complex of the cysteine desulfurase NFS1-ISD11 (sulfur donor) , frataxin (FXN, iron donor), and the iron sulfur assembly protein 1 and 2 (ISCU1/2, scaffold that contains cysteine residues for labile Fe-S binding) (165-169). From there, several chaperones and assembly proteins complete mitochondrial Fe-S maturation. The connection between mitochondrial Fe-S biogenesis exports and CIA is still incompletely defined but additional scaffolding proteins (*e.g.,* CFD1-NBP35, DRE2, MMS19) continue the Fe-S cluster maturation process in the cytoplasm ensuring appropriate transfer to cytosolic and nuclear apoproteins (155, 170).

1.2.2 Pulmonary hypertension in diseases due to Fe-S biogenesis gene deficiency

The essential nature of these ubiquitous clusters is further supported by several mitochondrial diseases linked to mutations in Fe-S biogenesis genes (152). For example, a splicing defect in the *ISCU* gene results in decreased expression iron sulfur assembly protein 1 and 2 (ISCU1/2) and myopathy characterized by decreased succinate dehydrogenase, aconitase, and IRP1 alongside intracellular iron overload (171, 172). In addition, patients with multiple mitochondrial dysfunctions syndrome 1 (MMDS1) and 2 (MMDS2), due to mutations in Fe-S assembly genes *NFU1* (173-175) and *BOLA3* (174, 176) respectively, present with similar metabolic reprogramming in the form of attenuated pyruvate dehydrogenase, respiratory complex I and II, and glycine cleavage system function. Notably, patients with MMDS exhibit a PH phenotype (173, 175). While the origins of PH in these populations had previously been ill-defined, recent work has causatively linked genetic deficiencies of Fe-S cluster assembly genes to pulmonary vascular disease (71, 72, 177).

Specifically, our laboratory's data demonstrated ISCU1/2 deficiency attenuated Fe-S cluster formation and subsequent mitochondrial respiration to increase endothelial apoptosis and promote PH development *in vivo* (70, 71). Importantly, these findings were confirmed via cardiopulmonary exercise testing of a woman with homozygous *ISCU* mutations, revealing the first known observation of pulmonary vascular dysfunction in an ISCU-deficient patient and expanding upon the list of genetic Fe-S biogenesis gene deficiencies that drive PH (71). Additionally, deficiency of BOLA3 resulted in similar Fe-S-dependent metabolic rewiring in the form of the Warburg effect (*i.e.*, decreased mitochondrial respiration coupled with increased glycolytic capacity (178)) as well as hyperglycinemia, which ultimately promoted endothelial dysfunction in the form of imbalanced vasomotor tone, reduced angiogenesis, and enhanced proliferation as well as PH *in vivo* (72). Importantly, beyond genetic mutations, multiple PH animal models and patient tissues showed decreased ISCU1/2 and BOLA3 levels in the pulmonary endothelium. Specifically, HIF-α, a well-characterized transcription factor involved in metabolic reprogramming in PH (42, 179), acted as a master regulator of endothelial ISCU1/2 (via microRNA-210) and BOLA3 expression (via histone deacetylase 1) in chronic hypoxia (70, 72). Together, our studies illustrated that not only genetic but acquired Fe-S assembly gene deficiency in the endothelium promoted PH development. Whether additional Fe-S cluster biogenesis proteins contribute to not only the endothelial metabolic but also genomic dysfunction that underlies PH has not yet been investigated.

1.3 Friedreich's ataxia

1.3.1 Trinucleotide repeat mutations in frataxin

Frataxin (FXN) is another highly conserved mitochondrial protein involved in the early steps of Fe-S cluster biogenesis via its interaction with ISCU1/2 as well as other assembly proteins, NFS1 and ISD11 (167-169). Although its exact function(s) are controversial, FXN is thought to act as an iron chaperone (180) and support NFS1 cysteine desulfurase activity (and thus provision of sulfur) (181) when bound to the aforementioned initiation complex during Fe-S cluster formation. FXN has also been characterized as an iron chaperone during heme synthesis (182) and an iron storage protein (180), contributing to mitochondrial as well as global iron balance.

Genetic FXN deficiency causes the autosomal recessive neurodegenerative disease, Friedreich's ataxia (FRDA). For this nuclear-encoded gene, homozygous trinucleotide repeat expansions in intron 1 represent the predominating mutation type compared to compound heterozygotes carrying a GAA expansion on one allele and a point mutation on the other (183-185). Full penetrance, disease-causing GAA repeats ranging from 66-1300 triplicates (as compared to between 5 and 35 in healthy individuals) alter genomic and heterochromatin structure with the formation of triplex, or 'sticky', DNA (186) and hypoacetylation of histone H3 and H4 combined with hypermethylation of H3 at Lys9 (187, 188), respectively. The resulting transcriptional silencing yields 5-35% of normal FXN levels in FRDA patients with the length of the expansion mutations inversely related to the amount of FXN produced (183). Interestingly, heterozygous carriers are asymptomatic, suggesting a FXN expression greater than 50% do not produce tissue dysfunction (189).

1.3.2 Epidemiology and clinical presentation

FRDA is the most common inherited ataxia in patients of European, Middle Eastern, and North African descent (190) with a prevalence of 3-4 in 100,000 and a carrier frequency of 1:60-1:100 (191, 192). A multisystem disease, the neurodegenerative and cardiovascular symptom profile represent the dominant and most debilitating phenotypes. Speaking to the former, progressive degeneration of large sensory neurons in the dorsal root ganglia (DRG), the spinocerebellar and corticospinal tracts of the spinal cord, and the dentate nucleus of the cerebellum result in a myriad of neurologic symptoms including limb ataxia, sensory neuropathy, loss of deep tendon reflexes, lower limb spasticity, dysarthria, and motor weakness (191, 193, 194). Limb ataxia and gait instability typically represent the initial sign and symptom and almost all patients will eventually require a wheel chair following loss of ambulation (193). Other non-neurologic symptoms include skeletal abnormalities like kyphoscoliosis and pes cavus, diabetes mellitus and glucose intolerance, and hypertrophic cardiomyopathy (HCM) (193). The length of the intronic expansion on the shorter allele dictates severity of symptoms and age of onset ; specifically, neurologic signs like ataxia, visual and auditory loss, dysarthria, and scoliosis as well as cardiomyopathy correlate with GAA repeat length (183, 195, 196). Age of onset typically occurs around puberty (10-15) and is often before age 25 and life expectancy is typically between 30 and 40 years old (197). Variability in these parameters is again related to length and/or interruption of trinucleotide repeats.

1.3.2.1 Hypertrophic cardiomyopathy

Cardiac dysfunction in FRDA is defined by concentric hypertrophy, fibrosis, and myocyte necrosis and causing severe left ventricular dysfunction and less often dilated cardiomyopathy and

arrhythmia (198). HCM occurs in approximately 60% of FRDA patients, driving mortality in this population (188, 197). In the broader context of Group 2 PH due to left heart disease, HCM is accompanied by PH in up to 40% of patients and the combination is associated with increased mortality (105, 199). Case reports have described pulmonary arteriolar vasculopathy in this population (200); however, PH and cardiopulmonary complications as a whole in FRDA have been underreported (201, 202), in part due to the lack of hemodynamic outcomes and lung specimens available for study. Of the FRDA heart failure reports that are available, focus has been given to the diastolic dysfunction and markedly elevated left ventricular filling pressures rather than the PH that, by definition, is present (202). Further studies are required to confirm the presence of PH in FRDA independent of or additive to HCM.

1.3.3 Cellular and molecular pathology

Underlying the severe neurologic and cardiovascular clinical presentation, there is significant tissue-specific dysfunction within the. Data have largely focused on the Fe-S cluster-dependent changes in these post-mitotic cell types like neurons of the spinocerebellar tracts (*e.g.*, dorsal root ganglia) and cardiomyocytes. Consistent with the roles of Fe-S centers in cytosolic iron sensing (IRP1/aconitase) and mitochondrial electron transport (153, 157), FXN deficiency decreased the activity of complexes I-III and aconitase in multiple tissue types (203, 204). This metabolic reprogramming is accompanied by tissue evidence of mitochondrial iron loading (205-207) and elevated oxidative stress (208, 209) due increased production and sensitivity to reactive oxygen species (ROS) (210, 211). Some controversy exists over the causative importance of iron accumulation; some data suggests iron overload enhances iron-dependent ROS (*i.e.*, hydroxyl radicals) via the Fenton reaction while others suggest it is a late-stage byproduct in FRDA (212,

213). Notably, both mitochondrial and nuclear DNA damage has been observed in FRDA and largely attributed to oxidative stress (214-217). Given the reliance of non-mitochondrial Fe-S-containing proteins on FXN-dependent mitochondrial Fe-S cluster formation (218), specific disruption of DNA replication and repair proteins with Fe-S centers may also result in DNA damage (219) but has not been investigated in the context of FXN deficiency and FRDA.

In addition, the pathological changes in metabolism and ROS handling have been associated with variable or incompletely defined cellular outcomes; most often, FXN deficiency seems to increase susceptibility to apoptosis (220-223) while more recent studies highlight FXN-driven cellular senescence (224, 225). The phenotypes of FXN-deficient pulmonary vascular cells, namely endothelial cells, have not been studied in FRDA; but the essential nature of FXN, Fe-S biology, and the potential pathobiological consequences of their deficiency could have a profound effects on pulmonary endothelial cell health.

1.3.4 Emerging therapies

With no available cure for FRDA, proposed therapies are primarily focused on either enhancing FXN expression or curbing downstream metabolic stress. First, given that GAA expansion mutations occur in a non-coding region, improving the transcription of FXN with epigenetic pharmacotherapies is a promising option. To this end, histone deacetylase inhibitors have been shown to relieve FXN repression in FRDA in both preclinical (187, 226) and early clinical studies (227). However, despite achieving the primary endpoint of up-regulated FXN expression, the nicotinamide treatment did not alter clinical parameters related to neurological deficits while cardiopulmonary dysfunction was not assessed. Future long-term studies of epigenetic pharmacotherapies may yield increased FXN alongside improved clinical outcomes,

specifically for HCM. With similar intentions, both interferon gamma (IFNγ) (228) and resveratrol (229) increased FXN *in vitro*; preliminary clinical trials did not restore FXN expression but did improve physical clinical parameters (230-232), suggesting an alternative mechanism of action.

Treatment targeting the downstream mitochondrial oxidative stress or iron accumulation have also been pursued in this population. Specifically, idebenone (a CoQ_{10} analog) initially appeared to improve disease by altering cardiac outcomes (233-235); however this drug failed to improve neurologic and cardiovascular disease parameters in in recent advanced-stage clinical trials (236, 237). Similarly, reduced antioxidant function of NRF2 in FRDA patient cells (238) encouraged the development of NRF2 activators (NCT02255435) (239). Mitochondrial-specific iron chelators, like deferiprone, yielded inconclusive clinical results (240). Another trial demonstrated the combination of idebenone and deferiprone did not alter neurologic parameters but did reduce intraventricular septum thickness as well as left ventricular mass index (241). On the whole, therapies combating the FXN-dependent oxidative stress and iron dysregulation have not been reliably effective in preventing disease progression to date; however, combination therapy may provide a way forward.

Current strategies for patient care are limited to symptom management and include comprehensive physical and occupational therapy as well as antispasmodics, hypoglycemic agents and insulin for diabetes mellitus, and traditional drug and device implantation to manage arrhythmia and heart failure (242). In summary, the diagnosis of FRDA and HCM represents tremendous morbidity and mortality for patients. A better understanding of the underlying pathophysiology of genetic FXN deficiency in the pulmonary vasculature may identify a group of FRDA patients at risk for PH.

1.4 Rationale

PH is an enigmatic, heterogeneous disease with increasing prevalence of Group 2 PH due to left heart disease (101, 102) and Group 3 PH due to hypoxic lung disease (103, 104) as the population ages. With no curative therapies for any WSPH group, a diagnosis of PH represents significant morbidity and mortality to patients (95, 115). Whether there is any molecular connection between PAH and the other PH groups is still under investigation. Endothelial cell dysfunction represents a defining feature of PH panvascular remodeling yet its molecular mechanisms remain poorly defined as compared to other cell types such as smooth muscle cells. Notably both endothelial mitochondrial dysfunction (1) and DNA damage (81, 93) have been independently associated with PH. However, whether they share mechanistic regulation, how they converge on resultant endothelial phenotypes, and their relevance across PH subtypes are still undefined.

Fe-S clusters are evolutionarily conserved, essential cofactors for multiple cellular processes, namely redox-dependent mitochondrial respiration (153) and genomic replication and maintenance (154), and provide a model to study the combined effect of endothelial metabolic reprogramming and DNA damage in PH. In particular, patients with genetic deficiencies of Fe-S biogenesis genes (ISCU-myopathy, MMDS) exhibit PH (71, 173, 175); moreover, HIF-α-mediated acquired reduction of ISCU1/2 and BOLA3 each drive metabolic rewiring, endothelial-specific dysfunction, and PH in vivo (70-72). Whether this causative link between endothelial Fe-S cluster deficiency and PH depends upon genotoxic as well as metabolic stress and extends to acquired or genetic deficiencies of other Fe-S assembly proteins has not been investigated.

Trinucleotide repeat mutations in the Fe-S biogenesis gene *FXN* cause FRDA (183). Mortality in this patient population is driven largely by hypertrophic cardiomyopathy (HCM)

(197). Case reports have described pulmonary arteriolar vasculopathy in this population (200), consistent with the fact that ~50% of patients with hypertrophic cardiomyopathy (HCM) in general suffer from PH due to left heart disease (105). However, little attention has been paid to the pulmonary vascular phenotypes in FRDA. Apart from the clinical potential for a PH phenotype concurrent with FRDA-dependent HCM, several studies have demonstrated mitochondrial dysfunction (184), oxidative stress, and DNA damage in FRDA tissues (208, 209, 214-217). Coupled with our laboratory's data on endothelial Fe-S deficiency promoting PH (70-72), there may be a role for coordination of Fe-S-driven metabolic and genomic integrity by FXN in the pulmonary endothelium.

Therefore, we hypothesized that genetic or acquired FXN deficiency disrupts Fe-S-dependent endothelial function to promote PH. Herein I will 1) interrogate whether FXN deficiency disrupts metabolic and genomic integrity and how these FXN-dependent stressors coordinate endothelial phenotypes, 2) determine how acquired drivers of PH alter endothelial FXN expression, and 3) establish pulmonary endothelial FXN deficiency predisposes to PH in multiple PH subtypes. The identification of FXN as a lynchpin in PH pathogenesis will improve our understanding of Fe-S biology, the shifting pathophenotypes of endothelial cells, and the development of PH. Furthermore, this study may provide mechanistic insight and thus new diagnostic and therapeutic targets for pulmonary vascular disease in FRDA as well as multiple PH groups, including Group 2 PH.

2.0 Frataxin deficiency disrupts pulmonary endothelial metabolism

This work was adapted from a published review (1) and a manuscript in preparation.

Culley MK, and Chan SY. Mitochondrial metabolism in pulmonary hypertension: beyond mountains there are mountains. *J Clin Invest.* 2018;128(9):3704-15.

Culley MK, Zhao J, Tang Y, Negi V, Yu Q, Perk D, Reynolds M, Pilli J, Shiva S, Chan SY. Frataxin deficiency disrupts iron-sulfur-dependent mitochondrial reprogramming in the pulmonary endothelium. *In preparation.*

Notably, iron-sulfur fluorescent sensor experimental design and imaging by Ying Tang and quantification by Jingsi Zhao (Figure 1A-B). Seahorse assay performed with the help of by Michael Reynolds and Dr. Sruti Shiva (Figure 2). Total nitrite and nitrate (Figure 3F) and contraction assay (Figure 5E) performed by Jingsi Zhao.

2.1 Introduction

Pulmonary hypertension (PH) is a progressive and fatal disease of the lung vasculature in which metabolic and mitochondrial dysfunction contribute to pathogenesis (1). A hallmark of the metabolic reprogramming in PH is the shift from mitochondrial oxidation to glycolysis, similar to the Warburg effect in cancer (38, 178), that has been observed in both pulmonary (10, 11, 47-50) and extrapulmonary tissues (51-55). Specifically, emerging data causatively links rewiring of

endothelial metabolic pathways in the pulmonary circuit (49, 50, 69-72); however the identification of any upstream driver as well as the downstream consequences for the dynamic endothelial cell fates observed in PH require further study.

Our laboratory identified iron-sulfur (Fe-S) cluster deficiency as a driver of disruption of endothelial cell metabolism and PH *in vivo* (70-72). Fe-S clusters are essential, redox-capable cofactors incorporated into different apoproteins across cellular compartments (152); for example, Fe-S centers facilitate electron transfer between mitochondrial complexes allowing for effective oxidative phosphorylation (153). Biogenesis of these bioinorganic clusters requires a number of evolutionarily conserved mitochondrial and cytoplasmic assembly proteins (152), the importance of which is underscored by rare, often fatal mitochondrial diseases driven by mutations in specific assembly genes, like *ISCU* (which encodes iron sulfur cluster assembly proteins 1 and 2) (171, 172), *BOLA3* (BolA 3 family member) (174, 176), and *NFU1* (173-175). While case reports have previously catalogued PH as an associated phenotype in these disorders (173, 175), new data supports a causative role for Fe-S biogenesis gene deficiency in this disease (70-72) with the most recent study demonstrating pulmonary vascular disease development in a rat model with the human *NFU1* mutation (Multiple mitochondrial dysfunctions syndrome 1, MMDS1)(177).

In addition to genetic deficiencies, our previous data established hypoxia-inducible factor alpha (HIF-α) as a shared regulator of microRNA-210-mediated ISCU1/2 reduction (70, 71) and histone deacetylase 1 (HDAC1)-mediated BOLA3 reduction (72) in cultured pulmonary artery endothelial cells (PAECs) exposed to chronic hypoxia, a widely recognized trigger relevant to both Group 1 and Group 3 PH (243). Both acquired and genetic deficiencies resulted in metabolic reprogramming in the form of the Warburg shift (*i.e.,* decreased respiration and compensatory glycolysis) (70-72) as well as altered glycine homeostasis (72). Given that BOLA3 provide the Fe-

S cluster required for lipoic acid synthesis (156), reduced expression of the lipoate-dependent enzyme, glycine cleavage system H (GCSH), led to increased glycine levels (72), consistent with the hyperglycinemia in MMSD2 patients (174, 176). These Fe-S-specific metabolic changes promoted shared endothelial-specific phenotypes relevant to PH including increased vasoconstrictive signaling and dysregulated angiogenesis. Despite differences in endothelial cell survival, with ISCU1/2 causing endothelial apoptosis and BOLA3, proliferation, both resulted in pulmonary vascular disease *in vivo* (70-72). Whether alternative Fe-S biogenesis gene deficiencies contribute to metabolic reprogramming and its dynamic consequences for endothelial cell phenotypes has not been studied.

The nuclear-encoded mitochondrial protein frataxin (FXN) acts as an iron chaperone and binding partner of ISCU1/2 during the initiation of Fe-S cluster assembly (169, 180, 181). This gene has been predominantly studied in the context of genetic deficiency: homozygous GAA repeat expansion mutations result in decreased functional FXN and the neurodegenerative disease Friedreich's ataxia (FRDA) (244). Much attention has been given to diseased tissues with high bioenergetic capacity such as the nervous system, myocardium, and endocrine pancreas; to date, there are no studies on genetic FXN deficiency in the endothelium. However, data in non-vascular cell types whereby FRDA-dependent FXN deficiency drives mitochondrial dysfunction (203), oxidative stress and DNA damage (214, 215), arrested growth and apoptosis (220), and more recently senescence (224, 225), suggest that these same phenotypes in endothelial cells could have profound pathobiological consequences. Furthermore, recent findings reported that exposing FXN-depleted models to anaerobic conditions may rescue Fe-S biogenesis, reverse the FRDA-specific ataxia phenotype, and improve viability (245). The consequences of the interaction between FXN deficiency and hypoxia have not been investigated in pulmonary endothelial cells.

Therefore, we investigated whether FXN deficiency controls Fe-S mediated metabolic reprogramming and endothelial dysfunction relevant to PH pathogenesis, similar to other biogenesis genes.

2.2 Materials & Methods

Cell culture

Primary human pulmonary artery endothelial cells (PAECs) (PromoCell) were plated in collagen-coated plastic and cultured in cell-specific basal media supplemented with a growth media kit (PromoCell; Lonza) and 5% fetal bovine serum (FBS) without antibiotics or antifungals added. Experiments were performed between passages 4 to 9. Serum-starved primary cells were exposed to hypoxia (0.2% O_2, 5% CO_2, with N_2 balance at 37 degrees C) using a modular hypoxia chamber or standard non-hypoxic conditions (20% O_2, 5% CO_2, with N_2 balance at 37 degrees C) or recombinant IL-1β (R&D Systems, 10ng/ml).

Transfection

Transfection was performed in PAECs at 70-80% confluency using 40nM of FXN siRNA (Santa Cruz Biotechnology, sc-40580) or pooled negative control siRNA (Santa Cruz Biotechnology, sc-44236) and Lipofectamine 2000 reagent (Life Technologies) in one-part OptiMEM (ThermoFisher) and three-parts serum-starved cell-specific media (Lonza). Following 6-8 hours incubation, transfection media was removed and replaced with full-serum cell-specific growth media. Experiments were performed 48 hours post-transfection unless otherwise specified.

RNA extraction and quantitative

RT-PCR Cells were lysed in Qiazol (Qiagen) and RNA extracted using Rneasy Mini Kit (Qiagen). Complementary DNA (cDNA) was synthesized via reverse transcription (ThermoFisher) on an Applied Biosystems Real Time PCR instrument (ThermoFisher). Quantitative RT-PCR (RT-qPCR) was performed on an Applied Biosystems QuantStudio 6 Flex Fast Real Time PCR device, and fold-change of RNA species was calculated using the formula ($2^{-\Delta\Delta Ct}$) normalized to β-actin or SIN3A expression. TaqMan primers were purchased from ThermoFisher and are listed in Appendix A Table 1.

Immunoblotting

Cells were lysed in RIPA buffer (ThermoFisher) with added protease inhibitor (Thermofisher) and phosphatase inhibitor (PhosSTOP, Roche), and the concentration of the soluble protein fraction was estimated using a Pierce BCA protein assay kit (ThermoFisher). Protein lysates (15-20μg) were separated by a 4-15% gradient SDS-PAGE gel system (Biorad) and transferred onto a PVDF membrane (ThermoFisher). Membranes were blocked in 5% non-fat milk in Phosphate-Buffered Saline (PBST) or BSA in Tris-buffered Saline with 0.1% Tween20 (TBST) for 1 hour at room temperature and incubated with primary antibodies at 4 degrees C overnight. A complete summary of primary antibodies is listed in Appendix A Table 2. After washing with PBST or TBST (≥10 minutes, three times), membranes were exposed to appropriate secondary antibodies (anti-rabbit, anti-mouse, and anti-rat) coupled to HRP (Dako) for 1 hour at room temperature. After another set of washes, immunoreactive bands were visualized with the Pierce ECL reagents (ThermoFisher) and Biorad ChemiDoc XRS+ and ImageLab 6.0.1 software.

Fe-S fluorescent sensor

Expression plasmids for GRX2 and GCN4 transgenes fused to the N-terminal or C-terminal portions of the Venus fluorescent protein were generously provided by Dr. J. Silberg (Rice University) (72, 246). Transgenes were subcloned into the pCDH-MCS-EF1-PURO lentiviral parent vector (System Biosciences) via BamHI and NotI sites. Cultured PAECs were incubated with Fe-S fluorescent sensor lentiviruses in the presence of 8μg/ml polybrene (Santa Cruz Biotechnology) for 24 hours. Virus-transduced human PAECs were transfected with FXN or control siRNAs as described above. Seventy-two hours post-transduction, fluorescence was imaged by EVOS FL microscope (Life Technologies), and Fe-S content was presented as percentage of PAECs with positive fluorescence. Manual quantification was performed blinded. Experiments were performed with the help of Ying Tang, M.S. and Jingsi Zhao, M.S.

Seahorse assay

In transfected PAECs (20,000 cells/well), oxygen consumption rate and extracellular acidification rate were measured on an XFe96 Extracellular Flux Analyzer (Agilent) following exposure to oligomycin (1μM), the uncoupler FCCP (0.5μM), and the Complex I and Complex III inhibitors rotenone (2μM), and antimycin (0.5μM). Basal DMEM contained either high (25mM) or low (1g/L) glucose. Etomoxir (40 μM), a CPT1a (carnitine palmitoyl transferase 1a) inhibitor, was added 15 minutes prior to the assay in a separate experiment to block fatty acid uptake by the mitochondria. Measurements were normalized to protein concentration. Experiments were performed with the help of Michael Reynolds, Jyotsna Pilli, and Sruti Shiva, Ph.D.

H_2O_2 assays

At 48 hours, transfected PAECs were counted and re-distributed in a 96-well plate (100,000 cells/well). Intracellular H_2O_2 was assessed by Amplex Red Hydrogen Peroxide/Peroxidase Assay kit (Invitrogen). Absorbance (560nm) and/or fluorescence (530nm/590nm) were measured by spectrophotometer (Synergy HTX multimode reader, Biotek). Alternatively, at 48 hours post-transfection, cultured PAECs were incubated with 2',7' –dichlorofluorescin diacetate (DCFDA; 1μM) for 10 minutes at 37 degrees C and then assessed by flow cytometry (BD LSRFortessa).

Endothelin-1 ELISA

Level of secreted endothelin in concentrated serum-free endothelial cell culture media was assessed by endothelin-1 ELISA kit (Enzo Life Sciences) while colorimetric change was measured by spectrophotometer (Biotek).

Contraction assay

Pulmonary artery smooth muscle cells (PASMCs) (50,000/well) were embedded in 100μl of matrix gel and plated into a 96-well plate as described previously (247). Briefly, to make the collagen matrix gel, collagen I solution (Corning 354249) was mixed on ice with a 1/8 volume of 0.1M NaOH and a 1/8 volume of 10X PBS followed by pH adjustment to 7.5 using 0.1M HCL. Matrigel (Corning, 356231) to make 3mg/ml collagen I. PASMCs were trypsinized, counted, and resuspended in growth medium; then 1 volume of cells was mixed with 1 volume of the collagen matrix gel. After 1 h at 37 °C, these matrices were overlaid with 100μl of conditioned PAEC serum-free medium (transfected with siRNA). The endothelin receptor antagonist, ambrisentan (10μM) was supplemented in conditioned media. Media for all groups were changed every 12

hours, and pictures were taken after 2 days. Image J software (NIH) was used to analyze percentage contraction (well diameter – gel diameter)/well diameter. Experiments were performed with the help of Jingsi Zhao, M.S.

Scratch assay

Confluent PAECs were scratched using sterile pipet tips and brightfield images of scratch closures were taken at 0, 8, and 12 hours using an EVOS XL CORE imaging system (Life Technologies). Scratch areas were quantified using NIH ImageJ software (http://rsb.info.nih.gov/ij/) while blinded.

In vitro tube formation assay

Capillary tube formation was assessed using an in vitro angiogenesis assay kit (Cultrex). Briefly, Matrigel with reduced growth factors was plated into 96-well plate (50 µl Matrigel per well) and allowed to solidify for 30 minutes at 37 degrees C. Transfected PAECs (30,000 cells/well) were resuspended in 100 µl of basal media and plated in the Matrigel-coated 96-well plate. After 6 hours, tubular structures were photographed using EVOS XL CORE imaging system (Life Technologies) with a 10× magnification. The number of branch points and total tube length were automatically quantified using NIH ImageJ software with Angiogenesis Analyzer plugin (http://rsb.info.nih.gov/ij/).

2.3 Primary Data

2.3.1 FXN knockdown attenuated mitochondrial respiration and elevated reactive oxygen species

To confirm FXN-mediated disruption of Fe-S integrity in pulmonary artery endothelial cells (PAECs), Fe-S clusters were first assessed using a fluorescent glutaredoxin 2 (GRX2) sensor, which homodimerizes and fluoresces in proportion to the level of intact Fe-S clusters (71, 72). Following transduction with GRX2 versus GCN4 (a homodimer sensor with Fe-S-independent fluorescence), siRNA knockdown of FXN (Supplemental Data Figure 4A) drove decreased GRX2-specific but not GCN4-specific fluorescence in normoxic (Figure 1A-B) and hypoxic conditions (Supplemental Data Figure 5A), reflecting a failure of low oxygen conditions to rescue Fe-S biogenesis in the presence of FXN knockdown.

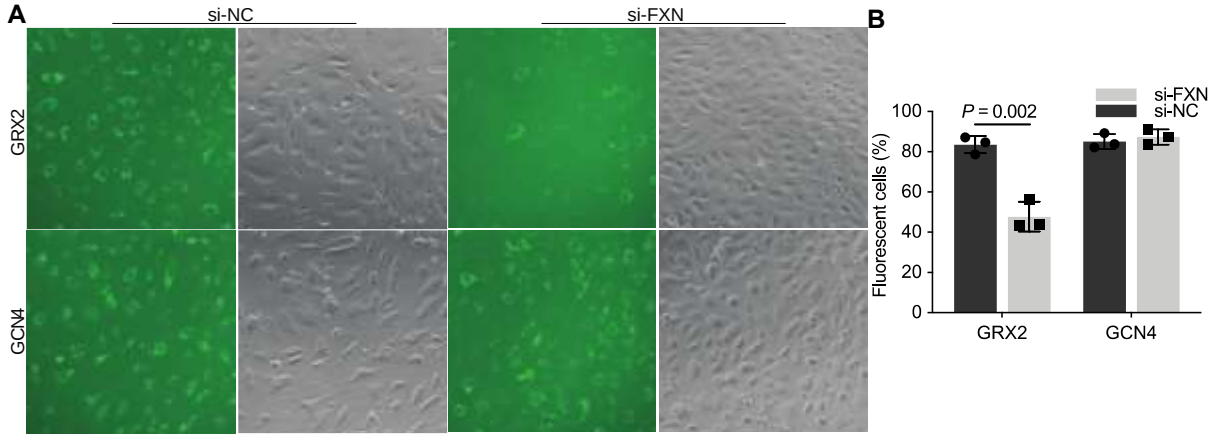

Figure 1. FXN knockdown attenuates Fe-S cluster integrity in pulmonary artery endothelial cells. (**A** and **B**) Representative images (scale bar indicates 400μm) and quantification of Fe-S cluster formation by fluorescent cell percentage in PAECs transduced with glutaredoxin (GRX2) or GCN4 control constructs and transfected with FXN siRNA or negative control (n=3).

Next, to directly assess mitochondrial respiration, extracellular acidification rate (ECAR), a surrogate for glycolysis, and oxygen consumption rate (OCR), a surrogate for oxidative

phosphorylation, were measured by Seahorse extracellular flux analysis in FXN-deficient PAECs. At baseline and following termination of oxidative phosphorylation by the ATP synthase inhibitor oligomycin (indicative of glycolytic capacity), FXN knockdown increased ECAR (Figure 2A-C) but did not alter OCR (Figure 2D-E, Supplemental Data Figure 4B). Unlike endothelial deficiencies of other Fe-S biogenesis genes such as BOLA3 (72), sustained OCR was not dependent upon fatty acid oxidation, as evidenced by a negligible change in baseline OCR with CPT1α inhibition by etomoxir (Supplemental Data Figure 4C). Instead, by reducing the available glucose, and thus flux through the mitochondria, we found that FXN deficiency decreased baseline and ATP-linked respiration (Figure 2F-H), consistent with the notion that oxidative phosphorylation is attenuated due to loss of Fe-S centers in the mitochondrial ETC. Measures of maximal respiratory capacity, proton leak, and non-mitochondrial O_2 consumption were not significantly different between groups (Supplemental Data Figure 4D). Separately, expression analysis demonstrated FXN-dependent up-regulation of glycolytic genes, hexokinase 2 (HK2), pyruvate dehydrogenase kinase 1 (PDK1), and lactate dehydrogenase A (LDHA) (Supplemental Data Figure 4E); however, FXN knockdown did not alter GCSH expression (Supplemental Data Figure 4F), suggesting limited involvement in glycine homeostasis compared to BOLA3 (72). Corresponding with this metabolic rewiring, FXN deficiency in PAECs increased reactive oxygen species (ROS), as measured by intracellular hydrogen peroxide levels (Figure 2I) with hypoxic enhancing ROS production (Supplemental Data Figure 5B). Thus, knockdown of FXN promotes metabolic rewiring and an imbalance in ROS in PAECs.

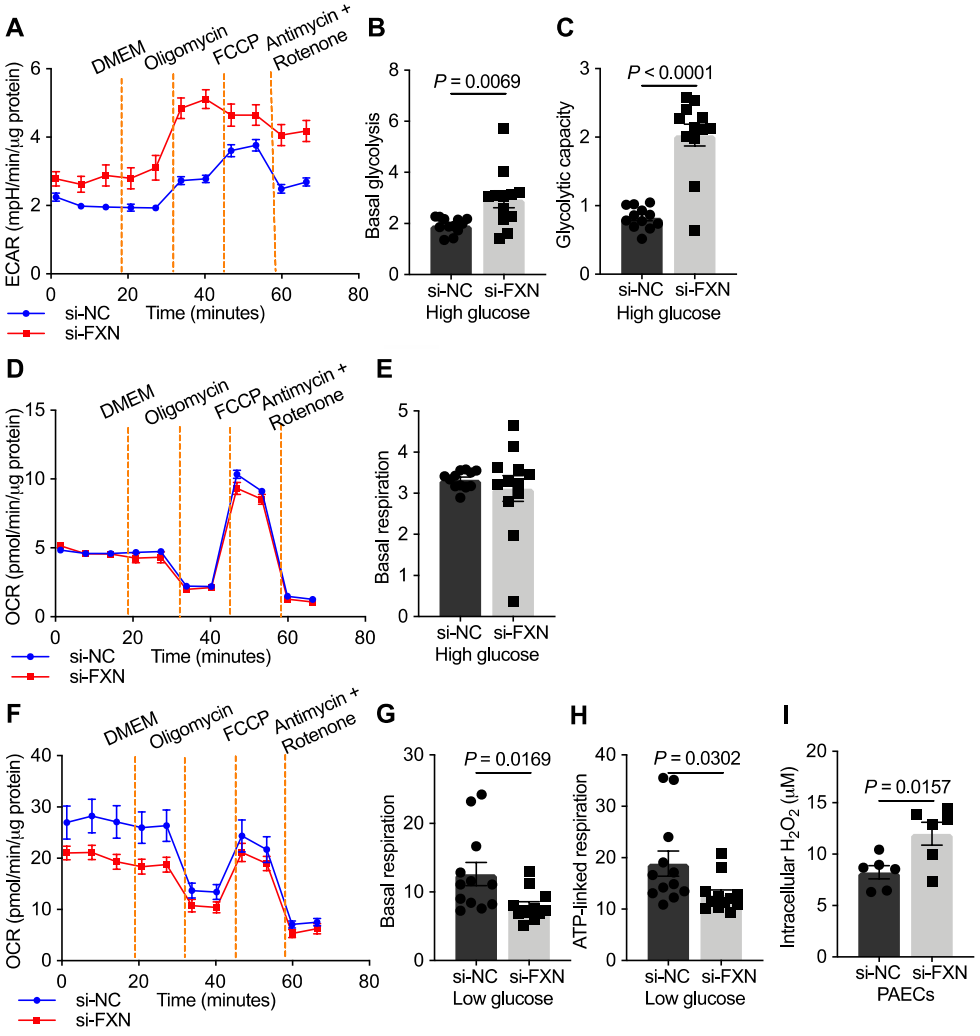

Figure 2. FXN deficiency abrogates mitochondrial respiration and increases oxidative stress. (**A**-**H**) Seahorse extracellular flux analysis measurements of PAECs transfected with FXN siRNA (red) or negative control (blue) (n=12) in response to media control (DMEM), the ATP synthase inhibitor oligomycin (1μM), the uncoupler FCCP (0.5μM), and the Complex I and Complex III inhibitors rotenone (2μM), and antimycin (0.5μM). Error bars reflect mean +/- SEM. (**A**) Extracellular acidification rate (ECAR; mpH/min/μg protein) of PAECs cultured in high glucose (25mM). (**B**) Measurement of basal glycolysis (post DMEM). (**C**) Measurement of glycolytic capacity (post oligomycin). (**D**) Oxygen consumption rate (OCR; pmol/min/μg protein) of PAECs in high glucose. Error bars reflect mean +/- SEM. (**E**) Measurement of basal respiration (post DMEM). (**F**) OCR of PAECs in low glucose (1g/L). (**G**) Measurement of basal respiration (post DMEM). (**H**) Measure of ATP-linked respiration (post oligomycin). (**I**) Amplex red colorimetric assay measuring intracellular hydrogen peroxide (H_2O_2) in PAECs transfected with FXN siRNA compared to control (n=6). Two-tailed Student's *t*-test with error bars that reflect mean +/- SD unless otherwise specified. Experiments performed at least three separate times.

2.3.2 FXN-dependent metabolic reprogramming contributes to endothelial dysfunction consistent with PH

Accompanying alterations in mitochondrial metabolism, we found that FXN deficiency promotes a number of endothelial-specific pathophenotypes also present in PH. Namely, in PAECs the vasoconstrictive mediator, endothelin-1 (*EDN1*/ET-1), was increased with FXN knockdown (Figure 3A-B), phenocopying chronic hypoxia. Moreover, the combination of hypoxia and FXN knockdown further elevated this pathologic response (Supplemental Figure 5C-D). Signifying the importance of oxidative stress in this response, EDN1 up-regulation was abrogated by a cell-permeable mimetic of superoxide dismutase and peroxynitrite scavenger and antioxidant, MnTBAP (Figure 3C). When cultured in matrigel, primary PASMCs exposed to media from FXN-deficient hypoxic PAECs exhibited increased contraction, which could be reversed with the EDN1 receptor antagonist ambrisentan, consistent with FXN-dependent elevation of EDN1 (Supplemental Data Figure 5E).

At the same time, FXN knockdown reduced nitric oxide synthase 3 (NOS3) (Figure 3D-E), the enzyme required for production of the vasodilator nitric oxide (NO); like ET-1 levels, NOS3 down-regulation was more pronounced during FXN knockdown in combination with chronic hypoxia (Supplemental Data Figure 5F-G). Importantly, quantification of total nitrite and nitrate levels, a surrogate measurement for NO, were diminished (Figure 3F), indicating a decrease of NO production by FXN-deficient PAECs and thus enhancing the vasoconstrictive phenotype. Furthermore, in hypoxia, NOS3 was increased with forced expression of FXN (Figure 3G), demonstrating that FXN is both necessary and sufficient for NOS3 expression.

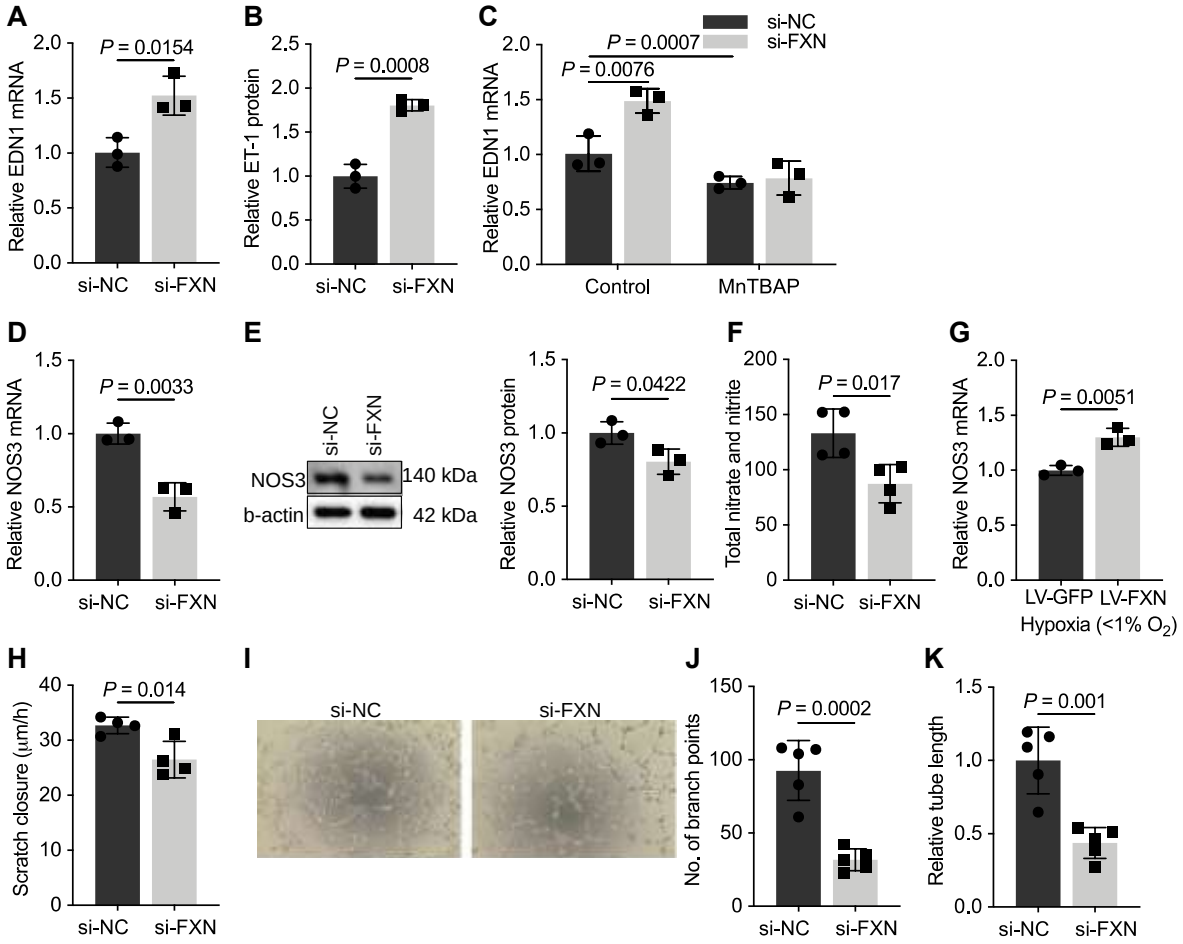

Figure 3. FXN-deficient pulmonary endothelial cells exhibit an imbalance in vasomotor tone effectors and reduced angiogenesis.

(**A** and **B**) Relative endothelin-1 (EDN1/ET-1) expression by RT-qPCR and ELISA in PAECs transfected with FXN siRNA or negative control and exposed to hypoxia or normoxia (n=3). (**C**) RT-qPCR of EDN1 in transfected PAECs treated with MnTBAP (50μM) or vehicle (≥24 hours) (n=3). (**D** and **E**) Relative nitric oxide synthase (NOS3) expression by RT-qPCR and immunoblot in PAECs with and without FXN knockdown and/or hypoxic exposure (n=3). (**F**) Total nitrate and nitrite levels (ng/ng) as measured by Griess reagent colorimetric assay in FXN-deficient PAECs compared to control (n=4). (**G**) NOS3 fold change by RT-qPCR after overexpression of FXN using a lentiviral vector(s) in hypoxic PAECs (n=3). (**H**) Scratch assay measured at baseline and 12 hours in PAECs with or without FXN knockdown and hypoxic exposure (n=3). (**I-K**) Tube formation assay measuring number of branch points and relative tube length (arbitrary units) in PAECs transfected with FXN siRNA or negative control and exposed to hypoxia or normoxia (n=4-5). Two-tailed Student's *t*-test with error bars that reflect mean +/- SD. Experiments were repeated three times.

Finally, FXN knockdown in normoxic and hypoxic PAECs decreased migration assessed by scratch assay (Figure 3H, Supplemental Figure 5H) as well as decreased branch points (Figure 3J, Supplemental Figure 5J) and total tube length (Figure 3K, Supplemental Figure 5K) in a tube

formation assay (Figure 3I, Supplemental Data Figure 5I). In sum, similar to our previous data in ISCU1/2- or BOLA3-deficient endothelial cells (22-24), FXN deficiency in PAECs disrupts Fe-S cluster biogenesis, ultimately leading to a dysfunctional endothelium characterized by mitochondrial dysfunction, an imbalance in vasomotor tone mediators, and diminished angiogenic potential. Moreover, the combination of FXN and hypoxia exacerbated these phenotypes.

2.4 Supplemental Data

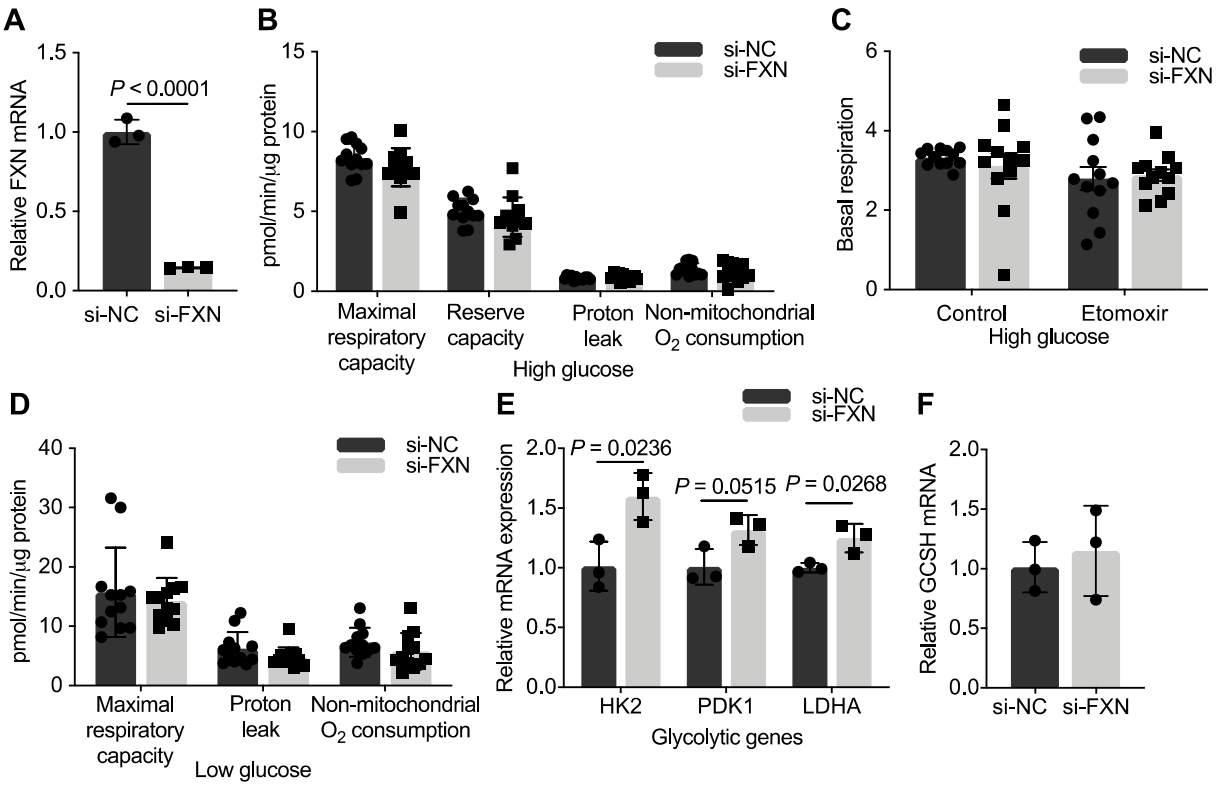

Figure 4. Effects of FXN deficiency on endothelial metabolism.

(**A**) 48-hour transfection control for FXN transcript expression by RT-qPCR following siRNA knockdown in PAECs. (**B**) PAEC oxygen consumption rate (OCR; pmol/min/μg protein) measurements of maximal respiratory capacity, reserve capacity, proton leak, and non-mitochondrial O2 consumption by Seahorse assay in high glucose media (25mM) (n=12). Error bars reflect +/- SEM. (**C**) Basal respiration following treatment with etomoxir (40μM) in high glucose media (n=12). Error bars reflect +/- SEM. (**D**) PAEC OCR measurements of maximal respiratory capacity, proton leak, and non-mitochondrial O2 consumption by Seahorse assay in low glucose media (1g/L) (n=12). Error bars reflect +/- SEM. (**E**) RT-qPCR expression analysis of glycolytic markers: hexokinase 2 (HK2), pyruvate dehydrogenase kinase 1 (PDK1), and lactate dehydrogenase A (LDHA) (n=3). (**F**) GCSH mRNA levels in FXN-deficient PAECs compared to negative control (n=3). Two-tailed Student's *t*-tests were performed and error bars reflect +/- SD unless otherwise specified.

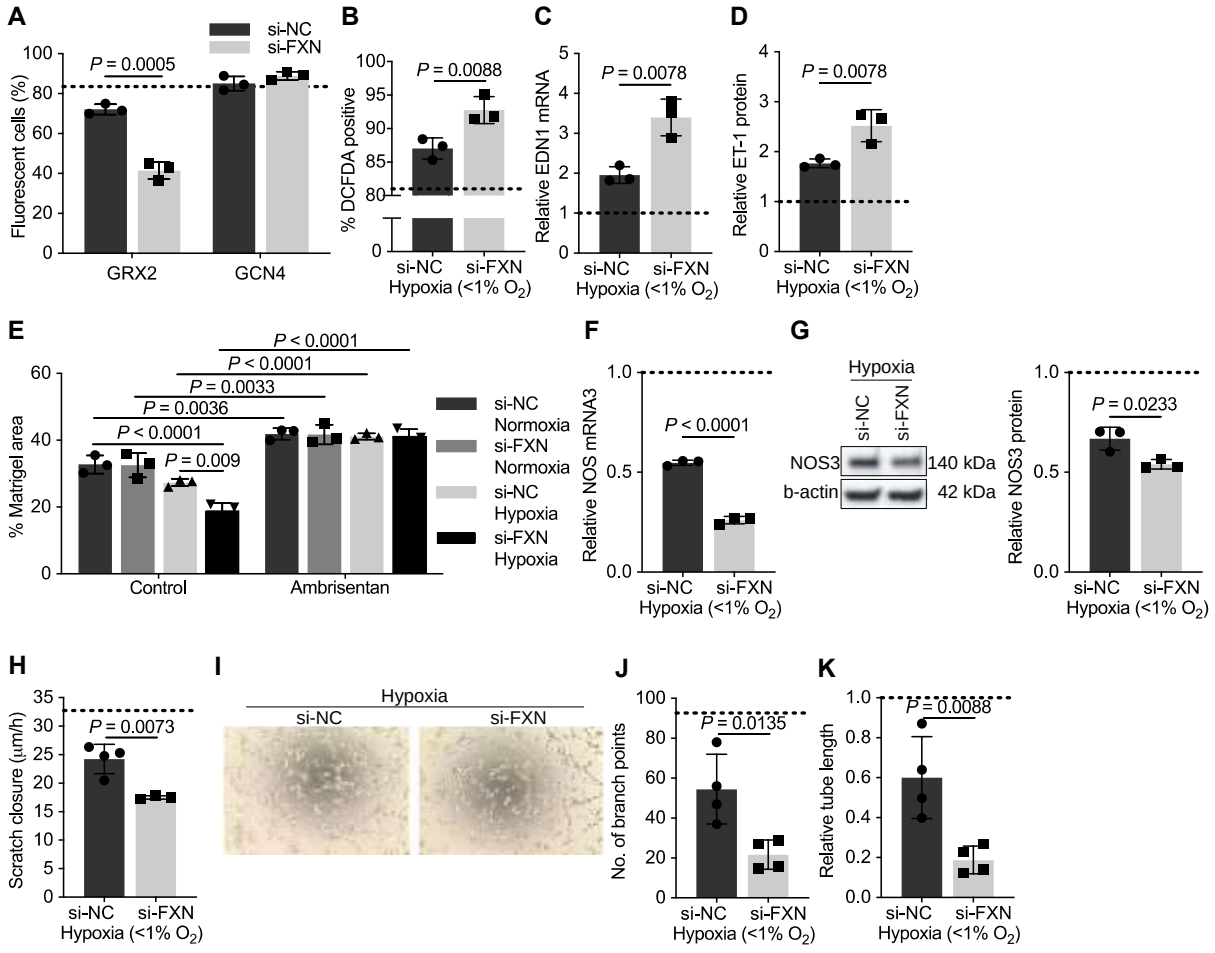

Figure 5. Chronic hypoxia worsens Fe-S-dependent endothelial dysfunction.

(**A**-**K**) Experiments reflect PAECs transfected with FXN siRNA (si-FXN) or negative control (si-NC) and exposed to hypoxia (<1% O_2, ≥ 24 hours) unless otherwise specified. The dotted line provides comparison relative to normoxic controls. (**A**) Fe-S cluster formation measured by GRX2-specific fluorescence compared to GCN4 constitutive fluorescence (n=3). (**B**) Flow cytometry of hypoxic PAECs pulsed with DCFDA (1μM) measuring intracellular H_2O_2 (n=3). (**C** and **D**) RT-qPCR and ELISA depict relative endothelin-1 (EDN1) expression (n=3). (**E**) Human PASMCs seeded in a collagen matrigel treated with conditioned media from FXN-deficient compared to control PAECs, exposed to hypoxic or normoxic conditions, and treated with ambrisentan (≥ 48 hours, 10μM). Contraction measured as a percentage of PASMC well area compared to baseline area. (n=3). (**F** and **G**) RT-qPCR and immunoblot of relative nitric oxide synthase (NOS3) expression (n=3). (**H**) Rate of scratch closure (m/h) after measurements at baseline (n=3-4). (**I**-**K**) Representative light microscopic imaging and quantification of PAEC tube formation measuring number of branch points and relative tube length (n=4). Two-tailed Student's *t*-test or one-way ANOVA (Tukey's post hoc analysis) with error bars that reflect mean +/- SD. Experiments repeated three times.

2.5 Discussion

In summary, these data represent the first step in understanding the effects of FXN deficiency on pulmonary endothelial cells. Taking cues from FRDA (203, 204) as well as recent data linking Fe-S biogenesis gene deficiencies with PH (70-72), we have confirmed similar metabolic dysfunction (Figure 2) and illustrated a pathological imbalance in vasomotor signaling and diminished capacity for angiogenesis (Figure 3). Both of these endothelial phenotypes are important in the pathophysiology of PH, suggesting a role for FXN in this disease. At the same time, while there has been little focus on the pulmonary endothelium or associated vascular diseases in FRDA (200), these findings support the potential for underlying, vascular dysfunction due to FXN mutations.

Whether additional metabolic pathways (*e.g.*, fatty acid synthesis versus oxidation (FAO), glutaminolysis, or the pentose phosphate pathway (PPP)) are dysregulated in FXN-deficient endothelial cells is not yet known. While these pathways do not include Fe-S-containing proteins, loss of appropriate Fe-S-dependent glucose oxidation alone can lead to compensatory alterations in bioenergetic production. For example, while the Warburg effect focuses on glycolysis, the PPP, which yields reductive NADPH and ribose-5-phosphate for nucleotide synthesis, is often augmented in parallel with glycolysis. PPP flux is upregulated in pulmonary vascular cells in multiple PH models (50, 60-62). Moreover, despite our focus on metabolic rewiring, it is also possible that endothelial deficiency of FXN may have additional effects on mitochondrial dynamics such as attenuated mitochondrial biogenesis. Distinct from but relevant to metabolic dysfunction, a disruption in mitochondrial biogenesis has been previously observed in non-vascular FRDA tissues (248) as well as pulmonary vascular cells in PH (53, 68).

Oxidative stress is a well-accepted yet incompletely understood driver of tissue dysfunction in FRDA (208, 214-217) and PH (63), separately. While our data are consistent with enhanced mitochondrial ROS observed in genetic FXN deficiency, a more detailed understanding of species production and signaling is possible. Supported by the potential accumulation of mitochondrial iron (205, 206) observed

in FRDA, future studies may identify other pertinent ROS products, such hydroxyl radicals via the Fenton reaction. These data will help inform the ROS-mediated effects on endothelial cell dysfunction in FXN-deficient conditions. While our data link mitochondrial ROS and EDN1 transcript expression (Figure 3C), connecting oxidative stress and vasomotor tone, further experimentation is required to uncover additional oxidative stress-driven pathophenotypes (*e.g.*, mtDNA or nuclear DNA damage) relevant to PH.

Furthermore, oxidative stress may not account for all of the Fe-S-dependent phenotypes presented here; the precise mechanisms that result in changes in vasomotor tone and angiogenesis remain incompletely defined. In the context of FXN-dependent down-regulation of NOS3 expression (Figure 3D-E), a possible explanation could center on FXN-specific inhibition of ferrochelatase activity (182), the Fe-S-dependent, rate-limiting enzyme in heme synthesis; thus FXN deficiency may impair heme production and ultimately reduce the expression and activity of NOS3, a heme-containing enzyme (249). resulting in diminished NO production. Separately, because nitric oxide can directly bind and damage Fe-S clusters, endothelial cell NOS3/NO may be inhibited by some unknown feedback mechanism in conditions of FXN deficiency and reduced Fe-S biogenesis (250). Regardless, Fe-S-mediated changes in effectors of vasomotor tone suggest current PAH-specific vasodilatory therapies that inhibit ET-1 and enhance NO signaling may be effective in circumstances of endothelial FXN deficiency.

Lastly, in response to recent data that suggested hypoxic exposure may be a useful therapy for FRDA patients (245), we interrogated the interaction of pulmonary endothelial FXN deficiency and chronic hypoxia. In contrast, our work demonstrated showed a hypoxia-dependent reduction in Fe-S cluster formation that worsened with FXN knockdown (Supplemental Data Figure 5A), indicating that anaerobic conditions do not rescue pulmonary endothelial Fe-S cluster formation. PH-relevant phenotypes worsened with a 'two-hit' model of endothelial FXN knockdown and chronic hypoxia including oxidative stress (Supplemental Data Figure 5B), vasoconstriction (Supplemental Data Figure 5C-G), and angiogenesis (Supplemental Data Figures 5H-K). Thus, our data caution against the systemic use of hypoxia treatment in FRDA which would not account for differences in cell-specific responses to hypoxia and instead could accelerate a patient's predisposition to PH.

These findings support FXN as a lynchpin connecting Fe-S-dependent oxidative respiration with endothelial metabolic reprogramming critical to PH development, reinforcing the importance of Fe-S biology in endothelial cell function (see working model below). Following these initial data, further experimentation is required to fully characterize the Fe-S-dependent endothelial phenotypes coordinated by FXN and to causatively link FXN deficiency to the development of disease *in vivo*.

3.0 FXN deficiency promotes pulmonary endothelial evolution from acute replication stress to cellular senescence

This work was adapted from a manuscript in revision:

Culley MK, Zhao J, Tai YY, Tang Y, Perk D, Negi V, Yu Q, Handen A, Speyer G, Kim S, Lai Y-C, Satoh T, Watson A, Al Aaraj Y, Sembrat J, Rojas M, Khan OF, Anderson DG, Dahlman JE, Norris KE, Gurkar A, Rabinovitch M, Gu M, Bertero T, Chan SY. Endothelial frataxin deficiency induces replication stress to promote senescence in pulmonary hypertension. *In revision.*

Notably, long RNA sequencing performed by the UPMC Children's Hospital Health Sciences Research Core and GO enrichment analysis performed by Adam Handen with technical support by Drs. Gil Speyer and Seungchan Kim (Figure 6). Senescence-associated -galactosidase staining quantified by Dror Perk (Figure 8D). Lentiviral vectors prepared by Ying Tang (Figure 12). Mouse hemodynamic assessments performed by Jingsi Zhao and Yi Yin Tai (Figure 9B, H-I, and L, Figure 13B-C and G-H). 7C1 nanoparticles prepared by Drs. Omar Khan, Dan Anderson, and James Dahlman (Figure 10A). Pharmacologic mouse data produced with the help of Yu Lu and Sophia Annis (BWH) (Figure 10, Figure 13J-M). Echocardiography performed and analyzed by Dr. Taijyu Satoh and Brenda McMahon (Figure 13D-F).

3.1 Introduction

Definitive endothelial phenotypes and their consequences for pulmonary vascular remodeling remain elusive in PAH and other WSPH groups. While many postulate the endothelium as the site of inciting injury and apoptosis followed by hyperproliferation (251), endothelial cells likely exhibit dynamic, spatio-temporal phenotypes that are incompletely defined. DNA damage represents a disease modifier recently linked to PAH (81) with several potential cell outcomes, namely apoptosis or senescence (86, 87). The latter describes a cellular phenotype of apoptosis resistance and irreversible growth arrest assessed by distinct set of markers including $p16^{INK4}$ and β-galactosidase and a potentially pathogenic senescence-associated secretory phenotype (SASP) (29). Although senescence represents an emerging phenotype in PAH (34) and other WSPH groups (252, 253), the role of senescence in the pulmonary endothelium has not been defined. Instead, studies have demonstrated DNA damage-induced apoptosis resulting from reduced expression of specific DNA damage response (DDR) markers in the pulmonary endothelium (92, 93). The complex regulatory events that control endothelial apoptosis versus senescence and how such events fit into the evolution of endothelial cell function in PH are not known. Any mechanistic insight into the coordination of endogenous mediators of DNA damage, such as oxidative stress or replication stress (defined as compromised fork progression) (84), have also not been characterized.

Fe-S clusters are required for metabolic (153) and genomic integrity (155). Specifically, evidence suggests FXN deficiency disrupts genomic integrity via oxidative damage (214-217). Given that mitochondrial Fe-S biogenesis influences cytoplasmic Fe-S assembly (CIA) and non-mitochondrial Fe-S protein maturation (154, 155), FXN deficiency may drive oxidative stress as well as insufficiency of nuclear Fe-S-containing proteins, compromising genomic replication and

repair and contributing to DNA damage. Therefore, these studies aim to causatively link FXN-dependent Fe-S deficiency and DNA damage and characterize the resultant endothelial phenotypes that may predispose to PH development, expanding upon the importance of Fe-S biology in pulmonary vascular disease.

3.2 Materials & Methods

Shared methods were referenced in a previous Materials & Methods section (2.2) while new materials and procedures have been described below.

Plasmids construction and lentivirus production

The coding sequence of FXN transcript 1 (mitochondrial isoform; Dharmacon, clone ID 4829356) and ISCU1 (cytosolic isoform; clone ID: 23479) and 2 (mitochondrial isoform; clone ID 66383) were purchased and sub-cloned in the pCDH-CMV-MCS-EF1-copGFP (System Biosciences #CD511B-1) using EcoRI and NotI restriction sites, respectively. All cloned plasmids were confirmed by DNA sequencing. HEK293T cells (American Type Culture Collection) were grown in DMEM containing 10% FBS and transfected using Lipofectamine 2000 (Life Technologies) with lentiviral plasmids along with a packaging plasmid system (pPACK, System Biosciences), according to the manufacturer's instructions. Viral particles were harvested 48 hours after transfection, concentrated, and sterile filtered (0.45 μm). Transduction was performed in cultured PAECs (70-80% confluence) by incubating lentiviral vectors compared to a parent vector expressing GFP and polybrene (8 μg/ml) in serum-free cell-specific media for 24 hours. Experiments were performed 72 hours after infection. Transduction efficiency was assessed in

each experiment by observing the GFP expression under a fluorescence microscope and assessing expression of lentiviral targets by RT-qPCR. Lentiviral vectors were prepared by Ying Tang, M.S.

RNA sequencing and gene set enrichment analysis

Following total RNA extraction from transfected PAECs and Broad Range RNA Qubit quality control, long RNA sequencing (Paired-end read 75 cycles, 40-50M reads/sample) was run by the Health Sciences Sequencing Core (UPMC Children's Hospital of Pittsburgh). Transcript quantification was performed using Salmon and differential expression using DESEQ (254, 255). Pathway enrichment of direct Gene Ontology biological processes was performed using DAVID version 6.8 (256-259) on genes with an absolute log fold change > and FDR corrected p-value < 0.05. Quality control and long RNA sequencing was performed with the help of William Horne and the Health Sciences Sequencing Core. Analysis was performed by Adam Handen, M.S. with the help of Gil Speyer, and Seungchan Kim, Ph.D.

Cell cycle analysis

Cell cycle phase was determined using the BD Pharmingen BrdU Flow Kit. To summarize, transfected PAECs were serum-starved overnight and then pulsed with BrdU (10μM) in serum replete endothelial cell media for 4 hours at 37 degrees C. Cells were washed with PBS three times, trypsinized, and fixed for 30 minutes on ice. Following fixation, samples were washed, spun down, and the supernatant discarded before permeabilization for 10 minutes on ice. Following another wash step, PAECs were re-fixed for 5 minutes on ice before incubation with Dnase (300μg/ml) for 1 hour at 37 degrees C. After an additional wash step, cells were incubated with anti-BrdU antibody (1:50) for 20 minutes at room temperature, washed again, and ultimately stained with 7-

amino-actinomycin D (7-AAD). Stained cells were gated based upon BrdU (FITC) and 7-AAD (PE-Texas Red-A, linear) following flow cytometry analysis (BD LSRFortessa and FlowJo).

Replication assays

Endothelial cells were plated in a 96-well plate (5000 cells/well) with overnight serum-starvation to sync cell cycle prior to BrdU pulse in full serum for 2 hours. BrdU Cell Proliferation Assay Kit (Cell Signaling Technology) was performed and colorimetric change (absorbance 450nm) was assessed by spectrophotometer (Biotek). Separately, transfected PAECs were also manually counted using a haemocytometer.

DNA fiber staining

DNA preparation, staining, and imaging was performed per the described protocol (260). Briefly, transfected PAECs were serum-starved overnight and then exposed to CldU (50μM) followed by IdU (250μM) with hydroxyurea (HU, 2mM) for 10 minutes each in serum-replete media; plated cells were washed with PBS three times after each pulse. On a glass slide, PAECs resuspended in PBS (1200 cells/μl) were lysed with 0.5% SDS, 200mM Tris HCl, 50mM EDTA, pH 7.4 for 5 minutes at room temperature before allowing the mixed solution to spread across the slide surface by tilting the slide to a 15 degree angle. After drying, DNA was fixed with 3:1 Methanol: Acetic acid for 5 minutes and denatured with 2.5M HCl for 30 minutes at room temperature. After washing, samples were blocked with 0.1% Triton X-100 and 10% goat serum in PBS for 1 hour at 37 degrees C and incubated with primary antibodies (rat anti-BrdU, mouse anti-BrdU) overnight at 4 degrees C. After washing, slides were incubated for 1 hour at 37 degrees C with secondary antibodies (488-conjugated anti-rat, Cy3-conjugated anti-mouse) and mounted

using gelvatol. Imaging was performed using a Nikon A1 confocal microscope and 60x oil immersion lens with 1.75x zoom. Quantification was blinded and performed on >100 fibers/samples using NIH ImageJ software (http://rsb.info.nih.gov/ij/).

Apoptosis assays

The Caspase-Glo 3/7 Assay (Promega) substrate was applied in equal volume to endothelial cells (5000 cells/well) in serum-depleted media and chemiluminescence was measured by spectrophotometer (Biotek). Results were normalized to protein concentration determined using the Pierce BCA protein assay kit.

Senescence-associated β-galactosidase staining

Endothelial cells at <80% confluency were washed with PBS twice and then PFA-fixed for 10 minutes at room temperature before staining with the Senescence β-galactosidase Staining Kit (Cell Signaling Technology) overnight at 37 degrees C in a dry incubator. After 12-18 hours incubation, images were taken using EVOS XL CORE imaging system (Life Technologies) with a 10x magnification. Blinded image analysis of the percentage of SA-β-gal positive cells per total cell number was performed by Dror Perk using NIH ImageJ software (http://rsb.info.nih.gov/ij/).

Immunofluorescent staining and confocal microscopy

Cryostat sections (5-7μm) from OCT-embedded lung tissues were mounted on gelatin-coated histological slides (Fisherbrand). Following rehydration with PBS for 5 minutes, sections were fixed (2% PFA, 30 minutes, room temperature), permeabilized (0.1% Triton X-100, 15 minutes, room temperature), and blocked (5% donkey serum and 2% BSA in PBS, 1 hour, room

temperature). Primary antibodies were diluted in 2% BSA and incubated at 4 degrees C overnight. A complete antibody summary is included in Appendix A Table 2. Alexa 488, 568 or 647-conjugated secondary antibodies (ThermoFisher Scientific) were applied at a 1:1000 dilution in 2% BSA for 1 hour at room temperature. Following counterstaining with Hoechst for 1 minute at room temperature, slides were mounted with gelvatol. Images were taken using a Nikon A1 confocal microscope and 40x oil immersion lens. Small pulmonary vessels (30-100μm diameter) present in a given tissue section (≥10 vessels/section) that were not associated with bronchial airways were selected for analysis. Intensity (integrated density) of staining was quantified using ImageJ software (NIH). Degree of pulmonary arteriolar muscularization was assessed in OCT lung sections stained for αSMA by calculation of the proportion of fully and partially muscularized peripheral pulmonary arterioles to total number. Analyses were performed blinded to condition.

Animal studies

All animal experiments were approved by the University of Pittsburgh (DLAR) and the Harvard Center for Comparative Medicine. Animal husbandry was managed with the help of Jingsi Zhao, M.S., Ying Tang, M.S., and Dror Perk.

Genetic models: Animal studies to assess the effects of cell-specific FXN deficiency included male EC *Fxn*-/- mice expressing Cdh5(PAC)-ERT2+-Cre (261) or male SMC Fxn-/- mice expressing Myh11-ERT2+-Cre recombinase (Jackson Laboratories, Catalog 019079) (262) compared to Fxn flox/flox controls (212). These conditional knockout mice received intraperitoneal injections of tamoxifen for 5 consecutive days at 10 weeks of age, exposed to hypoxia at 12 weeks of age, and subjected to hemodynamic analysis and tissue harvest at 15 weeks of age. For chronic hypoxia

exposure, 12 week-old mice were subjected to 3 weeks of normobaric hypoxia in a temperature-humidity controlled chamber (10% O_2, OxyCycler chamber, Biospherix Ltd.) compared with normoxia (21% O_2). The lyophilized senolytic ABT-263 (Selleckchem) was suspended in DMSO (0.25mg/ml) and diluted in corn oil for oral gavage. Mice were weighed at the beginning of week 2 and 3 of hypoxia and received 25mg/kg ABT-263 daily versus 2% DMSO in corn oil as a vehicle control. Additional experiments assessing the efficacy of a senolytic were performed with the same dosing and timeline in male C57BL/6 wild type mice or female IL-6 transgenic mice (19) (Taconic).

Pharmacologic model: The polymeric nanoparticle 7C1, composed of low molecular weight polyamines and lipids, was utilized for endothelial-specific delivery of FXN siRNA oligonucleotides in male C57Bl6 mice (71, 72, 263). Male mice received tail-vein intravenous doses 7C1 nanoparticles containing FXN siRNA (si-FXN:7C1) (Stealth siRNA, Life Technologies, 1mg/kg) or scramble control siRNA (si-NC:7C1) (Stealth siRNA, Life Technologies, 1mg/kg) in 5-day intervals before and during (day minus 5, day 0, day 5, day 10) the 2 weeks of hypoxic exposure (10% O_2).

Hemodynamic assessment: In 15 week-old mice, echocardiography was performed using a 15-45MHz transthoracic transducer and a VisualSonics Vevo770 system (Fujifilm). Inhaled isoflurane anesthesia was used at 2% in 100% O_2 during positioning and hair removal and then decreased to isoflurane 0.8% during imaging. Digital echocardiograms were analyzed by Taijyu Satoh in a blinded manner (264). Non-invasive tail plethysmography of systemic blood pressure was performed using the CODA system (Kent Scientific). Mice were either given

Ketamine/xylazine (9:1 ratio, Henry Schein) or subjected to isoflurane (Henry Schein) prior to the catheterization procedure. Isoflurane vaporizer was maintained at 1.5-2% with oxygen gas flow rate at 1L/min. To assess right ventricular systolic pressure, a surrogate for mPAP, Close-chest right ventricular systolic pressure was measured using Millar catheters (SPR-671, SPR-513). Catheters are inserted into jugular vein and guided through the right atrium into the right ventricle. Steady RVSP waveforms were measured for 2 minutes. Blood pressure measurements and catheterization were performed and analyzed in a blinded fashion by Yi Yin Tai, M.S. and Jingsi Zhao M.S.

Tissue processing: After hemodynamic measurements, terminal cardiac puncture blood collection is performed using an EDTA-coated syringe. Plasma is extracted following centrifugation at 3500rpm for 10 minutes at 4 degrees C. Whole-heart as well as separate right (RV) and left ventricle (LV) weights are recorded to assess cardiac hypertrophy. A portion of the lung, RV, LV, liver, kidney, and spleen are flash-frozen in liquid nitrogen while addition sections of lung are OCT-embedded or saved for CD31+ MACS separation. To isolate endothelial cells, mouse lungs were cut into small pieces and dissociated in HBSS containing collagenase IV (2.5mg/ml, Worthington Biochemical) and DNase (10ng/ml, Sigma) using a stir bar (1000rpm) at 37 degrees C for 40 minutes. Following filtration (45μm) and removal of red blood cells using ACK lysis buffer (Thermofisher Scientific), the cell pellet is resuspended in 80μl MACS separation buffer (0.5% bovine serum albumin and 2mM EDTA in PBS) and 20μl CD31 Mouse microbeads (Miltenyi) and incubated for 15 minutes on ice. After washing the MACS LS column mounted on a magnetic plate (Miltenyi) with separation buffer, 500μl of separation buffer is added to dissociated lung cells and the entire suspension is filtered through a washed; filtrate is discarded.

Placing the tip of the column in an Eppendorf tube, the plunger is used to collect CD31+ beads left on the column. From there, the cell pellet is prepared for RNA extraction and RT-qPCR analysis.

3.3 Primary Data

3.3.1 Acute replication stress and cell cycle arrest in FXN-deficient endothelial cells

To determine the predominate effects of FXN deficiency endothelial metabolic reprogramming, an unbiased high-throughput screening by RNA sequencing was performed in PAECs after transfection with FXN siRNA or control. Analysis of differentially expressed genes (498 total genes) was followed by Gene Ontology (GO) enrichment by DAVID. Of the top 30 most significant direct GO biological processes (FDR < 0.05, 66 total), a majority were associated with cell cycle (blue), DNA replication (green), and cellular response to DNA damage stimulus (orange) (Figure 6A and Appendix Table 3). No pathways pertained to mitochondrial metabolism. Using these GO terms as a guide, a hypergraph, which characterizes differentially expressed genes (nodes) by log fold change and the potential relationships between those nodes via edges (256, 257), highlighted pertinent genes within each selected GO pathway that were significantly upregulated by FXN knockdown (Figure 6B). These data propose FXN deficiency coordinates significant nuclear dysfunction with implications for cell cycle progression. Whether these transcriptional changes are reflective of the metabolic consequences of deficient mitochondrial Fe-S integrity or support a more direct insufficiency of nuclear Fe-S-containing proteins is yet-to-be defined.

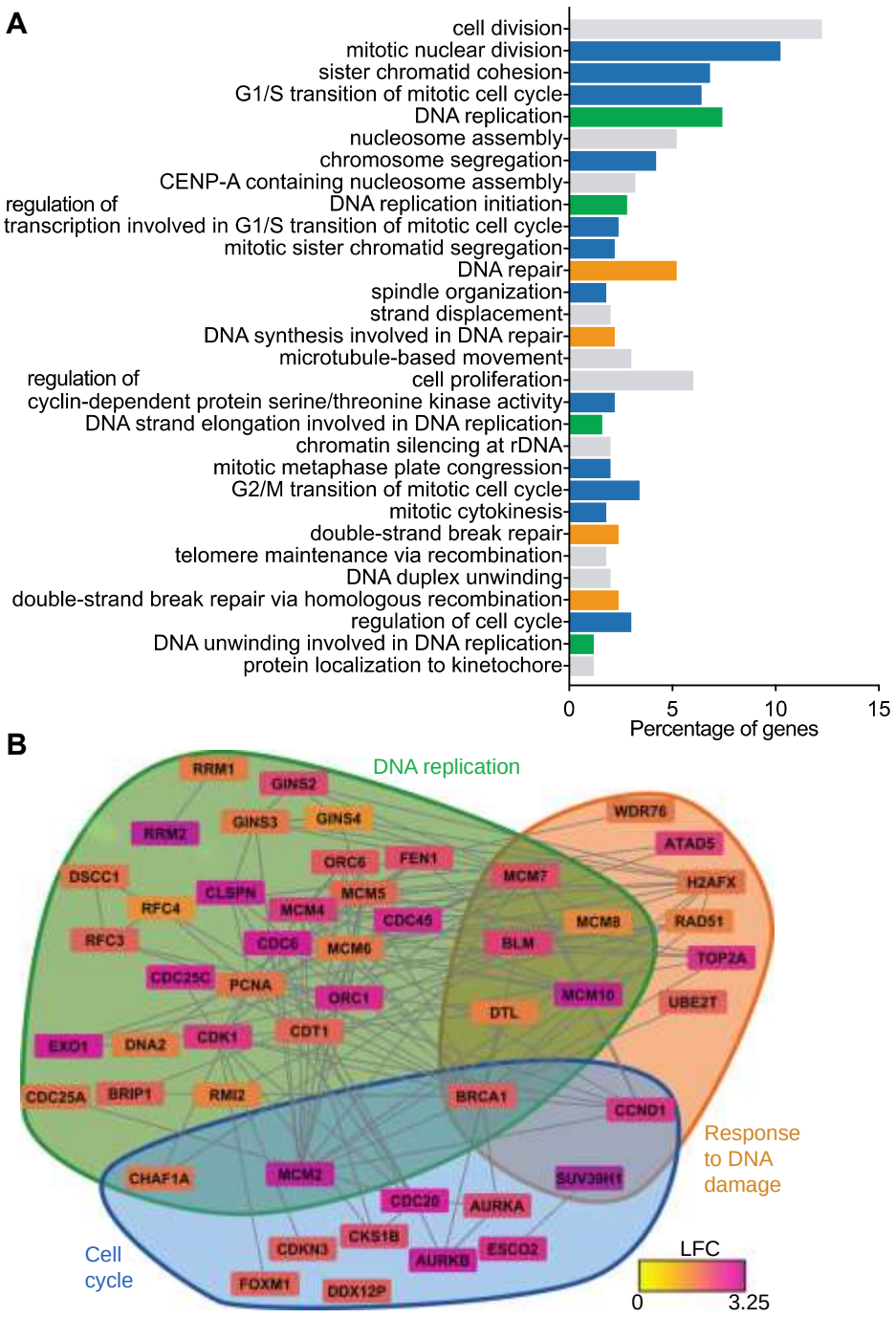

Figure 6. RNA sequencing of FXN-deficient pulmonary artery endothelial cells.

(**A**) Long RNA sequencing in PAECs transfected with FXN siRNA versus negative control following by Gene Ontology (GO) enrichment (n=3). Histogram of top 30 most significant direct GO terms (FDR < 0.05) representing the percentage of differentially expressed genes in the RNAseq data set within each pathway. GO terms related to cell cycle (blue), DNA replication (green), and cellular response to DNA damage stimulus (orange). (**B**) Hypergraph differentially expressed genes (FDR < 0.05) depicting log-fold change via a color scale within GO pathways pertaining to cell cycle (blue), DNA replication (green), and cellular response to DNA damage stimulus (orange).

To first assess the functional consequences of these gene changes, replication was measured by bromodeoxyuridine (BrdU) incorporation in PAECs. Despite the increase in nucleotide incorporation with FXN inhibition (Figure 7A), there was no increase in cell number (Figure 7B). Instead, BrdU pulse labeling combined with the fluorescent DNA intercalator 7-AAD revealed an increase of FXN-deficient PAECs in S phase with a corresponding decrease in G_0/G_1 or G_2 (Figure 7C), signifying cell cycle arrest. These data were supported by an increase in replication fork markers (MCM2, RPA70) and the cyclin-dependent kinase inhibitor $p21^{Cip1}$ associated with DNA damage-dependent cell cycle arrest (Supplemental Data Figure 11A).

To characterize this S-phase arrest, we assessed the replication stress marker phosphorylated RPA32 (84), observing elevated protein levels in FXN-deficient PAECs (Figure 7D). To specifically assess replication fork dynamics, chloro-deoxyuridine (CldU) and iodo-deoxyuridine (IdU) pulse labeling and DNA fiber staining of PAECs with FXN inhibition demonstrated a modest increase in CldU nucleotide incorporation; this FXN-dependent effect was robustly increased with hydroxyurea, a ribonucleotide reductase inhibitor that depletes nucleotide pools to induce fork stalling (Figure 7E). This aberrant increase in replication rate correlated with the up-regulation of the transcript of the M2 subunit of ribonucleotide reductase (RRM2), which was significantly up-regulated with FXN knockdown in the RNA sequencing data set (Figure 6B and Table 3) and confirmed by RT-qPCR (Supplemental Data Figure XB), potentially signaling elevated nucleotide synthesis by ribonucleotide reductase (265). In response to this replication stress, DDR markers (e.g. phosphorylated ATR, CHK1, and ubiquitinated γH2AX) assessed by immunoblot (Figure 7F) as well as 53BP1 foci by immunofluorescent staining and confocal microscopy (Figure 7G), were all up-regulated. To determine whether mitochondrial ROS accounts for this nuclear phenotype, these same markers were evaluated in PAECs with or with

FXN knockdown and in the presence of the antioxidant MnTBAP compared to control (Supplemental Data Figure 11C). MnTBAP treatment did not prevent replication stress or DNA damage-associated cell cycle arrest (Supplemental Data Figure 11D), suggesting DNA damage and replication stress are not dependent upon oxidative damage.

To determine whether FXN is both necessary and sufficient, phenotypic reversal in PAECs exposed to known triggers of PH, such as chronic hypoxia (243) or inflammation (266), was evaluated. First, lentiviral transduction of FXN in combination with its binding partner ISCU1/2 (Supplemental Data Figure 12A-B) reduced BrdU incorporation (Supplemental Data Figure 12C-D) Forced expression of FXN or ISCU1/2 alone slightly reduced certain replication stress (p-RPA32, γH2AX) and cell cycle arrest markers; additionally, overexpression of FXN in combination with ISCU1/2 most effectively reduced protein levels of all of these targets under conditions of chronic hypoxia (Supplemental Data Figure 12E), consistent with reversibility of replication above. The same reduction in BrdU incorporation (Supplemental Data Figure 12F-G) as well as in replication stress response and cell cycle arrest markers (Supplemental Data Figure 12H) was achieved by the combined overexpression of FXN and ISCU1/2 following IL-1β treatment. Taken together, these data reveal that acute replication stress and cell cycle arrest in endothelial cells are reversible processes. In summary, these data support a oxidative stress-independent, reversible mechanism by which acute FXN deficiency drives replication stress, resulting in genomic damage, early activation of the DDR, and endothelial cell cycle arrest.

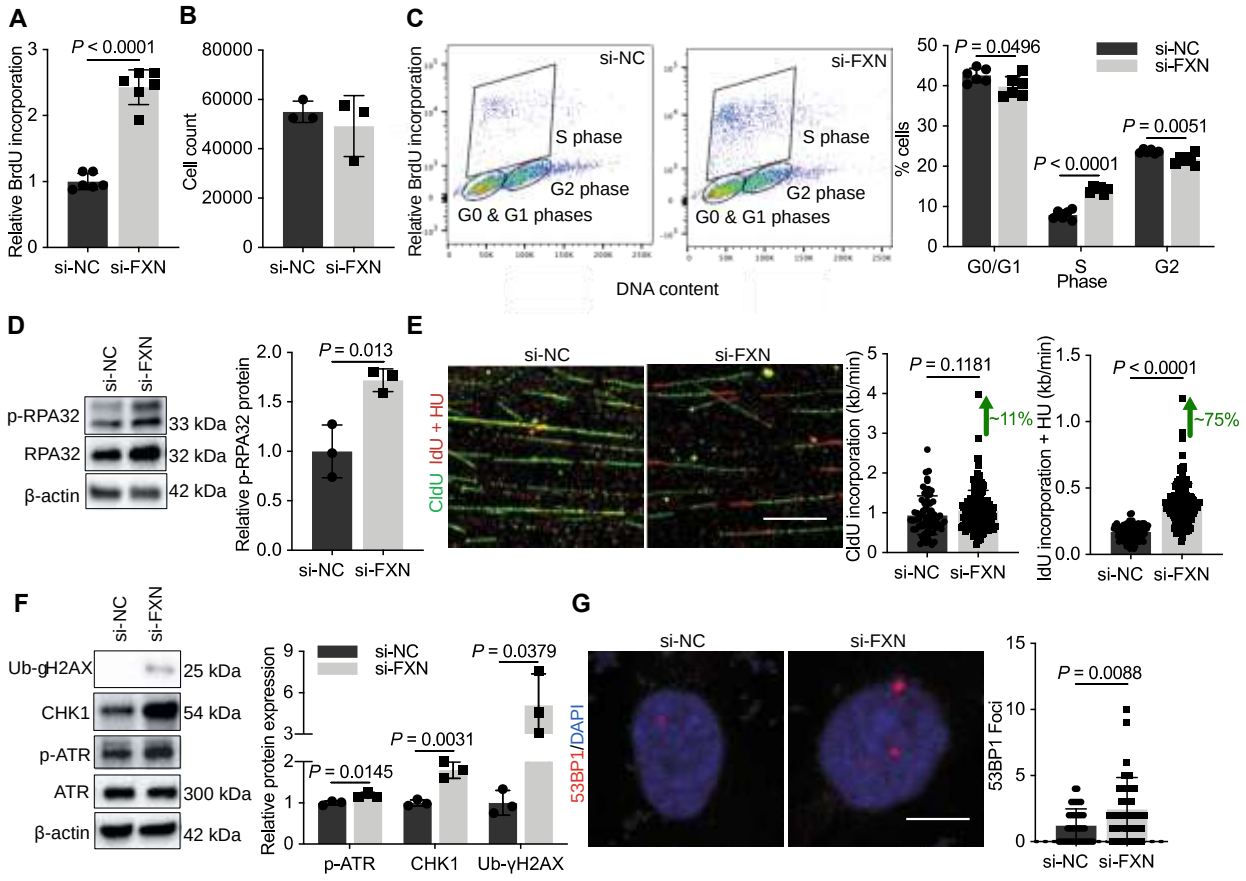

Figure 7. Acute FXN knockdown promotes replication stress and S-phase arrest.
(**A-G**) All experiments were performed 48 hours after transfection in PAECs with or without FXN inhibition by siRNA. (**A**) Colorimetric BrdU incorporation (n=6). (**B**) Manual cell count (n=3). (**C**) Flow cytometric analysis of FXN-deficient or control PAECs pulsed with BrdU and the DNA marker 7-AAD (n=6). (**D**) Immunoblot and quantification of the replication stress marker, phosphorylated RPA (p-RPA32) (n=3/group). (**E**) Representative confocal imaging and quantification of replication rate (kb/min) in FXN-deficient or control PAECs pulsed with CldU (20 minutes, 50μM; green) followed by IdU (20 minutes, 250μM; red) with hydroxyurea (2mM; HU). Scale bars represent 10μm. (**F**) Immunoblot and quantification of DNA damage response markers (p-ATR, CHK1, Ub-γH2AX). (**G**) Immunofluorescent staining and confocal microscopy of nuclear 53BP1 foci (red) in PAECs DAPI-stained nuclei (blue). Two-tailed Student's *t*-test with error bars that reflect mean +/- SD. Experiments were performed at least three separate times.

3.3.2 Sustained FXN deficiency leads to persistent DNA damage response and endothelial senescence

Because cell cycle arrest can result in apoptosis or senescence (87), we next sought to determine the evolving outcomes of chronic FXN deficiency induced by siRNA in PAECs over

an extended time course (Supplemental Data Figure 11E-F). Interestingly, the initial burst of BrdU incorporation in FXN-deficient PAECs was blunted between 3 and 8 days after transfection (Figure 8A). At the same time, chronic FXN knockdown resulted in increasing apoptosis resistance in PAECs (starting at 3 days post-transfection) (Figure 8B). In contrast to other studies in which DNA damage resulted in pulmonary endothelial apoptosis (92, 93), sustained FXN knockdown led to up-regulation of markers of senescence: $p16^{INK4}$ protein (Figure 8C) and senescence-associated-β-galactosidase (SA-β-gal) staining (Figure 8D).

To characterize a mechanism for the convergence of FXN deficiency on irreversible senescence, replication stress and DNA damage response pathways were reassessed. While replication and cell cycle protein (Supplemental Data Figure 11G) as well as RRM2 transcript (Supplemental Data Figure 11H) peaked and were eventually reduced at day 8 post-transfection, FXN-deficient PAECs exhibited chronic and more comprehensive DDR signaling including p-ATR, p-CHK1, p-CHK2, and p53 alongside γH2AX (Figure 8E). In sum, epigenetic FXN deficiency promotes an Fe-S dependent evolution in nuclear function starting with replication stress and reversible growth arrest and progressing to irreversible DDR-dependent senescence.

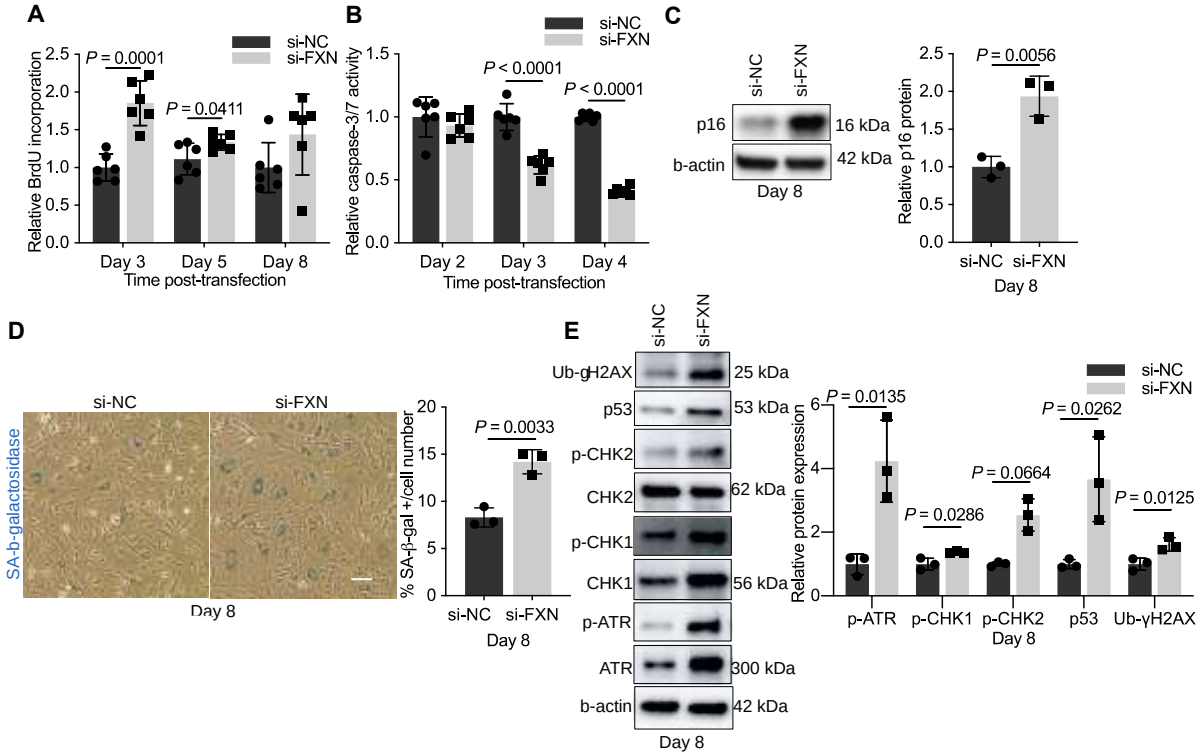

Figure 8. Endothelial evolution toward cellular senescence due to chronic FXN deficiency.
(**A**) Colorimetric BrdU incorporation in FXN-deficient PAECs compared to negative control at 3, 5, and 8 days after transfection (n=6). (**B**) Chemiluminescent measurement of caspase-3/7 activity in FXN-deficient PAECs compared to controls at 2, 3, and 4 days post-transfection (n=6). (**C**-**E**) Experiments reflect PAECs 8 days after transfection with FXN siRNA or negative control (**C**) Immunoblot of $p16^{INKA}$ protein expression (n=3). (**D**) Light microscopic images of senescence-associated (SA)-β-galactosidase staining (blue). Scale bar indicates 200μm. Quantification reflects average percentage of SA-β-gal stained PAECs out of total cell number (n=3). (**E**) Quantification of DNA damage response markers (p-ATR, p-CHK1, p-CHK2, p53, Ub-γH2AX) by immunoblot (n=3). Two-tailed Student's *t*-test with error bars that reflect mean +/- SD. Experiments were performed at least three separate times.

3.3.3 FXN deficiency promotes endothelial senescence and PH in vivo

To investigate the effects of FXN deficiency in the pulmonary endothelium *in vivo*, both genetic and pharmacologic FXN knockdown mouse models were investigated. First, tamoxifen-dependent endothelial (EC) *Fxn-/-* mice (expressing Cdh5(PAC)-Cre-ERT2+ mice (261)) compared to Fxn *flox/flox* control mice (212) were exposed to normoxia or chronic hypoxia to accelerate PH prior to hemodynamic measurement and histologic evaluation (Figure 9A). CD31+

pulmonary endothelial cells from the lungs of EC *Fxn-/-* mice exhibited appropriate knockout (Supplemental Figure 13A) and decreased Fxn transcript (Figure 9B). Consistent with our findings of FXN-driven genotoxicity (Figures 7F and 8E), confocal imaging revealed that EC *Fxn-/-* mice displayed increased γH2AX in the pulmonary endothelium (Figure 9C-D), in line with chronic up-regulation of the DDR. At the same time, RT-qPCR analysis of CD31+ endothelial cells isolated from FXN-deficient mice showed an increase in $p16^{INK4}$ (Figure 9E). Expression analysis of the pathogenic senescence-associated secretory phenotype (SASP) markers Tnf by RT-qPCR (Figure 9F) and IL-6 by ELISA in plasma (Figure 9G) reflected the underlying endothelial irreversible growth arrest in EC *Fxn*-/- mice. Correspondingly, right heart catheterization revealed hemodynamic manifestations of worsened PH in hypoxic mice, including increased right ventricular systolic pressure (RVSP; a surrogate for the clinical measurement of mean pulmonary arterial pressure (mPAP)) (Figure 9H) and increased Fulton index (a measurement of RV hypertrophy that indirectly reflects increased pulmonary vascular resistance) (Figure 9I) but not in normoxic EC *Fxn-/-* mice (Supplemental Data Figure 13B-C). To rule out any off-target effects relevant to the left ventricle or systemic hypertension, echocardiographic imaging prior to hemodynamic measurements demonstrated no alterations in left ventricular function (Supplemental Data Figure 13D-F). Additionally, alterations in mean arterial pressure (Supplemental Data Figure 13G) and heart rate (Supplemental Figure 13H) were not observed. To explore the contribution of FXN-dependent endothelial senescence to PH development *in vivo*, hypoxic EC *Fxn*-/- mice were treated with the senolytic ABT-263, a BCL2 inhibitor that successfully kills senescent cells (267), or vehicle control (Figure 9J). ABT-263 treatment prevented pulmonary vascular muscularization (Figure 9K) and reduced RVSP (Figure 9L), confirming endothelial senescence as a driver in FXN-dependent PH.

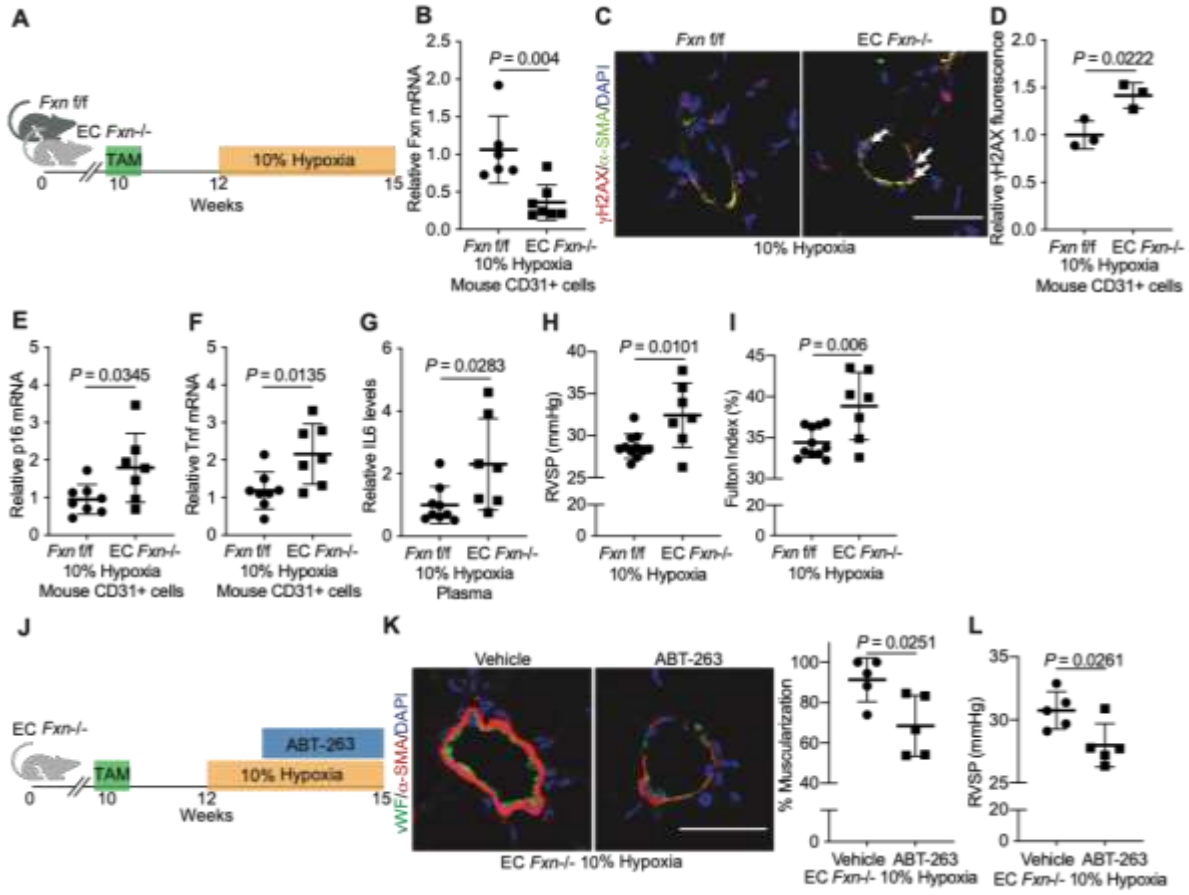

Figure 9. Genetic FXN deficiency promotes endothelial senescence and worsens PH.
(**A**) Diagram of conditional endothelial-specific Fxn knockout mouse model. Experiments compare male Fxn flox/flox (*Fxn* f/f) control mice to mice expressing a tamoxifen-dependent Cdh5(PAC)-ERT2+-Cre recombinase (EC *Fxn*-/-) following chronic hypoxia exposure (3 weeks, 10% O_2). (**B**) RT-qPCR of Fxn expression in CD31+ cells isolated from lungs (n=6-7). (**C** and **D**) Confocal microscopic imaging (50μm scale bar) and quantification of endothelial γH2AX (red signal represented by white arrows), αSMA (green), and DAPI (blue) in lung tissue (n=3). (**E** and **F**) Relative $p16^{INK4}$ and Tnf mRNA by RT-qPCR in CD31+ cells isolated from mouse lungs (n=6-7). (**G**) Plasma IL-6 protein expression measured via ELISA (n=9 v. n=7). (**H**) Right ventricular systolic pressure (RVSP, mmHg) measured by right heart catheterization (n=11 v. n=7). (**I**) Fulton index (RV/LV+S, %) (n=11 v. n = 7). (**J**) Diagram for senolytic treatment in female and male hypoxic EC *Fxn*-/- mice. Mice were given ABT-263 (25mg/kg) or vehicle control via daily oral gavage in weeks 2 and 3 of hypoxic exposure. (**K**) Representative confocal microscopic images and quantification of pulmonary vessel muscularization by immunofluorescent staining of vWF (green) and αSMA (red) (n=5). Scale bar represents 50μm. (**L**) RVSP following senolytic treatment (n=5). Two-tailed Student's *t*-test was performed, with error bars that reflect mean +/- SD.

Next, the effect of endothelial FXN deficiency was also assessed in a pharmacologic model. Polymeric nanoparticle 7C1, composed of low molecular weight polyamines and lipids encapsulating FXN siRNA oligonucleotides or negative control, were delivered to the endothelium

via tail-vein injection every five days in wildtype C57BL/6 mice briefly before and throughout chronic hypoxia exposure (Figure 10A) (71, 72, 263). In mice receiving siRNA against FXN, FXN was down-regulated in CD31+ cells isolated from normoxic (Supplemental Data Figure 13I) and hypoxic lungs (Figure 10B) as assessed by RT-qPCR. This knockdown of endothelial FXN increased pulmonary vascular muscularization, as measured by immunofluorescent staining of αSMA (Figure 10C). Moreover, pharmacologic FXN silencing increased Fulton index and RVSP in normoxic (Supplemental Data Figure 13J-K) and hypoxic conditions (Figure 10D-E). Notably, these FXN-deficient mice also did not exhibit altered mean arterial pressure (Supplemental Figure 13L) and pulse (Supplemental Figure 13M). Importantly, both genetic and pharmacologic models of Fxn deficiency highlight worsened PH in conditions with FXN knockdown and chronic hypoxic exposure. In sum, these data provide a unifying, endothelial-specific mechanism that connects FXN deficiency, DDR-dependent senescence, and PH development *in vivo*.

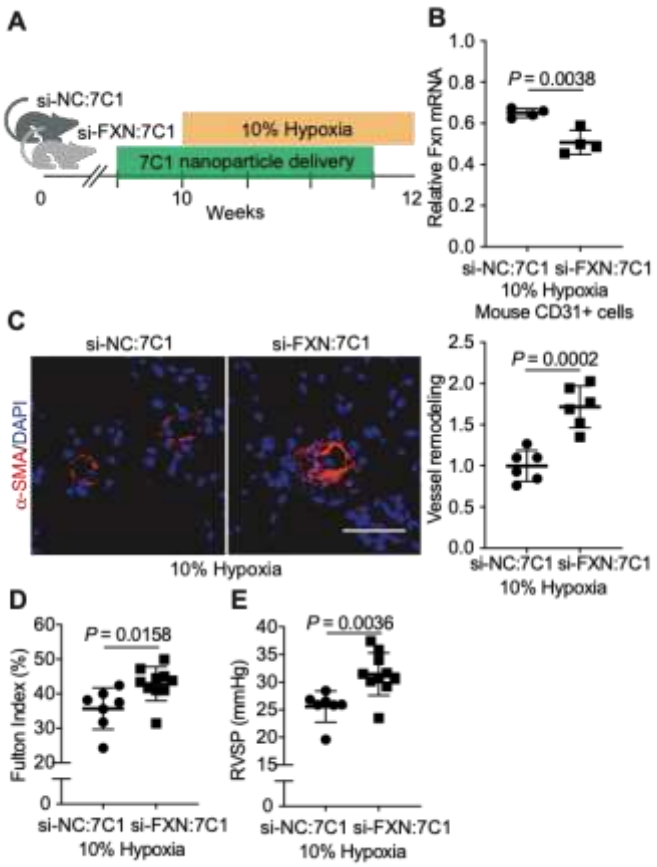

Figure 10. Mice with pharmacologic FXN knockdown develop PH.

(**A**) Experimental mouse model for pharmacologic Fxn knockdown. Endothelial delivery in male C57Bl6 using serial tail-vein injections of 7C1 nanoparticle containing Fxn (si-FXN:7C1) or negative control siRNA (si-NC:7C1) in hypoxic conditions (2 weeks, 10% O_2). (**B**) RT-qPCR of Fxn mRNA expression in CD31+ cells isolated from lungs (n=4). (**C**) Vessel remodeling measured by immunofluorescent staining and confocal microscopic imaging of αSMA (red) and DAPI (blue) in hypoxic mouse lungs (n=6). Scale bars represent 50μm. (**D**) Right heart catheterization measuring right ventricular systolic pressure (RVSP, mmHg) (n=7 v. n=10). (**E**) RV hypertrophy measured by Fulton index (RV/LV+S, %) (n=7 v. n= 10). Two-tailed Student's *t*-test was performed, with error bars that reflect mean +/- SD.

3.4 Supplemental Data

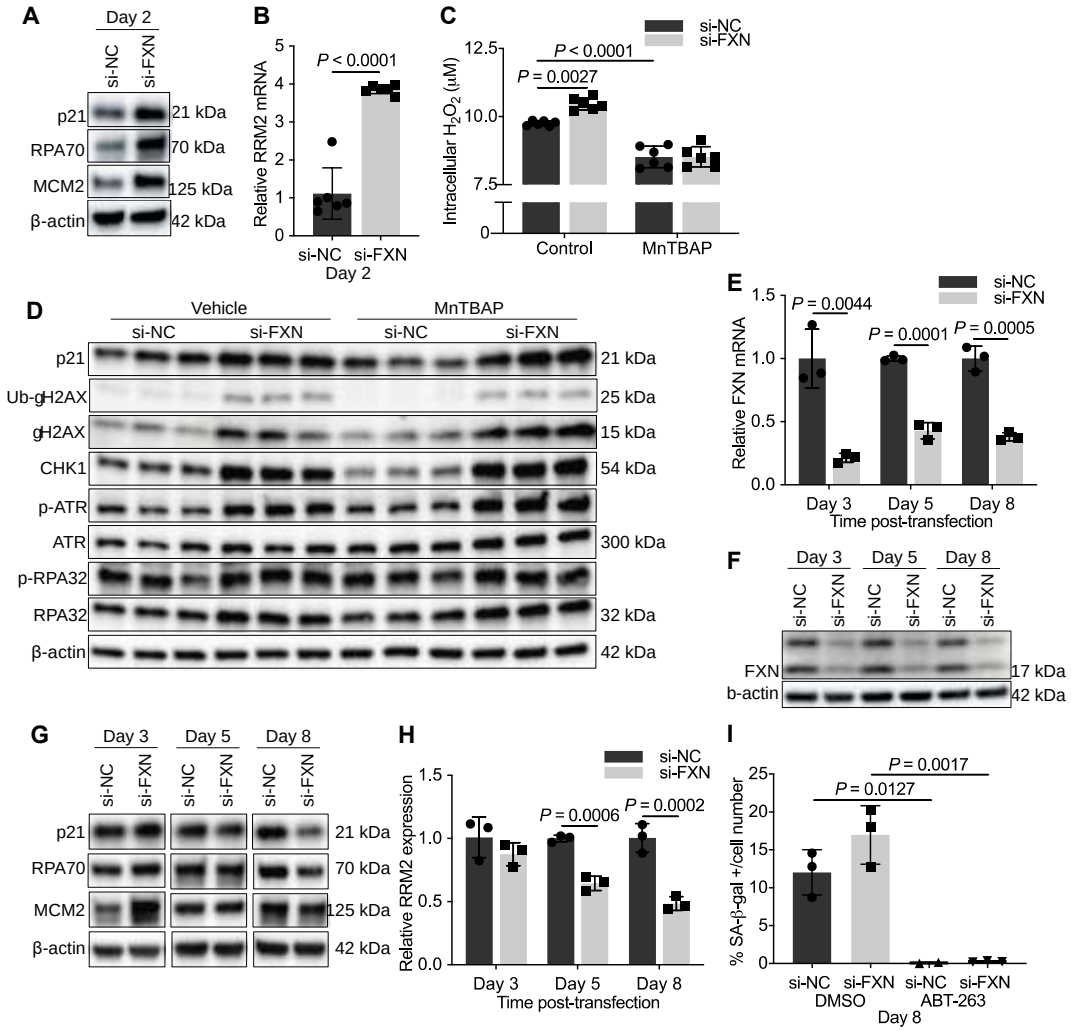

Figure 11. FXN deficient-endothelial cells shift from acute cell cycle arrest to DNA damage response-dependent senescence.

(**A**) Immunoblot of replication fork (MCM2, RPA70) and cell cycle (p21) markers measured in PAECs 2 days after transfection with FXN siRNA or negative control (NC). (**B**) RRM2 transcript levels in PAECs 2 days after transfection (n=6). (**C**) Amplex red hydrogen peroxide (H_2O_2) assay in PAECs treated with FXN siRNA compared to negative control (si-NC) and MnTBAP (50μM) compared to vehicle control (n=3). (**D**) Immunoblot of replication stress, DNA damage response, and growth arrest markers in FXN-deficient PAECs in response MnTBAP (n=3). (**E** and **F**) After transfection with FXN siRNA versus negative control, RT-qPCR (n=3) and representative immunoblot of FXN transcript and protein levels in PAECs over a time course (Days 3, 5, and 8). (**G**) Immunoblot of replication fork (MCM2, RPA70) and cell cycle (p21) markers measured in transfected PAECs over a time course (day 3, 5, 8) (n=3). (**H**) RRM2 mRNA expression at 3, 5, and 8 days post-transfection (n=3). (**I**) Quantification of SA-β-galactosidase staining in PAECs with FXN siRNA or negative control 8 days after transfection and treated with ABT-263 (≥24 hours, 0.25μM) or vehicle (n=3).

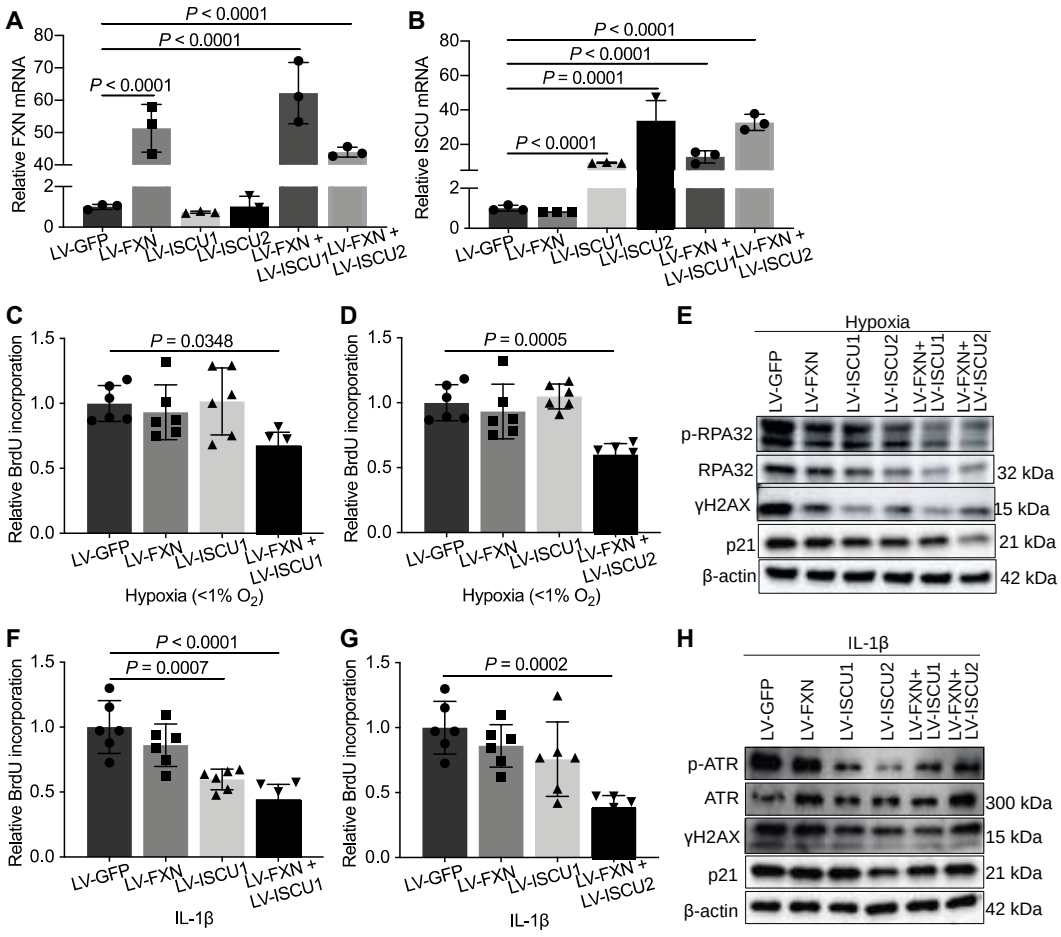

Figure 12. Forced expression of FXN and ISCU1/2 reversed acute replication stress and cell cycle arrest. (**A** and **B**) Transduction efficiency of forced overexpression with FXN, ISCU1, ISCU2, and combined lentiviruses compared to GFP control (n=3). (**C** and **D**) Colorimetric BrdU incorporation following lentiviral transduction of FXN and/or ISCU1 and 2 in hypoxic PAECs (n=6). (**E**) Representative immunoblot of cell cycle (p21) and replication stress (p-RPA32, γH2AX) markers in hypoxic PAECs with forced overexpression of FXN alone and in combination with ISCU1/2. (**F** and **G**) Colorimetric BrdU incorporation in IL-1β-treated PAECs with forced expression of FXN, ISCU1 and 2, or a combination (n=6). (**H**) Representative immunoblot of DNA damage response and growth arrest in PAECs treated with IL-1β. One-way ANOVA with Tukey's post hoc analysis.

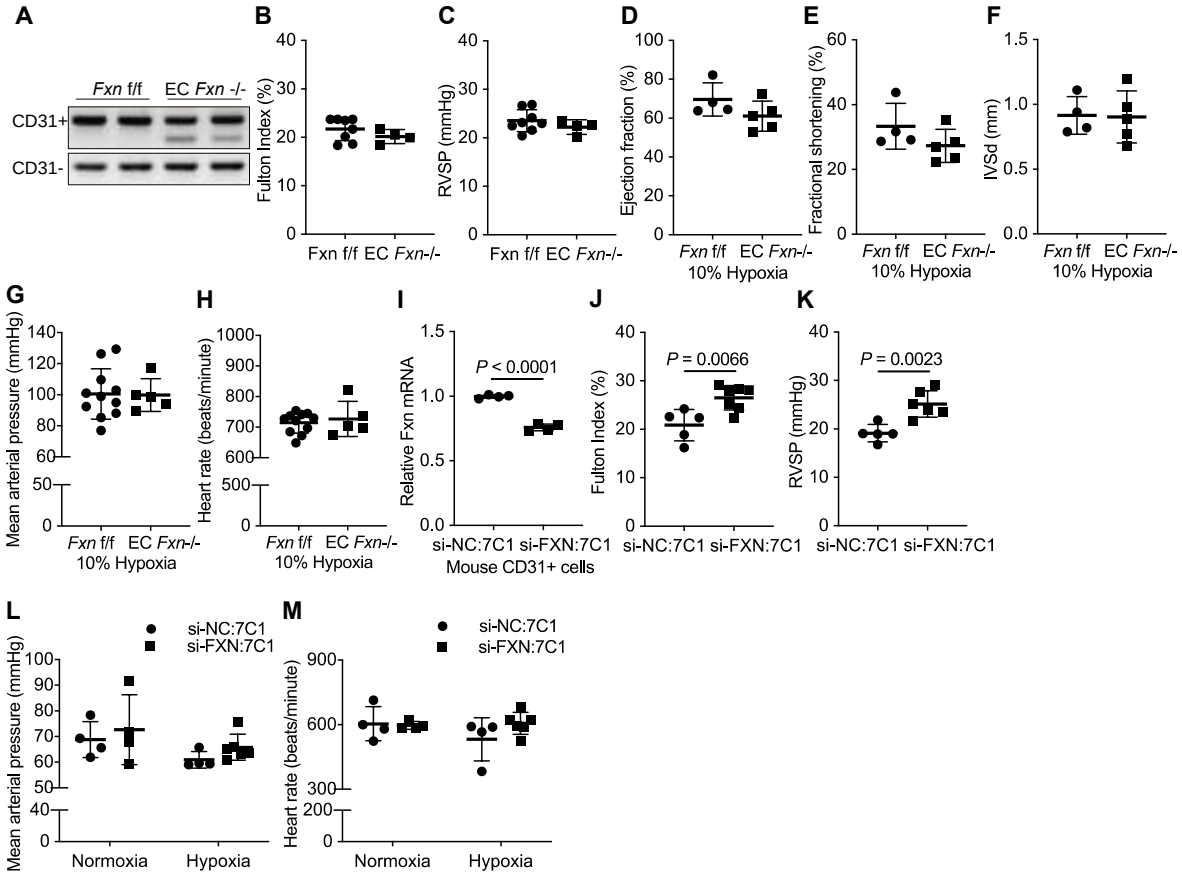

Figure 13. The effects of genetic and pharmacologic FXN deficiency.

(**A**-**H**) Experiments compare conditional EC *Fxn*-/- mice compared to *Fxn* f/f controls in normoxic or hypoxic conditions. (**A**) DNA gel of CD31+ and CD31- cells isolated from lungs of normoxic mice. (**B**) Fulton index (RV/LV+S, %) in normoxic mice (n=8 v. n=4). (**C**) Right ventricular systolic pressure (RVSP, mmHg) (n=8 v. n=4) in normoxic mice. (**D**-**F**) Echocardiography of hypoxic mice measuring ejection fraction (%), fractional shortening (%), and interventricular septal end diastole (IVSd) width (mm) (n=4 v. n=5). (**G**) Tail cuff measurement of mean arterial pressure (mmHg) in hypoxic mice (n=11 v. n=5). (**H**) Heart rate (beats/minute) (n=11 v. n=5). (**I**) In C57Bl6 mice treated with 7C1 nanoparticles containing Fxn (si-FXN:7C1) or negative control siRNA (si-NC:7C1) in normoxic conditions, RT-qPCR of Fxn mRNA expression in CD31+ cells isolated from lungs (n=4). (**J**) Fulton index (%) in normoxic mice (n=7 v. n= 10). (**K**) RVSP (mmHg) in normoxic mice (n=7 v. n=10). (**L**) Tail cuff measuring mean arterial pressure in normoxic or hypoxic mice treated with negative control (n=4) or FXN siRNA (n=6). (**M**) Heart rate (beats/minute) (n=4 v. n=6). Two-tailed Student's *t*-test with error bars that reflect mean +/- SD.

3.5 Discussion

In summary, we have demonstrated that FXN knockdown attenuated Fe-S cluster integrity (Figure 1), subsequently promoting nuclear replication stress and acute cell cycle arrest (Figure

7); chronic FXN knockdown ultimately induced DNA damage response-associated endothelial senescence (Figure 8). Correspondingly, senescence in mice with endothelial-specific FXN deficiency propelled PH development while treatment with a senolytic prevented it (Figures 9 and 10). In contrast to previous studies, our findings define FXN as an upstream mediator of endothelial DNA damage in PH, illustrate the DNA damage-dependent evolution of endothelial cell phenotype toward irreversible growth arrest, and causatively link PH development to FXN-driven senescence.

These results join our previous data on FXN deficiency and metabolic reprogramming. Importantly, DNA damage has been observed in FRDA patient tissues previously, presumed to result from incompletely defined oxidative processes (214, 215). While our work does not preclude the possibility that FXN-dependent mitochondrial dysfunction and oxidative DNA damage contribute to or enhance irreversible senescence (35, 268), acute FXN knockdown induced nuclear replication stress independent of mitochondrial ROS (Supplemental Data Figure 11D), consistent with the pleiotropic mitochondrial and nuclear activities of Fe-S clusters. Establishment of FXN as a lynchpin of both mitochondrial and nuclear dysfunction expands on the importance of Fe-S biology in the endothelium beyond those identified with other Fe-S biogenesis gene deficiencies.

Investigation of the precise Fe-S-dependent nuclear processes that promote replication stress and cell cycle arrest is still ongoing. First, by demonstrating an increased replication rate with FXN knockdown (Figure 7E), we highlight a lesser-known form of replication stress that has only recently been shown to promote DDR and ultimately genomic instability (269). With increased ribonucleotide reductase subunit RRM2 transcript expression (Figure 6B and Supplemental Data Figure 11B), up-regulation in replication fork elongation may be driven at least in part by altered ribonucleotide reductase (RNR) activity and a consequent imbalance in the

nucleotide pools, both of which have been shown to impact DNA integrity (270, 271). Interestingly, RNR contains an essential di-ferric tyrosyl radical cofactor donated by cytoplasmic Fe-S machinery (265), and its activity is preferentially preserved in the early stages of iron deficiency in yeast (272). This same acute sequestration of iron cofactors and conserved function may be characteristic of other critical DNA replication and repair machinery in conditions of acute FXN deficiency. In our work, RRM2 expression (Supplemental Data Figure 11H) also follows the simultaneous arc of nucleotide incorporation (Figure 8A) and replication fork markers (Supplemental Data Figure 11G) from acute replication stress to eventual senescence. Potentially similar to RRM2-deficient cancer cells exhibiting senescence-associated growth arrest (273), our data may reflect diminished RNR activity that leads to replication collapse and irreversible growth arrest.

In addition to an inappropriately elevated replication rate, decreased FXN-dependent activity of Fe-S containing polymerases and helicases required for efficient, error-free replication may result in decreased proof-reading and increased genomic damage during S-phase (154). It is also possible that a combination of these pathogenic processes -- for example, oxidative stress and failure of Fe-S-dependent error-prone replication -- represents a “double-hit” to genomic integrity.

By defining an evolution of endothelial cell behavior over time, our data also add detail and offer novel conceptual links to the hypotheses on dynamic endothelial dysfunction in PH. Although studies have characterized DNA damage (82, 92, 93) as promoting endothelial apoptosis in PH (274), genotoxic stress can result in either apoptosis or senescence (87), and our data provide mechanistic detail to support latter as a driver of PH. While our results emphasize DDR-driven senescence, there are alternative mitochondrial and nuclear mechanisms by which the endothelium may reach irreversible growth arrest that have yet to be explored.

Taking cues from aging and age-related diseases, senescent cells are inherently dysfunctional preventing tissue repair and propagating cell-autonomous damage via its inflammatory secretome. More specifically, senescent endothelial cells exhibit reduced NO signaling (275) and an increased susceptibility to apoptosis in comparison to other senescent cell types (276). Speaking to the latter, the mechanism by which pulmonary endothelial cells become apoptotic versus senescent is not fully defined but depends upon cell type as well as the severity and length of exposure to the genotoxic insult (29). Whether apoptosis and senescence co-exist on the same cellular continuum or represent two separate cell fates that differ based upon PH etiology requires further study (87). Our findings provide some insight into the pathobiological consequences of senescent endothelial cells, such as the release of senescence-associated secretory phase (SASP) mediators (such as IL-6 and TNF-α in Figure 9F-G). While both have been causatively linked to the immune-mediate pathogenesis of pulmonary vascular disease (277) and elevated plasma levels in PAH patients prognosticate mortality (44, 278-280), more work is required to fully characterize the FXN-specific endothelial SASP profile given its dependence upon cell type, inciting stressors, and stage of senescence (281). Moreover, how the FXN-dependent SASP signature contributes to pulmonary vascular inflammation and immune cell recruitment as well as vascular remodelling and fibrosis (29, 32) requires further study.

In total, this work offers a pivotal endothelial-specific mechanism converging on senescence, solidifying the regulatory actions of FXN across Fe-S biology, metabolism, and genomic integrity and offering compelling targets for more effective diagnostics and therapeutics in this deadly disease (see working model below). The relative importance of this novel endothelial

phenotype of irreversible senescence in the context of genetic FXN deficiency in FRDA or acquired FXN deficiency across WSPH PH groups is not yet known.

4.0 HIF-dependent epigenetic modulation drives acquired FXN deficiency and endothelial senescence in multiple PH subtypes

This work was adapted from a manuscript in revision:

Culley MK, Zhao J, Tai YY, Tang Y, Perk D, Negi V, Yu Q, Handen A, Speyer G, Kim S, Lai Y-C, Satoh T, Watson A, Al Aaraj Y, Sembrat J, Rojas M, Khan OF, Anderson DG, Dahlman JE, Norris KE, Gurkar A, Rabinovitch M, Gu M, Bertero T, Chan SY. Endothelial frataxin deficiency induces replication stress to promote senescence in pulmonary hypertension. *In revision.*

Notably, immunofluorescent staining and quantification in animal and human lung tissues performed in part by Dr. Thomas Bertero (Figure 14A and I, Figure 20A-B, D-E, and J, Figure 21C). Pulmonary microvascular endothelial cells from healthy versus Group 1 PAH patients provided by Drs. Dmitry and Elena Goncharova (Figure 14G-H, Figure 20I, Figure 21A-B). Hemodynamic assessments performed by Jingsi Zhao and Yi Yin Tai (Figure 15C-D and F, Figure 19F-G). Assistance with immunoblots provided by Jingsi Zhao (Figure 18E and G).

4.1 Introduction

PH is a heterogeneous disease caused by multiple disparate triggers. WSPH classifications seek to group patients based upon clinical parameters and etiology. These groupings ultimately inform prognosis and therapeutic choice as the available treatments are reserved for the particularly severe subtype, Group 1 PAH, which arises from idiopathic, hereditary causes, toxin exposure, and secondary disease associations. Separately, PH in groups 2–5 is associated with myriad

comorbidities (3). Notably, as the population ages and the number of patients with chronic diseases rises (100), PH due to left heart disease (Group 2), particularly PH associated with heart failure with preserved ejection fraction (HFpEF) (101) and metabolic syndrome (102), and PH due to hypoxic lung disease (Group 3) (103) represent a majority of PH patients. There is very little understanding of the pathological underpinnings in these subtypes and thus no PH-specific treatment options. How the molecular mechanisms that underlie PAH and other PH groups are connected is still under investigation.

Thus far, we have described a mechanism by which FXN deficiency coordinated both Fe-S-dependent metabolic and replication stress and have causatively linked the ensuing irreversible endothelial senescence to the development of PH *in vivo*. However, whether FXN expression is dynamically regulated in PH, independent of FRDA mutations, has not been investigated. Diverse triggers including acquired inflammation (266) and hypoxia (243) have been attributed to Group 1 PAH and Group 3 PH with triggers for other PH subtypes incompletely defined. Both elevated (282, 283) and reduced (284) FXN levels have been reported in non-vascular hypoxic cell types; specific studies attribute this transcriptional control to the HIF-responsive element in the *FXN* promoter (282). However, the impact of hypoxia, as well as other acquired PH triggers, on FXN levels in pulmonary vascular cells is undefined. Our prior work demonstrating how HIF-α, a well-characterized transcription factor involved in metabolic rewiring in PH (42, 179), acts as a master regulator of endothelial ISCU1/2 and BOLA3 expression in hypoxia (70, 72), Therefore, hypoxia might drive HIF-α-dependent acquired FXN deficiency, similar to other Fe-S biogenesis genes.

As previously mentioned, both endothelial apoptosis and proliferation contribute to the progressive pulmonary vasculopathy in this disease . By defining endothelial evolution toward irreversible senescence *in vitro*, we introduced a new phenotype to the “endothelial dysfunction”

that drives PH. Whether FXN deficiency and endothelial senescence are important in PAH or the lesser characterized Group 2 and 3 PH is not yet know. Therefore, we aimed to both characterize our endothelial-specific mechanism of FXN-dependent senescence and more specifically, define the dynamic control of FXN in response to known PH triggers.

4.2 Materials & Methods

Shared methods were referenced in previous Materials & Methods sections (2.2, 3.2) while new materials and procedures have been described below.

Transfection

Transfection was performed in both pulmonary artery endothelial cells (PAECs) and smooth muscle cells (PASMCs) using pre-determined concentrations of siRNA. Silencer Select siRNAs for BMPR2 (s2044, 40nM), ENG (s4678, 40nM), CAV1 (s2447, 40nM), ACRVL1 (s502493, 40nM), EIF2AK4 (s532694, 40nM), HIF1-α (s6541, 6.25nM), HIF2-α (s4699, 6.25nM), CTCF (s20967, 20nM), BRD2 (s12070, 6.25nM), BRD4 (s23901, 6.25nM), and negative control #1 and #2 were purchased from Life Technologies. FXN (sc-40580) as well as negative control (sc-44236) pooled siRNAs were purchased from Santa Cruz. Experiments were completed 48 hours after transfection.

Immunofluorescent staining and confocal microscopy

De-paraffinization using xylenes (30 minutes at room temperature) was followed by step-wise rehydration and high-temperature antigen retrieval. Samples were then permeabilized with 0.1% Triton X-100 (15 minutes) and blocked with 5% donkey serum and 2% BSA in PBS (1 hour

at room temperature). After primary antibodies were incubated overnight at 4 degrees C (Appendix A Table 2), Alexa 488, 568 and 647-conjugated secondary antibodies (ThermoFisher Scientific) for immunofluorescence (1 hour at room temperature) and Hoechst counterstain (~1 minute) were applied sequentially prior to mounting. Pictures were obtained using Nikon A1 confocal microscope and 40x oil immersion lens. Small pulmonary vessels (30-100μm diameter) present in a given tissue section (≥10 vessels/section) that were not associated with bronchial airways were selected for analysis. Intensity (integrated density) of staining was quantified using ImageJ software (NIH). Degree of pulmonary arteriolar muscularization was assessed in OCT lung sections stained for αSMA by calculation of the proportion of fully and partially muscularized peripheral pulmonary arterioles to total number. Relative vessel remodeling was quantified by measuring vessel wall thickness (*i.e.,* αSMA) compared to vessel diameter. Analyses were performed blinded to condition. Experiments were performed with the help of Ying Tang, M.S. and Thomas Bertero, Ph.D.

Animal studies

All animal experiments were approved by the University of Pittsburgh (DLAR) and the Harvard Center for Comparative Medicine. Animal husbandry was managed with the help of Jingsi Zhao, M.S., Ying Tang, M.S., and Dror Perk.

Group 1 PAH models:

Lung tissues from male Sprague-Dawley rats (10-14 weeks old) injected with 60 mg/kg monocrotaline were flash-frozen or paraffin-embedded via an ethanol-xylene dehydration series before downstream processing (285).

Male IL-6 transgenic (Tg) mice (12 weeks old) were exposed to 3 weeks of normobaric hypoxia in a temperature-humidity controlled chamber (10% O_2, OxyCycler chamber, Biospherix Ltd.) and compared to age-matched wild type kept in normoxic conditions (21% O_2) (19) (Taconic). Additional experiments assessing the efficacy of the senolytic ABT-263 (Selleckchem) were performed in female IL-6 Tg mice by administering the drug (25mg/kg/day) compared to vehicle control (2% DMSO in corn oil) via oral gavage during weeks 2 and 3 of hypoxic exposure.

In simian immunodeficiency virus (SIV)-infected rhesus macaques (aged 6-10 years), hemodynamic instability (No PH versus PAH) was measured prior to intravenous inoculation with SIV ΔB670, at 6 months, and then at 10-12 months after infection. Lung tissue was embedded in paraffin for downstream processing obtained as previously described (286).

Group 2 PH-HFpEF models: Sample were generously shared with us by Yen-Chun Lai. Flash-frozen and OCT-embedded lung tissue from male AKR/J mice (aged 6-12 weeks) fed a high-fat diet (60% lipids/kcal) for 16-20 weeks compared to normal chow diet were analyzed (Table 4) (287).

In a two-hit model of metabolic syndrome, double-leptin receptor defect (obese) ZSF1 male rats were treated with a subcutaneous injection of Sugen (SU4516, 100mg/kg) at 8-10 weeks-old compared to lean littermate controls. Hemodynamic assessment and tissue procurement were performed 14 weeks after injection (Table 5) (288).

Group 3 PH model:

10-12 week-old C57BL/6 wild type were subjected to 3 weeks of normobaric hypoxia in a temperature-humidity controlled chamber (10% O_2, OxyCycler chamber, Biospherix Ltd.) compared with normoxia (21% O_2). Male hypoxic wild type mice were also received oral administration of the senolytic ABT-263 (25mg/kg/day) or vehicle control during the final 2 weeks of hypoxic treatment.

Human samples

PH was defined by elevated mean pulmonary arterial pressure (mPAP) ≥ 25 mmHg. For paraffin-embedded lung samples, human PH specimens were collected from discarded surgical samples or rapid autopsy samples from subjects diagnosed with PH (Tables 6 and 7), some of which have been described previously (72). Non-diseased human lung specimens were from the Center for Organ Recovery & Education (CORE). Informed consent was obtained for patient right heart catheterization and tissue sampling. All experimental procedures involving the use of human tissue and plasma and the study of invasive and non-invasive hemodynamics were approved by the institutional review board at the University of Pittsburgh. Ethical approval for this study and informed consent conformed to the standards of the Declaration of Helsinki.

4.3 Primary Data

4.3.1 Acquired FXN deficiency and endothelial cellular senescence in Group 1, 2, and 3 PH animal and patient lungs

To determine whether FXN is dynamically regulated in PH beyond FRDA mutations, we evaluated FXN levels in multiple *in vivo* models of PH representing diverse clinical subtypes. At the same time, we performed expression analysis of the $p16^{INK4}$ transcript to begin to characterize potential FXN-dependent endothelial senescence in PH. Immunofluorescent staining of the pulmonary vasculature followed by confocal microscopy (Figure 14A) revealed a marked reduction in FXN in the CD31+ endothelium (Figure 14B), αSMA+ smooth muscle layer (Supplemental Data Figure 20A), and entire pulmonary vessel (Supplemental Data Figure 20B) in a monocrotaline rat model of Group 1 PAH (285). Correspondingly, expression analysis of $p16^{INK4}$ mRNA in whole rat lung homogenates revealed significant up-regulation of senescence (Figure 14C). In another model of Group 1 PAH (19), isolated lung CD31+ endothelial cells and whole-lung tissue in transgenic mice expressing the inflammatory cytokine interleukin-6 (IL-6) and exposed to chronic hypoxia displayed significantly reduced FXN (Figure 14D, Supplemental Data Figure 20C) and increased $p16^{INK4}$ transcript levels (Figure 14E) when compared to normoxic wild-type controls. In simian immunodeficiency virus (SIV)-infected rhesus macaques modeling HIV-induced Group 1 PAH (286), FXN expression was also decreased (Supplemental Data Figure 20D) by immunofluorescent staining and co-localized quantification with the CD31+ endothelium.

Apart from Group 1 PAH, we performed immunofluorescent staining and expression analysis in two rodent models that develop Group 2 PH due to heart failure with preserved ejection fraction (PH-HFpEF): AKR/J mice fed a high-fat diet versus a regular diet (287) (Table 4) and

obese ZSF1 rats treated with VEGF receptor antagonist SU-5416 (Ob-Su) compared to lean controls (288) (Tables 5). First, immunofluorescent staining and confocal microscopy reveals FXN levels (gray) were decreased in the pulmonary arteries of high-fat diet-fed AKR/J mice (Supplemental Data Figure 14E). Similarly, FXN transcript (Supplemental Data Figure 20F) and protein levels (Figure 14E) were reduced in lungs from obese, SU5416-treated ZSF1 rats compared to lean controls. Alongside FXN down-regulation, lungs from rats with PH-HFpEF exhibited elevated $p16^{INK4}$ expression (Figure 14F). Lastly, isolated lung CD31+ endothelial cells (Supplemental Data Figure 20G) and whole-lung tissue (Supplemental Data Figure 20H) from chronically hypoxic mice, modeling Group 3 PH, demonstrated decreased FXN expression.

Supporting data observed in multiple PH animal models, expression analysis in isolated pulmonary microvascular endothelial cells (PMVECs) from a Group 1 PAH patient and a healthy patient that were gender- and age-matched revealed decreased FXN mRNA (Supplemental Data Figure 20I) and protein expression (Figure 14G). Group 1 PAH PMVECs also showed an increase in $p16^{INK4}$ levels (Figure 14H) and in the percentage of β-galactosidase positive cells (Supplemental Data Figure 21A), both signaling irreversible senescence. Forced expression of FXN and its binding partner marginally decreased $p16^{INK4}$ protein expression (Supplemental Data Figure 22B), consistent with heterogeneity within the PMVECs population. Separately, FXN levels were reduced in CD31+ endothelium (Figure 14I) and αSMA+ smooth muscle layer (Supplemental Data Figure 23J) in patients with Group 1 PAH (Table 6) as well as interstitial pulmonary fibrosis (IPF)-associated PH (Group 3 PH) (Table 7) compared with non-diseased controls. Lungs from Group 1 PAH and Group 3 PH patients exhibit increased $p16^{INK4}$ transcript (Figure 14J) and immunofluorescent staining by confocal microscopy (Supplemental Data Figure

24C). Taken together, diverse PH triggers in rodent, non-human primate, and human models across various WSPH PH groups exhibited decreased endothelial FXN and increased $p16^{INK4}$ expression.

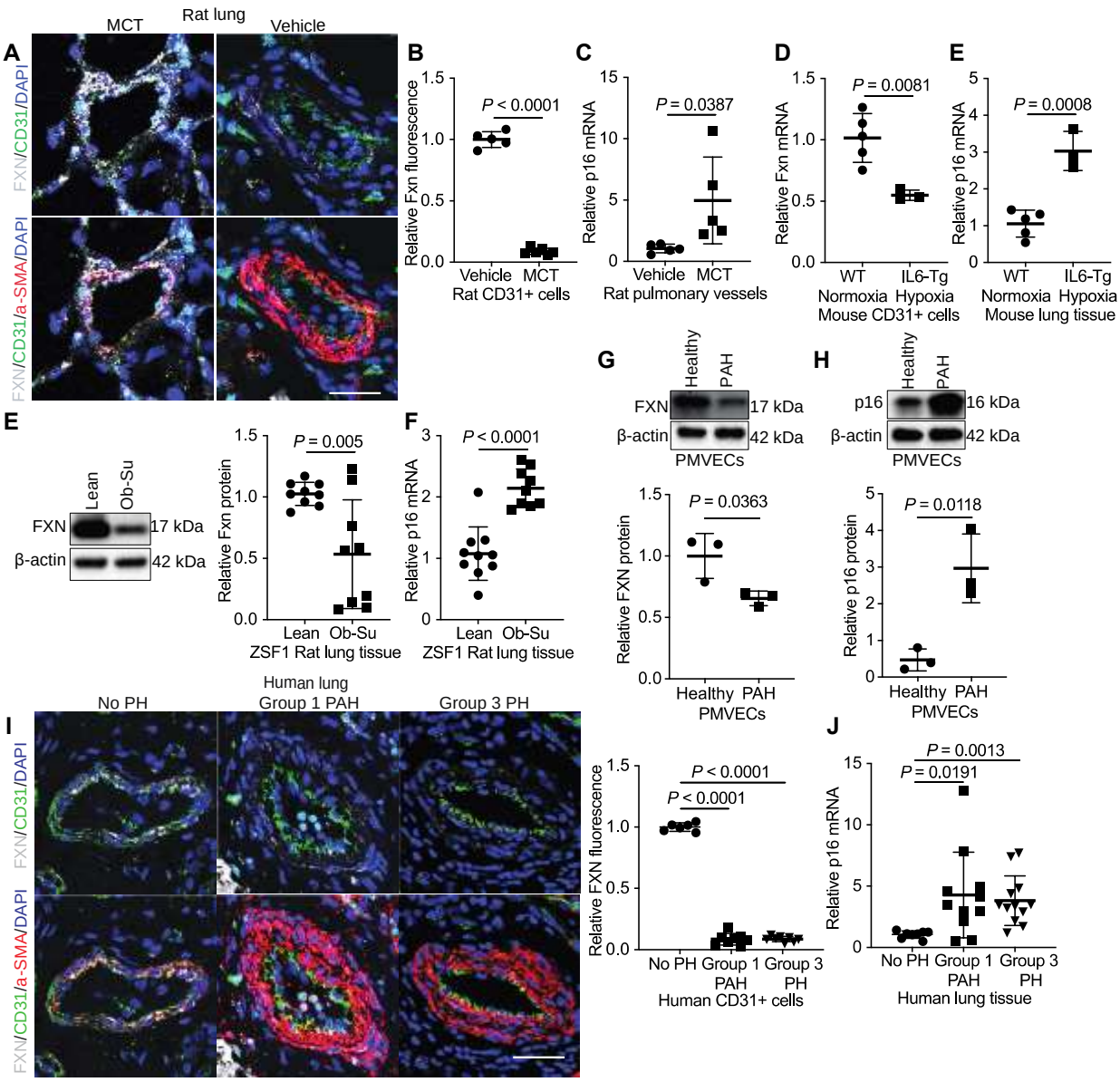

Figure 14. Reduced FXN and elevated p16INK4 expression in Group 1, 2, and 3 PH lungs.

(**A**) Representative images of lungs stained with immunofluorescent probes for Fxn (gray), CD31 (green), αSMA (red), counterstained with DAPI (blue), and imaged by confocal microscopy. Scale bars indicate 50μm. Quantification of Fxn co-localized within the CD31+ endothelium in rats treated with monocrotaline (MCT) (n=6) or vehicle (n=5). (**B**) Relative $p16^{INK4}$ expression by RT-qPCR in lung tissue from monocrotaline-treated rats compared to control (n=5/group). (**C**) Fxn mRNA expression in isolated CD31+ lung cells and (**D**) whole-lung $p16^{INKA}$ mRNA levels in hypoxic IL6-Tg (n=3) versus normoxic WT mice (n=5). (**E**) Fxn protein and (**F**) $p16^{INKA}$ transcript expression in lung tissue from ZSF1 obese rats treated with Sugen (SU5416) (Ob-Su) (n=9) versus lean controls (n=8). (**G** and **H**) Immunoblot of FXN and $p16^{INKA}$ protein in pulmonary microvascular endothelial cells (PMVECs) from a healthy versus Group 1 PAH patient (n=3/group). (**I**) Representative confocal images probing for FXN (gray), CD31 (green), SMA (red) and counterstained with DAPI (blue). Scale bars represent 50μm. Quantification of FXN in the CD31+ endothelium of Group 1 PAH (n=8) or Group 3 PH (n=8) patient lungs compared to controls (No PH) (n=6). (**J**) RT-qPCR of $p16^{INK4}$ mRNA levels in lung tissue of patient without PH, Group 1, or Group 3 PH. Two-tailed Student's *t*-test with error bars that reflect mean +/- SD.

To provide a causal link between FXN deficiency and elevated $p16^{INKA}$ across different PH classifications, Group 1 (Figure 15A) and Group 3 PH (Figure 15E) murine models were treated with senolytic ABT-263, which selectively removes BCL2-positive, apoptosis resistant cells (267), compared to vehicle control as disease developed. Following removal of senescent cells, ABT-263-treatment hypoxic IL-6 Tg mice exhibited a decrease in the percentage of muscularized vessels measured by immunofluorescent co-staining endothelial vWF and smooth muscle cell αSMA in mouse lung tissue (Figure 15B). Correspondingly, the senotherapy also reduced Fulton index (Figure 15C), measuring RV hypertrophy, and RVSP (Figure 15D). Similarly, the senolytic therapy also decreased RVSP (Figure 15F), suggesting removal of senescence can prevent PH development *in vivo*. In summary, these findings support the notion that acquired FXN deficiency and ensuing senescence represents a common and causative molecular feature among seemingly diverse clinical subtypes.

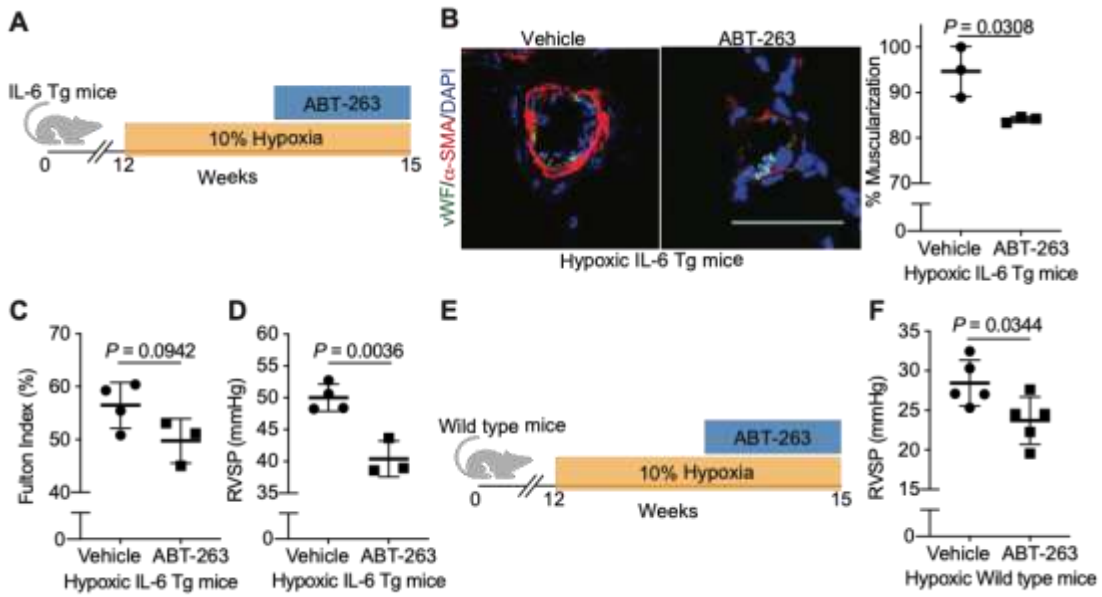

Figure 15. Senolytic therapy prevents Group 1 and 3 PH development.
(A) Diagram depicting senolytic treatment (25mg/kg/day via oral gavage) in female IL-6 Tg mice during weeks 2 and 3 of hypoxic exposure (3 weeks, 10% O_2). (**B**) Representative images and quantified percentage of muscularized pulmonary vessels measured by immunofluorescent staining of vWF (green) and αSMA (red) (n=3). (**C**) Fulton index (RV/LV+S, %) (n=4 v. n=3). (D) Right ventricular systolic pressure (RVSP, mmHg) (n=4 v. n=3). (**E**) Diagram of male wild type mice treated with ABT-263 (25mg/kg/day via oral gavage) in weeks 2 and 3 of hypoxia exposure. (**F**) RVSP (n=5). Two-tailed Student's *t*-test was performed with error bars that reflect mean +/- SD.

4.3.2 Acquired FXN down-regulation by known PH triggers

Given that animal and patient PH lung tissues exhibit acquired FXN reduction, primary pulmonary artery endothelial cells (PAECs) and smooth muscle cells (PASMCs) were exposed to known PH triggers. Exposure to hypoxia, a trigger associated with Group 1 PAH and Group 3 PH (243), robustly down-regulated FXN transcript and protein levels in cultured PAECs (Figure 16A-B). Similarly, exposure to the inflammatory cytokine interleukin-1 beta (IL-1β), which is elevated (44) and promotes vascular remodeling in Group 1 PAH (289), decreased FXN in PAECs (Figure 16C-D). Knockdown of genes associated with heritable PAH or exposure to increased matrix stiffness did not alter FXN expression in PAECs (Supplemental Data Figure 22A). Thus, both

hypoxic and inflammatory stimuli associated with Groups 1 and 3 PH down-regulated FXN in pulmonary endothelial cells.

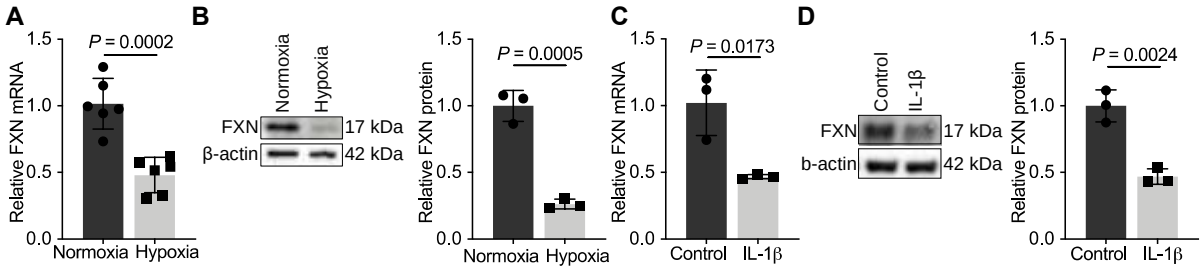

Figure 16. Chronic hypoxia and inflammation down-regulate FXN expression in pulmonary artery endothelial cells.

(**A**-**D**) FXN expression analysis in cultured human pulmonary artery endothelial cells (PAECs). (**A** and **B**) RT-qPCR analysis (n=6) and immunoblot with densitometry (n=3) after exposure to hypoxia (≥ 24 hours, <1% O_2). (**C** and **D**) RT-qPCR and immunoblot following IL-1β treatment (≥ 24 hours, 10 ng/ml) (n=3). Experiments performed at least three separate times. Two-tailed Student's *t*-test with error bars that reflect mean +/- SD.

4.3.3 HIF-α independently controls CTCF and BRD4 to down-regulate endothelial FXN

Given the importance of HIF-α activity in Fe-S biogenesis (70-72) and the link between hypoxia and FXN in PAECs, we aimed to determine whether hypoxic down-regulation of FXN was dependent upon HIF-α. PAECs were treated with siRNA specific for the HIF-α isoforms, HIF-1α and HIF-2α, alone and in combination, followed by exposure to chronic hypoxia (Supplemental Data Figure 22B-C). HIF-1α and HIF-2α knockdown together most effectively increased FXN mRNA (Figure 17A) and protein levels (Figure 17B) under hypoxic stimulus. Bolstering these results, HIF-1α activation by cobalt(II) chloride (290) robustly decreased FXN (Figure 17C-D), similar to hypoxia and inflammation, while HIF-1α-specific inhibition by siRNA reversed this effect (Figure 17E). Thus, despite the HIF-responsive element in the *FXN* promoter reported in other cell types (282, 283), the repressive activity of HIF-α on FXN in PAECs suggested a more complex, tissue-specific regulatory landscape.

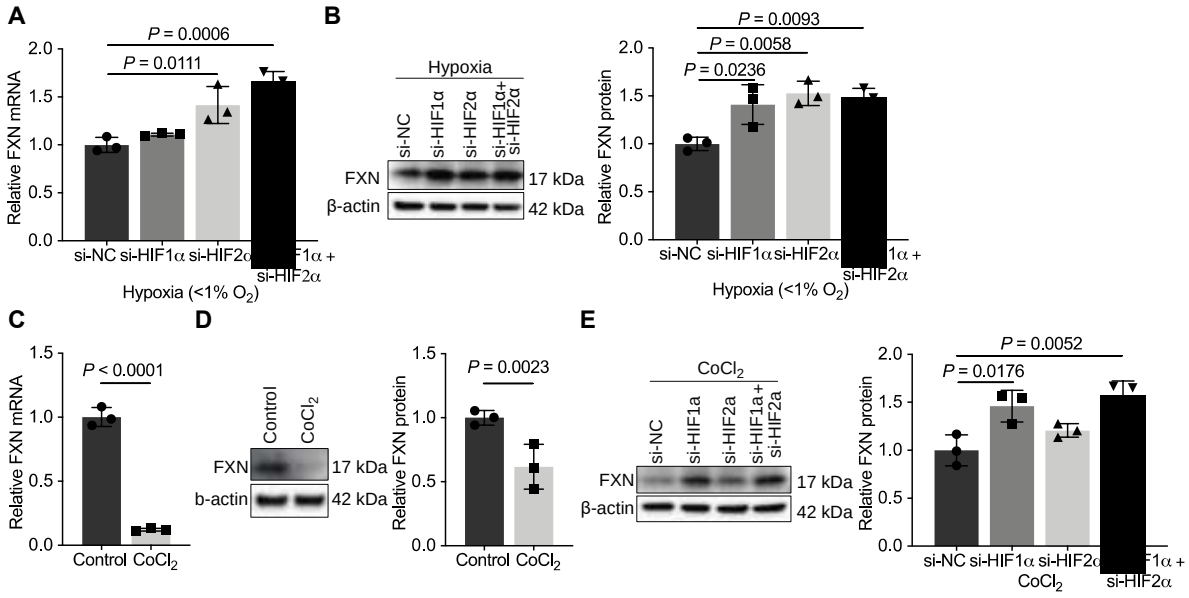

Figure 17. FXN is decreased by HIF.

(**A** and **B**) RT-qPCR and immunoblot of relative FXN transcript and protein expression in hypoxic PAECs transfected with HIF-1α, HIF-2α, or combined isoform-specific siRNAs compared to negative control (NC). (**C** and **D**) FXN expression analysis in PAECs treated with cobalt(II) chloride (≥ 24 hours, 750μM $CoCl_2$). (**E**) Immunoblot of FXN in PAECs treated with $CoCl_2$ and transfected with HIF-1α, HIF-2α, or both siRNAs compared to negative control. Two-tailed Student's *t*-test and one-way ANOVA (Tukey's post hoc analysis) with error bars that reflect mean +/- SD. Experiments were performed at least three separate times in triplicate.

Consistent with prior description of the chromatin insulator protein CCCTC-binding factor (CTCF) binding the *FXN* 5'UTR (291, 292), we showed that CTCF inhibition by siRNA (Supplemental Data Figure XD) markedly reduced FXN transcript (Figure 18A) and protein levels (Figure 18B) in PAECs. We observed reduced CTCF protein following chronic hypoxic exposure (Supplemental Data Figure 22E) and cobalt(II) chloride treatment (Supplemental Data Figure 22F), consistent with FXN knockdown under these conditions (Figure 16A-B). Moreover, knockdown of the HIF-1α and HIF-2α isoforms together rescued CTCF (Figure 18C), corresponding with rescue of FXN levels (Figure 17A-B). In sum, HIF-α controls CTCF-dependent modulation of FXN expression in PAECs.

Given the importance of heterochromatin silencing of FXN in FRDA (187, 293) and recent data that epigenetic pharmacotherapies reversed experimental PH (149, 294), we investigated whether other chromatin modulators, namely bromodomain and extra-terminal (BET) motif proteins (295), regulate FXN in PAECs in hypoxic and inflammatory conditions. First, PAECs were exposed to chronic PH triggers and simultaneously treated with vehicle control or I-BET151 – a selective inhibitor of BET family proteins BRD2, 3, and 4 (296). I-BET151 rescued FXN expression under hypoxia (Figure 18D-E) and IL-1β stimulation (Supplemental Data Figure 22G). Similarly, BRD4 inhibition (Supplemental Data Figure 22H) reversed the hypoxic reduction of FXN (Figure 18F-G), and BRD2 inhibition (Supplemental Data Figure 22I) reversed the IL-1β-mediated reduction (Supplemental Data Figure 22J). Furthermore, while cobalt(II) chloride treatment increased BRD2 and 4 expression (Supplemental Data Figure 22K) and decreased FXN (Figure 17C-D), BRD4 knockdown partially reversed the reduction of FXN mediated by cobalt(II) chloride (Supplemental Data Figure 22L). Moreover, siRNA knockdown of HIF-1α during cobalt(II) chloride exposure decreased BRD4 (Figure 18H), demonstrating that HIF-1α-dependent BRD4 expression may be responsible, at least in part, for modulation of FXN. In summary, these data highlight the complex HIF-α-driven epigenetic silencing of FXN following exposure to hypoxia or inflammation with rescue by epigenetic inhibitory therapies, similar to cases of genetic deficiency (187, 293).

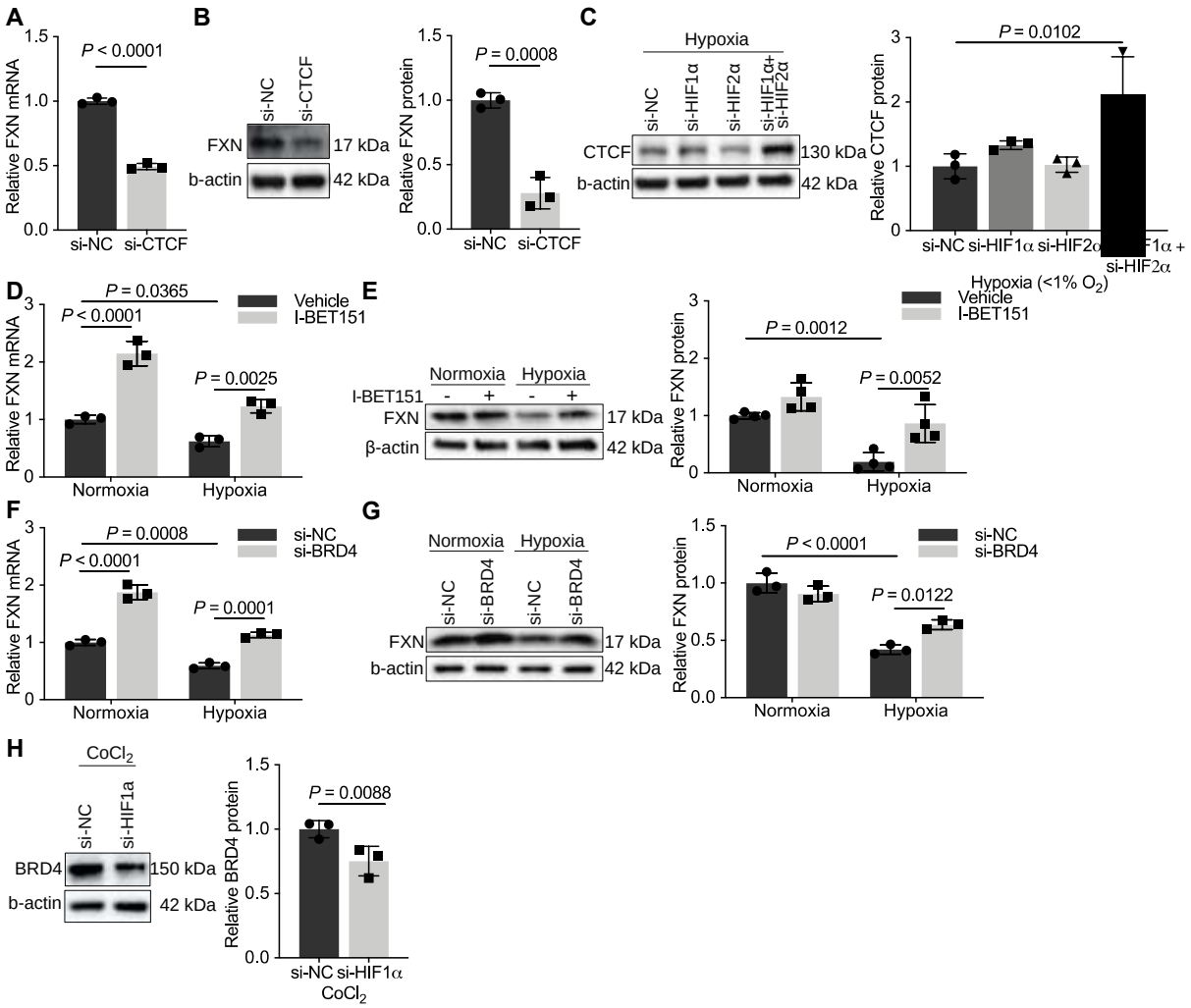

Figure 18. HIF independently coordinates both CTCF and BRD4 to down-regulate FXN.
(**A** and **B**) RT-qPCR and immunoblot of FXN in PAECs transfected with siRNA against CTCF or negative control. (**C**) Immunoblot of CTCF in hypoxic PAECs transfected with HIF-1α, HIF-2α, or both siRNAs compared to control. (**D** and **E**) FXN transcript and protein expression in PAECs treated with I-BET151 (500nM) or vehicle control (DMSO) and exposed to hypoxia or normoxia (≥24 hours). (**F** and **G**) RT-qPCR and immunoblot of FXN expression in PAECs treated with siRNA against bromodomain-containing protein 4 (BRD4) or negative control and with or without hypoxic exposure. (**H**) Immunoblot of BRD4 in PAECs transfected with HIF-1α compared to negative control and treated with $CoCl_2$. Two-tailed Student's *t*-test and one- or two-way ANOVA (Tukey's post hoc analysis) with error bars that reflect mean +/- SD. Experiments were performed at least three separate times in triplicate.

4.3.4 Smooth muscle FXN deficiency does not promote PH

Given that FXN was decreased in the SMA+ medial layer of several PH models (Figure 14 and Supplemental Data Figure 20), we sought to determine if the same acquired triggers might

control FXN expression in smooth muscle cells. Chronic hypoxic exposure down-regulated FXN transcript expression in cultured PASMCs (Figure 19A) while treatment with IL-1β did not (Figure 19B), suggesting tissue-specific responses to different triggers of PH.

Next, we aimed to establish whether acquired FXN deficiency exerts the same coordinated effect on replication stress-dependent senescence in smooth muscle cells. Unlike PAECs, transfected PASMCs with FXN siRNA knockdown did not exhibit changes in replication stress (p-RPA32) or cell cycle arrest (p21) compared to cells treated with negative control siRNA (Figure 19C). This acute FXN deficiency did not result in up-regulation of DDR markers, suggesting no underlying genomic damage (Figure 19D). Consistent with this lack of nuclear stress, conditional, smooth muscle-specific FXN knockout mice (SMC *Fxn*-/-) (Figure 19E) exposed to hypoxia did not develop PH as demonstrated by unchanging RVSP and Fulton index when compared to *Fxn* f/f controls (Figure 19F-G), altogether reinforcing the specificity of endothelial FXN deficiency in promoting pulmonary vascular disease.

In sum, these data define a mechanism of HIF-α-driven epigenetic FXN reduction in response to known PH triggers, illustrate the specific importance of FXN deficiency in pulmonary endothelium versus other vascular cell types, and support the relevance of FXN-dependent senescence in Group 1, 2, and 3 PH.

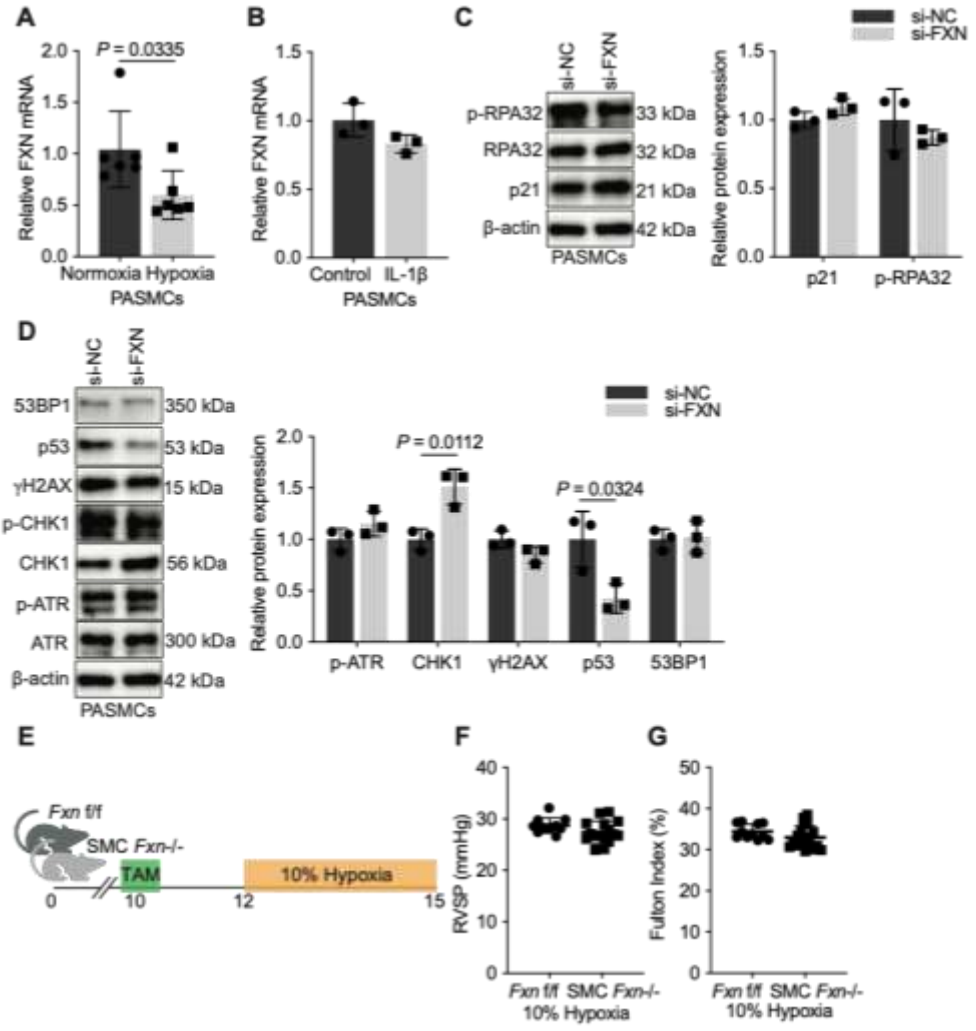

Figure 19. FXN deficiency in pulmonary smooth muscle cells does not promote PH.

(**A**) RT-qPCR analysis of FXN transcript levels in PASMCs after exposure to normoxia or hypoxia (≥ 24 hours, <1% O_2) (n=6). (**B**) Relative FXN expression by in PASMCs treated with IL-1β (≥ 24 hours, 10 ng/ml) compared to control (n=3). (**C** and **D**) Immunoblot evaluation of cell cycle arrest (p21), replication stress (p-RPA32), DDR markers (p-ATR, CHK1, γH2AX) in PASMCs transfected with FXN siRNA compared to negative control (n=3). (**E**) Diagram of conditional smooth muscle cell (SMC) *Fxn*-/- (Myh11-ERT2+-Cre+) mice compared to *Fxn* f/f control exposed to chronic hypoxia (3 weeks, 10% hypoxia). (**F**) Right heart catheterization measuring right ventricular systolic pressure (RVSP, mmHg) in *Fxn* f/f (n=11) and SMC *Fxn*-/- (n=16) hypoxic mice. (**G**) Fulton index (RV/LV+S) (n=11 versus 16). Two-tailed Student's *t*-test with error bars that reflect mean +/- SD. Experiments performed in primary cultured cells performed at least three separate times.

4.4 Supplemental Data

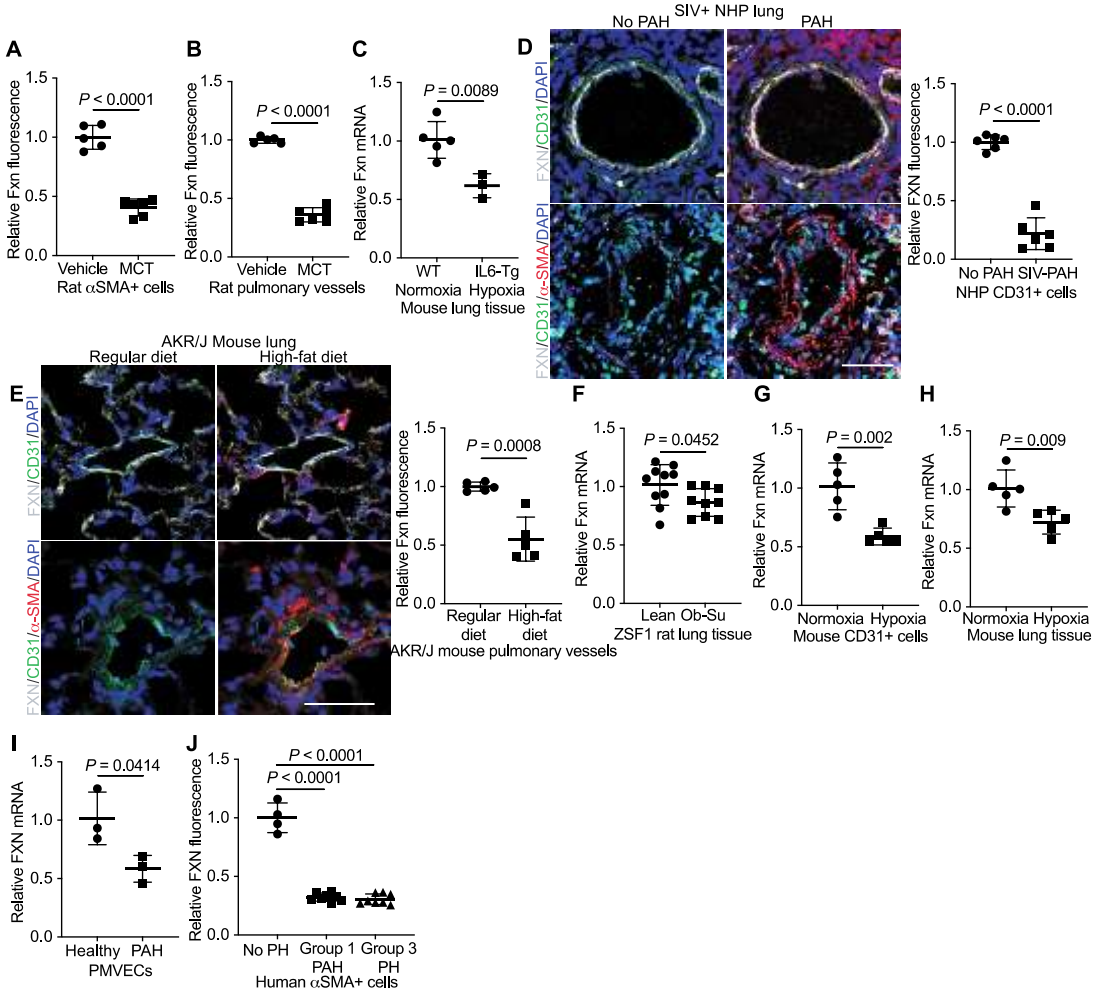

Figure 20. FXN expression in the pulmonary vasculature of Group 1, 2, and 3 PH models.
(**A** and **B**) Fxn co-localized with pulmonary medial layer (αSMA+) for Group 1 PAH monocrotaline-treated rats (n=6) versus vehicle control (n=5). (**C**) RT-qPCR of Fxn transcript expression in whole-lung tissue from hypoxic IL-6 Tg mice (n=3) versus normoxic wild type control (n=5). (**D**) Immunofluorescent staining of αSMA (red), CD31 (green), FXN (gray), and counterstaining nuclei with DAPI (blue) followed by confocal microscopy. Quantification of FXN levels colocalized in CD31+ cells in the pulmonary vessels of SIV-infected nonhuman primates (NHP) with and without PAH (n=6). (**E**) Representative immunofluorescent images and quantification of Fxn (gray) in pulmonary vessels from AKR/J mice fed a high-fat or regular diet (n=5). Scale bars indicate 50μm. (**F**) RT-qPCR of Fxn levels in whole-lung from SU5416-treated obese ZSF1 (n=9) versus lean rats (n=10). (**G** and **H**) Fxn mRNA in CD31+ cells or whole lung from C57Bl6 mice exposed to chronic hypoxia (10% O_2, 3 weeks) or normoxia (n=5). (**I**) FXN expression by RT-qPCR in PMVECs from patients with no PH compared to Group 1 PAH (n=3/group). (**J**) FXN levels co-localized with αSMA+ cells in Group 1 PAH (n=8) or Group 3 PH (n=8) lungs compared to control (No PH) (n=6). Two-tailed Student's *t*-test with error bars that reflect mean +/- SD.

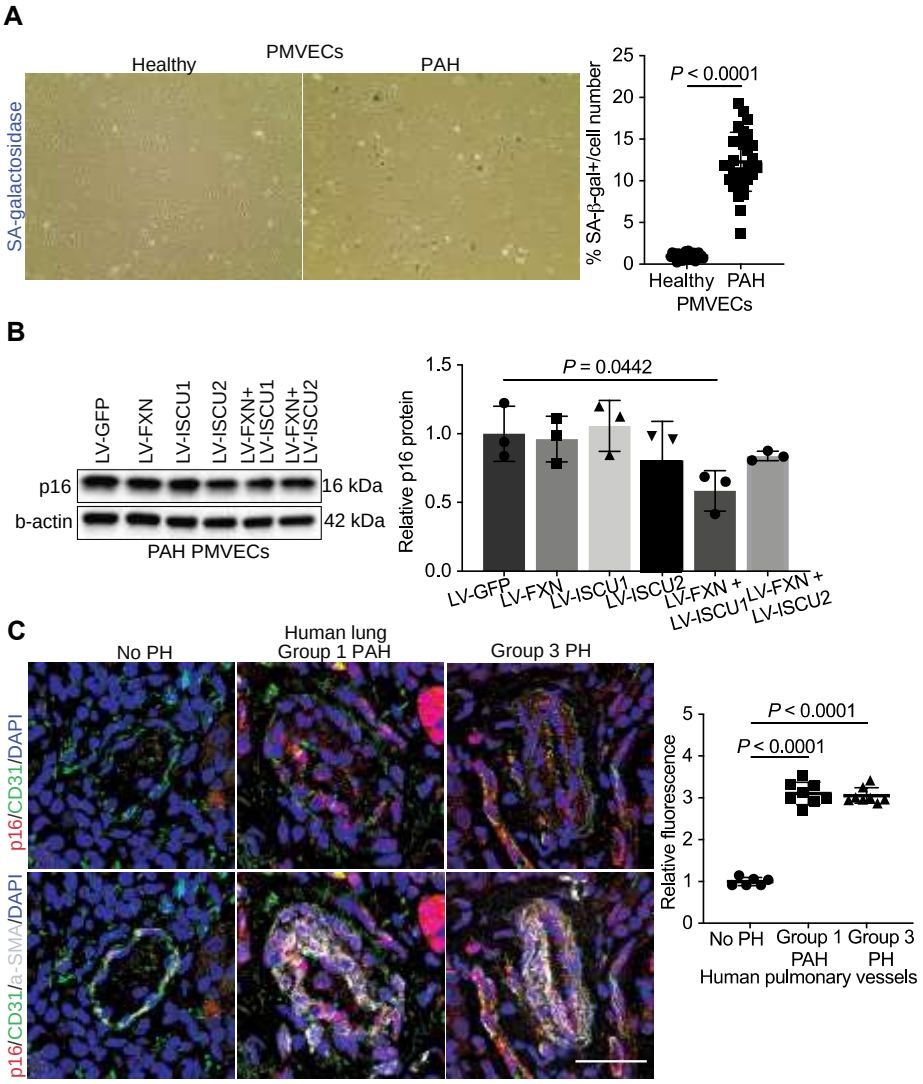

Figure 21. Elevated markers of senescence in PH patient pulmonary vascular cells.

(**A**) Representative brightfield images and quantification of senescence-associated (SA)-β-galactosidase positive PMVECs from a healthy versus a Group 1 PAH patient. (**B**) $p16^{INK4}$ protein levels following forced overexpression of FXN and ISCU1/2 in Group 1 PAH PMVECs (n=3). (**C**) Immunofluorescent staining of $p16^{INK4}$ (red), CD31 (green), αSMA (white), and DAPI (blue) and confocal microscopy of No PH (n=6), Group 1 PAH (n=8), or Group 3 PH patient lungs (n=8). Scale bars indicate 50μm. Two-tailed Student's *t*-test with error bars that reflect mean +/- SD.

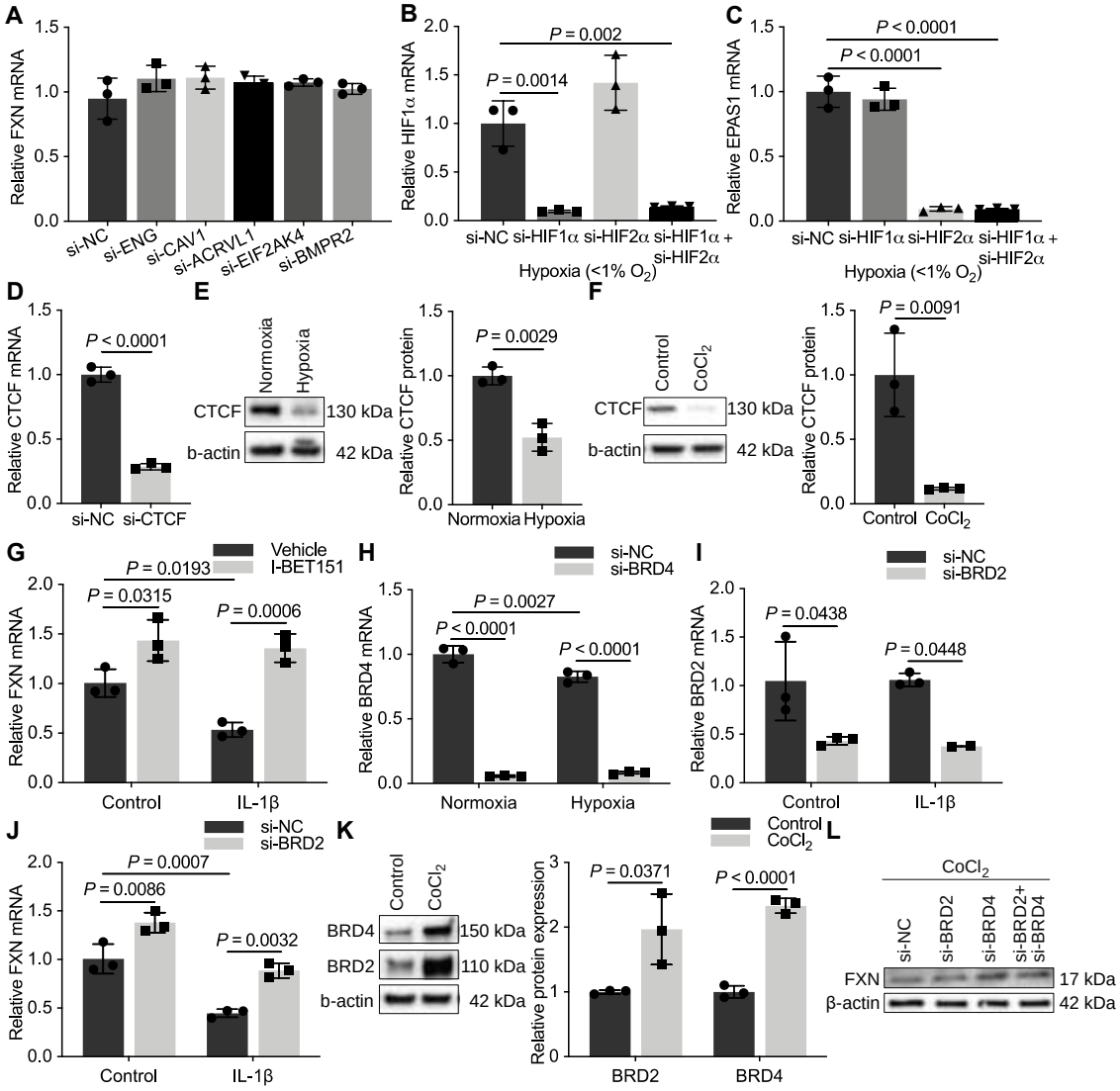

Figure 22. Epigenetic repression of FXN in response to acquired PH triggers.

(**A**) Pulmonary artery endothelial cell (PAEC) FXN mRNA levels following siRNA transfection of targets associated with mutations in PH (ENG, CAV1, ACRVL1, EIF2AK4, BMPR2) compared to negative control (NC) (n=3). (**B** and **C**) RT-qPCR of relative HIF-1α and EPAS1 levels for PAEC transfection control of HIF-1α, HIF-2α, or combined isoform-specific siRNA. (**D**) RT-qPCR of CTCF transcript for PAEC transfection control of CTCF siRNA. (**E**) Immunoblot of CTCF protein in hypoxic PAECs (≥ 24 hours, <1% O_2). (**F**) Immunoblot of CTCF protein in PAECs treated with $CoCl_2$ (≥ 24 hours, 750μM). (**G**) FXN mRNA levels in PAECs treated with I-BET151 (500nM) or vehicle control with or without IL-1β stimulation (≥24 hours). (**H** and **I**) PAEC transfection control of BRD4 or BRD2 siRNA in normoxia and hypoxia conditions. (**J**) RT-qPCR of FXN levels in PAECs transfected with BRD2 siRNA and exposed to IL-1β or control. (**K**) Immunoblot of BRD2 and BRD4 expression in PAECs treated with $CoCl_2$. (**L**) Representative immunoblot of FXN in PAECs transfected with BRD2, BRD4, and combined siRNAs compared to negative control and treated with $CoCl_2$. Two-tailed Student's *t*-test and two-way ANOVA (Tukey's post hoc analysis) with error bars that reflect mean +/- SD. Experiments were performed at least three separate times in triplicate.

4.5 Discussion

Expanding upon the relevance of FXN in pulmonary vascular disease beyond FRDA mutations, we observed decreased FXN and increased $p16^{INK4}$ expression in the lungs of Group 1, 2, and 3 PH animal models and patient tissues. Moreover, removal of apoptosis-resistant, senescent cells with the senolytic drug ABT-263 prevented PH development in Group 1 and 3 PH mouse models, supporting a causal role for FXN-dependent senescence across multiple PH subtypes. In addition, our data highlighted how triggers of PH, such as chronic hypoxia and inflammation, lead to HIF-α-mediated regulation of known (CTCF) and novel (BRD4) epigenetic modifiers of FXN transcription in PAECs. Notably, acquired FXN deficiency in pulmonary smooth muscle cells did not promote the genomic stress that precipitates senescence or PH development *in vivo* (Figure 19), further distinguishing the importance of endothelial Fe-S cluster deficiency in pulmonary vascular disease.

FXN joins a growing number of Fe-S assembly genes dynamically repressed by HIF-α signaling in the endothelium (70-72). It is likely that these acquired HIF-α-driven deficiencies and their specific cell fates cumulatively contribute to the shifting pulmonary endothelial pathophenotypes throughout PH progression and across WSPH classifications. However, the contributions of this dynamic network of Fe-S biogenesis genes are only just emerging. Notably, this acquired reduction in FXN opposes prior studies which identified a HIF-dependent increase of FXN in non-vascular cells (282, 283). While the reasons for divergent gene regulation are not known in different hypoxic tissues, there may be cell-type specificity of the chromatin structure and its modulators, CTCF and BRD4, in exerting control of FXN. By expanding upon the comprehensive landscape of epigenetic factors involved in FXN regulation, our data endorse

epigenetic pharmacotherapies, specifically BRD4 inhibitors (149), that may work in multiple PH subtypes, at least in part, by increasing FXN levels in the pulmonary endothelium. Though not explored here, HDAC inhibition is an emerging therapeutic model in FRDA (187, 226, 227), and may apply to acquired FXN deficiency as well; conversely, given the importance of heterochromatic silencing in FXN mutations, BET-specific remodeling may be beneficial in the setting of FRDA.

Our data support the relevance of endothelial senescence driven by FXN deficiency across multiple PH subtypes. Importantly, these observations offer an explanation for a predisposition to pre-capillary PH, especially in the context of combined pre- and post-capillary PH in Group 2 patients. Further studies are warranted to elucidate the individual or additive effect of pulmonary endothelial FXN deficiency in the setting of left heart disease. Regardless, this shared FXN-dependent mechanism holds therapeutic potential not only for patients with PAH but other PH groups with no currently available treatment options. Specifically, our findings endorse the use of emerging senotherapies (32, 297) in PH. Additional studies are required to explore the benefits of therapies that decelerate cellular progression toward senescence (*e.g.*, rapamycin (298), resveratrol (231, 299)), senolytic therapies that remove senescent cells (300), and senomorphic therapies that suppress markers of senescence or their secretory phenotype without inducing apoptosis (297). Senomorphics represent an opportunity to prevent senescence-dependent pulmonary vascular remodeling while avoiding the potentially detrimental effects of drug-induced endothelial apoptosis. In fact, p38 kinase inhibitors were recently characterized as a potential senomorphic therapy in the setting of FRDA mutation-induced fibroblast senescence (301). Moreover, since the age of prevalent PH patients is increasing worldwide and older PH patients are more commonly afflicted by HFpEF (302), FXN-dependent endothelial senescence could also serve as a key

molecular driver for PH in the elderly. If so, determination of appropriate therapeutic timing of these drugs during PH development will be crucial as will determination of administration efficacy in young versus old patients.

Altogether, we have defined a shared endothelial mechanism contingent on acquired FXN deficiency in Group 1, 2, and 3 PH (see working model below), thus providing a basis for therapies targeting senescence, particularly for PH patient groups with no treatment options. Whether FXN mutations result in similar metabolic dysfunction and PH is not yet defined.

5.0 FXN-dependent endothelial dysfunction in Friedreich's ataxia patients

This work was adapted from a manuscript in revision:

Culley MK, Zhao J, Tai YY, Tang Y, Perk D, Negi V, Yu Q, Handen A, Speyer G, Kim S, Lai Y-C, Satoh T, Watson A, Al Aaraj Y, Sembrat J, Rojas M, Khan OF, Anderson DG, Dahlman JE, Norris KE, Gurkar A, Rabinovitch M, Gu M, Bertero T, Chan SY. Endothelial frataxin deficiency induces replication stress to promote senescence in pulmonary hypertension. *In revision.*

Notably, Drs. Mingxia Gu and Marlene Rabinovitch provided differentiated inducible pluripotent stem cell-derived endothelial cells from patients with Friedreich's ataxia compared to healthy age- and gender-matched controls (Figures 23 and 24).

5.1 Introduction

Trinucleotide repeat expansion mutations in the frataxin (*FXN)* gene cause Friedreich's ataxia (FRDA) (183). This multisystem disease is defined by neurodegeneration and hypertrophic cardiomyopathy (and less often dilated cardiomyopathy) (194) with the latter driving mortality in roughly 60% of patients (197). Case reports have described pulmonary arteriolar vasculopathy in this population (200), consistent with the fact that up to 40% of patients with hypertrophic cardiomyopathy (HCM) in general suffer from Group 2 pulmonary hypertension (PH) (105, 199). Yet, PH and cardiopulmonary complications as a whole in FRDA have been surprisingly underreported (201, 202), in part due to the lack of hemodynamic outcomes and lung specimens available for study. Of the FRDA heart failure reports that are available, focus has been given to

the diastolic dysfunction and markedly elevated left ventricular filling pressures rather than the PH that, by definition, is present (202).

Similarly, the molecular underpinnings of pulmonary vascular cells has not been investigated. Rather, studies have largely focused on cell types, such as cardiomyocytes and neurons, with high mitochondrial content and high metabolic rate as well as higher levels of baseline FXN than initially characterized in whole-lung tissues (303). Common in multiple non-vascular cell types, FRDA-dependent FXN deficiency led to mitochondrial dysfunction in the form of decreased mitochondrial respiration (203), reduced mitochondrial biogenesis (248), as well as oxidative stress and ensuing mtDNA and nuclear DNA damage (208, 209, 214, 215). While tissue damage in the form of slowed growth or apoptosis have been widely described in models of FRDA (220, 222, 223, 304), cellular senescence is an emerging characteristic of FXN deficiency in specific tissues (*e.g.*, neurons, islet cells, fibroblasts) (224, 225) with specific data supporting irreversible growth arrest may be related to decreased mitochondrial respiration and aberrant Ca^{2+} signaling (224), mtDNA damage (305), telomere dysfunction (306, 307). FXN's direct disruption of Fe-S-dependent DNA replication and repair machinery in FRDA has not been characterized; however, studies have directly linked mitochondrial Fe-S biogenesis and genomic instability (219). The complete mechanism by which FXN orchestrates these and other consequences of Fe-S deficiency to promotes senescence remains ill-defined. Moreover, how these examples of FXN-driven dysfunction relate to endothelial cell function in patients with FRDA is not yet known. However, given that we have already demonstrated FXN-dependent senescence promotes PH pathogenesis and that this mechanism is pervasive in multiple PH subtypes, including Group 2 PH due to HFpEF, we hypothesized FXN mutations may promote similar endothelial phenotypes that could explain a potential predisposition for pulmonary vascular disease in the setting of HCM.

5.2 Materials & Methods

Shared methods were referenced in previous Materials & Methods sections (2.2, 3.2, 4.2) while new procedures have been described below.

Cell culture

Skin fibroblasts from a 36-year-old female (330 and 380 repeat expansions on each allele) and 30-year-old male (541 and 420 repeat expansions) with Friedreich's ataxia were reprogrammed using retroviral by the Coriell Institute for Medical Research. These purchased inducible pluripotent stem cells (iPSCs) were differentiated into endothelial cells (iPSC-ECs) (308, 309) by Mingxia Gu, Ph.D., who generously provided healthy, gender- and age-matched iPSC-ECs for comparison. These cells were cultured on 0.2% gelatin in endothelial basal media supplemented with a growth media kit (PromoCell; Lonza) and 5% fetal bovine serum (FBS) without antibiotics or antifungals added. Experiments were performed between passages 2 to 6.

Proximity ligation assay

Endogenous interaction of the DNA Pol δ protein subunits (POLD1 and 3) was assessed using a Duolink Proximity Ligation Assay kit (Sigma Aldrich) per the manufacturer's instructions. Briefly, iPSC-ECs were plated in Lab-Tek II chamber slides (5000 cells/well), fixed with 4% paraformaldehyde for 15 minutes, permeabilized with 0.25% Triton X-100 for 15 minutes, and blocked for 30 minutes at 37 degrees C before incubation with mouse monoclonal antibody POLD1 (MA1-23200 Thermofisher Scientific) and rabbit monoclonal antibody POLD3 (ab182564 Abcam) at 1:250 overnight at 4 degrees C. After washing, fixed cells were exposed to PLUS and MINUS PLA probes for 1 hour, ligated for 30 minutes, and amplified with polymerase for 1 hour and 40 minutes all at 37 degrees C. Cells were counterstained and mounted with DAPI

solution. Imaging was performed on a Nikon A1 microscope with 60x oil immersion objective at 1.75x zoom; >10 images were taken per sample. Quantification was blinded and performed manually.

5.3 Primary Data

5.3.1 Genetic FXN deficiency mirrors the metabolic and genomic dysfunction that drives endothelial senescence

To begin to causatively link genetic FXN deficiency to endothelial senescence, we employed inducible pluripotent stem cells from patients with FRDA mutations (310) that were differentiated into endothelial cells (iPSC-ECs), as previously described (311). Importantly, FRDA patient iPSC-ECs exhibited normal endothelial cell expression markers (Supplemental Data Figure 24A-B), function (Supplemental Data Figure 24C), and markedly reduced FXN levels (Supplemental Data Figure 24D-E). By comparing these genetically FXN-deficient cells to their gender- and age-matched controls, we sought to compare endothelial-specific alterations controlled by FRDA mutations in addition to acquired deficiencies. Using the mechanism delineated in FXN-deficient PAECs as a guide, similar pathophenotypes were assessed in our iPSC-EC model. First, both male (Figure 23A) and female (Supplemental Data Figure 24F) FRDA mutant endothelial cells exhibited definitively reduced BrdU incorporation. Simultaneously, genetic FXN deficiency resulted in decreased caspase-3/7 activity (Figure 23B, Supplemental Data Figure 24G) and elevated BCL2 protein expression (Figure 23C, Supplemental Data Figure 24H) compared to healthy control. Similar to transfected PAECs at day 8 (Figure 8A-B), loss of

replicative potential alongside apoptosis resistance signaled FXN-dependent permanent growth arrest. Consequently, FXN-deficient iPSC-ECs displayed increased $p16^{INK4}$ transcript (Figure 23D, Supplemental Figure 24I) and protein expression (Figure 23E) and senescence-associated-β-galactosidase (SA-β-gal) staining (Figure 23F). This senescent phenotype was accompanied by elevated IL-6 expression (Supplemental Figure 24J), indicative of the senescence-associated secretory phase (SASP), and a marked reduction in RRM2 transcript expression (Supplemental Data Figure 24K). Attempts to rescue this phenotype with FXN replacement did not alter BCL2 or $p16^{INK4}$ protein levels (BCL2, suggesting irreversibility of this endothelial phenotype. In addition, FRDA iPSC-ECs exhibited an imbalance in vasomotor tone effectors with increased EDN1 transcript and secreted protein levels (Figure 23G-H) and reduced NOS3 transcript levels (Figure 23I).

To establish the molecular drivers of this pathogenic endothelial dysfunction with genetic FXN deficiency, we interrogated both genomic and metabolic modifiers. To start, immunoblot showed markedly increased ubiquitinated (Ub-γH2AX) and phosphorylated H2AX (γH2AX) in FRDA iPSC-ECs (Figure 23J), suggesting senescence is driven by persistent DDR and mirroring chronic FXN knockdown in PAECs. Given this FXN-dependent genotoxicity, we aimed to demonstrate that FXN deficiency directly impairs nuclear replication and repair. Using a proximity ligation assay, the Fe-S-dependent association of the DNA polymerase δ catalytic subunit POLD1 with its accessory subunits, in this case, POLD3 was measured (163). Confocal imaging showed iPSC-ECs with FRDA mutations exhibited decreased nuclear signal, denoting a FXN-driven reduction in the intact form of this high-fidelity polymerase (Figure 23K). Therefore, these findings delineate a FXN-driven mechanism in which direct attenuation of Fe-S-containing nuclear machinery may contribute to compromised DNA replication and repair. This FXN-driven

genotoxicity is accompanied by an increase in intracellular hydrogen peroxide in FRDA patient-derived iPSC-ECs compared to healthy controls (Figure 23L). Cumulatively, these data identify shared endothelial pathophenotypes between both epigenetic and genetic FXN deficiency. Namely, chronic FXN deficiency attenuated mitochondrial and nuclear Fe-S-containing protein function which led to oxidative stress and compromised genomic integrity, and ultimately, dysfunctional endothelial cells characterized by increased vasomotor tone and senescence.

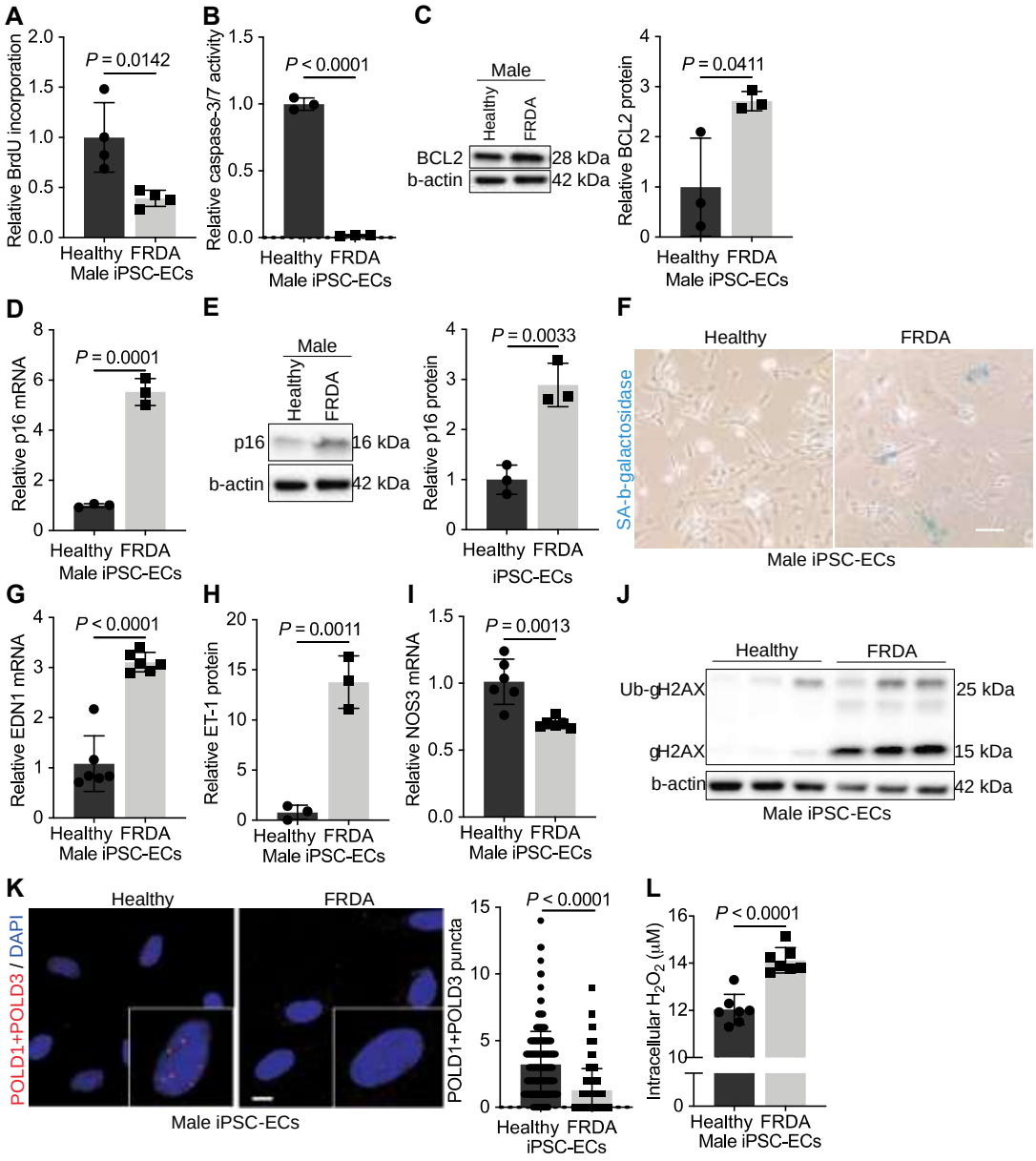

Figure 23. Genetic FXN deficiency coordinates senescence via metabolic and genomic stress.

(**A**-**L**) Phenotypic experiments performed in male age-matched inducible pluripotent stem cell-derived endothelial cells (iPSC-ECs) from healthy versus patients. (**A**) Colorimetric BrdU incorporation assay. (**B**) Chemiluminescent caspase-3/7 activity. (**C**) Immunoblot quantification of apoptosis resistance BCL2 protein. (**D**) RT-qPCR of $p16^{INKA}$ transcript levels. (**E**) Relative $p16^{INKA}$ protein expression in male FRDA iPSC-ECs compared to healthy controls (n=3). (**F**) Representative light microscopic images of SA-galactosidase (blue) in male iPSC-ECs. Scale bar represents 200μm. (**G** and **H**) Transcript by RT-qPCR (n=6) and secreted protein by ELISA (n=3) of EDN1 in FXN-deficient iPSC-ECs. (**I**) RT-qPCR of NOS3 transcript in mutated versus healthy endothelial cells (n=6). (**J**) Immunoblot phosphorylated (γH2AX) and ubiquitinated (Ub-γH2AX) forms of H2AX in FRDA patient iPSC-ECs compared to control (n=3). (**K**) Proximity ligation assay followed by confocal microscopy showing quantification of associated POLD1 and POLD3 subunits of DNA Pol δ in FRDA iPSC-ECs compared to healthy controls. Scale bars indicate 10μm. (**L**) Amplex red colorimetric assay measuring intracellular hydrogen peroxide (H_2O_2) in FRDA mutant iPSC-ECs compared to healthy controls (n=6). Two-tailed Student's *t*-test with error bars that reflect mean +/- SD.

5.4 Supplemental Data

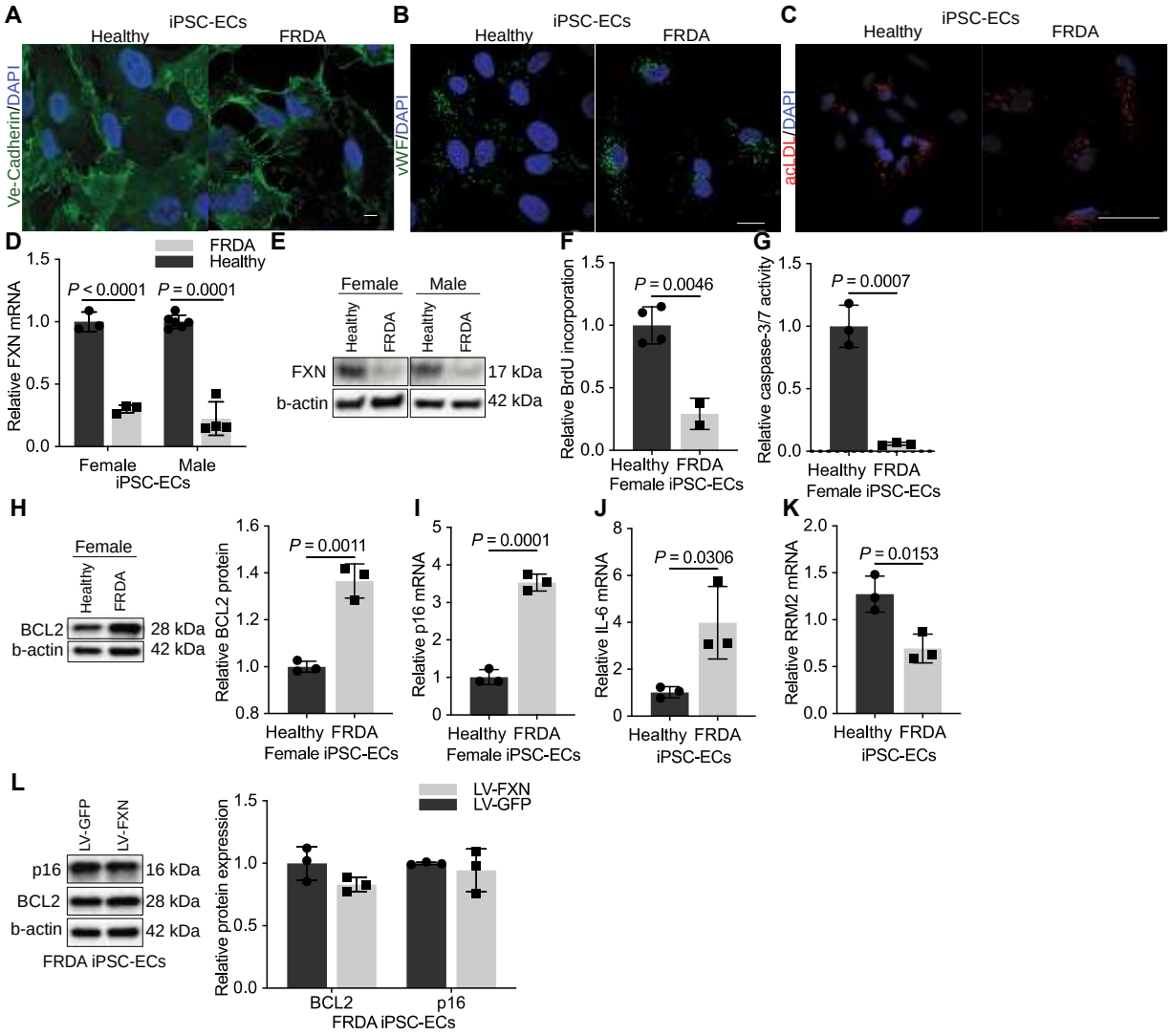

Figure 24. Characterization of inducible pluripotent stem cell-derived endothelial cells from patients with Friedreich's ataxia.

(**A**) Representative immunofluorescent staining and confocal imaging of FRDA and healthy iPSC-ECs stained with endothelial marker VE-Cadherin (green) and counterstained with DAPI (blue). Scale bars indicate 10μm. (**B**) Representative images of FRDA and healthy iPSC-ECs stained with vWF (green) and counterstained with DAPI (blue). Scale bars indicate 50μm. (**C**) Representative images of FRDA or healthy iPSC-EC uptake of fluorescent ac-LDL (red) and counterstained with DAPI (blue). Scale bars indicate 50μm. (**D** and **E**) RT-qPCR and immunoblot of FXN levels in FRDA compared to healthy iPSC-ECs (n=3). (**F-I**) Phenotypic experiments performed in female age-matched inducible pluripotent stem cell-derived endothelial cells (iPSC-ECs) from healthy versus patients. (**F**) Replication measured by colorimetric BrdU incorporation assay (n=2-4). (**G**) Chemiluminescent caspase-3/7 activity (n=3). (**H**) BCL2 protein levels by immunoblot (n=3). (**I-K**) $p16^{INKA}$, IL-6, and RRM2 transcript levels by RT-qPCR in gender-matched iPSC-ECs (n=3). (**L**) Immunoblot of BCL2 and p16 protein expression in male FRDA iPSC-ECs with forced overexpression via lentivirus of FXN (LV-FXN) compared to control (LV-GFP) (n=3).

5.5 Discussion

Little attention has been paid to the role of FXN mutations in vascular cell types, in particular endothelial cells. By utilizing unique iPS-derived endothelial cells from patients with FRDA, we were able to identify the same metabolic and genotoxic stress in the setting of not only epigenetic but genetic FXN deficiency. Specifically, similar to primary PAECs with extended FXN inhibition, FRDA iPSC-ECs exhibited irreversible senescence, driven by disruption of Fe-S-dependent replication and repair machinery and persistent DDR. Simultaneously, FXN mutations resulted in an imbalance in vasomotor effectors which favored a pathological vasoconstrictive phenotype. This shift, specifically the increased ET-1, may be partially dependent upon oxidative stress, similar to results in PAECs. Therefore, these results provide a mechanism of endothelial cell senescence and, coupled with our data on how epigenetic FXN deficiency promotes senescence and PH, support the notion that FXN deficiency may drive pulmonary vascular disease in this population.

Our data join upon a few recent publications that have illustrated cellular senescence in non-vascular tissues; in these studies, the focus has largely been on how FXN-driven mitochondrial dysfunction induces irreversible growth arrest (224, 225). While our data do not preclude the added effects of persistent oxidative stress on genomic stability, our findings provide mechanistic evidence for the direct effects of Fe-S deficiency in replication and repair machinery by highlighting a reduction in intact DNA Pol δ (Figure 23K), which relies on Fe-S center integration for catalytic subunit assembly (163). Here we argue FXN-specific attenuation of Fe-S-dependent nuclear protein function propels endothelial genomic instability and thus DDR and cellular senescence; this notion is reinforced by a recent study describing replicative stress, including altered fork dynamics and DNA damage in fibroblasts and PBMCs collected from

patients with germline biallelic mutations in POLD1 and POLD2 subunit genes (162). However, reduction of in intact DNA Pol δ represents only one of several nuclear proteins that rely on Fe-S centers for structural and functional integrity. There are alternative nuclear mechanisms by which the endothelium may reach irreversible growth arrest , including telomere damage (29). RTEL1 is an Fe-S-containing helicase that aids in the stability and elongation of telomeres (154), and its function may be disrupted by FXN deficiency. For example, in FRDA, telomere shortening has been observed in PBMCs (306) and linked to senescence in fibroblasts (307). Separately, telomerase activity has been linked to PH (312), supporting the value of future studies focused on defining putative telomere-dependent senescence in endothelial cells and PH.

Further study in our unique endothelial model of genetic FXN deficiency may provide insight into mitochondria-specific changes (Ca^{2+} signaling (224), mtDNA damage (208, 209, 214, 215, 305) as well as the interaction between Fe-S cluster deficiency in the mitochondria versus the nucleus. Moreover, the inclusion of additional patient samples with varying GAA expansion mutation lengths could provide valuable information about the relationship between extent of FXN reduction and the consequential endothelial phenotypes.

To build upon this *in vitro* data, future experimentation should focus on characterizing FXN-dependent endothelial senescence and PH *in vivo*. Available animal models with GAA repeat expansions (KIKO, YG8R) exhibit consistent molecular changes with FRDA but very mild tissue dysfunction (313). Endothelial-specific changes as well as a PH phenotype have not been investigated in any of these mutated mice. Cell-specific knockout mice most effectively recapitulate FRDA-specific tissue dysfunction, including muscle creatinine kinase Cre recombinase mice which development cardiomyopathy (212). Evaluation of the cardiopulmonary pressures along with lung tissue histology could provide insight into HCM-induced PH. With this

in mind, endothelial- and cardiomyocyte-specific Fxn knockout mice alone and in combination may provide insight into the independent or additive consequences of endothelial FXN deficiency in the setting of HCM.

The contribution of pulmonary vascular disease in FRDA relatively ignored, despite observations of pulmonary vascular remodeling in FRDA patient tissues (200) coupled with data on HCM patients suffering from pre-capillary PH (105, 199). Our findings support the notion that intrinsic FXN-driven endothelial senescence may serve as a primary predisposing mechanism for PH that could be exacerbated by worsening left heart hemodynamics in FRDA and/or Group 2 PH overall. While patient samples, particularly lung tissue, are rare, making the study of endothelial-specific phenotypes difficult, initial pathology reports from two new FRDA patients describe pulmonary vascular changes consistent with those described by James and Fisch (200) and suggestive of PH. Future studies are warranted to confirm endothelial senescence and clinically characterize hemodynamic instability over time in this population (pre- *versus* post- *versus* combined pre- & post-capillary PH) (NCT02594917).

Together, these data may ultimately provide a foundation for the genetic identification of a novel cohort of FXN-deficient patients at risk for PH. Our data also suggest patients with FRDA and PH might benefit from pre-existing vasodilatory treatments (117) or emerging epigenetic therapies (149). Second, endothelial senescence is an emerging characteristic of vascular diseases and may be prevented with targeted pharmacologic intervention (32). Bolstered by our data using a senolytic to prevent FXN-driven PH (Figure 9), additional studies may help determine whether senolytics (300) or therapies that decelerate cellular senescence (*e.g.*, rapamycin (298), resveratrol (231, 299)) may be beneficial for FRDA-associated PH. In fact, resveratrol treatment has provided some clinical benefit to FRDA patients in preliminary clinical trial but its mechanism remains

incompletely defined; our data on the importance of FXN-driven senescence may support the molecular benefits of this therapy (231). If so, given that senescence is an irreversible phenotype, appropriate therapeutic timing of these drugs will be crucial during PH development as will determination of administration efficacy in young versus old patients.

In summary, this study represents the first step in understanding endothelial FXN deficiency in FRDA, providing foundational evidence for pulmonary vascular dysfunction independent of or additive to the often fatal HCM in this patient population.

6.0 Significance

There has been a long standing controversy surrounding the shifting phenotypes of endothelial cells in PH with a predominating theory of early apoptosis followed by hyperproliferation (21, 23, 274). While metabolic reprogramming (1) and DNA damage (82, 88, 92, 93, 314) have been reported in PH, identification of a common master regulator of these processes as well as their coordinated contribution to the dynamic endothelial pathophenotypes in this disease have been elusive. In response, we established FXN as a lynchpin in both mitochondrial and nuclear function in the pulmonary endothelium. Specifically, FXN deficiency independently promoted both Fe-S-dependent metabolic reprogramming (Chapter 2) as well as replication stress and DNA damage (Chapter 3). These data define a unifying upstream driver for these previously disparate pathological processes in the endothelium and expand our understanding of the consequences of Fe-S cluster deficiency beyond the mitochondria in PH pathogenesis.

Correspondingly, our findings delineate a FXN-specific mechanism by which reversible cell cycle arrest induced by metabolic and replication stress evolved toward DDR-dependent senescence *in vitro*. We then causatively linked this new endothelial phenotype to pulmonary vascular disease, showing endothelial FXN deficiency and senescence in mice propelled PH development while treatment with a senolytic prevented it (Figures 9 and 10). Importantly, FXN knockdown in smooth muscle cells did not induce the genomic stress that predisposed to senescence in endothelial cells and thus did not induce PH development *in vivo* (Figure 19), illustrating the distinctive role of Fe-S cluster deficiency in the pulmonary endothelium. These results are among the first to describe endothelial senescence as a true pathological driver in PH

and offer an Fe-S-driven molecular explanation of the spatio-temporal nature of endothelial pathobiology in this disease.

In Chapter 4, we established how triggers associated with different PH subtypes, such as chronic hypoxia (Group 3) (243) and inflammation (Group 1) (44), induced HIF-α-mediated regulation of FXN transcription via CTCF and BRD4 epigenetic modification in pulmonary endothelial cells (Figures 16-18). While in opposition to previous data supporting HIF-α-dependent increases in FXN in hypoxic non-vascular cell types (282, 283), FXN joins other Fe-S biogenesis genes dynamically regulated by HIF-α in the pulmonary endothelium (70-72). Bolstering this *in vitro* data, we illustrated reduction in FXN alongside elevated $p16^{INKA}$ expression in animal models and patient lung tissues across multiple WSPH groups (Figure 14 and Supplemental Data Figure 20), illustrating the relevance of acquired FXN deficiency and its coordination of endothelial senescence in Group 1, 2, and 3 PH. Moreover, using a senolytic, we defined the causative importance of endothelial senescence in disease development in different PH murine models (Figure 15). Notably, the identification of FXN-dependent mechanism in a model of Group 2 PH-HFpEF provides a novel molecular explanation for the development of PH in left heart disease that is not solely driven by vascular reactions to increased left heart afterload (105, 113). These data may provide the basis for a mixed PH phenotype in which "Group 1-like" primary vascular dysfunction contributes to Group 2 PH (*i.e.*, combined pre- and post-capillary hemodynamic alterations) (112).

While mitochondrial dysfunction (203, 204), oxidative stress and DNA damage (208, 209, 214-217), and more recently senescence (224, 225) have all been described in non-vascular tissues in the context of FRDA, the effects of FXN mutations in endothelial biology have not been characterized. Utilizing unique patients iPS-derived endothelial cells, we confirmed that genetic

FXN deficiency and its metabolic and genotoxic consequences similarly converged on DDR-associated senescence and endothelial dysfunction (Chapter 5). In particular, FXN mutations attenuated the Fe-S-dependent structural integrity of DNA Pol δ and thus disrupted functional replication and repair processes (Figure 23). These results highlighted how genomic damage in FRDA may be driven not only by oxidative stress but also direct insufficiency of nuclear Fe-S-containing proteins. More broadly, HCM cardiomyopathy drives mortality in most FRDA patients (197); yet, PH and cardiopulmonary complications as a whole in FRDA have been surprisingly underreported (201, 202). However, a single case report from over fifty years ago described pulmonary arteriolar vasculopathy in this population (200), consistent with the fact that up to 50% of patients with HCM in general suffer from Group 2 PH (105, 315). Therefore, these results offer a plausible explanation for a predisposition for PH, independent of or additive to left ventricular dysfunction, and ultimately may contribute to the identification of a group of FRDA patients with PH.

By characterizing a shared mechanism across diverse WSPH groups, our FXN-driven model may provide several targets for diagnostic and therapeutic intervention. First, given that we expand upon the comprehensive landscape of epigenetic factors involved in FXN regulation, our data endorse epigenetic pharmacotherapies, including BRD4 inhibitors (149), that may work in multiple PH subtypes, at least in part, by increasing FXN levels in the pulmonary endothelium. Second, endothelial senescence is an emerging characteristic of vascular diseases and may be improved with targeted pharmacologic intervention (32). Bolstered by our data using a senolytic to prevent FXN-driven PH (Figures 9 and 15), additional studies may help determine whether senotherapies (297, 300) or therapies that decelerate cellular senescence (*e.g.*, rapamycin (298), resveratrol (299)) may be beneficial in patients with Group 1 as well as Group 2 and 3 PH.

Moreover, these data may similarly provide therapeutic insight for FRDA. First, our results on HIF-α-dependent epigenetic FXN reduction provide insight into the potential interaction between hypoxia and genetic FXN deficiency. While a recent study suggests sustained low oxygen tension improves Fe-S biogenesis in FXN-deficient models and proposes the symptomatic benefit of chronic hypoxic exposure in FRDA patients (245), our cumulative data oppose this notion. Instead, anaerobic conditions did not rescue pulmonary endothelial Fe-S cluster formation (Supplemental Data Figure 5A). Correspondingly, several PH manifestations (Supplemental Data Figure 5), including hemodynamic instability (Figure 9G-H), worsened with a 'two-hit' model of endothelial FXN knockdown and chronic hypoxia, cautioning against the systemic use of hypoxia treatment in FRDA which would not account for differences in cell-specific responses to hypoxia and instead could accelerate a patient's predisposition to PH. Instead, by demonstrating endothelial vasomotor tone imbalance and senescence in the context of genetic FXN deficiency (Figure 23), we endorse the potential use of existing PAH-specific vasodilatory treatment (117) as well as senotherapies for cardiopulmonary disease in FRDA (301).

In total, this work offers a pivotal endothelial-driven mechanism of across multiple PH etiologies, adding complexity to the spatio-temporal endothelial phenotypes in this vascular disease. Furthermore, our data solidify the regulatory actions of FXN in Fe-S biology, metabolism, and genomic integrity and offering compelling targets for more effective diagnostics and therapeutics in this deadly disease.

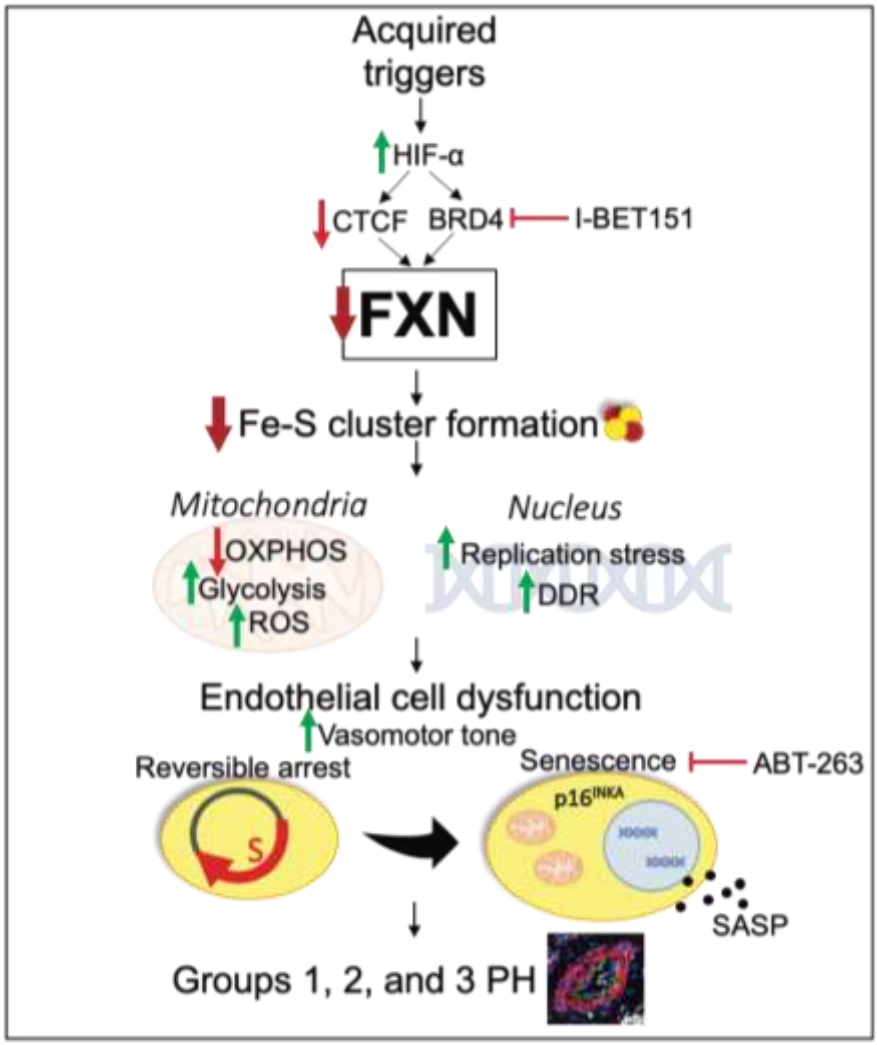

Figure 25. Working mechanism of FXN-dependent endothelial senescence in pulmonary hypertension.
HIF-α - hypoxia inducible factor alpha, CTCF - , BRD4 – bromodomain-containing protein 4, FXN – frataxin, Fe-S – iron-sulfur, OXPHOS – oxidative phosphorylation, ROS – reactive oxygen species, DDR – DNA damage response, SASP – senescence-associated secretory phenotype

7.0 Future Directions

Short term experiments to address the limitations of the presented data have been described in their corresponding Discussion sections (2.5, 3.5, 4.5, 5.5). More broadly, our results inspire new questions relevant to endothelial Fe-S biology and the translational implications for our FXN-dependent mechanism in FRDA and in PH generally.

7.1 Mechanistic insight into Fe-S-dependent endothelial phenotypes

7.1.1 Determine the interaction of FXN-dependent mitochondrial *versus* nuclear dysfunction

Our data demonstrated deficiency of mitochondrial FXN independently coordinates the Fe-S-dependent disruption of mitochondrial respiration and nuclear replication (Chapter 2, 3, and 5), supporting a specific role for FXN in nuclear Fe-S integrity. However, the relative contributions of attenuated organelle function to resultant endothelial senescence is not yet known. Experiments that determine the importance of metabolic reprogramming versus DNA damage in PH may provide insight into the value of metabolic versus genomic treatment intervention. To begin to understand this interaction, bi-directional cross-talk between the mitochondria and nucleus must be considered. Our preliminary data suggested that the FXN-dependent elevation in mitochondrial ROS does not acutely increase nuclear replication stress, DDR, and cell cycle arrest (Supplemental Data Figure 11C-D). However, mitochondria-driven oxidative stress may still contribute to

ongoing DNA damage in conditions of chronic FXN deficiency (316); and this idea is supported by the presence of oxidative damage of nuclear DNA in patients with FRDA (214-217).

Beyond mitochondrial ROS, Fe-S-specific nuclear dysfunction may conversely attenuate mitochondrial metabolism and dynamics. For example, Sahin *et al*. have shown that telomere dysfunction decreased mitochondrial biogenesis via a p53-PGC1α axis (317). Decreased mitochondrial biogenesis has been observed in FRDA models and patient tissues (248). Therefore, it is possible that the mechanism described by Sahin and colleagues could be driven by the disruption of RTEL1, the Fe-S-containing helicase that aids in the stability and elongation of telomeres (154), in conditions of FXN deficiency. The implications for FXN-dependent telomere instability or attenuated mitochondrial biogenesis have not been explored in endothelial cells. Separately, Fang and colleagues describe a mechanism by which insufficient nucleotide excision repair (NER) by XPA decreased mitophagy via PARP1-SIRT1 axis. Notably, hierarchical clustering of XPA and other diseases associated with NER pathways (*e.g.*, Cockayne syndrome and ataxia telangiectasia) was associated with phenotypically similar mitochondrial diseases including FRDA (318). Given that XPD, another NER protein, is reliant on Fe-S clusters for helicase function (319), FXN-dependent alterations in NER may contribute to defective mitophagy. Both of these studies highlight how nuclear damage shapes or even propagates mitochondrial dysfunction and suggest FXN-dependent genotoxicity may in turn disrupt mitochondrial integrity.

Altogether, the complexities of bi-directional signaling between these organelles may suggest the need for combination therapies deficiency to simultaneously preserve mitochondrial and nuclear integrity in the setting of Fe-S cluster. Moreover, the potential reciprocal relationships between these organelles may favor targeting FXN directly and require the identification of new

drugs in addition to potentially emerging epigenetic therapies for FRDA (*e.g.*, HDAC inhibitors (187, 226, 227)) and for PH (*e.g.*, BRD4 inhibitors (149)).

7.1.2 Interrogate the interaction between Fe-S biogenesis genes in the pulmonary endothelium

Our laboratory has now definitively demonstrated that deficiencies of multiple Fe-S cluster assembly proteins independently drive the development of PH. In particular, HIF-α dynamically controls acquired reduction of ISCU1/2, BOLA3, and now FXN in hypoxic conditions (70-72) (Figure 17). This *in vitro* regulation is reinforced by end-stage animal and patient lung tissues, particularly hypoxic Group 3 PH models, that exhibit decreased pulmonary endothelial expression of these genes simultaneously (70-72) (Figure 14 and Supplemental Data Figure 20). However, the interaction between these assembly proteins and their convergence on PH has not been characterized.

To start, while certain metabolic phenotypes are conserved, certain Fe-S-dependent processes seem to differ between these biogenesis genes. Specifically, separate from synthetic role of ISCU1/2 and FXN in Fe-S biogenesis, BOLA3 acts a scaffolding protein that inserts previously synthesized Fe-S cofactors into a subset of mitochondrial proteins including lipoate synthase and ETC complexes (156, 176, 320). This process suggests that BOLA3-mediated Fe-S integration is dependent upon ISCU1/2, and this notion is reinforced by acquired and genetic deficiencies of each of these three genes resulting in attenuated mitochondrial respiration. However, disruption of the glycine cleavage system and ensuing hyperglycinemia driven by acquired and genetic BOLA3 deficiency (72) is not a predominant phenotype in our data (Supplemental Data Figure 4F) or in patients with FRDA. Therefore, despite being positioned “downstream” of ISCU1/2 and FXN,

BOLA3 exerts specific and independent effects on metabolism, suggesting Fe-S biogenesis is a complex process rather than a linear one.

Similarly, despite each coordinating a Warburg-like shift and oxidative stress, our results support that each protein can exert unique and predominate outcomes on endothelial phenotype (proliferation promoted by BOLA3 deficiency (72) vs. apoptosis by ISCU deficiency (70) vs. senescence by FXN deficiency). In addition to functional differences in the process of Fe-S cluster formation, several factors including timing, anatomic position, and disease etiology may explain these differences. First, a more thorough examination of each of these assembly proteins over the course of disease may provide insight into the time-dependent coordination of Fe-S gene biogenesis expression and corresponding endothelial outcomes. For example, it is possible that ISCU1/2 down-regulation precedes BOLA3 reduction partially explaining apoptotic injury in early disease hyperproliferation in late-stage lesions in PAH (21). Second, the employment of technologies (*e.g.,* single-cell RNA sequencing) that interrogate diverse endothelial sub-populations along the pulmonary vascular tree may reveal spatial differences in expression of these assembly genes and endothelial phenotype. Our data highlighted the shared contribution of binding partners, ISCU1/2 and FXN, to Fe-S-dependent processes outside of the mitochondria with rescue of replication stress and reversible growth arrest requiring forced expression of both proteins in hypoxic and inflammatory conditions when the endogenous protein levels are reduced (Supplemental Data Figure 12), demonstrating the interdependency of this network. Given that genotoxic stress can result in either apoptosis or senescence (87), it is conceivable that the divergence between apoptotic or senescent phenotypes in the pulmonary endothelium is partially dependent upon the relative spatio-temporal balance of these two Fe-S biogenesis genes. Lastly, these Fe-S-dependent endothelial phenotypes may change based upon PH etiology. Our study

expanded upon the importance of FXN and Fe-S cluster deficiency in multiple subtypes, including Group 2 PH; thus, comprehensive expression analysis across WSPH classifications will help answer whether FXN-dependent endothelial senescence plays a larger role in this lesser characterized, age-associated subtypes compared to other biogenesis genes.

Altogether, spatio-temporal, etiological, and functional differences in ISCU1/2, BOLA3, and FXN-dependent endothelial dysfunction may partially explain the shifting phenotypes present in PH. This specific molecular signature may provide diagnostic and therapeutic insight with the advent of Fe-S-specific therapies.

7.1.3 Explore the relationship between endothelial FXN deficiency and iron handling

Mitochondrial iron handling includes not only Fe-S cluster formation but heme synthesis and iron storage (321). Despite FXN's roles in Fe-S assembly (167), heme synthesis (182), and iron storage (180), iron imbalance as a result of FXN deficiency is controversial and incompletely defined. Mitochondrial iron overload was observed in tissues from FRDA patients and hypothesized as driving pathogenic oxidative stress via the Fenton reaction (205-207); in response, iron chelators have been explored as a potential therapeutic option but with variable results (240). Opposing studies suggest iron loading is merely an epiphenomenon (212) and even support that initial iron regulator protein 1 (IRP1)-mediated iron loading protects mitochondrial function in instances of FXN deficiency (322). Beyond cellular iron distribution, the heme synthesis enzyme ferrochelatase activity relies upon FXN and Fe-S biogenesis (182); however, FRDA patients do not have anemia despite the potential for FXN-dependent disruption of heme, possibly suggesting tissue-specific differences in iron handling (323). How FXN deficiency alters mitochondrial iron homeostasis and, in turn, how aberrant iron handling affects pulmonary endothelial phenotype,

particularly irreversible senescence, requires further study. There is some evidence that connects senescence with decreased heme oxygenase-1, the rate-limited enzyme involved in heme degradation (324, 325), which has already been linked to lung diseases including PH (326). However the complete connection between heme balance and senescence is not defined. Additional experiments exploring acute versus chronic heme homeostasis in FXN-deficient endothelial models may provide insight into another iron-dependent process that converges on irreversible cellular senescence.

More broadly, whether FXN deficiency and iron imbalance in the pulmonary endothelium are relevant to PH is unclear. Data supports the association of iron deficiency and PAH (327, 328), and clinical trials for iron replacement in Group 1 PAH (64, 148) and Group 3 PH (329) are in progress. Given that our data reinforces endothelial Fe-S cluster deficiency as a driver of PH (70-72), the broader relationship between FXN deficiency, endothelial iron handling, and disease should be explored. Specifically, it is not clear how systemic iron deficiency directly impacts FXN and Fe-S biogenesis or influences intracellular mitochondrial iron handling in the context of pre-existing FXN deficiency. However, mice lacking the Fe-S cluster-dependent protein iron regulatory protein 1 (IRP1), *Irp1*-/-, develop PH in iron-deficient conditions (330), potentially indicating FXN-driven Fe-S deficiency and systemic iron deficiency would worsen disease. However, whether iron supplementation in FXN-dependent PH would an effective long-term treatment, given the potential for ineffective biogenesis and mitochondrial iron accumulation, is not yet understood. In fact, given that opposing data in sickle cell disease suggests iron overload may be a causative trigger in PH, our data may caution against excessive iron repletion (331). In total, our data on Fe-S integrity in this disease add to the complexity of intracellular and systemic iron balance in PH.

7.1.4 Define reversible *versus* irreversible FXN-driven endothelial phenotypes

The reversibility of pulmonary vascular remodeling in PH across WSPH groups is largely undefined. Studies have demonstrated the reversal of PH in different animal models following hemodynamic unloading (332, 333). These studies mirror the reversible nature of specific PH groups such as congenital heart disease (CHD)-associated PAH following surgical correction (334) and Group 2 PH associated with congestive heart failure following placement of a left ventricular assist device (LVAD) (335). Conversely, certain patients experience persistent Group 2 PH due to valvular disease even after aortic valve replacement (336) or mitral balloon valvuloplasty (337). Similarly, a significant subset of corrected CHD patients experience PAH (338) and this irreversible phenotype has been linked to and anti-apoptotic endothelium (339). Beyond hemodynamic unloading, certain preclinical models driven by hypoxic and inflammatory triggers exhibit spontaneous reversal of smooth muscle remodeling over while models with significant neointimal proliferation do not, suggesting reversibility may be dependent upon shifting pulmonary endothelial phenotypes (340). The temporal molecular changes in the pulmonary endothelium that define reversible versus irreversible PH are not known.

Our *in vitro* data illustrated a FXN-dependent transition from reversible growth arrest to irreversible endothelial senescence (Chapter 3). Specifically, experiments rescuing FXN (alongside its binding partner ISCU1/2) were able to reverse acute replication stress and cell cycle arrest (Supplemental Data Figure 12) but were ineffective when endothelial senescence was already present (Supplemental Data Figures 21B and 24L), suggesting a potential window in which FXN-driven phenotypes can be reversed. In this way, temporal insight into FXN-driven endothelial evolution may provide molecular insight into reversible versus irreversible endothelial phenotypes and thus stages of PH pathogenesis. Moreover, these data may highlight the

importance of therapeutic selection dependent upon the reversibility of endothelial phenotype. For our study specifically, additional *in vivo* experiments are required to confirm this evolution in our endothelial *Fxn*-/- mouse model and to compare the efficacy of FXN and ISCU1/2 replacement to senolytic treatment in preventing or reversing hemodynamic instability in different PH animal models (Figures 15). Future studies exploring how these separate treatments reverse pre-existing pulmonary vascular disease will be particularly important given that PH patients often have advanced disease at the time of therapy initiation (341).

Clinically, characterization of this time-dependent mechanism will provide insight into the shifting pathophenotypes of the pulmonary endothelium and may ultimately inform treatment selection based upon endothelial disease stage. Confirming the relevance of this evolving endothelial mechanism in patients over the course of disease will be challenging. Immunofluorescent co-staining and single-cell RNA sequencing in post-mortem tissues coupled with expression analysis in blood outgrowth endothelial cells (342, 343) represent possible methods to approach this problem; however, feasible assessment of disease stage based upon endothelial phenotype to inform corresponding treatment choice will likely require the development of more sophisticated diagnostic tools.

7.2 Translational implications of FXN-dependent endothelial senescence

7.2.1 Establish the senescence-associated secretory phenotype in endothelial FXN deficiency

Diagnosis and therapeutic selection in PH are largely dependent upon invasive hemodynamic testing. Noninvasive measurements are currently limited to cardiac brain natriuretic peptide (BNP) and the N-terminal fragment of proBNP (NTproBNP) levels, which associate with exercise capacity (e.g. 6MWD), hemodynamic measurements (*e.g.*, mPAP, PVR), functional class, and mortality for PAH (344, 345). The search for more definitive circulating biomarkers that could aid in the determination of diagnosis, prognosis, and therapeutic selection as well as response is ongoing (346, 347). Specifically, several inflammatory markers have been found to be elevated in the plasma of PAH patient; in particular, IL-6 levels predict patient mortality (44, 278-280).

Separately, the senescence-associated secretory phenotype (SASP) includes an assemblage of pro-inflammatory molecules such as cytokines and metalloproteases that reflect and propagate the underlying tissue dysfunction; these markers may differ depending upon the stage of senescence, inciting stressors, and tissue type (281). Therefore, SASP profiles may hold potential as biomarkers for aging and age-related diseases with some level of specificity.

Our limited data identified potential SASP markers by showing elevated levels of IL-6 and TNFα driven by FXN deficiency (Figures 9F-G and Supplemental Data Figure 24J). As previously mentioned, further experimentation is required to define a complete FXN-dependent SASP profile as well as its subsequent control of immune cell recruitment and inflammatory signaling in PH. However, our genetic models of endothelial FXN deficiency provide an opportunity to screen for a cohort of secreted markers that could potentially be confirmed in the plasma of FRDA patients

as well as PH patients from diverse WSPH groups. In this way, Circulating SASP markers could reflect the underlying pulmonary endothelial evolution toward senescence and therefore provide value information about reversible and irreversible stages of disease, and thus the potential effectiveness of therapies that increase FXN versus remove senescent cells. Correlative data between these secreted inflammatory markers and clinical parameters of PH (*e.g.*, 6MWT, NYHA/WHO functional class) could improve prognostication as evidenced by the existing predictive value of IL-6 and other cytokines (44, 278-280). Overall, characterization of SASP panels support a move towards minimally noninvasive, precision medicine-based practices in the diagnostic and therapeutic management of PH.

7.2.2 Establish whether endothelial FXN deficiency predisposes to pulmonary hypertension independent of left heart dysfunction

Identification of a senescent phenotype coordinated by FXN mutations in iPSC-ECs (Chapter 5) provides a potential endothelial mechanism for pulmonary vascular disease in FRDA. Although underreported in FRDA, HCM is often accompanied by Group 2 PH with a certain subset of patients exhibiting combined pre- and post-capillary PH (105). Therefore, the relative contribution of endothelial versus myocardial FXN deficiency on PH development is unclear. Furthermore, whether genetic FXN deficiency in the pulmonary endothelium contributes to this mixed, Group 1-like hemodynamic phenotype in Group 2 PH is not yet known. To begin to address this question, I propose using tissue-specific conditional Fxn knockout mice: Fxn flox/flox mice (212) expressing VE-Cadherin (Cdh5(PAC)-CreERT2^{+}) (261) and/or α-myosin heavy chain Cre recombinase (αMHC-MerCreMer$^{+/+}$) (262). By evaluating the individual and combined endothelial and cardiomyocyte FXN knockout models compared to Fxn f/f controls, the

independent or synergistic effects of endothelial FXN deficiency on pulmonary vascular disease can be established. These animal experiments could supplement studies aiming to better characterize PH in the FRDA population (NCT02594917).

Given that animal models of Group 2 PH due to HFpEF showed decreased FXN and increased $p16^{INKA}$ (Figure 14E-F and Supplemental Data Figure 20E-F), our findings support the notion that intrinsic FXN-driven endothelial senescence may predispose to PH in setting of left heart disease more generally. Assessing this mechanism in other acquired models of left ventricular dysfunction would confirm its application to a broader set of cardiovascular diseases. More work is also required to either confirm HIF-α-dependent epigenetic modulation or characterize new mechanistic control of FXN down-regulation in left heart disease. Additionally, the identification of new triggers associated with Group 2 PH (*e.g.*, elevated left ventricular filling pressures) reduce FXN expression requires further studies. In summary, our data extend the importance of endothelial Fe-S biology to FRDA-induced HCM and more broadly Group 2 PH, providing new molecular targets in this lesser characterized but increasingly prevalent population. These findings may also provide an opportunity to clarify the molecular differences between pre-, post-, and combined pre- and post-capillary PH.

7.2.3 Determine if FXN-dependent senescence in the myocardial endothelium promotes ventricular dysfunction

While our data have focused on the role of FXN-dependent senescence in the pulmonary endothelium, genetic FXN deficiency may promote similar pathology in extrapulmonary vascular beds. In particular, a few case reports have provided clinical and histologic evidence of some large artery stenosis (200, 348) as well as panvascular remodeling in the smaller myocardial vessels

(200) in the setting of FRDA. These findings are reinforced by decreased myocardial perfusion reserve index on cardiac MRI in patients with FRDA compared to healthy controls; interestingly, this reduction in myocardial perfusion was observed prior to development of HCM (349). However, cumulative data confirming potential coronary or microvascular disease in the FRDA population is lacking because diagnostic assessment and the majority of research in the field have been focused on the predominant HCM phenotype. Supporting these limited data in FRDA-induced HCM, microvascular dysfunction is common, predates left ventricular dysfunction, and predicts clinical deterioration and mortality in patients with HCM generally (350, 351). The diseased microvasculature is characterized by increased vessel wall thickness and fibrosis and decreased lumen diameter (350, 352).

To this point, FXN deficiency may contribute to the underlying microvascular remodeling in cardiac tissue and, in turn, induce or worsen HCM development in FRDA. While endothelial *Fxn*-/- mice do not exhibit gross alterations in left ventricular function (*i.e.,* ejection fraction, fractional shortening) (Supplemental Data Figure 13D-F) , LV and RV pressure-volume loop analysis could provide a more detailed picture of subclinical left ventricular dysfunction that may predispose to HCM. Moreover, these measurements in mice treated with and without the senolytic may endorse the use of senotherapies to prevent microvascular dysfunction. More thorough histologic evaluation of RV and LV coronary vessels and the microvasculature from patients with FRDA would support these notions. It is also possible that FXN-dependent endothelial senescence promotes microvascular disease in other genetic and acquired forms of HCM, beyond FRDA. More broadly, cellular senescence represents an emerging mediator in peripheral vascular disease (31, 275); therefore, despite the potential endothelial heterogeneity, FXN-dependent senescence may also contribute to pathologies outside of the cardiopulmonary circuit.

7.2.4 FXN deficiency, sex differences, and pulmonary hypertension

Studies to understand the PAH gender paradox of increased prevalence and also survival in female patients are ongoing with a focus on the importance of sex hormones in the context of pulmonary vascular and right ventricular function (96, 353). Very little preclinical or clinical data exists describing the effects of sex on Group 2-5 PH. Separately, relevant to Fe-S-dependent PH, Niihori *et al.* recently demonstrated that a rat model with the human MMDS1 mutations drove sex-specific disease development (354); more work is required to determine if the PH phenotype in MMDS1 patients occurs more often in females versus males similar to this preclinical animal model (175). Together, these data lead to questions about whether FXN and Fe-S cluster deficiency contribute to sex differences in PH development.

Speaking first to genetic FXN deficiency, our data in gender-matched iPS-derived endothelial cells from healthy versus FRDA patients illustrated comparable metabolic and genomic phenotypes (Chapter 5). These results suggest sex chromosome differences do not contribute to FXN-dependent endothelial senescence but do not preclude sex-driven differences due to sex hormones. More generally, age of onset and neurological disease severity in FRDA are largely driven by trinucleotide repeat mutation length (183, 195, 196); sex has not been identified as a major risk factor for the development of disease phenotypes. However, a few preclinical studies explore the benefits of the female sex hormone, estrogen, on mitochondrial function in conditions of FXN mutations (355, 356). Also, a recent study demonstrated female patients exhibited increased ejection fraction and slightly decreased left ventricular poster wall thickness at diastole (LVPWd) compared to male patients after adjusting for trinucleotide expansion length and age of onset (357), suggesting potential sex differences in HCM. As previously mentioned, PH in FRDA-induced HCM has not been adequately documented; however, if more attention were

given to characterizing clinical PH in this population, it is possible that gender-driven differences independent of or additive to HCM may affect morbidity and mortality. There is some evidence to support that females represent a greater proportion of patients with Group 2 PH (due to HFpEF (358)); however, additional studies are required to understand the sex-specific differences in acquired FXN deficiency and its coordination of endothelial senescence across diverse PH etiologies.

7.2.5 Aging, FXN-dependent senescence, and pulmonary hypertension

The age of patients diagnosed with PAH has steadily risen in recent decades (95, 359), and interest in age-associated alterations in pulmonary vascular function has grown (302, 360). Moreover, the increasing prevalence of Group 2 and 3 PH is partially driven by an increase of age-associated diseases in the population (100). However, the molecular underpinnings of age-dependent pulmonary vascular disease have not yet been defined. In general, cellular senescence contributes to aging and age-related diseases by imposing irreversible growth arrest that prevents tissue-repair capacity and producing a senescence-associated secretory phenotype (SASP) that promotes tissue inflammation (300, 361, 362). Notably, emerging evidence supports the efficacy of therapeutically targeting these pathogenic cells using senotherapies (32, 297).

Several endogenous stressors, including metabolic and genotoxic stress, converge on irreversible senescence; both of these examples have already been associated with aging (30, 35-37, 363) and separately linked to PH (1, 81). Our data highlight FXN as an upstream driver of these pathological processes related to senescence and aging; moreover, our results causatively link cellular senescence to multiple subtypes of PH. With this in mind, FXN-dependent endothelial

senescence could also serve as a key molecular mechanism for PH as patients age. Furthermore, while FRDA is not traditionally considered an age-related disease, our findings illustrated FXN-dependent genotoxicity due to specific disruption of the Fe-S-containing nuclear protein, DNA Pol δ (Figure 23K), strengthening the association between FRDA and several progeroid conditions caused by loss-of-functions mutations in these same Fe-S-containing nuclear proteins (159-162). Connecting genetic FXN deficiency to endothelial senescence, suggests FXN mutations may exert enough stress to mimic pathologic aging of the endothelium. Whether FXN deficiency and endothelial senescence promote age-related disease progression in PH or specifically in FRDA is not yet known. To begin to address these questions, models of PH, FRDA, or even models of physiologic or accelerated aging could be evaluated for an association between FXN-dependent senescence in the pulmonary endothelium and worsening pulmonary vascular dysfunction with increasing age.

Investigating PH perturbations through the lens of aging may provide valuable opportunities to adapt PH management in an increasingly older population. With the continued development of senotherapies (32, 297), our data place pulmonary vascular disease on the list of conditions that respond to these drugs. Thus, these finding may provide a novel therapeutic strategies for those patients with no existing therapeutic options, particularly patients with Group 2 and 3 PH and FRDA patients with potential cardiopulmonary involvement.

Appendix A

Table 1. Taqman primers

Targets	Species	Assay ID
ACTB	Human	Hs99999903_m1
	Rat	Rn00667869_m1
	Mouse	Mm02619580_g1
BRD2	Human	Hs01121986_m1
BRD4	Human	Hs04188087_m1
CDH5	Human	Hs00901465_m1
CDKN2A	Human	Hs00923894_m1
	Rat	Rn00580664_m1
	Mouse	Mm00494449_m1
CTCF	Human	Hs00902016_m1
EDN1	Human	Hs01574659_m1
EPAS1	Human	Hs01026149_m1
FXN	Human	Hs00175940_m1
	Rat	Rn01501403_m1
	Mouse	Mm00784016_m1
HIF1A	Human	Hs00153153_m1
IL1B	Human	Hs01555410_m1
IL6	Human	Hs00174131_m1
ISCU	Human	Hs00384510_m1
NOS3	Human	Hs01574659_m1
PECAM1	Human	Hs01065279_m1
SIN3A	Human	Hs00411592_m1
	Rat	Rn01417686_m1
	Mouse	Mm00488255_m1
TNFA	Mouse	Mm00443258_m1

Table 2. Antibodies

Target	Company	Cat. No.	Species	Concentration
Immunoblot				
ATM	Cell Signaling Technologies	2873T	Rabbit	1 / 1000
p-ATM (Ser1981)	Abcam	ab81292	Rabbit	1 / 1000
ATR	Cell Signaling Technologies	2790S	Rabbit	1 / 1000
p-ATR (Ser428)	Cell Signaling Technologies	2853T	Rabbit	1 / 1000
β-actin	Santa Cruz Biotechnologies	sc47778	Mouse	1 / 1000
BRD2	Abcam	ab139690	Rabbit	1 / 1000
BRD4	Abcam	ab128874	Rabbit	1 / 1000
CHK1	Cell Signaling Technologies	2360S	Mouse	1 / 1000
p-CHK1 (Ser345)	Cell Signaling Technologies	2341T	Rabbit	1 / 1000
CHK2	Cell Signaling Technologies	2662T	Rabbit	1 / 1000
p-CHK2 (Thr68)	Cell Signaling Technologies	2661T	Rabbit	1 / 1000
CTCF	Abcam	ab70303	Rabbit	1 / 1000
FXN	Abcam	ab110328	Mouse	1 / 200
γH2AX (Ser139)	Abcam	ab11174	Rabbit	1 / 500
MCM2	Cell Signaling Technologies	3619T	Rabbit	1 / 1000
NOS3	Santa Cruz Biotechnologies	sc376751	Mouse	1 / 1000
CDKN2A/p16INKA	Abcam	ab108349	Rabbit	1 / 1000
p21Cip1	Abcam	ab188224	Rabbit	1 / 1000
p53	Cell Signaling Technologies	9282T	Rabbit	1 / 500
RPA32	Cell Signaling Technologies	2208T	Rat	1 / 1000
p-RPA32 (Ser4/Ser8)	Bethyl Laboratories	A300-245A-M	Rabbit	1 / 500
RPA70/RPA1	Cell Signaling Technologies	2267S	Rabbit	1 / 1000
Immunofluorescent staining				
CD31	Santa Cruz	sc376764	Mouse	1 / 100
CD144	Abcam	ab33168	Rabbit	1 / 100
BrdU	BD Biosciences	347580	Mouse	1 / 50
BrdU	Abcam	ab6326	Rat	1 / 75
FXN	Abcam	ab113691	Mouse	1 / 100
CDKN2A/p16INKA	Abcam	ab108349	Rabbit	1 / 100
αSMA	Abcam	ab21027	Goat	1 / 350
vWF	Abcam	ab8822	Goat	1 / 50

Table 3. Differential gene expression from long RNA sequencing

GeneID	baseMean	log2FC	lfcSE	stat	pvalue	padj
RIBC2	23.117334	3.569134422	0.40084769	8.90396658	5.39E-19	2.37E-17
SUV39H1	51.181708	3.226929067	0.68461537	4.71349198	2.44E-06	2.52E-05
RRM2	2133.2882	2.93278685	0.13532202	21.67265	3.72E-104	3.85E-101
PLK1	555.19806	2.875692761	0.24310308	11.8291089	2.76E-32	3.05E-30
MCM2	1033.9317	2.803988837	0.23731556	11.8154444	3.25E-32	3.57E-30
MND1	56.974405	2.748418509	0.2565398	10.7134196	8.80E-27	6.90E-25
MCM10	371.18842	2.743411594	0.13004953	21.0951293	8.82E-99	6.73E-96
PBK	658.13171	2.705440546	0.1627312	16.6252114	4.58E-62	1.44E-59
HIST1H2AI	3318.1463	2.69730566	0.21432872	12.5849005	2.56E-36	3.34E-34
FAM111B	359.46324	2.68469146	0.30452109	8.81611018	1.19E-18	4.97E-17
KIF14	447.10367	2.674996165	0.19380813	13.8022911	2.47E-43	4.02E-41
CCNA1	1079.2252	2.655432007	0.15922976	16.6767314	1.94E-62	6.23E-60
PKMYT1	174.80079	2.634660924	0.27584973	9.55107296	1.28E-21	7.00E-20
CLSPN	460.63331	2.621023469	0.12221305	21.4463471	4.94E-102	4.21E-99
AURKB	441.27513	2.6049598	0.14511667	17.9507959	4.73E-72	2.14E-69
HMMR	725.1965	2.575849472	0.2423893	10.6269108	2.23E-26	1.70E-24
EXO1	216.6497	2.570756578	0.30475354	8.43552651	3.30E-17	1.25E-15
E2F2	71.314683	2.559136062	0.2884234	8.8728448	7.13E-19	3.08E-17
AC112777.1	44.199984	2.557590933	0.2776906	9.21021785	3.25E-20	1.60E-18
DEPDC1B	252.40774	2.549993068	0.22654773	11.2558758	2.17E-29	2.00E-27
AC112198.2	26.976993	2.549583269	0.41371374	6.16267493	7.15E-10	1.29E-08
ZNF367	210.45391	2.548969437	0.25452612	10.0145691	1.32E-23	8.25E-22
CDC6	664.70275	2.537647741	0.16269008	15.5980489	7.51E-55	1.75E-52
E2F8	110.39371	2.514100594	0.22948874	10.955224	6.27E-28	5.35E-26
HIST1H3J	1859.1948	2.512567742	0.21516153	11.6775881	1.66E-31	1.74E-29
HIST1H1A	193.75132	2.507398563	0.1875544	13.3689136	9.19E-41	1.40E-38
CDC20P1	63.554892	2.491629084	0.26057261	9.56212973	1.15E-21	6.31E-20
HIST1H1B	5651.246	2.478934387	0.20385236	12.1604399	5.05E-34	6.10E-32
MKI67	1668.0947	2.45326694	0.17296232	14.1838229	1.15E-45	2.04E-43
ZWINT	879.97087	2.435619918	0.1412515	17.2431441	1.26E-66	4.94E-64
UBE2C	603.41074	2.430239053	0.12257958	19.8258072	1.78E-87	1.03E-84
SHCBP1	936.84993	2.428479982	0.0898679	27.022775	7.98E-161	3.86E-157
CDC20	1102.4648	2.422717273	0.14975042	16.1783668	7.17E-59	2.00E-56
LMNB1	1301.7786	2.419973442	0.17025555	14.2137713	7.53E-46	1.38E-43
E2F1	263.13655	2.411863468	0.29677528	8.12690154	4.40E-16	1.52E-14
BUB1B	786.39282	2.404951519	0.1187358	20.254646	3.23E-91	2.13E-88

Table 3 continued

HIST1H2BL	949.04334	2.384675789	0.21436308	11.1244706	9.54E-29	8.48E-27
CDC25C	199.68914	2.379738654	0.16395652	14.5144493	9.81E-48	1.92E-45
SPC25	239.56428	2.373687699	0.15306607	15.5076023	3.08E-54	6.87E-52
CENPF	2135.9149	2.372068558	0.19591321	12.1077518	9.61E-34	1.14E-31
HIST2H3D	639.49303	2.36909182	0.22318751	10.6148049	2.54E-26	1.93E-24
HIST1H1D	1247.9422	2.367605192	0.20999998	11.2743115	1.76E-29	1.63E-27
LOC100505658	11.071309	2.354041222	0.79816867	2.94930297	0.0031849	0.01469969
ESPL1	329.83775	2.333527851	0.18544492	12.5834014	2.61E-36	3.37E-34
HIST2H3A	906.11625	2.326928898	0.19096621	12.1850295	3.74E-34	4.55E-32
HIST2H3C	906.11625	2.326928898	0.19096621	12.1850295	3.74E-34	4.55E-32
CDC45	468.82521	2.30452412	0.11140239	20.6864866	4.58E-95	3.32E-92
CDCA2	558.48322	2.300918068	0.09648038	23.8485601	1.05E-125	1.52E-122
ORC1	197.87128	2.295665737	0.14601077	15.7225785	1.06E-55	2.60E-53
FBXO43	25.692352	2.287580956	0.32196659	7.10502587	1.20E-12	3.07E-11
ASPM	1913.051	2.28456541	0.168372	13.5685588	6.15E-42	9.80E-40
GAPDHP55	17.15148	2.282182233	0.79216611	2.88093901	0.0039649	0.01770856
NEK2	290.41379	2.279906597	0.19495737	11.6943853	1.36E-31	1.44E-29
NCAPG	1221.166	2.253717777	0.18947267	11.8946853	1.26E-32	1.41E-30
ESCO2	419.77004	2.252081432	0.28761578	7.83017348	4.87E-15	1.55E-13
PIMREG	351.90192	2.24965097	0.13017961	17.2811312	6.53E-67	2.63E-64
KIF15	338.12363	2.249587063	0.18804309	11.9631464	5.54E-33	6.23E-31
CENPE	957.94646	2.244570255	0.27161739	8.26372078	1.41E-16	5.09E-15
MFSD2A	43.486035	2.232941161	0.30366346	7.35334171	1.93E-13	5.28E-12
NCAPG2	777.3632	2.232745025	0.07644273	29.2080738	1.53E-187	2.22E-183
HIST1H2AG	2757.9971	2.217633033	0.21553675	10.2888858	7.91E-25	5.33E-23
CENPM	198.80897	2.217543584	0.16096854	13.7762547	3.54E-43	5.70E-41
ERCC6L	203.89231	2.214179955	0.39134647	5.65785087	1.53E-08	2.29E-07
FST	194.44762	2.197534288	0.18309086	12.0024247	3.45E-33	3.94E-31
CEP55	1376.2562	2.197443918	0.22926376	9.58478522	9.27E-22	5.19E-20
HIST1H3D	2423.1019	2.192605613	0.22832591	9.60296455	7.77E-22	4.36E-20
SPAG5	755.71633	2.189401636	0.0873912	25.0528846	1.62E-138	2.94E-135
SNORD3B-2	1063.0217	2.188683118	0.34071207	6.42384972	1.33E-10	2.62E-09
TOP2A	3592.7566	2.185275396	0.20868936	10.4714272	1.17E-25	8.64E-24
PSMC3IP	93.269868	2.180037755	0.19602555	11.121192	9.89E-29	8.75E-27
NUF2	397.02345	2.175473196	0.2234938	9.73393102	2.16E-22	1.29E-20
HJURP	631.5794	2.172582131	0.10762561	20.1864796	1.29E-90	8.11E-88
GTSE1	369.70861	2.171515245	0.19101179	11.3684878	6.00E-30	5.69E-28

Table 3 continued

CCND1	11354.4	2.167255495	0.17129233	12.6523791	1.09E-36	1.46E-34
CDCA8	428.17365	2.166042451	0.13583607	15.9460036	3.04E-57	7.72E-55
POLQ	364.56533	2.165160413	0.15240582	14.2065467	8.34E-46	1.51E-43
CCSAP	198.53413	2.147179649	0.14306312	15.0086179	6.45E-51	1.42E-48
AC016394.1	54.058352	2.146829451	0.2578957	8.32440952	8.48E-17	3.13E-15
CCNA2	1394.4858	2.144868339	0.07924809	27.0652364	2.53E-161	1.83E-157
DLGAP5	1483.4594	2.144091356	0.24318919	8.81655694	1.18E-18	4.96E-17
TTK	617.01186	2.141556617	0.27189285	7.87647262	3.37E-15	1.09E-13
TROAP	215.23853	2.134561195	0.14252768	14.9764673	1.05E-50	2.26E-48
SAPCD2	219.61279	2.125469841	0.46528573	4.56809596	4.92E-06	4.76E-05
KIF18B	183.90643	2.125282521	0.24445254	8.69404982	3.50E-18	1.41E-16
NCAPH	372.90994	2.124126711	0.21318988	9.96354393	2.20E-23	1.37E-21
TRBC2	79.710599	2.121370833	0.17520061	12.1082386	9.55E-34	1.14E-31
RAD51AP1	339.74136	2.10566617	0.20867813	10.0904974	6.09E-24	3.90E-22
KIF2C	803.65626	2.101283936	0.09960801	21.0955325	8.74E-99	6.73E-96
MCM4	1866.4084	2.098748743	0.16045329	13.080123	4.28E-39	6.20E-37
CDK1	1330.4448	2.097086049	0.21627325	9.69646518	3.12E-22	1.82E-20
SPC24	821.7186	2.070427734	0.18146983	11.4092118	3.76E-30	3.64E-28
KIF4A	763.92282	2.070127899	0.11295472	18.3270603	5.03E-75	2.61E-72
CENPU	402.85578	2.065807556	0.30987322	6.66662186	2.62E-11	5.63E-10
TICRR	184.44546	2.060711046	0.18176948	11.3369477	8.61E-30	8.10E-28
SLC26A2	1269.7059	2.052786087	0.09389449	21.8626906	5.89E-106	7.11E-103
MYBL2	597.2461	2.0430817	0.22281904	9.1692422	4.76E-20	2.31E-18
SH2D5	30.825609	2.040567437	0.33013671	6.18097705	6.37E-10	1.15E-08
TK1	1119.1573	2.037600989	0.18801916	10.8371988	2.29E-27	1.88E-25
PRC1	2081.3417	2.037180554	0.08908885	22.8668417	9.94E-116	1.31E-112
VCL	5919.3093	2.032048674	0.19971337	10.1748252	2.57E-24	1.71E-22
APOBEC3B	163.45022	2.031809067	0.20074963	10.1211101	4.45E-24	2.90E-22
FANCB	118.13057	2.03025104	0.21890633	9.27451957	1.78E-20	8.95E-19
BUB1	1201.9966	2.027684504	0.12349027	16.4197921	1.38E-60	4.00E-58
SKA1	216.10806	2.022150418	0.1117698	18.0920997	3.68E-73	1.78E-70
CENPA	244.43194	2.018394381	0.11761203	17.1614625	5.16E-66	1.97E-63
ZNF695	28.306929	2.007080077	0.27924381	7.1875544	6.60E-13	1.73E-11
BLM	277.27749	2.005132525	0.25726949	7.79389952	6.50E-15	2.05E-13
ATAD5	283.07492	1.997823769	0.1202672	16.6115425	5.75E-62	1.77E-59
HIST2H4A	3404.3519	1.995383418	0.18856604	10.5818809	3.62E-26	2.72E-24
HIST2H4B	3404.3519	1.995383418	0.18856604	10.5818809	3.62E-26	2.72E-24

Table 3 continued

BIRC5	1172.9219	1.9832642	0.09190578	21.5793189	2.81E-103	2.72E-100
CDCA5	372.12853	1.983178292	0.15705716	12.6271119	1.50E-36	1.99E-34
TPX2	1846.267	1.975850844	0.12376283	15.9648163	2.25E-57	5.82E-55
TYMS	760.51926	1.972073853	0.11189341	17.6245757	1.60E-69	6.80E-67
RAD54L	85.648872	1.971130072	0.29070234	6.78057867	1.20E-11	2.67E-10
ARHGAP11A	802.34191	1.967961615	0.15219773	12.9302951	3.04E-38	4.27E-36
TCF19	306.30475	1.96769542	0.15814141	12.4426324	1.53E-35	1.95E-33
HIST2H2AA4	5357.1638	1.96521137	0.20789943	9.45270189	3.30E-21	1.73E-19
KNL1	1155.6739	1.962987281	0.19048447	10.3052352	6.67E-25	4.54E-23
HIST1H2BJ	3586.2545	1.961684374	0.18896645	10.381125	3.02E-25	2.16E-23
ANLN	2484.7996	1.96122788	0.19548341	10.0327075	1.09E-23	6.96E-22
CKAP2L	318.82222	1.952740864	0.22278079	8.76530197	1.86E-18	7.72E-17
NDUFS1	3107.7453	1.941843152	0.07223054	26.8839634	3.38E-159	1.23E-155
KIF11	1051.0482	1.935206946	0.13801018	14.0222042	1.14E-44	1.97E-42
AC009533.1	25.906451	1.931136329	0.29700163	6.50210688	7.92E-11	1.61E-09
GINS2	385.0208	1.929025238	0.09870457	19.5434245	4.69E-85	2.52E-82
U1	4835.3306	1.924579639	0.28544449	6.74239554	1.56E-11	3.43E-10
DHFRP1	83.40605	1.916018058	0.1754542	10.9203319	9.22E-28	7.72E-26
ATAD2	1125.4919	1.910718204	0.19878264	9.61209778	7.11E-22	4.01E-20
AURKA	836.81632	1.910217944	0.07809639	24.4597464	3.96E-132	6.38E-129
KIF18A	313.15119	1.906901454	0.33477428	5.69608106	1.23E-08	1.86E-07
CCNB1	2469.5881	1.896521268	0.1124428	16.8665429	7.93E-64	2.67E-61
DMC1	22.2276	1.893908916	0.31707873	5.9729927	2.33E-09	3.94E-08
CDCA3	106.0391	1.893725992	0.15725271	12.0425649	2.12E-33	2.46E-31
DEPDC1	626.76901	1.893061776	0.22360531	8.46608595	2.54E-17	9.68E-16
GINS1	626.28783	1.891110811	0.07182429	26.3296851	8.77E-153	2.54E-149
CENPW	571.14488	1.891032662	0.1814102	10.4240702	1.93E-25	1.40E-23
HMOX1	9691.9738	1.88979321	0.19073062	9.90817932	3.84E-23	2.37E-21
PTTG1	1175.0803	1.885430478	0.162134	11.6288406	2.94E-31	3.05E-29
RTKN2	34.062609	1.877431788	0.24755164	7.58400065	3.35E-14	1.01E-12
HIST2H2BF	1208.0429	1.873433958	0.11823272	15.845309	1.51E-56	3.79E-54
HIST2H2BB	137.73334	1.872271499	0.25323567	7.39339561	1.43E-13	3.95E-12
FEN1	1124.0882	1.869096579	0.08552383	21.8546863	7.02E-106	7.82E-103
CCNB2	646.64882	1.86781101	0.11360708	16.440974	9.73E-61	2.88E-58
MCM7	2060.0388	1.862612514	0.16230068	11.4763072	1.74E-30	1.72E-28
NUSAP1	1190.3152	1.857066384	0.23098008	8.03994188	8.99E-16	3.03E-14
CKS1B	899.95306	1.84910032	0.20171066	9.16709285	4.86E-20	2.34E-18

Table 3 continued

NDC80	691.63119	1.845181819	0.19408883	9.50689359	1.96E-21	1.05E-19
ASF1B	320.88132	1.841096821	0.19428109	9.47645938	2.63E-21	1.40E-19
SKA3	182.55414	1.831288296	0.27320183	6.70306025	2.04E-11	4.42E-10
RN7SL411P	51.279588	1.825204802	0.62557496	2.91764363	0.0035269	0.01603294
PCLAF	538.76221	1.818238668	0.1884228	9.64978069	4.93E-22	2.82E-20
SGO1	136.36186	1.815518439	0.15523739	11.6951102	1.35E-31	1.44E-29
POLE2	191.241	1.809180142	0.2182282	8.29031344	1.13E-16	4.10E-15
KIF20B	772.92577	1.804635151	0.22035611	8.18963052	2.62E-16	9.18E-15
CPA3	323.40374	1.803660824	0.22039324	8.18383023	2.75E-16	9.58E-15
KSR2	223.70979	1.791187903	0.33768881	5.30425608	1.13E-07	1.47E-06
PLK4	396.5061	1.788755834	0.25544433	7.00252705	2.51E-12	6.16E-11
IQGAP3	611.28639	1.780899961	0.2760468	6.45144226	1.11E-10	2.20E-09
AUNIP	78.423145	1.772130172	0.20082512	8.82424561	1.10E-18	4.66E-17
SCN10A	11.979003	1.76903547	0.33435735	5.29085262	1.22E-07	1.57E-06
MTFR2	100.35275	1.766605077	0.15455364	11.4303684	2.95E-30	2.87E-28
RNU2-63P	54.342688	1.765862412	0.37050817	4.7660553	1.88E-06	1.99E-05
CIP2A	581.8738	1.765408631	0.17080136	10.3360337	4.84E-25	3.37E-23
TRAIP	115.66301	1.763669423	0.18711151	9.42576641	4.27E-21	2.21E-19
KIF20A	1675.3065	1.758355786	0.1035358	16.9830702	1.10E-64	3.97E-62
MAD2L1	1004.4273	1.753616184	0.29816866	5.8812895	4.07E-09	6.59E-08
FBXO5	345.89994	1.753416649	0.17587975	9.96940583	2.07E-23	1.30E-21
ORC6	496.26601	1.750242541	0.15921553	10.9929136	4.13E-28	3.57E-26
OIP5	144.29159	1.746750427	0.19356266	9.02421165	1.81E-19	8.25E-18
HIST1H4H	2328.891	1.746332521	0.24526864	7.12008086	1.08E-12	2.77E-11
FANCD2	559.37199	1.739478041	0.09961083	17.4627398	2.75E-68	1.14E-65
BRCA1	635.89418	1.727748408	0.2461515	7.0190447	2.23E-12	5.51E-11
DIAPH3	678.12383	1.719223135	0.06590147	26.0877828	5.02E-150	1.21E-146
HPDL	18.070531	1.716726485	0.41835119	4.10355345	4.07E-05	0.00032195
HELLS	753.19571	1.714486027	0.18495439	9.26977724	1.87E-20	9.32E-19
MEX3A	217.97298	1.699883818	0.24070428	7.06212548	1.64E-12	4.14E-11
KIF23	824.04743	1.697711737	0.15153902	11.2031327	3.94E-29	3.57E-27
CDKN3	392.25386	1.694736443	0.23839276	7.10900983	1.17E-12	2.99E-11
DDX12P	37.166453	1.690357233	0.24640194	6.860162	6.88E-12	1.58E-10
KIF22	871.61658	1.686732846	0.17037063	9.90037345	4.15E-23	2.55E-21
RACGAP1	1134.706	1.686475252	0.09391937	17.9566285	4.26E-72	1.99E-69
UBE2T	527.19773	1.669031519	0.22271007	7.49418968	6.67E-14	1.94E-12
PSKH1	496.667	1.66610044	0.25631925	6.50009867	8.03E-11	1.63E-09

Table 3 continued

BRIP1	473.77015	1.663633058	0.19072779	8.72255174	2.72E-18	1.11E-16
FOXM1	515.17246	1.657876762	0.18655773	8.88666899	6.30E-19	2.75E-17
RFC3	334.42454	1.656086929	0.22679367	7.3021743	2.83E-13	7.62E-12
CENPN	653.65795	1.653951254	0.14374712	11.5059786	1.23E-30	1.24E-28
HIST1H1C	7969.1127	1.653230961	0.14087128	11.7357562	8.36E-32	8.97E-30
ERBB4	16.032415	1.64879566	0.36137769	4.56252753	5.05E-06	4.88E-05
AMMECR1	207.7059	1.64750642	0.11766157	14.0020776	1.51E-44	2.58E-42
HIST1H2AD	2082.4186	1.629814817	0.24893513	6.54714665	5.86E-11	1.21E-09
CDT1	216.72694	1.624616336	0.27177726	5.97774924	2.26E-09	3.83E-08
ELOA	1427.9888	1.619931888	0.09603037	16.8689541	7.61E-64	2.63E-61
SGO2	536.70956	1.618376613	0.26447353	6.11923863	9.40E-10	1.65E-08
FANCI	949.00572	1.611617021	0.17036556	9.45975835	3.09E-21	1.63E-19
KIF24	191.8654	1.611142944	0.15503142	10.3923637	2.69E-25	1.93E-23
MCM5	1411.3884	1.610272601	0.22444778	7.17437522	7.26E-13	1.89E-11
MELK	869.37716	1.599830917	0.09991731	16.0115487	1.06E-57	2.80E-55
ESM1	9899.4797	1.598155711	0.12190473	13.1098741	2.89E-39	4.23E-37
HIST2H2AB	425.28317	1.593343061	0.22247799	7.16180073	7.96E-13	2.07E-11
HMGB3	498.52991	1.593084779	0.13760763	11.5770091	5.39E-31	5.50E-29
CENPI	424.04432	1.592636565	0.17609886	9.04399137	1.51E-19	6.97E-18
AC025186.1	27.996867	1.589836916	0.58660983	2.71021186	0.006724	0.0276064
EZH2	412.05357	1.587865025	0.10735051	14.791407	1.66E-49	3.45E-47
PSRC1	176.29214	1.568642191	0.14637334	10.716721	8.50E-27	6.69E-25
HMGB2	2292.604	1.568040553	0.1559332	10.0558477	8.66E-24	5.53E-22
TRIP13	614.84366	1.565748672	0.09338421	16.7667394	4.27E-63	1.41E-60
ZGRF1	322.83503	1.560556364	0.31250432	4.99371131	5.92E-07	6.83E-06
EME1	85.803992	1.545264262	0.19478388	7.93322461	2.14E-15	7.04E-14
CDCA7	200.6527	1.544947061	0.16155121	9.56320326	1.14E-21	6.29E-20
DNAJC9	1592.8551	1.54045667	0.14461746	10.6519412	1.71E-26	1.32E-24
BRI3BP	378.99044	1.539131333	0.12822362	12.0034927	3.41E-33	3.92E-31
CDC25A	502.48238	1.528392527	0.20436295	7.47881401	7.50E-14	2.16E-12
NCR3LG1	342.75209	1.526528918	0.14811436	10.306421	6.59E-25	4.51E-23
AC099850.3	55.063654	1.526193909	0.20695005	7.37469682	1.65E-13	4.51E-12
PCNA	2464.1064	1.526114909	0.12738515	11.9803204	4.51E-33	5.10E-31
POC1A	335.70946	1.523358479	0.15573835	9.78152466	1.35E-22	8.23E-21
H2AFX	928.5996	1.518253001	0.21647455	7.01354055	2.32E-12	5.70E-11
PMCH	46.670173	1.514486083	0.31331529	4.83374463	1.34E-06	1.45E-05
XRCC2	227.97307	1.512620554	0.18455117	8.19621239	2.48E-16	8.71E-15

Table 3 continued

PRC1-AS1	30.406321	1.511133029	0.29491081	5.124034	2.99E-07	3.63E-06
PRR11	517.51051	1.511015786	0.15551776	9.71603392	2.58E-22	1.52E-20
CHAF1A	436.34831	1.509722452	0.20293421	7.43946762	1.01E-13	2.85E-12
MT1L	244.61351	1.508905864	0.17653856	8.54717452	1.26E-17	4.89E-16
DSCC1	115.55902	1.504964796	0.20130435	7.47606696	7.66E-14	2.19E-12
CENPH	250.50041	1.499182622	0.19387576	7.73269752	1.05E-14	3.26E-13
HIST1H4C	2872.3958	1.496480525	0.26621009	5.62142686	1.89E-08	2.77E-07
ITPRIPL1	15.913448	1.495747648	0.41715724	3.58557276	0.0003363	0.00211006
WDR76	400.57419	1.492004765	0.18006539	8.28590547	1.17E-16	4.25E-15
RECQL4	214.0686	1.481551566	0.39916842	3.71159514	0.000206	0.00137087
ATXN7L3B	1790.6603	1.478658665	0.07360439	20.0892738	9.16E-90	5.53E-87
PRIM1	230.5377	1.476483709	0.23386558	6.31338608	2.73E-10	5.21E-09
FRMD3	309.82484	1.474895613	0.14540763	10.1431791	3.55E-24	2.34E-22
TMPPE	151.17379	1.463599399	0.1788081	8.18530804	2.72E-16	9.49E-15
LOC101928000	58.851503	1.463464179	0.36173637	4.04566504	5.22E-05	0.00040084
DHFR	826.74501	1.455652558	0.15577119	9.34481231	9.21E-21	4.70E-19
WDR62	164.99055	1.45562888	0.14418215	10.0957633	5.77E-24	3.72E-22
MTBP	227.81888	1.450294584	0.22987411	6.30908184	2.81E-10	5.35E-09
MCM6	1093.2605	1.448839803	0.11016625	13.1513949	1.67E-39	2.47E-37
GINS3	395.83036	1.448665964	0.09231665	15.6923586	1.71E-55	4.12E-53
RNU5A-8P	448.00294	1.441365996	0.55443936	2.59968193	0.009331	0.0361496
AC124798.1	49.553494	1.43547415	0.28892029	4.96840886	6.75E-07	7.72E-06
AC025257.1	28.261761	1.435323873	0.42306591	3.39267202	0.0006921	0.00395196
NEIL3	148.53789	1.42613477	0.17180474	8.3009046	1.03E-16	3.78E-15
CORO1A	41.272285	1.422687989	0.32233682	4.4136689	1.02E-05	9.17E-05
C17orf53	107.8356	1.417045651	0.20658554	6.85936511	6.92E-12	1.58E-10
RRM1	2324.373	1.415645322	0.12924335	10.953332	6.40E-28	5.43E-26
HIST1H2BK	2770.5042	1.414069006	0.13589213	10.4058198	2.33E-25	1.68E-23
DKC1	613.1487	1.412619666	0.08562058	16.4985988	3.76E-61	1.13E-58
DNA2	317.00432	1.411034139	0.25021615	5.63926093	1.71E-08	2.53E-07
H2AFZ	7415.6934	1.410132108	0.16124548	8.74525068	2.23E-18	9.14E-17
POLR3G	242.36435	1.408553799	0.26868684	5.24236236	1.59E-07	2.01E-06
STIL	557.46654	1.408315062	0.18861484	7.46661866	8.23E-14	2.34E-12
CIT	524.8398	1.402590634	0.14820621	9.46377795	2.97E-21	1.57E-19
ANKRD18B	87.122203	1.401137311	0.20301662	6.90158921	5.14E-12	1.20E-10
LMNB2	3076.3963	1.400383081	0.2580708	5.42635239	5.75E-08	7.79E-07
CAAP1	470.16262	1.398951442	0.11087844	12.6169836	1.70E-36	2.24E-34

Table 3 continued

DTL	441.36332	1.392999398	0.13440562	10.3641455	3.61E-25	2.53E-23
CEP128	160.82571	1.392216033	0.15645781	8.8983477	5.67E-19	2.49E-17
AC129102.1	63.299976	1.388891685	0.22425367	6.19339546	5.89E-10	1.07E-08
SASS6	141.82151	1.388453037	0.25187815	5.5123998	3.54E-08	4.98E-07
CCDC190	174.68451	1.378607546	0.33248392	4.14638859	3.38E-05	0.00027279
TEDC2	96.554256	1.375736918	0.27869982	4.93626771	7.96E-07	9.00E-06
RMI2	111.75327	1.369175441	0.1665085	8.22285591	1.99E-16	7.04E-15
RNU5D-1	1014.4104	1.367146431	0.45962806	2.97446251	0.002935	0.01372992
CENPK	657.8913	1.366143922	0.2155155	6.33895911	2.31E-10	4.44E-09
CDKN2C	231.44259	1.363052746	0.25201054	5.40871331	6.35E-08	8.54E-07
CCDC150	94.613768	1.359950427	0.17618617	7.71882617	1.17E-14	3.61E-13
MMS22L	528.12247	1.35992528	0.24120761	5.63798674	1.72E-08	2.54E-07
RAD51	303.43119	1.358335984	0.14195506	9.56877435	1.08E-21	6.01E-20
MYBL1	86.056227	1.350848346	0.19585593	6.89715308	5.31E-12	1.23E-10
SKINT1L	151.94016	1.349785709	0.47444464	2.84498043	0.0044414	0.01950536
MAT2B	2430.1136	1.348570166	0.12109971	11.1360313	8.38E-29	7.50E-27
AC012073.1	21.399341	1.348303005	0.27202601	4.95652245	7.18E-07	8.19E-06
TACC3	1019.3557	1.344151684	0.24267276	5.53894757	3.04E-08	4.33E-07
SMC2	1186.346	1.33804234	0.23534636	5.68541756	1.30E-08	1.97E-07
EPS15	1365.6275	1.336006531	0.15148377	8.81946971	1.15E-18	4.85E-17
SNRPD1	1251.9534	1.332255115	0.15439352	8.62895758	6.19E-18	2.46E-16
HASPIN	188.49686	1.331510418	0.2771571	4.80417206	1.55E-06	1.67E-05
PARPBP	398.80953	1.330128058	0.26556572	5.00865879	5.48E-07	6.37E-06
NCAPD3	807.35733	1.328894028	0.14919952	8.9068249	5.25E-19	2.32E-17
FAM217B	213.98647	1.323541842	0.19603573	6.75153362	1.46E-11	3.24E-10
NPIPB13	36.932537	1.322955488	0.47883262	2.76287669	0.0057294	0.02413824
AC093724.1	98.493058	1.321790257	0.19924135	6.63411616	3.26E-11	6.96E-10
INCENP	422.71843	1.320502427	0.29495413	4.47697555	7.57E-06	7.02E-05
HDAC9	464.40399	1.318398361	0.18689678	7.0541525	1.74E-12	4.37E-11
DPF1	36.215744	1.31004718	0.22105813	5.92625643	3.10E-09	5.11E-08
UBE2L2	11.24113	1.307386758	0.49619484	2.63482538	0.0084181	0.03331602
MCM8	329.99701	1.306006611	0.18760037	6.96164191	3.36E-12	8.10E-11
COPZ1	2846.0648	1.304481998	0.11875968	10.9842162	4.55E-28	3.90E-26
KIF21A	367.73939	1.301018403	0.18787941	6.92475236	4.37E-12	1.04E-10
ARHGAP11B	203.74858	1.296531029	0.22919474	5.65689707	1.54E-08	2.30E-07
LOC100288637	203.74858	1.296531029	0.22919474	5.65689707	1.54E-08	2.30E-07
HK2	341.53522	1.293134263	0.3190438	4.05315585	5.05E-05	0.00038924

Table 3 continued

HIST1H2BD	2986.6156	1.292667751	0.17472561	7.39827286	1.38E-13	3.82E-12
CCNE2	281.0081	1.290631503	0.25381687	5.08489259	3.68E-07	4.40E-06
BRCA2	639.10801	1.287333456	0.25720159	5.00515356	5.58E-07	6.47E-06
SNAPIN	632.58885	1.28388851	0.1390747	9.23164686	2.67E-20	1.32E-18
KNSTRN	815.49035	1.283829918	0.15206914	8.44240906	3.11E-17	1.18E-15
PANK3	3485.3471	1.283706085	0.12438467	10.3204527	5.70E-25	3.93E-23
C1orf112	347.88823	1.277229114	0.2086281	6.12203766	9.24E-10	1.63E-08
AC007952.4	387.62091	1.27694874	0.17378916	7.34768906	2.02E-13	5.50E-12
HIST2H2BE	1185.9087	1.276167311	0.11107175	11.4895762	1.49E-30	1.49E-28
SPINT1	14.439956	1.275970425	0.41064633	3.10722472	0.0018885	0.00944069
NUP43	1139.7512	1.273228155	0.08765341	14.525712	8.33E-48	1.65E-45
CCNF	1037.6789	1.266696247	0.22580938	5.60958218	2.03E-08	2.96E-07
RNVU1-15	111.82175	1.264210997	0.35892605	3.52220462	0.000428	0.00260467
FANCA	328.64935	1.260435183	0.14176809	8.89082436	6.07E-19	2.66E-17
WDHD1	646.4879	1.259835604	0.20241265	6.22409519	4.84E-10	8.91E-09
AC092718.4	61.548606	1.258282344	0.17209119	7.31171871	2.64E-13	7.12E-12
EMC8	734.44259	1.251031503	0.12813652	9.76327051	1.62E-22	9.82E-21
AC004837.3	106.5479	1.247782254	0.19218869	6.49248525	8.44E-11	1.71E-09
GINS4	180.23854	1.242146216	0.25651152	4.84245789	1.28E-06	1.40E-05
PDE4A	69.797885	1.239440025	0.22756656	5.44649452	5.14E-08	7.00E-07
HIST1H1E	5468.6793	1.235739421	0.13600611	9.0859113	1.03E-19	4.81E-18
PAQR4	244.27634	1.235049262	0.34890282	3.53980873	0.0004004	0.00245864
CCDC34	138.43867	1.234596999	0.19685491	6.27160875	3.57E-10	6.75E-09
AP005901.5	17.452557	1.227887421	0.47877078	2.5646666	0.0103275	0.03930631
HIST1H2BN	788.76664	1.226429625	0.13643512	8.98910522	2.49E-19	1.12E-17
RFC4	353.70216	1.22200686	0.16466739	7.42106179	1.16E-13	3.25E-12
CEP72	58.200039	1.215965959	0.27761433	4.3800548	1.19E-05	0.00010571
AC016205.1	16.448007	1.21231496	0.39976685	3.03255498	0.0024249	0.01164818
CENPL	361.35842	1.210675566	0.15902836	7.61295392	2.68E-14	8.07E-13
INHBA	746.78687	1.207369506	0.13167166	9.16954731	4.75E-20	2.31E-18
AL359955.1	656.36579	1.207003409	0.37238622	3.24126767	0.00119	0.00629611
TGFBR2	17498.128	-1.201063689	0.13583514	-8.8420689	9.40E-19	3.99E-17
BAALC	58.127567	-1.204504116	0.24066304	-5.0049402	5.59E-07	6.48E-06
PDGFRA	42.767575	-1.204727365	0.25821248	-4.6656435	3.08E-06	3.12E-05
ZNF366	99.52198	-1.206200258	0.15367372	-7.8490989	4.19E-15	1.34E-13
GADD45A	945.0534	-1.207406483	0.13480245	-8.9568588	3.34E-19	1.49E-17
UST	27.766104	-1.210405836	0.35446632	-3.4147274	0.0006385	0.00367875

Table 3 continued

AC046143.1	50.848978	-1.210724048	0.22991655	-5.2659281	1.39E-07	1.79E-06
FAM129A	396.37557	-1.217603711	0.19192417	-6.3441918	2.24E-10	4.30E-09
NOTCH4	413.53144	-1.219238441	0.39052028	-3.1220874	0.0017957	0.00901725
KAT2B	582.45842	-1.225794323	0.14938567	-8.2055684	2.30E-16	8.10E-15
CLU	10468.9	-1.226028833	0.27933796	-4.389052	1.14E-05	0.00010186
COL1A2	364.78877	-1.233110106	0.24978001	-4.9367846	7.94E-07	8.99E-06
P4HA3	664.30837	-1.233504589	0.12706612	-9.7075807	2.80E-22	1.64E-20
TCTEX1D1	61.359636	-1.234669381	0.15640635	-7.8939849	2.93E-15	9.51E-14
ADIRF	878.10435	-1.235885215	0.11346566	-10.892152	1.26E-27	1.03E-25
LYNX1	103.76244	-1.237324861	0.43556852	-2.8407123	0.0045013	0.01973842
AL162591.2	128.81737	-1.239596279	0.18610089	-6.6608832	2.72E-11	5.85E-10
SCG5	22.525507	-1.240790136	0.347984	-3.5656528	0.000363	0.00225148
LIMCH1	1280.1678	-1.241228008	0.07713306	-16.092036	2.90E-58	7.94E-56
PCDHB14	20.839867	-1.246577463	0.28439491	-4.3832622	1.17E-05	0.00010424
RAET1E	21.635233	-1.250679218	0.27400525	-4.5644352	5.01E-06	4.84E-05
LAYN	54.80174	-1.251019562	0.24303208	-5.1475492	2.64E-07	3.23E-06
C5orf24	1870.644	-1.251849991	0.1009674	-12.398557	2.66E-35	3.35E-33
LRRC17	135.91509	-1.256482265	0.24476972	-5.1333239	2.85E-07	3.46E-06
A2M	718.56177	-1.264572276	0.23854371	-5.3012183	1.15E-07	1.49E-06
ARRDC2	565.25509	-1.267367564	0.23353216	-5.426951	5.73E-08	7.77E-07
HTR1D	44.20154	-1.274253533	0.27722038	-4.5965363	4.30E-06	4.21E-05
GPR153	79.396324	-1.274446617	0.41049347	-3.1046696	0.0019049	0.00951277
ECM1	41.636062	-1.27838442	0.32946009	-3.8802406	0.0001044	0.00074012
ERV3-1-ZNF117	1230.7988	-1.283426189	0.25395321	-5.05379	4.33E-07	5.10E-06
ZNF117	1230.7988	-1.283426189	0.25395321	-5.05379	4.33E-07	5.10E-06
ST6GALNAC3	1254.0912	-1.285673243	0.20883554	-6.1563911	7.44E-10	1.34E-08
TFPI	11563.945	-1.286311191	0.18582101	-6.9223131	4.44E-12	1.05E-10
COMMD8	601.58342	-1.290753736	0.19964332	-6.465299	1.01E-10	2.03E-09
SULT1A4	212.98652	-1.291052888	0.47099947	-2.741092	0.0061235	0.02550945
RAET1G	35.621521	-1.292043371	0.37273833	-3.466355	0.0005276	0.00312296
CTNNBIP1	671.32944	-1.292256361	0.17829776	-7.247743	4.24E-13	1.13E-11
LRRC4	41.32126	-1.292639173	0.3278491	-3.942787	8.05E-05	0.00059029
ERMAP	185.05008	-1.297277846	0.10530606	-12.319119	7.15E-35	8.93E-33
DKK3	9125.1752	-1.300223282	0.17715016	-7.3396675	2.14E-13	5.80E-12
C16orf45	382.18734	-1.303789826	0.09672878	-13.478821	2.08E-41	3.25E-39
AL359075.2	30.578831	-1.308667027	0.24694457	-5.2994364	1.16E-07	1.51E-06
FABP5P7	1809.8448	-1.317383831	0.19904471	-6.6185323	3.63E-11	7.68E-10

Table 3 continued

LZTS3	118.95805	-1.319350695	0.43868144	-3.0075371	0.0026337	0.01249798
MRC2	1406.136	-1.32361	0.30966229	-4.2743661	1.92E-05	0.00016336
VWCE	69.39641	-1.327737587	0.23453306	-5.6611959	1.50E-08	2.26E-07
TGFBI	2043.78	-1.33110736	0.23136557	-5.7532648	8.75E-09	1.36E-07
CACNA2D4	15.757074	-1.33212132	0.28917169	-4.6066796	4.09E-06	4.03E-05
SLFN5	2036.4851	-1.333378369	0.10117199	-13.179323	1.15E-39	1.73E-37
DPP4	381.77811	-1.336267281	0.0832259	-16.055906	5.20E-58	1.40E-55
CLDN10	49.411962	-1.339695961	0.28642659	-4.6772751	2.91E-06	2.96E-05
CD302	206.64002	-1.34165915	0.15761415	-8.5123014	1.71E-17	6.56E-16
UNC5A	20.21472	-1.342312134	0.3138887	-4.2763953	1.90E-05	0.00016198
TNFRSF10C	628.86495	-1.343264628	0.1913228	-7.0209332	2.20E-12	5.45E-11
OLFML3	133.08632	-1.344992827	0.14915613	-9.0173484	1.93E-19	8.76E-18
NIPAL2	352.99401	-1.348545197	0.21734338	-6.2046757	5.48E-10	1.00E-08
MAN2A1	3193.2091	-1.349793534	0.10382015	-13.001267	1.20E-38	1.73E-36
TNFRSF4	36.34785	-1.353258871	0.36659772	-3.6914001	0.000223	0.00147096
GALNT15	774.75198	-1.360911938	0.10075937	-13.506555	1.43E-41	2.25E-39
ANGPTL4	2293.4956	-1.3631653	0.29389014	-4.6383499	3.51E-06	3.50E-05
VSIR	251.98626	-1.364493736	0.32928785	-4.1437719	3.42E-05	0.00027577
VAV3	82.893286	-1.367763011	0.20845175	-6.561533	5.33E-11	1.10E-09
CTSO	210.17955	-1.370401505	0.12391916	-11.058835	1.99E-28	1.73E-26
CREG2	60.642394	-1.373646934	0.16318822	-8.417562	3.84E-17	1.45E-15
TMEM273	99.362736	-1.38454	0.21591871	-6.4123208	1.43E-10	2.82E-09
HDHD2	240.71987	-1.391232217	0.14439287	-9.6350481	5.69E-22	3.23E-20
DDR1	177.51728	-1.395929448	0.47341534	-2.9486359	0.0031918	0.01471487
SEPTIN4	46.787194	-1.399458563	0.23480816	-5.9600083	2.52E-09	4.23E-08
FABP5	3342.2236	-1.408454587	0.10945736	-12.86761	6.85E-38	9.37E-36
PCDH12	2076.812	-1.40937066	0.2300461	-6.1264706	8.98E-10	1.59E-08
PKHD1L1	185.82948	-1.416110326	0.25073323	-5.6478766	1.62E-08	2.41E-07
WASF3	410.16945	-1.424469548	0.16338001	-8.7187507	2.81E-18	1.14E-16
C3AR1	21.67256	-1.42450288	0.31492485	-4.5233105	6.09E-06	5.78E-05
NR1H3	195.38941	-1.437999209	0.1373323	-10.470947	1.17E-25	8.64E-24
MRAP2	113.18589	-1.447566236	0.15328803	-9.4434392	3.61E-21	1.89E-19
ITGA1	139.43635	-1.449989601	0.19417018	-7.4676225	8.17E-14	2.33E-12
ANGPTL2	688.69628	-1.453009958	0.24504229	-5.9296293	3.04E-09	5.02E-08
TSPAN7	99.357979	-1.461962488	0.25932825	-5.637498	1.73E-08	2.54E-07
GBP1P1	22.91641	-1.46198008	0.3361011	-4.3498224	1.36E-05	0.00011906
PDE1A	13.016007	-1.464651647	0.50082939	-2.9244523	0.0034506	0.01573075

Table 3 continued

LINC01676	45.585381	-1.472476651	0.49166342	-2.9948876	0.0027455	0.01295182
ANK2	27.210849	-1.472971609	0.27332792	-5.3890273	7.08E-08	9.47E-07
GJA4	82.955669	-1.479241009	0.21187292	-6.9817369	2.92E-12	7.09E-11
CCDC85A	329.84583	-1.485488714	0.24204687	-6.1371944	8.40E-10	1.49E-08
NT5E	12672.711	-1.487471422	0.08779254	-16.943028	2.17E-64	7.66E-62
RCSD1	40.694565	-1.494365563	0.21427317	-6.9741141	3.08E-12	7.46E-11
C7orf61	63.48895	-1.494857446	0.16713655	-8.9439288	3.76E-19	1.67E-17
PPP1R3C	131.65505	-1.500423247	0.22312511	-6.7245826	1.76E-11	3.86E-10
CASP12	52.876803	-1.502340871	0.22849552	-6.5749249	4.87E-11	1.02E-09
NPR1	538.83256	-1.513189899	0.20824066	-7.2665439	3.69E-13	9.86E-12
STK38L	1284.7612	-1.521639063	0.21095545	-7.2130823	5.47E-13	1.44E-11
KLF3-AS1	38.40152	-1.531333521	0.22152124	-6.9128067	4.75E-12	1.12E-10
FKBP9	3350.2897	-1.540300878	0.24547188	-6.2748568	3.50E-10	6.63E-09
CASP7	2248.9129	-1.555491842	0.10957606	-14.195544	9.76E-46	1.75E-43
SCN9A	68.465392	-1.566055956	0.21539668	-7.2705667	3.58E-13	9.59E-12
SELE	594.27571	-1.569000578	0.14695114	-10.677022	1.30E-26	1.02E-24
GIMAP5	320.29696	-1.571824555	0.08807523	-17.846386	3.08E-71	1.35E-68
STAT4	12.328683	-1.581922948	0.39830987	-3.9715886	7.14E-05	0.00052861
NOD2	18.672904	-1.59323019	0.42836653	-3.7193153	0.0001998	0.00133332
DIRAS3	94.993933	-1.595976249	0.16439344	-9.708272	2.78E-22	1.64E-20
FLT4	259.78441	-1.596372751	0.24589262	-6.492154	8.46E-11	1.71E-09
AFAP1L2	64.634125	-1.598931167	0.16543282	-9.665139	4.24E-22	2.44E-20
CRACR2B	85.69024	-1.60070439	0.20887683	-7.6633889	1.81E-14	5.52E-13
GPER1	45.900124	-1.601020752	0.3306841	-4.8415413	1.29E-06	1.40E-05
ENPP2	15.395559	-1.601802395	0.35708251	-4.4858047	7.26E-06	6.76E-05
CAPN11	44.670411	-1.606357347	0.34410282	-4.6682482	3.04E-06	3.08E-05
TSPAN11	30.207552	-1.613577268	0.2580819	-6.2521908	4.05E-10	7.59E-09
ADAM19	1218.4925	-1.615213679	0.21117747	-7.6486079	2.03E-14	6.16E-13
APOL3	2613.8586	-1.629875908	0.08953184	-18.204428	4.76E-74	2.38E-71
STS	410.37233	-1.639048235	0.12668918	-12.937555	2.76E-38	3.93E-36
MAMDC2	570.01204	-1.642942096	0.41803565	-3.9301483	8.49E-05	0.00061751
CROT	494.65672	-1.664783399	0.14609709	-11.395048	4.43E-30	4.25E-28
IL17D	567.08646	-1.66600686	0.28077056	-5.9336949	2.96E-09	4.91E-08
C11orf96	122.74701	-1.666152227	0.24803567	-6.7173895	1.85E-11	4.04E-10
GPR143	94.378224	-1.668640683	0.20657015	-8.0778404	6.59E-16	2.24E-14
SLC46A3	205.2689	-1.670558374	0.1202486	-13.892539	7.03E-44	1.19E-41
DLL4	927.46527	-1.672419411	0.16801058	-9.9542504	2.42E-23	1.50E-21

Table 3 continued

PRDM8	24.313391	-1.676699531	0.32905314	-5.0955281	3.48E-07	4.17E-06
SELP	28.850907	-1.677875242	0.43475381	-3.8593687	0.0001137	0.00079846
PDE6G	15.30847	-1.677884802	0.40648409	-4.1277994	3.66E-05	0.00029351
ACOX2	31.844044	-1.684081238	0.26915083	-6.2570166	3.92E-10	7.37E-09
PIK3IP1	695.62969	-1.687564552	0.13077209	-12.904623	4.24E-38	5.85E-36
AC073957.2	144.3911	-1.689300448	0.16284788	-10.373487	3.27E-25	2.31E-23
AXL	3963.1907	-1.690147602	0.2408561	-7.0172506	2.26E-12	5.57E-11
GPR146	87.304749	-1.692432063	0.45754436	-3.6989464	0.0002165	0.00143378
UBE2V2	825.44376	-1.69897173	0.19877018	-8.5474178	1.26E-17	4.89E-16
FER1L6	56.291428	-1.703367572	0.19243015	-8.8518747	8.61E-19	3.67E-17
LOC643733	334.50835	-1.707144071	0.11523939	-14.813893	1.19E-49	2.54E-47
AC011462.1	63.131586	-1.733490512	0.39577988	-4.3799359	1.19E-05	0.00010571
SLCO2A1	44.566787	-1.74164529	0.47712497	-3.6502917	0.0002619	0.00169224
CSF3	183.37549	-1.758957931	0.35044791	-5.0191708	5.19E-07	6.04E-06
SLC16A6	51.645752	-1.805787395	0.21681435	-8.3287264	8.17E-17	3.03E-15
MAN2B2	1025.1129	-1.824615948	0.28286585	-6.4504639	1.12E-10	2.21E-09
FLVCR2	143.19376	-1.826378202	0.20629595	-8.8531946	8.50E-19	3.64E-17
CXCL11	1722.5106	-1.837373834	0.12550171	-14.64023	1.56E-48	3.13E-46
RARRES1	62.023695	-1.851800234	0.19436637	-9.5273693	1.61E-21	8.73E-20
CADM3	360.84828	-1.87950193	0.37104409	-5.065441	4.07E-07	4.83E-06
CETP	49.883219	-1.886917403	0.21533765	-8.7625989	1.91E-18	7.88E-17
CDA	47.662579	-1.895993165	0.28969317	-6.5448322	5.96E-11	1.22E-09
EFCC1	15.575221	-1.916545005	0.30249242	-6.3358447	2.36E-10	4.53E-09
COL3A1	40.400174	-1.922798034	0.40076982	-4.7977615	1.60E-06	1.72E-05
PDE2A	869.24503	-1.923922854	0.20927135	-9.1934366	3.80E-20	1.87E-18
HTRA3	379.95067	-1.936347208	0.29980628	-6.4586612	1.06E-10	2.10E-09
AC104211.1	13.171417	-1.937970507	0.34061324	-5.6896512	1.27E-08	1.92E-07
ABCG2	375.38901	-1.944187952	0.1249885	-15.554934	1.47E-54	3.39E-52
DPH6-AS1	21.470913	-1.951397289	0.37109627	-5.2584664	1.45E-07	1.85E-06
C6orf120	959.69983	-1.986479752	0.09786296	-20.298587	1.32E-91	9.14E-89
CYBRD1	1923.1816	-1.990120579	0.09277984	-21.449925	4.57E-102	4.14E-99
B3GNT9	149.8303	-1.990880579	0.3286008	-6.0586601	1.37E-09	2.38E-08
CX3CL1	131.14226	-2.001551956	0.27568449	-7.2602995	3.86E-13	1.03E-11
AC007744.1	124.5417	-2.046991166	0.36502761	-5.6077707	2.05E-08	2.98E-07
ATE1-AS1	16.284309	-2.054612175	0.3515136	-5.8450432	5.06E-09	8.12E-08
RHOU	22.118653	-2.055930413	0.42150817	-4.8775577	1.07E-06	1.19E-05
TXLNB	48.198802	-2.123405715	0.27466031	-7.7310251	1.07E-14	3.30E-13

Table 3 continued

HCRTR1	21.5268	-2.13529697	0.30281633	-7.0514592	1.77E-12	4.45E-11
PDK4	525.95048	-2.233637083	0.08723376	-25.605192	1.34E-144	2.77E-141
CLEC10A	13.640022	-2.247771733	0.38441087	-5.8473157	5.00E-09	8.02E-08
SERPINB2	42.227974	-2.264074712	0.85179122	-2.658016	0.0078602	0.03143228
INHBB	90.948833	-2.285054054	0.14081579	-16.227258	3.24E-59	9.20E-57
TMOD1	22.331191	-2.303103918	0.33327003	-6.9106241	4.83E-12	1.13E-10
IFIT2	1948.7785	-2.333650107	0.1825531	-12.783404	2.03E-37	2.75E-35
FXN	174.63685	-2.344964395	0.15031999	-15.599817	7.30E-55	1.73E-52
MMP28	36.726355	-2.502987493	0.5600543	-4.4691872	7.85E-06	7.23E-05
GALNT1	13427.198	-2.519354332	0.17835095	-14.125825	2.63E-45	4.60E-43
ABCA1	715.05659	-2.570443708	0.16541236	-15.539611	1.87E-54	4.24E-52
IDO1	87.981361	-2.652000567	0.18492875	-14.340662	1.22E-46	2.27E-44
IL33	390.49746	-2.761173874	0.25297676	-10.914733	9.80E-28	8.17E-26
AQP1	228.76836	-2.787729624	0.24684464	-11.293458	1.41E-29	1.32E-27
CXCL10	325.97754	-2.913522824	0.25181125	-11.570265	5.83E-31	5.91E-29
AL731556.1	21.20983	-3.440277005	0.99422203	-3.4602704	0.0005396	0.00317882
INTS6P1	14.203793	-4.236036704	1.46793486	-2.8857116	0.0039053	0.01751163
UBD	55.751544	-5.303267085	1.34407913	-3.9456509	7.96E-05	0.00058387

Table 4. Hemodynamic data for AKR/J mouse model of Group 2 PH-HFpEF

Treatment	***RVSP (mmHg)**	**Relative Vessel Remodeling**
Regular diet	27	1.09
Regular diet	30	0.80
Regular diet	29	1.14
Regular diet	27	0.97
Regular diet	25	1.00
High-fat diet	38	1.64
High-fat diet	47	2.74
High-fat diet	34	2.68
High-fat diet	32	2.26
High-fat diet	38	3.14

* RVSP – right ventricular systolic pressure

Table 5. Hemodynamic data for ZSF1 rat model of Group 2 PH-HFpEF

Treatment	*RVSP (mmHg)
Lean	28
Lean	23
Lean	15
Lean	17
Lean	30
Lean	28
Lean	29
Lean	33
Lean	28
Ob-Su	43
Ob-Su	43
Ob-Su	37
Ob-Su	36
Ob-Su	42
Ob-Su	40
Ob-Su	36
Ob-Su	31
Ob-Su	39

* RVSP – right ventricular systolic pressure

Table 6. Clinical information for Group 1 PAH patients

Age	Gender	*mPAP (mmHg)	Diagnosis	Clinical description
34	Female	50	Idiopathic	Cardiopulmonary arrest (autopsy)
64	Female	55	Idiopathic	Cardiopulmonary arrest (autopsy)
68	Female	44	Scleroderma	Bilateral lung transplant
1	Male	50	Trisomy 21	Lung resection
12	Male	53	BMPR2 Mutation	Bilateral lung transplant
16	Male	62	Idiopathic	Bilateral lung transplant
19	Male	48	Idiopathic	Lung resection
42	Male	57	Scleroderma	Bilateral lung transplant

* mPAP – mean pulmonary arterial pressure

Table 7. Clinical information for Group 3 IPF-PH PH patients

Age	Gender	*mPAP (mmHg)	Diagnosis	Clinical description
69	Female	29	IPF and PH	Bilateral lung transplant
50	Male	30	IPF and PH	Bilateral lung transplant
58	Male	28	IPF and PH	Bilateral lung transplant
61	Male	37	IPF and PH	Bilateral lung transplant
62	Male	28	IPF and PH	Bilateral lung transplant
63	Male	27	IPF and PH	Bilateral lung transplant
66	Male	34	IPF and PH	Bilateral lung transplant
72	Male	46	IPF and PH	Rapid autopsy

* mPAP – mean pulmonary arterial pressure

Bibliography

1. Culley MK, and Chan SY. Mitochondrial metabolism in pulmonary hypertension: beyond mountains there are mountains. *J Clin Invest.* 2018;128(9):3704-15.
2. Lai Y-C, Potoka KC, Champion HC, Mora AL, and Gladwin MT. Pulmonary Arterial Hypertension: The Clinical Syndrome. *J Clin Invest.* 2014;115(1):115-30.
3. Simonneau G, Montani D, Celermajer DS, Denton CP, Gatzoulis MA, Krowka M, et al. Haemodynamic definitions and updated clinical classification of pulmonary hypertension. *Eur Respir J.* 2019;53(1).
4. Humbert M, Guignabert C, Bonnet S, Dorfmuller P, Klinger JR, Nicolls MR, et al. Pathology and pathobiology of pulmonary hypertension: state of the art and research perspectives. *Eur Respir J.* 2019;53(1).
5. Paulin R, and Michelakis ED. The Metabolic Theory of Pulmonary Arterial Hypertension. *Circulation Research.* 2014;115(1):148-64.
6. Stenmark KR, Yeager ME, El Kasmi KC, Nozik-Grayck E, Gerasimovskaya EV, Li M, et al. The adventitia: essential regulator of vascular wall structure and function. *Annu Rev Physiol.* 2013;75:23-47.
7. Platoshyn O, Golovina VA, Bailey CL, Limsuwan A, Krick S, Juhaszova M, et al. Sustained membrane depolarization and pulmonary artery smooth muscle cell proliferation. *Am J Physiol Cell Physiol.* 2000;279(5):C1540-9.
8. Thenappan T, Chan SY, and Weir EK. Role of extracellular matrix in the pathogenesis of pulmonary arterial hypertension. *Am J Physiol Heart Circ Physiol.* 2018;315(5):H1322-H31.
9. Hassoun PM. Deciphering the "matrix" in pulmonary vascular remodelling. *Eur Respir J.* 2005;25(5):778-9.
10. Li M, Riddle S, Zhang H, D'Alessandro A, Flockton A, Serkova NJ, et al. Metabolic Reprogramming Regulates the Proliferative and Inflammatory Phenotype of Adventitial Fibroblasts in Pulmonary Hypertension Through the Transcriptional Corepressor C-Terminal Binding Protein-1. *Circulation.* 2016;134(15):1105-21.
11. Zhang H, Wang D, Li M, Plecita-Hlavata L, D'Alessandro A, Tauber J, et al. Metabolic and Proliferative State of Vascular Adventitial Fibroblasts in Pulmonary Hypertension Is Regulated Through a MicroRNA-124/PTBP1 (Polypyrimidine Tract Binding Protein 1)/Pyruvate Kinase Muscle Axis. *Circulation.* 2017;136(25):2468-85.
12. Michelakis ED, Wilkins MR, and Rabinovitch M. Emerging concepts and translational priorities in pulmonary arterial hypertension. *Circulation.* 2008;118(14):1486-95.
13. Moledina S, de Bruyn A, Schievano S, Owens CM, Young C, Haworth SG, et al. Fractal branching quantifies vascular changes and predicts survival in pulmonary hypertension: a proof of principle study. *Heart.* 2011;97(15):1245-9.

14. Chaudhary KR, Taha M, Cadete VJ, Godoy RS, and Stewart DJ. Proliferative Versus Degenerative Paradigms in Pulmonary Arterial Hypertension: Have We Put the Cart Before the Horse? *Circ Res.* 2017;120(8):1237-9.

15. Kuebler WM, Nicolls MR, Olschewski A, Abe K, Rabinovitch M, Stewart D, et al. A pro-con debate: current controversies in PAH pathogenesis at the American Thoracic Society International Conference in 2017. *American Journal of Physiology-Lung Cellular and Molecular Physiology.* 2018;315(4):L502-L16.

16. Ranchoux B, Harvey LD, Ayon RJ, Babicheva A, Bonnet S, Chan SY, et al. Endothelial dysfunction in pulmonary arterial hypertension: an evolving landscape (2017 Grover Conference Series). *Pulm Circ.* 2018;8(1):2045893217752912.

17. Taraseviciene-Stewart L, Kasahara Y, Alger L, Hirth P, Mc Mahon G, Waltenberger J, et al. Inhibition of the VEGF receptor 2 combined with chronic hypoxia causes cell death-dependent pulmonary endothelial cell proliferation and severe pulmonary hypertension. *FASEB J.* 2001;15(2):427-38.

18. Goldthorpe H, Jiang JY, Taha M, Deng Y, Sinclair T, Ge CX, et al. Occlusive lung arterial lesions in endothelial-targeted, fas-induced apoptosis transgenic mice. *Am J Respir Cell Mol Biol.* 2015;53(5):712-8.

19. Steiner MK, Syrkina OL, Kolliputi N, Mark EJ, Hales CA, and Waxman AB. Interleukin-6 overexpression induces pulmonary hypertension. *Circ Res.* 2009;104.

20. Kim J, Kang Y, Kojima Y, Lighthouse JK, Hu X, Aldred MA, et al. An endothelial apelin-FGF link mediated by miR-424 and miR-503 is disrupted in pulmonary arterial hypertension. *Nat Med.* 2013;19(1):74-82.

21. Sakao S, Taraseviciene-Stewart L, Lee JD, Wood K, Cool CD, and Voelkel NF. Initial apoptosis is followed by increased proliferation of apoptosis-resistant endothelial cells. *FASEB J.* 2005;19(9):1178-80.

22. Michelakis ED. Spatio-temporal diversity of apoptosis within the vascular wall in pulmonary arterial hypertension: heterogeneous BMP signaling may have therapeutic implications. *Circ Res.* 2006;98(2):172-5.

23. Masri FA, Xu W, Comhair SAA, Asosingh K, Koo M, Vasanji A, et al. Hyperproliferative apoptosis-resistant endothelial cells in idiopathic pulmonary arterial hypertension. *American Journal of Physiology - Lung Cellular and Molecular Physiology.* 2007;293(3):L548-L54.

24. Lee SD, Shroyer KR, Markham NE, Cool CD, Voelkel NF, and Tuder RM. Monoclonal endothelial cell proliferation is present in primary but not secondary pulmonary hypertension. *J Clin Invest.* 1998;101(5):927-34.

25. Huertas A, Guignabert C, Barbera JA, Bartsch P, Bhattacharya J, Bhattacharya S, et al. Pulmonary vascular endothelium: the orchestra conductor in respiratory diseases: Highlights from basic research to therapy. *Eur Respir J.* 2018;51(4).

26. Hopper RK, Moonen JR, Diebold I, Cao A, Rhodes CJ, Tojais NF, et al. In Pulmonary Arterial Hypertension, Reduced BMPR2 Promotes Endothelial-to-Mesenchymal Transition via HMGA1 and Its Target Slug. *Circulation.* 2016;133(18):1783-94.

27. Ranchoux B, Antigny F, Rucker-Martin C, Hautefort A, Pechoux C, Bogaard HJ, et al. Endothelial-to-mesenchymal transition in pulmonary hypertension. *Circulation.* 2015;131(11):1006-18.

28. Suzuki T, Carrier EJ, Talati MH, Rathinasabapathy A, Chen X, Nishimura R, et al. Isolation and characterization of endothelial-to-mesenchymal transition cells in pulmonary arterial hypertension. *American Journal of Physiology-Lung Cellular and Molecular Physiology.* 2018;314(1):L118-L26.

29. Campisi J, and d'Adda di Fagagna F. Cellular senescence: when bad things happen to good cells. *Nat Rev Mol Cell Biol.* 2007;8(9):729-40.

30. Rodier F, Coppé JP, Patil CK, Hoeijmakers WA, Muñoz DP, Raza SR, et al. Persistent DNA damage signalling triggers senescence-associated inflammatory cytokine secretion. *Nat Cell Biol.* 2009;11(8):973-9.

31. Childs BG, Baker DJ, Wijshake T, Conover CA, Campisi J, and van Deursen JM. Senescent intimal foam cells are deleterious at all stages of atherosclerosis. *Science.* 2016;354(6311):472-7.

32. Childs BG, Li H, and van Deursen JM. Senescent cells: a therapeutic target for cardiovascular disease. *J Clin Invest.* 2018;128(4):1217-28.

33. Sugimoto K, Yokokawa T, Misaka T, Nakazato K, Ishida T, and Takeishi Y. Senescence Marker Protein 30 Deficiency Exacerbates Pulmonary Hypertension in Hypoxia-Exposed Mice. *Int Heart J.* 2019;60(6):1430-4.

34. van der Feen DE, Berger RMF, and Bartelds B. Converging Paths of Pulmonary Arterial Hypertension and Cellular Senescence. *Am J Respir Cell Mol Biol.* 2019;61(1):11-20.

35. Wiley CD, Velarde MC, Lecot P, Liu S, Sarnoski EA, Freund A, et al. Mitochondrial Dysfunction Induces Senescence with a Distinct Secretory Phenotype. *Cell Metab.* 2016;23(2):303-14.

36. Moiseeva O, Bourdeau V, Roux A, Deschênes-Simard X, and Ferbeyre G. Mitochondrial dysfunction contributes to oncogene-induced senescence. *Mol Cell Biol.* 2009;29(16):4495-507.

37. Velarde MC, Demaria M, Melov S, and Campisi J. Pleiotropic age-dependent effects of mitochondrial dysfunction on epidermal stem cells. *Proceedings of the National Academy of Sciences.* 2015;112(33):10407.

38. Warburg O. On the Origin of Cancer Cells. *Science.* 1956;123(3191):309-14.

39. Vander Heiden MG, Cantley LC, and Thompson CB. Understanding the Warburg Effect: The Metabolic Requirements of Cell Proliferation. *Science (New York, NY).* 2009;324(5930):1029-33.

40. Bonnet S, Michelakis ED, Porter CJ, Andrade-Navarro MA, Thébaud B, Bonnet S, et al. An Abnormal Mitochondrial–Hypoxia Inducible Factor-1α–Kv Channel Pathway Disrupts Oxygen Sensing and Triggers Pulmonary Arterial Hypertension in Fawn Hooded Rats. *Similarities to Human Pulmonary Arterial Hypertension.* 2006;113(22):2630-41.

41. Archer SL, Gomberg-Maitland M, Maitland ML, Rich S, Garcia JGN, and Weir EK. Mitochondrial metabolism, redox signaling, and fusion: a mitochondria-ROS-HIF-1α-Kv1.5 O2-sensing pathway at the intersection of pulmonary hypertension and cancer.

American Journal of Physiology-Heart and Circulatory Physiology. 2008;294(2):H570-H8.

42. Yu AY, Shimoda LA, Iyer NV, Huso DL, Sun X, McWilliams R, et al. Impaired physiological responses to chronic hypoxia in mice partially deficient for hypoxia-inducible factor 1α. *J Clin Invest.* 1999;103(5):691-6.

43. Ball MK, Waypa GB, Mungai PT, Nielsen JM, Czech L, Dudley VJ, et al. Regulation of Hypoxia-induced Pulmonary Hypertension by Vascular Smooth Muscle Hypoxia-Inducible Factor-1α. *Am J Respir Crit Care Med.* 2014;189(3):314-24.

44. Humbert M, Monti G, Brenot F, Sitbon O, Portier A, Grangeot-Keros L, et al. Increased interleukin-1 and interleukin-6 serum concentrations in severe primary pulmonary hypertension. *Am J Respir Crit Care Med.* 1995;151.

45. McMurtry MS, Bonnet S, Wu X, Dyck JR, Haromy A, Hashimoto K, et al. Dichloroacetate prevents and reverses pulmonary hypertension by inducing pulmonary artery smooth muscle cell apoptosis. *Circ Res.* 2004;95(8):830-40.

46. Bonnet S, Rochefort G, Sutendra G, Archer SL, Haromy A, Webster L, et al. The nuclear factor of activated T cells in pulmonary arterial hypertension can be therapeutically targeted. *Proc Natl Acad Sci U S A.* 2007;104(27):11418-23.

47. Plecitá-Hlavatá L, Tauber J, Li M, Zhang H, Flockton AR, Pullamsetti SS, et al. Constitutive Reprogramming of Fibroblast Mitochondrial Metabolism in Pulmonary Hypertension. *American Journal of Respiratory Cell and Molecular Biology.* 2016;55(1):47-57.

48. Xu W, and Erzurum SC. *Comprehensive Physiology*. John Wiley & Sons, Inc.; 2010.

49. Fijalkowska I, Xu W, Comhair SAA, Janocha AJ, Mavrakis LA, Krishnamachary B, et al. Hypoxia Inducible-Factor1α Regulates the Metabolic Shift of Pulmonary Hypertensive Endothelial Cells. *The American Journal of Pathology.* 2010;176(3):1130-8.

50. Fessel JP, Hamid R, Wittmann BM, Robinson LJ, Blackwell T, Tada Y, et al. Metabolomic analysis of bone morphogenetic protein receptor type 2 mutations in human pulmonary endothelium reveals widespread metabolic reprogramming. *Pulmonary Circulation.* 2012;2(2):201-13.

51. Drake JI, Bogaard HJ, Mizuno S, Clifton B, Xie B, Gao Y, et al. Molecular Signature of a Right Heart Failure Program in Chronic Severe Pulmonary Hypertension. *American Journal of Respiratory Cell and Molecular Biology.* 2011;45(6):1239-47.

52. Mainguy V, Maltais F, Saey D, Gagnon P, Martel S, Simon M, et al. Peripheral muscle dysfunction in idiopathic pulmonary arterial hypertension. *Thorax.* 2010;65(2):113-7.

53. Malenfant S, Potus F, Fournier F, Breuils-Bonnet S, Pflieger A, Bourassa S, et al. Skeletal muscle proteomic signature and metabolic impairment in pulmonary hypertension. *Journal of Molecular Medicine.* 2015;93(5):573-84.

54. Nguyen QL, Corey C, White P, Watson A, Gladwin MT, Simon MA, et al. Platelets from pulmonary hypertension patients show increased mitochondrial reserve capacity. *JCI Insight.* 2017;2(5).

55. Caruso P, Dunmore BJ, Schlosser K, Schoors S, Dos Santos C, Perez-Iratxeta C, et al. Identification of MicroRNA-124 as a Major Regulator of Enhanced Endothelial Cell

Glycolysis in Pulmonary Arterial Hypertension via PTBP1 (Polypyrimidine Tract Binding Protein) and Pyruvate Kinase M2. *Circulation.* 2017;136(25):2451-67.

56. Bertero T, Oldham WM, Cottrill KA, Pisano S, Vanderpool RR, Yu Q, et al. Vascular stiffness mechanoactivates YAP/TAZ-dependent glutaminolysis to drive pulmonary hypertension. *The Journal of Clinical Investigation.* 2016;126(9):3313-35.

57. Piao L, Fang Y-H, Parikh K, Ryan JJ, Toth PT, and Archer SL. Cardiac Glutaminolysis: A Maladaptive Cancer Metabolism Pathway in the Right Ventricle in Pulmonary Hypertension. *Journal of molecular medicine (Berlin, Germany).* 2013;91(10):1185-97.

58. Sutendra G, Dromparis P, Paulin R, Zervopoulos S, Haromy A, Nagendran J, et al. A metabolic remodeling in right ventricular hypertrophy is associated with decreased angiogenesis and a transition from a compensated to a decompensated state in pulmonary hypertension. *Journal of Molecular Medicine.* 2013;91(11):1315-27.

59. Singh N, Manhas A, Kaur G, Jagavelu K, and Hanif K. Inhibition of fatty acid synthase is protective in pulmonary hypertension. *British Journal of Pharmacology.* 2016;173(12):2030-45.

60. Chettimada S, Joshi SR, Alzoubi A, Gebb SA, McMurtry IF, Gupte R, et al. Glucose-6-phosphate dehydrogenase plays a critical role in hypoxia-induced CD133+ progenitor cells self-renewal and stimulates their accumulation in the lungs of pulmonary hypertensive rats. *American Journal of Physiology-Lung Cellular and Molecular Physiology.* 2014;307(7):L545-L56.

61. Chettimada S, Gupte R, Rawat D, Gebb SA, McMurtry IF, and Gupte SA. Hypoxia-induced glucose-6-phosphate dehydrogenase overexpression and -activation in pulmonary artery smooth muscle cells: implication in pulmonary hypertension. *American Journal of Physiology - Lung Cellular and Molecular Physiology.* 2015;308(3):L287-L300.

62. Boehme J, Sun X, Tormos KV, Gong W, Kellner M, Datar SA, et al. Pulmonary artery smooth muscle cell hyperproliferation and metabolic shift triggered by pulmonary overcirculation. *American Journal of Physiology - Heart and Circulatory Physiology.* 2016;311(4):H944-H57.

63. Tabima DM, Frizzell S, and Gladwin MT. REACTIVE OXYGEN AND NITROGEN SPECIES IN PULMONARY HYPERTENSION. *Free radical biology & medicine.* 2012;52(9):10.1016/j.freeradbiomed.2012.02.041.

64. Rhodes CJ, Wharton J, Howard L, Gibbs JSR, Vonk-Noordegraaf A, and Wilkins MR. Iron deficiency in pulmonary arterial hypertension: a potential therapeutic target. *European Respiratory Journal.* 2011;38(6):1453-60.

65. Marsboom G, Toth PT, RyaN JJ, Hong Z, Wu X, Fang Y-H, et al. Dynamin-Related Protein 1 (DRP1)-Mediated Mitochondrial Mitotic Fission Permits Hyperproliferation of Vascular Smooth Muscle Cells and Offers a Novel Therapeutic Target in Pulmonary Hypertension. *Circulation research.* 2012;110(11):1484-97.

66. Parra V, Bravo-Sagua R, Norambuena-Soto I, Hernández-Fuentes CP, Gómez-Contreras AG, Verdejo HE, et al. Inhibition of mitochondrial fission prevents hypoxia-induced metabolic shift and cellular proliferation of pulmonary arterial smooth muscle cells. *Biochimica et Biophysica Acta (BBA) - Molecular Basis of Disease.* 2017;1863(11):2891-903.

67. Tian L, Neuber-Hess M, Mewburn J, Dasgupta A, Dunham-Snary K, Wu D, et al. Ischemia-induced Drp1 and Fis1-mediated mitochondrial fission and right ventricular dysfunction in pulmonary hypertension. *J Mol Med (Berl).* 2017;95(4):381-93.

68. Gomez-Arroyo J, Mizuno S, Szczepanek K, Van Tassell B, Natarajan R, dos Remedios CG, et al. Metabolic Gene Remodeling and Mitochondrial Dysfunction in Failing Right Ventricular Hypertrophy due to Pulmonary Arterial Hypertension. *Circulation Heart failure.* 2013;6(1):136-44.

69. Xu W, Koeck T, Lara AR, Neumann D, DiFilippo FP, Koo M, et al. Alterations of cellular bioenergetics in pulmonary artery endothelial cells. *Proc Natl Acad Sci U S A.* 2007;104(4):1342-7.

70. Chan SY, Zhang YY, Hemann C, Mahoney CE, Zweier JL, and Loscalzo J. MicroRNA-210 controls mitochondrial metabolism during hypoxia by repressing the iron-sulfur cluster assembly proteins ISCU1/2. *Cell Metab.* 2009;10(4):273-84.

71. White K, Lu Y, Annis S, Hale AE, Chau BN, Dahlman JE, et al. Genetic and hypoxic alterations of the microRNA-210-ISCU1/2 axis promote iron-sulfur deficiency and pulmonary hypertension. *EMBO Mol Med.* 2015;7(6):695-713.

72. Yu Q, Tai YY, Tang Y, Zhao J, Negi V, Culley MK, et al. BOLA (BolA Family Member 3) Deficiency Controls Endothelial Metabolism and Glycine Homeostasis in Pulmonary Hypertension. *Circulation.* 2019;139(19):2238-55.

73. Singh N, Singh H, Jagavelu K, Wahajuddin M, and Hanif K. Fatty acid synthase modulates proliferation, metabolic functions and angiogenesis in hypoxic pulmonary artery endothelial cells. *European Journal of Pharmacology.* 2017;815:462-9.

74. Bertero T, Oldham WM, Cottrill KA, Pisano S, Vanderpool RR, Yu Q, et al. Vascular stiffness mechanoactivates YAP/TAZ-dependent glutaminolysis to drive pulmonary hypertension. *J Clin Invest.* 2016;126(9):3313-35.

75. Egnatchik RA, Brittain EL, Shah AT, Fares WH, Ford HJ, Monahan K, et al. Dysfunctional BMPR2 signaling drives an abnormal endothelial requirement for glutamine in pulmonary arterial hypertension. *Pulmonary Circulation.* 2017;7(1):186-99.

76. Diebold I, Hennigs Jan K, Miyagawa K, Li Caiyun G, Nickel Nils P, Kaschwich M, et al. BMPR2 Preserves Mitochondrial Function and DNA during Reoxygenation to Promote Endothelial Cell Survival and Reverse Pulmonary Hypertension. *Cell Metabolism.* 2015;21(4):596-608.

77. Ye J-X, Wang S-S, Ge M, and Wang D-J. Suppression of endothelial PGC-1α is associated with hypoxia-induced endothelial dysfunction and provides a new therapeutic target in pulmonary arterial hypertension. *American Journal of Physiology-Lung Cellular and Molecular Physiology.* 2016;310(11):L1233-L42.

78. Haslip M, Dostanic I, Huang Y, Zhang Y, Russell KS, Jurczak MJ, et al. Endothelial Ucp2 regulates mitophagy and pulmonary hypertension during intermittent-hypoxia. *Arteriosclerosis, thrombosis, and vascular biology.* 2015;35(5):1166-78.

79. Xiong J, Kawagishi H, Yan Y, Liu J, Wells QS, Edmunds LR, et al. A Metabolic Basis for Endothelial-to-Mesenchymal Transition. *Molecular Cell.* 2018;69(4):689-98.e7.

80. Rohlenova K, Veys K, Miranda-Santos I, De Bock K, and Carmeliet P. Endothelial Cell Metabolism in Health and Disease. *Trends in Cell Biology.* 2018;28(3):224-36.

81. Ranchoux B, Meloche J, Paulin R, Boucherat O, Provencher S, and Bonnet S. DNA Damage and Pulmonary Hypertension. *Int J Mol Sci.* 2016;17(6).

82. Federici C, Drake KM, Rigelsky CM, McNelly LN, Meade SL, Comhair SA, et al. Increased Mutagen Sensitivity and DNA Damage in Pulmonary Arterial Hypertension. *Am J Respir Crit Care Med.* 2015;192(2):219-28.

83. Van Houten B. Pulmonary Arterial Hypertension Is Associated with Oxidative Stress-induced Genome Instability. *Am J Respir Crit Care Med.* 2015;192(2):129-30.

84. Zeman MK, and Cimprich KA. Causes and consequences of replication stress. *Nat Cell Biol.* 2014;16(1):2-9.

85. Jackson SP, and Bartek J. The DNA-damage response in human biology and disease. *Nature.* 2009;461(7267):1071-8.

86. Roos WP, Thomas AD, and Kaina B. DNA damage and the balance between survival and death in cancer biology. *Nat Rev Cancer.* 2016;16(1):20-33.

87. Childs BG, Baker DJ, Kirkland JL, Campisi J, and van Deursen JM. Senescence and apoptosis: dueling or complementary cell fates? *EMBO Rep.* 2014;15(11):1139-53.

88. Meloche J, Pflieger A, Vaillancourt M, Paulin R, Potus F, Zervopoulos S, et al. Role for DNA damage signaling in pulmonary arterial hypertension. *Circulation.* 2014;129(7):786-97.

89. Lee SD, Shroyer KR, Markham NE, Cool CD, Voelkel NF, and Tuder RM. Monoclonal endothelial cell proliferation is present in primary but not secondary pulmonary hypertension. *Journal of Clinical Investigation.* 1998;101(5):927-34.

90. Yeager ME, Halley GR, Golpon HA, Voelkel NF, and Tuder RM. Microsatellite instability of endothelial cell growth and apoptosis genes within plexiform lesions in primary pulmonary hypertension. *Circ Res.* 2001;88(1):E2-e11.

91. Yeager ME, Golpon HA, Voelkel NF, and Tuder RM. Microsatellite mutational analysis of endothelial cells within plexiform lesions from patients with familial, pediatric, and sporadic pulmonary hypertension. *Chest.* 2002;121(3 Suppl):61s.

92. de Jesus Perez VA, Yuan K, Lyuksyutova MA, Dewey F, Orcholski ME, Shuffle EM, et al. Whole-exome sequencing reveals TopBP1 as a novel gene in idiopathic pulmonary arterial hypertension. *Am J Respir Crit Care Med.* 2014;189(10):1260-72.

93. Li CG, Mahon C, Sweeney NM, Verschueren E, Kantamani V, Li D, et al. PPARgamma Interaction with UBR5/ATMIN Promotes DNA Repair to Maintain Endothelial Homeostasis. *Cell Rep.* 2019;26(5):1333-43 e7.

94. McGoon MD, and Miller DP. REVEAL: a contemporary US pulmonary arterial hypertension registry. *Eur Respir Rev.* 2012;21(123):8-18.

95. Benza RL, Miller DP, Barst RJ, Badesch DB, Frost AE, and McGoon MD. An Evaluation of Long-term Survival From Time of Diagnosis in Pulmonary Arterial Hypertension From the REVEAL Registry. *Chest.* 2012;142(2):448-56.

96. Shapiro S, Traiger GL, Turner M, McGoon MD, Wason P, and Barst RJ. Sex differences in the diagnosis, treatment, and outcome of patients with pulmonary arterial hypertension enrolled in the registry to evaluate early and long-term pulmonary arterial hypertension disease management. *Chest.* 2012;141(2):363-73.

97. Badesch DB, Raskob GE, Elliott CG, Krichman AM, Farber HW, Frost AE, et al. Pulmonary arterial hypertension: baseline characteristics from the REVEAL Registry. *Chest.* 2010;137(2):376-87.

98. Frost AE, Badesch DB, Barst RJ, Benza RL, Elliott CG, Farber HW, et al. The changing picture of patients with pulmonary arterial hypertension in the United States: how REVEAL differs from historic and non-US Contemporary Registries. *Chest.* 2011;139(1):128-37.

99. Hoeper MM, Boucly A, and Sitbon O. Age, risk and outcomes in idiopathic pulmonary arterial hypertension. *Eur Respir J.* 2018;51(5).

100. Prince MJ, Wu F, Guo Y, Gutierrez Robledo LM, O'Donnell M, Sullivan R, et al. The burden of disease in older people and implications for health policy and practice. *Lancet.* 2015;385(9967):549-62.

101. Guazzi M. Pulmonary hypertension in heart failure preserved ejection fraction: prevalence, pathophysiology, and clinical perspectives. *Circ Heart Fail.* 2014;7(2):367-77.

102. Gopal DM, Santhanakrishnan R, Wang YC, Ayalon N, Donohue C, Rahban Y, et al. Impaired Right Ventricular Hemodynamics Indicate Preclinical Pulmonary Hypertension in Patients With Metabolic Syndrome. *Journal of the American Heart Association: Cardiovascular and Cerebrovascular Disease.* 2015;4(3):e001597.

103. Seeger W, Adir Y, Barbera JA, Champion H, Coghlan JG, Cottin V, et al. Pulmonary hypertension in chronic lung diseases. *J Am Coll Cardiol.* 2013;62(25 Suppl):D109-16.

104. Gulati S, and Thannickal VJ. The Aging Lung and Idiopathic Pulmonary Fibrosis. *Am J Med Sci.* 2019;357(5):384-9.

105. Covella M, Rowin EJ, Hill NS, Preston IR, Milan A, Opotowsky AR, et al. Mechanism of Progressive Heart Failure and Significance of Pulmonary Hypertension in Obstructive Hypertrophic Cardiomyopathy. *Circ Heart Fail.* 2017;10(4):e003689.

106. Lam CS, Roger VL, Rodeheffer RJ, Borlaug BA, Enders FT, and Redfield MM. Pulmonary hypertension in heart failure with preserved ejection fraction: a community-based study. *J Am Coll Cardiol.* 2009;53(13):1119-26.

107. Chaouat A, Savale L, Chouaid C, Tu L, Sztrymf B, Canuet M, et al. Role for interleukin-6 in COPD-related pulmonary hypertension. *Chest.* 2009;136.

108. Andersen KH, Iversen M, Kjaergaard J, Mortensen J, Nielsen-Kudsk JE, Bendstrup E, et al. Prevalence, predictors, and survival in pulmonary hypertension related to end-stage chronic obstructive pulmonary disease. *J Heart Lung Transplant.* 2012;31(4):373-80.

109. Cottin V, Le Pavec J, Prevot G, Mal H, Humbert M, Simonneau G, et al. Pulmonary hypertension in patients with combined pulmonary fibrosis and emphysema syndrome. *Eur Respir J.* 2010;35(1):105-11.

110. Nathan SD, Shlobin OA, Ahmad S, Urbanek S, and Barnett SD. Pulmonary hypertension and pulmonary function testing in idiopathic pulmonary fibrosis. *Chest.* 2007;131(3):657-63.

111. Behr J, and Ryu JH. Pulmonary hypertension in interstitial lung disease. *Eur Respir J.* 2008;31(6):1357-67.

112. Naeije R, Gerges M, Vachiery JL, Caravita S, Gerges C, and Lang IM. Hemodynamic Phenotyping of Pulmonary Hypertension in Left Heart Failure. *Circ Heart Fail.* 2017;10(9).

113. Lai YC, Wang L, and Gladwin MT. Insights into the pulmonary vascular complications of heart failure with preserved ejection fraction. *J Physiol.* 2019;597(4):1143-56.

114. Fang JC, DeMarco T, Givertz MM, Borlaug BA, Lewis GD, Rame JE, et al. World Health Organization Pulmonary Hypertension group 2: pulmonary hypertension due to left heart disease in the adult--a summary statement from the Pulmonary Hypertension Council of the International Society for Heart and Lung Transplantation. *J Heart Lung Transplant.* 2012;31(9):913-33.

115. Farber HW, Miller DP, Poms AD, Badesch DB, Frost AE, Rouzic EM-L, et al. Five-Year Outcomes of Patients Enrolled in the REVEAL Registry. *Chest.* 2015;148(4):1043-54.

116. Nickel N, Golpon H, Greer M, Knudsen L, Olsson K, Westerkamp V, et al. The prognostic impact of follow-up assessments in patients with idiopathic pulmonary arterial hypertension. *Eur Respir J.* 2012;39(3):589-96.

117. Lau EMT, Giannoulatou E, Celermajer DS, and Humbert M. Epidemiology and treatment of pulmonary arterial hypertension. *Nature Reviews Cardiology.* 2017;14(10):603-14.

118. Davie N, Haleen SJ, Upton PD, Polak JM, Yacoub MH, Morrell NW, et al. ET(A) and ET(B) receptors modulate the proliferation of human pulmonary artery smooth muscle cells. *Am J Respir Crit Care Med.* 2002;165(3):398-405.

119. Stewart DJ, Levy RD, Cernacek P, and Langleben D. Increased plasma endothelin-1 in pulmonary hypertension: marker or mediator of disease? *Ann Intern Med.* 1991;114(6):464-9.

120. Giaid A, Yanagisawa M, Langleben D, Michel RP, Levy R, Shennib H, et al. Expression of Endothelin-1 in the Lungs of Patients with Pulmonary Hypertension. *New England Journal of Medicine.* 1993;328(24):1732-9.

121. Rubin LJ, Badesch DB, Barst RJ, Galie N, Black CM, Keogh A, et al. Bosentan therapy for pulmonary arterial hypertension. *N Engl J Med.* 2002;346(12):896-903.

122. Galie N, Olschewski H, Oudiz RJ, Torres F, Frost A, Ghofrani HA, et al. Ambrisentan for the treatment of pulmonary arterial hypertension: results of the ambrisentan in pulmonary arterial hypertension, randomized, double-blind, placebo-controlled, multicenter, efficacy (ARIES) study 1 and 2. *Circulation.* 2008;117(23):3010-9.

123. Pulido T, Adzerikho I, Channick RN, Delcroix M, Galie N, Ghofrani HA, et al. Macitentan and morbidity and mortality in pulmonary arterial hypertension. *N Engl J Med.* 2013;369(9):809-18.

124. Giaid A, and Saleh D. Reduced expression of endothelial nitric oxide synthase in the lungs of patients with pulmonary hypertension. *N Engl J Med.* 1995;333(4):214-21.

125. Alp NJ, and Channon KM. Regulation of endothelial nitric oxide synthase by tetrahydrobiopterin in vascular disease. *Arterioscler Thromb Vasc Biol.* 2004;24(3):413-20.

126. Khoo JP, Zhao L, Alp NJ, Bendall JK, Nicoli T, Rockett K, et al. Pivotal role for endothelial tetrahydrobiopterin in pulmonary hypertension. *Circulation.* 2005;111(16):2126-33.

127. Schermuly RT, Stasch JP, Pullamsetti SS, Middendorff R, Müller D, Schlüter KD, et al. Expression and function of soluble guanylate cyclase in pulmonary arterial hypertension. *European Respiratory Journal.* 2008;32(4):881.

128. Rubin LJ, Galie N, Grimminger F, Grunig E, Humbert M, Jing ZC, et al. Riociguat for the treatment of pulmonary arterial hypertension: a long-term extension study (PATENT-2). *Eur Respir J.* 2015;45(5):1303-13.

129. Humbert M, Coghlan JG, Ghofrani HA, Grimminger F, He JG, Riemekasten G, et al. Riociguat for the treatment of pulmonary arterial hypertension associated with connective tissue disease: results from PATENT-1 and PATENT-2. *Ann Rheum Dis.* 2017;76(2):422-6.

130. Cartin-Ceba R, Halank M, Ghofrani HA, Humbert M, Mattson J, Fritsch A, et al. Riociguat treatment for portopulmonary hypertension: a subgroup analysis from the PATENT-1/-2 studies. *Pulm Circ.* 2018;8(2):2045894018769305.

131. Ghofrani HA, D'Armini AM, Grimminger F, Hoeper MM, Jansa P, Kim NH, et al. Riociguat for the treatment of chronic thromboembolic pulmonary hypertension. *N Engl J Med.* 2013;369(4):319-29.

132. Pichl A, Sommer N, Bednorz M, Seimetz M, Hadzic S, Kuhnert S, et al. Riociguat for treatment of pulmonary hypertension in COPD: a translational study. *Eur Respir J.* 2019;53(6).

133. Rybalkin SD, Rybalkina IG, Feil R, Hofmann F, and Beavo JA. Regulation of cGMP-specific phosphodiesterase (PDE5) phosphorylation in smooth muscle cells. *J Biol Chem.* 2002;277(5):3310-7.

134. Galie N, Ghofrani HA, Torbicki A, Barst RJ, Rubin LJ, Badesch D, et al. Sildenafil citrate therapy for pulmonary arterial hypertension. *N Engl J Med.* 2005;353(20):2148-57.

135. Galie N, Brundage BH, Ghofrani HA, Oudiz RJ, Simonneau G, Safdar Z, et al. Tadalafil therapy for pulmonary arterial hypertension. *Circulation.* 2009;119(22):2894-903.

136. Rubin LJ, Badesch DB, Fleming TR, Galie N, Simonneau G, Ghofrani HA, et al. Long-term treatment with sildenafil citrate in pulmonary arterial hypertension: the SUPER-2 study. *Chest.* 2011;140(5):1274-83.

137. Gomberg-Maitland M, and Olschewski H. Prostacyclin therapies for the treatment of pulmonary arterial hypertension. *Eur Respir J.* 2008;31(4):891-901.

138. Christman BW, McPherson CD, Newman JH, King GA, Bernard GR, Groves BM, et al. An imbalance between the excretion of thromboxane and prostacyclin metabolites in pulmonary hypertension. *N Engl J Med.* 1992;327(2):70-5.

139. Tuder RM, Cool CD, Geraci MW, Wang J, Abman SH, Wright L, et al. Prostacyclin synthase expression is decreased in lungs from patients with severe pulmonary hypertension. *Am J Respir Crit Care Med.* 1999;159.

140. Hoshikawa Y, Voelkel NF, Gesell TL, Moore MD, Morris KG, Alger LA, et al. Prostacyclin receptor-dependent modulation of pulmonary vascular remodeling. *Am J Respir Crit Care Med.* 2001;164(2):314-8.

141. Jing ZC, Parikh K, Pulido T, Jerjes-Sanchez C, White RJ, Allen R, et al. Efficacy and safety of oral treprostinil monotherapy for the treatment of pulmonary arterial hypertension: a randomized, controlled trial. *Circulation.* 2013;127(5):624-33.

142. McLaughlin VV, Benza RL, Rubin LJ, Channick RN, Voswinckel R, Tapson VF, et al. Addition of inhaled treprostinil to oral therapy for pulmonary arterial hypertension: a randomized controlled clinical trial. *J Am Coll Cardiol.* 2010;55(18):1915-22.

143. Sitbon O, Channick R, Chin KM, Frey A, Gaine S, Galie N, et al. Selexipag for the Treatment of Pulmonary Arterial Hypertension. *N Engl J Med.* 2015;373(26):2522-33.

144. Lajoie AC, Lauziere G, Lega JC, Lacasse Y, Martin S, Simard S, et al. Combination therapy versus monotherapy for pulmonary arterial hypertension: a meta-analysis. *Lancet Respir Med.* 2016;4(4):291-305.

145. Galiè N, Corris PA, Frost A, Girgis RE, Granton J, Jing ZC, et al. Updated treatment algorithm of pulmonary arterial hypertension. *J Am Coll Cardiol.* 2013;62(25 Suppl):D60-72.

146. Al-Omary MS, Sugito S, Boyle AJ, Sverdlov AL, and Collins NJ. Pulmonary Hypertension Due to Left Heart Disease: Diagnosis, Pathophysiology, and Therapy. *Hypertension.* 2020;75(6):1397-408.

147. Michelakis ED, Gurtu V, Webster L, Barnes G, Watson G, Howard L, et al. Inhibition of pyruvate dehydrogenase kinase improves pulmonary arterial hypertension in genetically susceptible patients. *Science Translational Medicine.* 2017;9(413).

148. Ruiter G, Manders E, Happe CM, Schalij I, Groepenhoff H, Howard LS, et al. Intravenous iron therapy in patients with idiopathic pulmonary arterial hypertension and iron deficiency. *Pulm Circ.* 2015;5(3):466-72.

149. Van der Feen DE, Kurakula K, Tremblay E, Boucherat O, Bossers GP, Szulcek R, et al. Multicenter Preclinical Validation of BET Inhibition for the Treatment of Pulmonary Arterial Hypertension. *Am J Respir Crit Care Med.* 2019.

150. Sitbon O, Gomberg-Maitland M, Granton J, Lewis MI, Mathai SC, Rainisio M, et al. Clinical trial design and new therapies for pulmonary arterial hypertension. *Eur Respir J.* 2019;53(1).

151. Grinnan D, Trankle C, Andruska A, Bloom B, and Spiekerkoetter E. Drug repositioning in pulmonary arterial hypertension: challenges and opportunities. *Pulm Circ.* 2019;9(1):2045894019832226.

152. Lill R. Function and biogenesis of iron–sulphur proteins. *Nature.* 2009;460(7257):831-8.

153. Rouault TA. Mammalian iron-sulphur proteins: novel insights into biogenesis and function. *Nat Rev Mol Cell Biol.* 2015;16(1):45-55.

154. Fuss JO, Tsai CL, Ishida JP, and Tainer JA. Emerging critical roles of Fe-S clusters in DNA replication and repair. *Biochim Biophys Acta.* 2015;1853(6):1253-71.

155. Paul VD, and Lill R. Biogenesis of cytosolic and nuclear iron-sulfur proteins and their role in genome stability. *Biochim Biophys Acta.* 2015;1853(6):1528-39.

156. Uzarska MA, Nasta V, Weiler BD, Spantgar F, Ciofi-Baffoni S, Saviello MR, et al. Mitochondrial Bol1 and Bol3 function as assembly factors for specific iron-sulfur proteins. *Elife.* 2016;5.

157. Rouault TA, and Maio N. Biogenesis and functions of mammalian iron-sulfur proteins in the regulation of iron homeostasis and pivotal metabolic pathways. *Journal of Biological Chemistry.* 2017;292(31):12744-53.

158. Rudolf J, Makrantoni V, Ingledew WJ, Stark MJR, and White MF. The DNA Repair Helicases XPD and FancJ Have Essential Iron-Sulfur Domains. *Molecular Cell.* 2006;23(6):801-8.

159. Lehmann AR. The xeroderma pigmentosum group D (XPD) gene: one gene, two functions, three diseases. *Genes Dev.* 2001;15(1):15-23.

160. Cantor S, Drapkin R, Zhang F, Lin Y, Han J, Pamidi S, et al. The BRCA1-associated protein BACH1 is a DNA helicase targeted by clinically relevant inactivating mutations. *Proc Natl Acad Sci U S A.* 2004;101(8):2357-62.

161. Deng Z, Glousker G, Molczan A, Fox AJ, Lamm N, Dheekollu J, et al. Inherited mutations in the helicase RTEL1 cause telomere dysfunction and Hoyeraal–Hreidarsson syndrome. *Proceedings of the National Academy of Sciences.* 2013;110(36):E3408.

162. Conde CD, Petronczki ÖY, Baris S, Willmann KL, Girardi E, Salzer E, et al. Polymerase δ deficiency causes syndromic immunodeficiency with replicative stress. *The Journal of clinical investigation.* 2019;129(10):4194-206.

163. Netz DJA, Stith CM, Stümpfig M, Köpf G, Vogel D, Genau HM, et al. Eukaryotic DNA polymerases require an iron-sulfur cluster for the formation of active complexes. *Nature chemical biology.* 2012;8(1):125-32.

164. Kispal G, Csere P, Prohl C, and Lill R. The mitochondrial proteins Atm1p and Nfs1p are essential for biogenesis of cytosolic Fe/S proteins. *EMBO J.* 1999;18(14):3981-9.

165. Tong W-H, and Rouault TA. Functions of mitochondrial ISCU and cytosolic ISCU in mammalian iron-sulfur cluster biogenesis and iron homeostasis. *Cell Metabolism.* 2006;3(3):199-210.

166. Adam AC, Bornhövd C, Prokisch H, Neupert W, and Hell K. The Nfs1 interacting protein Isd11 has an essential role in Fe/S cluster biogenesis in mitochondria. *EMBO J.* 2006;25(1):174-83.

167. Gerber J, Mühlenhoff U, and Lill R. An interaction between frataxin and Isu1/Nfs1 that is crucial for Fe/S cluster synthesis on Isu1. *EMBO Rep.* 2003;4(9):906-11.

168. Wang T, and Craig EA. Binding of yeast frataxin to the scaffold for Fe-S cluster biogenesis, Isu. *The Journal of biological chemistry.* 2008;283(18):12674-9.

169. Schmucker S, Martelli A, Colin F, Page A, Wattenhofer-Donzé M, Reutenauer L, et al. Mammalian frataxin: an essential function for cellular viability through an interaction with a preformed ISCU/NFS1/ISD11 iron-sulfur assembly complex. *PLoS One.* 2011;6(1):e16199.

170. Stehling O, Vashisht AA, Mascarenhas J, Jonsson ZO, Sharma T, Netz DJA, et al. MMS19 Assembles Iron-Sulfur Proteins Required for DNA Metabolism and Genomic Integrity. *Science.* 2012;337(6091):195.

171. Mochel F, Knight MA, Tong WH, Hernandez D, Ayyad K, Taivassalo T, et al. Splice mutation in the iron-sulfur cluster scaffold protein ISCU causes myopathy with exercise intolerance. *Am J Hum Genet.* 2008;82(3):652-60.

172. Olsson A, Lind L, Thornell LE, and Holmberg M. Myopathy with lactic acidosis is linked to chromosome 12q23.3-24.11 and caused by an intron mutation in the ISCU gene resulting in a splicing defect. *Hum Mol Genet.* 2008;17(11):1666-72.

173. Navarro-Sastre A, Tort F, Stehling O, Uzarska Marta A, Arranz José A, del Toro M, et al. A Fatal Mitochondrial Disease Is Associated with Defective NFU1 Function in the Maturation of a Subset of Mitochondrial Fe-S Proteins. *American Journal of Human Genetics.* 2011;89(5):656-67.

174. Cameron JM, Janer A, Levandovskiy V, Mackay N, Rouault TA, Tong W-H, et al. Mutations in iron-sulfur cluster scaffold genes NFU1 and BOLA3 cause a fatal deficiency of multiple respiratory chain and 2-oxoacid dehydrogenase enzymes. *American journal of human genetics.* 2011;89(4):486-95.

175. Ahting U, Mayr JA, Vanlander AV, Hardy SA, Santra S, Makowski C, et al. Clinical, biochemical, and genetic spectrum of seven patients with NFU1 deficiency. *Frontiers in Genetics.* 2015;6:123.

176. Haack TB, Rolinski B, Haberberger B, Zimmermann F, Schum J, Strecker V, et al. Homozygous missense mutation in BOLA3 causes multiple mitochondrial dysfunctions syndrome in two siblings. *Journal of Inherited Metabolic Disease.* 2013;36(1):55-62.

177. Niihori M, Eccles CA, Kurdyukov S, Zemskova M, Varghese MV, Stepanova AA, et al. Rats with Human Mutation of NFU1 Develop Pulmonary Hypertension. *Am J Respir Cell Mol Biol.* 2019.

178. Vander Heiden MG, Cantley LC, and Thompson CB. Understanding the Warburg Effect: The Metabolic Requirements of Cell Proliferation. *Science.* 2009;324(5930):1029-33.

179. Brusselmans K, Compernolle V, Tjwa M, Wiesener MS, Maxwell PH, Collen D, et al. Heterozygous deficiency of hypoxia-inducible factor–2α protects mice against pulmonary hypertension and right ventricular dysfunction during prolonged hypoxia. *J Clin Invest.* 2003;111(10):1519-27.

180. Bencze KZ, Kondapalli KC, Cook JD, McMahon S, Millán-Pacheco C, Pastor N, et al. The Structure and Function of Frataxin. *Critical reviews in biochemistry and molecular biology.* 2006;41(5):269-91.

181. Bridwell-Rabb J, Fox NG, Tsai C-L, Winn AM, and Barondeau DP. Human Frataxin Activates Fe–S Cluster Biosynthesis by Facilitating Sulfur Transfer Chemistry. *Biochemistry.* 2014;53(30):4904-13.

182. Yoon T, and Cowan JA. Frataxin-mediated iron delivery to ferrochelatase in the final step of heme biosynthesis. *J Biol Chem.* 2004;279(25):25943-6.

183. Campuzano V, Montermini L, Moltò MD, Pianese L, Cossée M, Cavalcanti F, et al. Friedreich's ataxia: autosomal recessive disease caused by an intronic GAA triplet repeat expansion. *Science.* 1996;271(5254):1423-7.

184. Campuzano V, Montermini L, Lutz Y, Cova L, Hindelang C, Jiralerspong S, et al. Frataxin is reduced in Friedreich ataxia patients and is associated with mitochondrial membranes. *Hum Mol Genet.* 1997;6(11):1771-80.

185. Cossée M, Dürr A, Schmitt M, Dahl N, Trouillas P, Allinson P, et al. Friedreich's ataxia: point mutations and clinical presentation of compound heterozygotes. *Ann Neurol.* 1999;45(2):200-6.

186. Sakamoto N, Ohshima K, Montermini L, Pandolfo M, and Wells RD. Sticky DNA, a self-associated complex formed at long GAA*TTC repeats in intron 1 of the frataxin gene, inhibits transcription. *J Biol Chem.* 2001;276(29):27171-7.

187. Herman D, Jenssen K, Burnett R, Soragni E, Perlman SL, and Gottesfeld JM. Histone deacetylase inhibitors reverse gene silencing in Friedreich's ataxia. *Nat Chem Biol.* 2006;2(10):551-8.

188. Kvistholm Jensen M, and Bundgaard H. Cardiomyopathy in Friedreich Ataxia. *Exemplifying the Challenges Faced by Cardiologists in the Management of Rare Diseases.* 2012;125(13):1591-3.

189. Saccà F, Puorro G, Antenora A, Marsili A, Denaro A, Piro R, et al. A combined nucleic acid and protein analysis in Friedreich ataxia: implications for diagnosis, pathogenesis and clinical trial design. *PLoS One.* 2011;6(3):e17627.

190. Labuda M, Labuda D, Miranda C, Poirier J, Soong BW, Barucha NE, et al. Unique origin and specific ethnic distribution of the Friedreich ataxia GAA expansion. *Neurology.* 2000;54(12):2322-4.

191. Koeppen AH. Friedreich's ataxia: Pathology, pathogenesis, and molecular genetics. *Journal of the neurological sciences.* 2011;303(1-2):1-12.

192. Schulz JB, Boesch S, Bürk K, Dürr A, Giunti P, Mariotti C, et al. Diagnosis and treatment of Friedreich ataxia: a European perspective. *Nature Reviews Neurology.* 2009;5(4):222-34.

193. Harding AE. Friedreich's ataxia: a clinical and genetic study of 90 families with an analysis of early diagnostic criteria and intrafamilial clustering of clinical features. *Brain.* 1981;104(3):589-620.

194. Pandolfo M. Friedreich ataxia: the clinical picture. *J Neurol.* 2009;256 Suppl 1:3-8.

195. Filla A, De Michele G, Cavalcanti F, Pianese L, Monticelli A, Campanella G, et al. The relationship between trinucleotide (GAA) repeat length and clinical features in Friedreich ataxia. *Am J Hum Genet.* 1996;59(3):554-60.

196. Dürr A, Cossee M, Agid Y, Campuzano V, Mignard C, Penet C, et al. Clinical and genetic abnormalities in patients with Friedreich's ataxia. *N Engl J Med.* 1996;335(16):1169-75.

197. Tsou AY, Paulsen EK, Lagedrost SJ, Perlman SL, Mathews KD, Wilmot GR, et al. Mortality in Friedreich Ataxia. *Journal of the Neurological Sciences.* 2011;307(1–2):46-9.

198. Hanson E, Sheldon M, Pacheco B, Alkubeysi M, and Raizada V. Heart disease in Friedreich's ataxia. *World J Cardiol.* 2019;11(1):1-12.

199. Ong KC, Geske JB, Hebl VB, Nishimura RA, Schaff HV, Ackerman MJ, et al. Pulmonary hypertension is associated with worse survival in hypertrophic cardiomyopathy. *European Heart Journal – Cardiovascular Imaging.* 2016;17(6):604-10.

200. James TN, and Fisch C. Observations on the Cardiovascular Involvement in Friedreich's Ataxia. *Am Heart J.* 1963;66:164-75.

201. Payne RM. The Heart in Friedreich's Ataxia: Basic Findings and Clinical Implications. *Prog Pediatr Cardiol.* 2011;31(2):103-9.

202. Hanson E, Sheldon M, Pacheco B, Alkubeysi M, and Raizada V. Heart disease in Friedreich's ataxia. *World J Cardiol.* 2019;11(1):1-12.

203. Rotig A, de Lonlay P, Chretien D, Foury F, Koenig M, Sidi D, et al. Aconitase and mitochondrial iron-sulphur protein deficiency in Friedreich ataxia. *Nat Genet.* 1997;17(2):215-7.

204. Lodi R, Cooper JM, Bradley JL, Manners D, Styles P, Taylor DJ, et al. Deficit of in vivo mitochondrial ATP production in patients with Friedreich ataxia. *Proc Natl Acad Sci U S A.* 1999;96(20):11492-5.

205. Lamarche JB, Côté M, and Lemieux B. The cardiomyopathy of Friedreich's ataxia morphological observations in 3 cases. *Can J Neurol Sci.* 1980;7(4):389-96.

206. Ramirez RL, Qian J, Santambrogio P, Levi S, and Koeppen AH. Relation of cytosolic iron excess to cardiomyopathy of Friedreich's ataxia. *Am J Cardiol.* 2012;110(12):1820-7.

207. Michael S, Petrocine SV, Qian J, Lamarche JB, Knutson MD, Garrick MD, et al. Iron and iron-responsive proteins in the cardiomyopathy of Friedreich's ataxia. *Cerebellum.* 2006;5(4):257-67.

208. Schulz JB, Dehmer T, Schols L, Mende H, Hardt C, Vorgerd M, et al. Oxidative stress in patients with Friedreich ataxia. *Neurology.* 2000;55(11):1719-21.

209. Bradley JL, Homayoun S, Hart PE, Schapira AH, and Cooper JM. Role of oxidative damage in Friedreich's ataxia. *Neurochem Res.* 2004;29(3):561-7.

210. Wong A, Yang J, Cavadini P, Gellera C, Lonnerdal B, Taroni F, et al. The Friedreich's ataxia mutation confers cellular sensitivity to oxidant stress which is rescued by chelators of iron and calcium and inhibitors of apoptosis. *Hum Mol Genet.* 1999;8(3):425-30.

211. Chantrel-Groussard K, Geromel V, Puccio H, Koenig M, Munnich A, Rötig A, et al. Disabled early recruitment of antioxidant defenses in Friedreich's ataxia. *Hum Mol Genet.* 2001;10(19):2061-7.

212. Puccio H, Simon D, Cossee M, Criqui-Filipe P, Tiziano F, Melki J, et al. Mouse models for Friedreich ataxia exhibit cardiomyopathy, sensory nerve defect and Fe-S enzyme deficiency followed by intramitochondrial iron deposits. *Nat Genet.* 2001;27(2):181-6.

213. Huang ML, Sivagurunathan S, Ting S, Jansson PJ, Austin CJ, Kelly M, et al. Molecular and functional alterations in a mouse cardiac model of Friedreich ataxia: activation of the integrated stress response, eIF2α phosphorylation, and the induction of downstream targets. *Am J Pathol.* 2013;183(3):745-57.

214. Karthikeyan G, Lewis LK, and Resnick MA. The mitochondrial protein frataxin prevents nuclear damage. *Hum Mol Genet.* 2002;11(11):1351-62.

215. Haugen AC, Di Prospero NA, Parker JS, Fannin RD, Chou J, Meyer JN, et al. Altered Gene Expression and DNA Damage in Peripheral Blood Cells from Friedreich's Ataxia Patients: Cellular Model of Pathology. *PLoS Genetics.* 2010;6(1):e1000812.

216. Karthikeyan G, Santos JH, Graziewicz MA, Copeland WC, Isaya G, Houten BV, et al. Reduction in frataxin causes progressive accumulation of mitochondrial damage. *Human Molecular Genetics.* 2003;12(24):3331-42.

217. Khonsari H, Schneider M, Al-Mahdawi S, Chianea YG, Themis M, Parris C, et al. Lentivirus-meditated frataxin gene delivery reverses genome instability in Friedreich ataxia patient and mouse model fibroblasts. *Gene Ther.* 2016;23(12):846-56.

218. Martelli A, Wattenhofer-Donzé M, Schmucker S, Bouvet S, Reutenauer L, and Puccio H. Frataxin is essential for extramitochondrial Fe-S cluster proteins in mammalian tissues. *Hum Mol Genet.* 2007;16(22):2651-8.

219. Veatch JR, McMurray MA, Nelson ZW, and Gottschling DE. Mitochondrial dysfunction leads to nuclear genome instability via an iron-sulfur cluster defect. *Cell.* 2009;137(7):1247-58.

220. Igoillo-Esteve M, Gurgul-Convey E, Hu A, Romagueira Bichara Dos Santos L, Abdulkarim B, Chintawar S, et al. Unveiling a common mechanism of apoptosis in beta-cells and neurons in Friedreich's ataxia. *Hum Mol Genet.* 2015;24(8):2274-86.

221. Santos MM, Ohshima K, and Pandolfo M. Frataxin deficiency enhances apoptosis in cells differentiating into neuroectoderm. *Hum Mol Genet.* 2001;10(18):1935-44.

222. Palomo GM, Cerrato T, Gargini R, and Diaz-Nido J. Silencing of frataxin gene expression triggers p53-dependent apoptosis in human neuron-like cells. *Hum Mol Genet.* 2011;20(14):2807-22.

223. Mincheva-Tasheva S, Obis E, Tamarit J, and Ros J. Apoptotic cell death and altered calcium homeostasis caused by frataxin depletion in dorsal root ganglia neurons can be prevented by BH4 domain of Bcl-xL protein. *Hum Mol Genet.* 2014;23(7):1829-41.

224. Bolinches-Amoros A, Molla B, Pla-Martin D, Palau F, and Gonzalez-Cabo P. Mitochondrial dysfunction induced by frataxin deficiency is associated with cellular senescence and abnormal calcium metabolism. *Front Cell Neurosci.* 2014;8:124.

225. Molla B, Riveiro F, Bolinches-Amoros A, Munoz-Lasso DC, Palau F, and Gonzalez-Cabo P. Two different pathogenic mechanisms, dying-back axonal neuropathy and pancreatic senescence, are present in the YG8R mouse model of Friedreich's ataxia. *Dis Model Mech.* 2016;9(6):647-57.

226. Gottesfeld JM, Rusche JR, and Pandolfo M. Increasing frataxin gene expression with histone deacetylase inhibitors as a therapeutic approach for Friedreich's ataxia. *J Neurochem.* 2013;126 Suppl 1(0 1):147-54.

227. Libri V, Yandim C, Athanasopoulos S, Loyse N, Natisvili T, Law PP, et al. Epigenetic and neurological effects and safety of high-dose nicotinamide in patients with Friedreich's ataxia: an exploratory, open-label, dose-escalation study. *The Lancet.* 2014;384(9942):504-13.

228. Interferon-γ shows promise in a mouse model of Friedreich ataxia. *Nature Reviews Neurology.* 2012;8(5):242-.

229. Li L, Voullaire L, Sandi C, Pook MA, Ioannou PA, Delatycki MB, et al. Pharmacological screening using an FXN-EGFP cellular genomic reporter assay for the therapy of Friedreich ataxia. *PLoS One.* 2013;8(2):e55940.

230. Seyer L, Greeley N, Foerster D, Strawser C, Gelbard S, Dong Y, et al. Open-label pilot study of interferon gamma-1b in Friedreich ataxia. *Acta Neurol Scand.* 2015;132(1):7-15.

231. Yiu EM, Tai G, Peverill RE, Lee KJ, Croft KD, Mori TA, et al. An open-label trial in Friedreich ataxia suggests clinical benefit with high-dose resveratrol, without effect on frataxin levels. *J Neurol.* 2015;262(5):1344-53.

232. Lynch DR, Hauser L, McCormick A, Wells M, Dong YN, McCormack S, et al. Randomized, double-blind, placebo-controlled study of interferon-γ 1b in Friedreich Ataxia. *Annals of Clinical and Translational Neurology.* 2019;6(3):546-53.

233. Rustin P, von Kleist-Retzow JC, Chantrel-Groussard K, Sidi D, Munnich A, and Rotig A. Effect of idebenone on cardiomyopathy in Friedreich's ataxia: a preliminary study. *Lancet.* 1999;354(9177):477-9.

234. Hausse AO, Aggoun Y, Bonnet D, Sidi D, Munnich A, Rötig A, et al. Idebenone and reduced cardiac hypertrophy in Friedreich's ataxia. *Heart.* 2002;87(4):346-9.

235. Mariotti C, Solari A, Torta D, Marano L, Fiorentini C, and Di Donato S. Idebenone treatment in Friedreich patients: one-year-long randomized placebo-controlled trial. *Neurology.* 2003;60(10):1676-9.

236. Lynch DR, Perlman SL, and Meier T. A phase 3, double-blind, placebo-controlled trial of idebenone in friedreich ataxia. *Arch Neurol.* 2010;67(8):941-7.

237. Lagedrost SJ, Sutton MS, Cohen MS, Satou GM, Kaufman BD, Perlman SL, et al. Idebenone in Friedreich ataxia cardiomyopathy-results from a 6-month phase III study (IONIA). *Am Heart J.* 2011;161(3):639-45 e1.

238. Paupe V, Dassa EP, Goncalves S, Auchère F, Lönn M, Holmgren A, et al. Impaired nuclear Nrf2 translocation undermines the oxidative stress response in Friedreich ataxia. *PLoS One.* 2009;4(1):e4253.

239. Zesiewicz T, Salemi JL, Perlman S, Sullivan KL, Shaw JD, Huang Y, et al. Double-blind, randomized and controlled trial of EPI-743 in Friedreich's ataxia. *Neurodegener Dis Manag.* 2018;8(4):233-42.

240. Pandolfo M, and Hausmann L. Deferiprone for the treatment of Friedreich's ataxia. *J Neurochem.* 2013;126 Suppl 1:142-6.

241. Velasco-Sánchez D, Aracil A, Montero R, Mas A, Jiménez L, O'Callaghan M, et al. Combined therapy with idebenone and deferiprone in patients with Friedreich's ataxia. *Cerebellum.* 2011;10(1):1-8.

242. Jensen MK, and Bundgaard H. Cardiomyopathy in Friedreich ataxia: exemplifying the challenges faced by cardiologists in the management of rare diseases. *Circulation.* 2012;125(13):1591-3.

243. Nathan SD, Barbera JA, Gaine SP, Harari S, Martinez FJ, Olschewski H, et al. Pulmonary hypertension in chronic lung disease and hypoxia. *Eur Respir J.* 2019;53(1).

244. Campuzano V, Montermini L, Lutz Y, Cova L, Hindelang C, Jiralerspong S, et al. Frataxin is reduced in Friedreich ataxia patients and is associated with mitochondrial membranes. *Hum Mol Genet.* 1997;6(11):1771-80.

245. Ast T, Meisel JD, Patra S, Wang H, Grange RMH, Kim SH, et al. Hypoxia Rescues Frataxin Loss by Restoring Iron Sulfur Cluster Biogenesis. *Cell.* 2019;177(6):1507-21 e16.

246. Hoff KG, Culler SJ, Nguyen PQ, McGuire RM, Silberg JJ, and Smolke CD. In Vivo Fluorescent Detection of Fe-S Clusters Coordinated by Human GRX2. *Chemistry & Biology.* 2009;16(12):1299-308.

247. Bertero T, Cottrill K, Krauszman A, Lu Y, Annis S, Hale A, et al. The microRNA-130/301 family controls vasoconstriction in pulmonary hypertension. *J Biol Chem.* 2014;290(4):2069-85.

248. Jasoliya MJ, McMackin MZ, Henderson CK, Perlman SL, and Cortopassi GA. Frataxin deficiency impairs mitochondrial biogenesis in cells, mice and humans. *Hum Mol Genet.* 2017;26(14):2627-33.

249. Zhang B, Alruwaili N, Kandhi S, Deng W, Huang A, Wolin MS, et al. Inhibition of ferrochelatase impairs vascular eNOS/NO and sGC/cGMP signaling. *PLoS One.* 2018;13(7):e0200307.

250. Cooper CE. Nitric oxide and iron proteins. *Biochimica et Biophysica Acta (BBA) - Bioenergetics.* 1999;1411(2):290-309.

251. Sakao S, Tatsumi K, and Voelkel NF. Endothelial cells and pulmonary arterial hypertension: apoptosis, proliferation, interaction and transdifferentiation. *Respir Res.* 2009;10(1):95.

252. Guignabert C, Tu L, Drascovic I, François C, Dartevelle P, Simonneau G, et al. p53-dependent, replicative cell senescence suppresses chronic hypoxia-Induced pulmonary hypertension in mice. *European Respiratory Journal.* 2011;38(Suppl 55):3436.

253. Noureddine H, Gary-Bobo G, Alifano M, Marcos E, Saker M, Vienney N, et al. Pulmonary artery smooth muscle cell senescence is a pathogenic mechanism for pulmonary hypertension in chronic lung disease. *Circ Res.* 2011;109(5):543-53.

254. Patro R, Duggal G, Love MI, Irizarry RA, and Kingsford C. Salmon provides fast and bias-aware quantification of transcript expression. *Nat Methods.* 2017;14(4):417-9.

255. Anders S, and Huber W. Differential expression analysis for sequence count data. *Genome Biol.* 2010;11(10):R106.

256. Huang da W, Sherman BT, and Lempicki RA. Systematic and integrative analysis of large gene lists using DAVID bioinformatics resources. *Nat Protoc.* 2009;4(1):44-57.

257. Huang da W, Sherman BT, and Lempicki RA. Bioinformatics enrichment tools: paths toward the comprehensive functional analysis of large gene lists. *Nucleic Acids Res.* 2009;37(1):1-13.

258. The Gene Ontology C. Expansion of the Gene Ontology knowledgebase and resources. *Nucleic Acids Res.* 2017;45(D1):D331-D8.

259. Ashburner M, Ball CA, Blake JA, Botstein D, Butler H, Cherry JM, et al. Gene ontology: tool for the unification of biology. The Gene Ontology Consortium. *Nat Genet.* 2000;25(1):25-9.

260. Nieminuszczy J, Schwab RA, and Niedzwiedz W. The DNA fibre technique - tracking helicases at work. *Methods.* 2016;108:92-8.

261. Wang Y, Nakayama M, Pitulescu ME, Schmidt TS, Bochenek ML, Sakakibara A, et al. Ephrin-B2 controls VEGF-induced angiogenesis and lymphangiogenesis. *Nature.* 2010;465(7297):483-6.

262. Wirth A, Benyo Z, Lukasova M, Leutgeb B, Wettschureck N, Gorbey S, et al. G12-G13-LARG-mediated signaling in vascular smooth muscle is required for salt-induced hypertension. *Nat Med.* 2008;14(1):64-8.

263. Dahlman JE, Barnes C, Khan OF, Thiriot A, Jhunjunwala S, Shaw TE, et al. In vivo endothelial siRNA delivery using polymeric nanoparticles with low molecular weight. *Nat Nano.* 2014;9(8):648-55.

264. Bertero T, Lu Y, Annis S, Hale A, Bhat B, Saggar R, et al. Systems-level regulation of microRNA networks by miR-130/301 promotes pulmonary hypertension. *J Clin Invest.* 2014;124(8):3514-28.

265. Zhang Y, Li H, Zhang C, An X, Liu L, Stubbe J, et al. Conserved electron donor complex Dre2-Tah18 is required for ribonucleotide reductase metallocofactor assembly and DNA synthesis. *Proc Natl Acad Sci U S A.* 2014;111(17):E1695-704.

266. Rabinovitch M, Guignabert C, Humbert M, and Nicolls MR. Inflammation and Immunity in the Pathogenesis of Pulmonary Arterial Hypertension. *Circulation research.* 2014;115(1):165-75.

267. Chang J, Wang Y, Shao L, Laberge RM, Demaria M, Campisi J, et al. Clearance of senescent cells by ABT263 rejuvenates aged hematopoietic stem cells in mice. *Nat Med.* 2016;22(1):78-83.

268. Shackelford RE, Kaufmann WK, and Paules RS. Oxidative stress and cell cycle checkpoint function. *Free Radic Biol Med.* 2000;28(9):1387-404.

269. Maya-Mendoza A, Moudry P, Merchut-Maya JM, Lee M, Strauss R, and Bartek J. High speed of fork progression induces DNA replication stress and genomic instability. *Nature.* 2018;559(7713):279-84.

270. Poli J, Tsaponina O, Crabbe L, Keszthelyi A, Pantesco V, Chabes A, et al. dNTP pools determine fork progression and origin usage under replication stress. *EMBO J.* 2012;31(4):883-94.

271. Davidson MB, Katou Y, Keszthelyi A, Sing TL, Xia T, Ou J, et al. Endogenous DNA replication stress results in expansion of dNTP pools and a mutator phenotype. *EMBO J.* 2012;31(4):895-907.

272. Sanvisens N, Bano MC, Huang M, and Puig S. Regulation of ribonucleotide reductase in response to iron deficiency. *Mol Cell.* 2011;44(5):759-69.

273. Aird KM, Zhang G, Li H, Tu Z, Bitler BG, Garipov A, et al. Suppression of nucleotide metabolism underlies the establishment and maintenance of oncogene-induced senescence. *Cell Rep.* 2013;3(4):1252-65.

274. Sakao S, Tatsumi K, and Voelkel NF. Endothelial cells and pulmonary arterial hypertension: apoptosis, proliferation, interaction and transdifferentiation. *Respiratory Research.* 2009;10(1):95-.

275. Minamino T, Miyauchi H, Yoshida T, Ishida Y, Yoshida H, and Komuro I. Endothelial Cell Senescence in Human Atherosclerosis. *Circulation.* 2002;105(13):1541-4.

276. Jia G, Aroor AR, Jia C, and Sowers JR. Endothelial cell senescence in aging-related vascular dysfunction. *Biochimica et Biophysica Acta (BBA) - Molecular Basis of Disease.* 2019;1865(7):1802-9.

277. Steiner MK, Syrkina OL, Kolliputi N, Mark EJ, Hales CA, and Waxman AB. IL-6 Overexpression Induces Pulmonary Hypertension. *Circulation research.* 2009;104(2):236-44.

278. Soon E, Holmes AM, Treacy CM, Doughty NJ, Southgate L, Machado RD, et al. Elevated levels of inflammatory cytokines predict survival in idiopathic and familial pulmonary arterial hypertension. *Circulation.* 2010;122.

279. Heresi GA, Aytekin M, Hammel JP, Wang S, Chatterjee S, and Dweik RA. Plasma interleukin-6 adds prognostic information in pulmonary arterial hypertension. *Eur Respir J.* 2014;43(3):912-4.

280. Cracowski JL, Chabot F, Labarere J, Faure P, Degano B, Schwebel C, et al. Proinflammatory cytokine levels are linked to death in pulmonary arterial hypertension. *Eur Respir J.* 2014;43(3):915-7.

281. Herranz N, and Gil J. Mechanisms and functions of cellular senescence. *J Clin Invest.* 2018;128(4):1238-46.

282. Oktay Y, Dioum E, Matsuzaki S, Ding K, Yan LJ, Haller RG, et al. Hypoxia-inducible factor 2alpha regulates expression of the mitochondrial aconitase chaperone protein frataxin. *J Biol Chem.* 2007;282(16):11750-6.

283. Nanayakkara G, Alasmari A, Mouli S, Eldoumani H, Quindry J, McGinnis G, et al. Cardioprotective HIF-1alpha-frataxin signaling against ischemia-reperfusion injury. *Am J Physiol Heart Circ Physiol.* 2015;309(5):H867-79.

284. Ferecatu I, Canal F, Fabbri L, Mazure NM, Bouton C, and Golinelli-Cohen MP. Dysfunction in the mitochondrial Fe-S assembly machinery leads to formation of the chemoresistant truncated VDAC1 isoform without HIF-1alpha activation. *PLoS One.* 2018;13(3):e0194782.

285. Gomez-Arroyo JG, Farkas L, Alhussaini AA, Farkas D, Kraskauskas D, Voelkel NF, et al. The monocrotaline model of pulmonary hypertension in perspective. *Am J Physiol Lung Cell Mol Physiol.* 2012;302(4):L363-9.

286. George MP, Champion HC, Simon M, Guyach S, Tarantelli R, Kling HM, et al. Physiologic changes in a nonhuman primate model of HIV-associated pulmonary arterial hypertension. *Am J Respir Cell Mol Biol.* 2013;48(3):374-81.

287. Meng Q, Lai YC, Kelly NJ, Bueno M, Baust JJ, Bachman TN, et al. Development of a Mouse Model of Metabolic Syndrome, Pulmonary Hypertension, and Heart Failure with Preserved Ejection Fraction. *Am J Respir Cell Mol Biol.* 2017;56(4):497-505.

288. Lai YC, Tabima DM, Dube JJ, Hughan KS, Vanderpool RR, Goncharov DA, et al. SIRT3-AMP-Activated Protein Kinase Activation by Nitrite and Metformin Improves Hyperglycemia and Normalizes Pulmonary Hypertension Associated With Heart Failure With Preserved Ejection Fraction. *Circulation.* 2016;133(8):717-31.

289. Rabinovitch M, Guignabert C, Humbert M, and Nicolls MR. Inflammation and Immunity in the Pathogenesis of Pulmonary Arterial Hypertension. *Circ Res.* 2014;115(1):165-75.

290. Yuan Y, Hilliard G, Ferguson T, and Millhorn DE. Cobalt inhibits the interaction between hypoxia-inducible factor-alpha and von Hippel-Lindau protein by direct binding to hypoxia-inducible factor-alpha. *J Biol Chem.* 2003;278(18):15911-6.

291. De Biase I, Chutake YK, Rindler PM, and Bidichandani SI. Epigenetic silencing in Friedreich ataxia is associated with depletion of CTCF (CCCTC-binding factor) and antisense transcription. *PLoS One.* 2009;4(11):e7914.

292. Roy AR, Ahmed A, DiStefano PV, Chi L, Khyzha N, Galjart N, et al. The transcriptional regulator CCCTC-binding factor limits oxidative stress in endothelial cells. *Journal of Biological Chemistry.* 2018;293(22):8449-61.

293. Gottesfeld JM, Rusche JR, and Pandolfo M. Increasing frataxin gene expression with histone deacetylase inhibitors as a therapeutic approach for Friedreich's ataxia. *J Neurochem.* 2013;126 Suppl 1:147-54.

294. Meloche J, Potus F, Vaillancourt M, Bourgeois A, Johnson I, Deschamps L, et al. Bromodomain-Containing Protein 4: The Epigenetic Origin of Pulmonary Arterial Hypertension. *Circ Res.* 2015;117(6):525-35.

295. Filippakopoulos P, and Knapp S. Targeting bromodomains: epigenetic readers of lysine acetylation. *Nat Rev Drug Discov.* 2014;13(5):337-56.

296. Seal J, Lamotte Y, Donche F, Bouillot A, Mirguet O, Gellibert F, et al. Identification of a novel series of BET family bromodomain inhibitors: Binding mode and profile of I-BET151 (GSK1210151A). *Bioorganic & Medicinal Chemistry Letters.* 2012;22(8):2968-72.

297. Niedernhofer LJ, and Robbins PD. Senotherapeutics for healthy ageing. *Nature Reviews Drug Discovery.* 2018;17(5):377-.

298. Lesniewski LA, Seals DR, Walker AE, Henson GD, Blimline MW, Trott DW, et al. Dietary rapamycin supplementation reverses age-related vascular dysfunction and oxidative stress, while modulating nutrient-sensing, cell cycle, and senescence pathways. *Aging Cell.* 2017;16(1):17-26.

299. Csiszar A, Labinskyy N, Olson S, Pinto JT, Gupte S, Wu JM, et al. Resveratrol prevents monocrotaline-induced pulmonary hypertension in rats. *Hypertension.* 2009;54(3):668-75.

300. Childs BG, Gluscevic M, Baker DJ, Laberge RM, Marquess D, Dananberg J, et al. Senescent cells: an emerging target for diseases of ageing. *Nat Rev Drug Discov.* 2017;16(10):718-35.

301. Cotticelli MG, Xia S, Kaur A, Lin D, Wang Y, Ruff E, et al. Identification of p38 MAPK as a novel therapeutic target for Friedreich's ataxia. *Sci Rep.* 2018;8(1):5007.

302. Kane GC, Sachdev A, Villarraga HR, Ammash NM, Oh JK, McGoon MD, et al. Impact of age on pulmonary artery systolic pressures at rest and with exercise. *Echo Research and Practice.* 2016;3(2):53-61.

303. Koutnikova H, Campuzano V, Foury F, Dollé P, Cazzalini O, and Koenig M. Studies of human, mouse and yeast homologues indicate a mitochondrial function for frataxin. *Nature Genetics.* 1997;16(4):345-51.

304. Loría F, and Díaz-Nido J. Frataxin knockdown in human astrocytes triggers cell death and the release of factors that cause neuronal toxicity. *Neurobiol Dis.* 2015;76:1-12.

305. Fil D, Chacko BK, Conley R, Ouyang X, Zhang J, Darley-Usmar VM, et al. Mitochondrial damage and senescence phenotype of cells derived from a novel frataxin G127V point mutation mouse model of Friedreich's ataxia. *Disease Models & Mechanisms.* 2020:dmm.045229.

306. Castaldo I, Vergara P, Pinelli M, Filla A, De Michele G, Cocozza S, et al. Can telomere shortening in human peripheral blood leukocytes serve as a disease biomarker of Friedreich's ataxia? *Antioxid Redox Signal.* 2013;18(11):1303-6.

307. Anjomani Virmouni S, Al-Mahdawi S, Sandi C, Yasaei H, Giunti P, Slijepcevic P, et al. Identification of telomere dysfunction in Friedreich ataxia. *Mol Neurodegener.* 2015;10:22-.

308. Gu M, Mordwinkin NM, Kooreman NG, Lee J, Wu H, Hu S, et al. Pravastatin reverses obesity-induced dysfunction of induced pluripotent stem cell-derived endothelial cells via a nitric oxide-dependent mechanism. *European Heart Journal.* 2015;36(13):806-16.

309. Gu M, Shao N-Y, Sa S, Li D, Termglinchan V, Ameen M, et al. Patient-Specific iPSC-Derived Endothelial Cells Uncover Pathways that Protect against Pulmonary Hypertension in BMPR2 Mutation Carriers. *Cell Stem Cell.* 2017;20(4):490-504.e5.

310. Ku S, Soragni E, Campau E, Thomas EA, Altun G, Laurent LC, et al. Friedreich's ataxia induced pluripotent stem cells model intergenerational GAATTC triplet repeat instability. *Cell Stem Cell.* 2010;7(5):631-7.

311. Gu M, Shao NY, Sa S, Li D, Termglinchan V, Ameen M, et al. Patient-Specific iPSC-Derived Endothelial Cells Uncover Pathways that Protect against Pulmonary Hypertension in BMPR2 Mutation Carriers. *Cell Stem Cell.* 2017;20(4):490-504 e5.

312. Mouraret N, Houssaini A, Abid S, Quarck R, Marcos E, Parpaleix A, et al. Role for telomerase in pulmonary hypertension. *Circulation.* 2015;131(8):742-55.

313. Perdomini M, Hick A, Puccio H, and Pook MA. Animal and cellular models of Friedreich ataxia. *Journal of Neurochemistry.* 2013;126:65-79.

314. Bourgeois A, Bonnet S, Breuils-Bonnet S, Habbout K, Paradis R, Tremblay E, et al. Inhibition of CHK1 (Checkpoint Kinase 1) Elicits Therapeutic Effects in Pulmonary Arterial Hypertension. *Arterioscler Thromb Vasc Biol.* 2019:ATVBAHA119312537.

315. Ong KC, Geske JB, Hebl VB, Nishimura RA, Schaff HV, Ackerman MJ, et al. Pulmonary hypertension is associated with worse survival in hypertrophic cardiomyopathy. *Eur Heart J Cardiovasc Imaging.* 2016;17(6):604-10.

316. Qian W, Kumar N, Roginskaya V, Fouquerel E, Opresko PL, Shiva S, et al. Chemoptogenetic damage to mitochondria causes rapid telomere dysfunction. *Proc Natl Acad Sci U S A.* 2019;116(37):18435-44.

317. Sahin E, Colla S, Liesa M, Moslehi J, Müller FL, Guo M, et al. Telomere dysfunction induces metabolic and mitochondrial compromise. *Nature.* 2011;470(7334):359-65.

318. Fang EF, Scheibye-Knudsen M, Brace LE, Kassahun H, SenGupta T, Nilsen H, et al. Defective mitophagy in XPA via PARP-1 hyperactivation and NAD(+)/SIRT1 reduction. *Cell.* 2014;157(4):882-96.

319. Rudolf J, Makrantoni V, Ingledew WJ, Stark MJ, and White MF. The DNA repair helicases XPD and FancJ have essential iron-sulfur domains. *Mol Cell.* 2006;23(6):801-8.

320. Cameron Jessie M, Janer A, Levandovskiy V, MacKay N, Rouault Tracey A, Tong W-H, et al. Mutations in Iron-Sulfur Cluster Scaffold Genes NFU1 and BOLA3 Cause a Fatal Deficiency of Multiple Respiratory Chain and 2-Oxoacid Dehydrogenase Enzymes. *The American Journal of Human Genetics.* 2011;89(4):486-95.

321. Richardson DR, Lane DJR, Becker EM, Huang MLH, Whitnall M, Rahmanto YS, et al. Mitochondrial iron trafficking and the integration of iron metabolism between the mitochondrion and cytosol. *Proceedings of the National Academy of Sciences.* 2010;107(24):10775.

322. Martelli A, Schmucker S, Reutenauer L, Mathieu Jacques RR, Peyssonnaux C, Karim Z, et al. Iron Regulatory Protein 1 Sustains Mitochondrial Iron Loading and Function in Frataxin Deficiency. *Cell Metabolism.* 2015;21(2):311-22.

323. Steinkellner H, Singh HN, Muckenthaler MU, Goldenberg H, Moganty RR, Scheiber-Mojdehkar B, et al. No changes in heme synthesis in human Friedreich´s ataxia erythroid progenitor cells. *Gene.* 2017;621:5-11.

324. Hedblom A, Hejazi SM, Canesin G, Choudhury R, Hanafy KA, Csizmadia E, et al. Heme detoxification by heme oxygenase-1 reinstates proliferative and immune balances upon genotoxic tissue injury. *Cell Death & Disease.* 2019;10(2):72.

325. Shan H, Li T, Zhang L, Yang R, Li Y, Zhang M, et al. Heme oxygenase-1 prevents heart against myocardial infarction by attenuating ischemic injury-induced cardiomyocytes senescence. *EBioMedicine.* 2019;39:59-68.

326. Fredenburgh LE, Perrella MA, and Mitsialis SA. The role of heme oxygenase-1 in pulmonary disease. *American journal of respiratory cell and molecular biology.* 2007;36(2):158-65.

327. Rhodes CJ, Howard LS, Busbridge M, Ashby D, Kondili E, Gibbs JSR, et al. Iron Deficiency and Raised Hepcidin in Idiopathic Pulmonary Arterial Hypertension: Clinical Prevalence, Outcomes, and Mechanistic Insights. *Journal of the American College of Cardiology.* 2011;58(3):300-9.

328. Lakhal-Littleton S, Crosby A, Frise MC, Mohammad G, Carr CA, Loick PAM, et al. Intracellular iron deficiency in pulmonary arterial smooth muscle cells induces pulmonary arterial hypertension in mice. *Proceedings of the National Academy of Sciences.* 2019;116(26):13122.

329. Frise MC, Cheng HY, Nickol AH, Curtis MK, Pollard KA, Roberts DJ, et al. Clinical iron deficiency disturbs normal human responses to hypoxia. *J Clin Invest.* 2016;126(6):2139-50.

330. Ghosh MC, Zhang D-L, Jeong SY, Kovtunovych G, Ollivierre-Wilson H, Noguchi A, et al. Deletion of Iron Regulatory Protein 1 Causes Polycythemia and Pulmonary Hypertension in Mice through Translational De-repression of HIF2α. *Cell metabolism.* 2013;17(2):271-81.

331. Wang X, Mendelsohn L, Rogers H, Leitman S, Raghavachari N, Yang Y, et al. Heme-bound iron activates placenta growth factor in erythroid cells via erythroid Krüppel-like factor. *Blood.* 2014;124(6):946-54.

332. O'Blenes SB, Fischer S, McIntyre B, Keshavjee S, and Rabinovitch M. Hemodynamic unloading leads to regression of pulmonary vascular disease in rats. *J Thorac Cardiovasc Surg.* 2001;121(2):279-89.

333. Abe K, Shinoda M, Tanaka M, Kuwabara Y, Yoshida K, Hirooka Y, et al. Haemodynamic unloading reverses occlusive vascular lesions in severe pulmonary hypertension. *Cardiovasc Res.* 2016;111(1):16-25.

334. Wagenvoort CA, Wagenvoort N, and Draulans-Noë Y. Reversibility of plexogenic pulmonary arteriopathy following banding of the pulmonary artery. *J Thorac Cardiovasc Surg.* 1984;87(6):876-86.

335. Mikus E, Stepanenko A, Krabatsch T, Loforte A, Dandel M, Lehmkuhl HB, et al. Reversibility of fixed pulmonary hypertension in left ventricular assist device support recipients. *European Journal of Cardio-Thoracic Surgery.* 2011;40(4):971-7.

336. Testa L, Latib A, De Marco F, De Carlo M, Fiorina C, Montone R, et al. Persistence of Severe Pulmonary Hypertension After Transcatheter Aortic Valve Replacement. *Circulation: Cardiovascular Interventions.* 2016;9(6):e003563.

337. Fawzy ME, Osman A, Nambiar V, Nowayhed O, El DA, Badr A, et al. Immediate and long-term results of mitral balloon valvuloplasty in patients with severe pulmonary hypertension. *J Heart Valve Dis.* 2008;17(5):485-91.

338. van Riel AC, Schuuring MJ, van Hessen ID, Zwinderman AH, Cozijnsen L, Reichert CL, et al. Contemporary prevalence of pulmonary arterial hypertension in adult congenital heart disease following the updated clinical classification. *Int J Cardiol.* 2014;174(2):299-305.

339. Lévy M, Maurey C, Celermajer DS, Vouhé PR, Danel C, Bonnet D, et al. Impaired apoptosis of pulmonary endothelial cells is associated with intimal proliferation and irreversibility of pulmonary hypertension in congenital heart disease. *J Am Coll Cardiol.* 2007;49(7):803-10.

340. Sakao S, Tatsumi K, and Voelkel NF. Reversible or irreversible remodeling in pulmonary arterial hypertension. *American journal of respiratory cell and molecular biology.* 2010;43(6):629-34.

341. Brown LM, Chen H, Halpern S, Taichman D, McGoon MD, Farber HW, et al. Delay in recognition of pulmonary arterial hypertension: factors identified from the REVEAL Registry. *Chest.* 2011;140(1):19-26.

342. Ormiston ML, Southgate L, Treacy C, Pepke-Zaba J, Trembath RC, Machado RD, et al. Assessment of a Pulmonary Origin for Blood Outgrowth Endothelial Cells by Examination of Identical Twins Harboring a BMPR2 Mutation. *American Journal of Respiratory and Critical Care Medicine.* 2013;188(2):258-60.

343. Smits J, Tasev D, Andersen S, Szulcek R, Botros L, Ringgaard S, et al. Blood Outgrowth and Proliferation of Endothelial Colony Forming Cells are Related to Markers of Disease Severity in Patients with Pulmonary Arterial Hypertension. *International journal of molecular sciences.* 2018;19(12):3763.

344. Mathai SC, Bueso M, Hummers LK, Boyce D, Lechtzin N, Le Pavec J, et al. Disproportionate elevation of N-terminal pro-brain natriuretic peptide in scleroderma-related pulmonary hypertension. *European Respiratory Journal.* 2010;35(1):95.

345. Mauritz G-J, Rizopoulos D, Groepenhoff H, Tiede H, Felix J, Eilers P, et al. Usefulness of Serial N-Terminal Pro–B-Type Natriuretic Peptide Measurements for Determining Prognosis in Patients With Pulmonary Arterial Hypertension. *The American Journal of Cardiology.* 2011;108(11):1645-50.

346. Pezzuto B, Badagliacca R, Poscia R, Ghio S, D'Alto M, Vitulo P, et al. Circulating biomarkers in pulmonary arterial hypertension: update and future direction. *J Heart Lung Transplant.* 2015;34(3):282-305.

347. Hemnes AR. Current and Emerging Biomarkers for Pulmonary Hypertension. *Advances in Pulmonary Hypertension.* 2018;16(3):136-40.

348. Giugliano GR, and Sethi PS. Friedreich's ataxia as a cause of premature coronary artery disease. *Tex Heart Inst J.* 2007;34(2):214-7.

349. Raman SV, Phatak K, Hoyle JC, Pennell ML, McCarthy B, Tran T, et al. Impaired myocardial perfusion reserve and fibrosis in Friedreich ataxia: a mitochondrial cardiomyopathy with metabolic syndrome. *Eur Heart J.* 2011;32(5):561-7.

350. Maron BJ, Wolfson JK, Epstein SE, and Roberts WC. Intramural ("small vessel") coronary artery disease in hypertrophic cardiomyopathy. *J Am Coll Cardiol.* 1986;8(3):545-57.

351. Cecchi F, Olivotto I, Gistri R, Lorenzoni R, Chiriatti G, and Camici PG. Coronary microvascular dysfunction and prognosis in hypertrophic cardiomyopathy. *N Engl J Med.* 2003;349(11):1027-35.

352. Galati G, Leone O, Pasquale F, Olivotto I, Biagini E, Grigioni F, et al. Histological and Histometric Characterization of Myocardial Fibrosis in End-Stage Hypertrophic Cardiomyopathy: A Clinical-Pathological Study of 30 Explanted Hearts. *Circ Heart Fail.* 2016;9(9).

353. Jacobs W, van de Veerdonk MC, Trip P, de Man F, Heymans MW, Marcus JT, et al. The right ventricle explains sex differences in survival in idiopathic pulmonary arterial hypertension. *Chest.* 2014;145(6):1230-6.

354. Niihori M, Eccles CA, Kurdyukov S, Zemskova M, Varghese MV, Stepanova AA, et al. Rats with a Human Mutation of NFU1 Develop Pulmonary Hypertension. *Am J Respir Cell Mol Biol.* 2020;62(2):231-42.

355. Richardson TE, Yang S-H, Wen Y, and Simpkins JW. Estrogen Protection in Friedreich's Ataxia Skin Fibroblasts. *Endocrinology.* 2011;152(7):2742-9.

356. Richardson TE, Yu AE, Wen Y, Yang S-H, and Simpkins JW. Estrogen Prevents Oxidative Damage to the Mitochondria in Friedreich's Ataxia Skin Fibroblasts. *PLoS One.* 2012;7(4):e34600.

357. Ghorbani M, Pousset F, Tucker A, Swift S, Giunti P, Parkinson M, et al. Analysis of Friedreich's ataxia patient clinical data reveals importance of accurate GAA repeat determination in disease prognosis and gender differences in cardiac measures. *Informatics in Medicine Unlocked.* 2019;17:100266.

358. Thenappan T, Shah SJ, Gomberg-Maitland M, Collander B, Vallakati A, Shroff P, et al. Clinical characteristics of pulmonary hypertension in patients with heart failure and preserved ejection fraction. *Circ Heart Fail.* 2011;4(3):257-65.

359. Hyduk A, Croft JB, Ayala C, Zheng K, Zheng ZJ, and Mensah GA. Pulmonary hypertension surveillance--United States, 1980-2002. *MMWR Surveill Summ.* 2005;54(5):1-28.

360. Lam CSP, Borlaug BA, Kane GC, Enders FT, Rodeheffer RJ, and Redfield MM. Age-Associated Increases in Pulmonary Artery Systolic Pressure in the General Population. *Circulation.* 2009;119(20):2663-70.

361. Baker DJ, Wijshake T, Tchkonia T, LeBrasseur NK, Childs BG, van de Sluis B, et al. Clearance of p16Ink4a-positive senescent cells delays ageing-associated disorders. *Nature.* 2011;479(7372):232-6.

362. Baker DJ, Childs BG, Durik M, Wijers ME, Sieben CJ, Zhong J, et al. Naturally occurring p16(Ink4a)-positive cells shorten healthy lifespan. *Nature.* 2016;530(7589):184-9.

363. Sun N, Youle RJ, and Finkel T. The Mitochondrial Basis of Aging. *Molecular cell.* 2016;61(5):654-66.